The hydrodynamic analysis of a vertical axis tidal current turbine

Gareth I Gretton

A thesis submitted for the degree of Doctor of Philosophy.
The University of Edinburgh.
18th August 2009

Abstract

Tidal currents can be used as a predictable source of sustainable energy, and have the potential to make a useful contribution to the energy needs of the UK and other countries with such a resource.

One of the technologies which may be used to transform tidal power into mechanical power is a vertical axis turbine, the hydrodynamic analysis of which this thesis is concerned with. The aim of this analysis is to gain a better understanding of the power transformation process, from which position there is the possibility of improving the conversion efficiency. A second aim is to compare the results from different modelling approaches.

Two types of mathematical modelling are used: a basic blade element momentum model and a more complex Reynolds-averaged Navier Stokes (RANS) model. The former model has been programmed in Matlab by the present author while the latter model uses a commercial computational fluid dynamics (CFD) code, ANSYS CFX. This RANS model uses the SST k-ω turbulence model.

The CFD analysis of hydrofoils (equally airfoils), for both fixed and oscillating pitch conditions, is a significant proportion of the present work. Such analysis is used as part of the verification and validation of the CFD model of the turbine. It is also used as input to the blade element momentum model, thereby permitting a novel comparison between the blade element momentum model and the CFD model of the turbine.

Both types of turbine model were used to explore the variation in turbine efficiency (and other factors) with tip speed ratio and with and without an angle of attack limiting variable pitch strategy. It is shown that the use of such a variable pitch strategy both increases the peak efficiency and broadens the peak.

The comparison of the results from the two different turbine modelling approaches shows that when the present CFD hydrofoil results are used as input to the blade element model, and when dynamic effects are small and the turbine induction factor is low, there is generally good agreement between the two models.

Declaration of originality

I hereby declare that this thesis has been composed by myself and that except where stated, the work contained is my own.

I also declare that the work contained in this thesis has not been submitted for any other degree or professional qualification except as specified.

Gareth Gretton

Acknowledgements

I would like to begin by thanking Stephen Salter for proposing this thesis topic and for his unorthodox insight. For their formal and informal supervision of this project I would like to thank Tom Bruce and David Ingram; more specifically, I would like to thank Tom for being persistently encouraging and supportive, and David for his help with the theory and practice of CFD.

Thanks are due to my office mates Jamie Taylor, Grégory Payne, Jorge Lucas and Rémy Pascal (in order of appearance) for everything that good office mates should be thanked for. In a similar vein thanks also to the wider community of the Institute for Energy Systems and the School of Engineering.

For doing what is often a thankless job I would like to thank the staff of the IT department within the School of Engineering. In particular, thanks to Bruce Duncan, Michael Gordon, and David Stewart for getting things working on the cluster and managing recalcitrant license servers.

Others I would like to thank personally for their help with this project are Paul Cooper, Peter Fraenkel, Peter Johnson, Liz McRae and Joanna Whelan.

For funding this work I would like to thank Edinburgh Designs and the Engineering and Physical Sciences Research Council (i.e. the UK taxpayer).

Those staff of the ANSYS CFX support team who have given helpful and detailed replies are gratefully acknowledged.

I would also like to say thanks to those people whom I have never met that provided helpful responses to emails. Such replies have often resulted in the very satisfying tying up of loose ends.

Finally, and on a more personal level, I would like to thank my girlfriend Rebecca Day and my parents Ron and Kay for their support of, and perseverance with, me.

Contents

List of figures

List of tables

Chapter 1
Introduction

1.1 The need for sustainable energy

Climate change is real and is very likely the result of anthropogenic greenhouse gas emissions (IPCC, 2007, pp. 2, 5). These greenhouse gas emissions are due primarily to fossil fuel use (IPCC, 2007, p. 5) i.e. the combustion of oil, natural gas and coal which accounts for approximately 80% of global primary energy supply (IEA, 2008, p. 6). Clearly a solution, or almost inevitably a range of solutions (Pacala and Socolow, 2004), is or are required. Tidal current turbines, the hydrodynamic analysis of which this thesis is concerned with, could usefully be part of the solution.

1.2 The advantages of tidal current energy

The key advantage of tidal energy relative to many other renewable energy technologies lies in its predictability. Neglecting effects due to changing weather patterns, which are small in all but extreme cases, tidal generation can be predicted years into the future, essentially with as much accuracy as is required.

Two issues arise due to the nature of tidal cycles. First, it is only possible to generate power during a certain part of the tidal cycle, basically around a period half way between high and low (and low and high) tide. This problem is offset to a certain extent by the different phasing of the tidal cycle around the British Isles. The second issue relates to the differing magnitudes of the peak tidal currents over the 14 day spring-neap cycle.[1] The ratio of peak spring current to peak neap current is often around two; given the cubic relation between power and speed this means that there is almost an order of magnitude difference in the power available. Economic considerations in selecting a rated speed for the turbine will likely reduce this ratio; in addition some form of energy storage might be considered.

[1] Peak current refers to the maximum value during a given 6.2 hour period between high and low or low and high. The spring-neap cycle is due to the changing alignment of the sun-earth-moon system. See section 2.6.1 for further details.

The energy potential of the UK's tidal current resource has been estimated at 18 TWh/y (Black and Veatch, 2005a); such a figure represents the energy that could be extracted subject to certain technological limits. By comparison the UK's primary energy demand in 2007 was 2742 TWh while total electricity demand was 400 TWh.[2] The tidal current energy potential thus represents 0.7% of the UK's primary energy demand and 4.5% of its electricity demand. Both figures are given here because whilst the latter are more often given, the former give a more realistic impression of the scale of the energy problem. Whether tidal current energy can make a 'significant', 'considerable' or 'meaningful' contribution to the UK's energy demand must be a philosophical question. The view of the author is that it can be, but only if demand can be reduced. Given that 21% of primary energy supply is currently wasted in the form of heat rejected to the environment from conventional power stations, this would seem possible.[3]

1.3 A brief history of tidal energy

As with many other sources of sustainable energy, the idea of extracting energy from the tides is not new. Tidal power was originally harnessed in tide mills, the earliest known examples of which (at least in Europe) are found in Ireland; the oldest of these, found in Strangford Lough, has been dated to 620 AD (Spain, 2002). These tide mills were based on impounding a body of water at high tide and using this to power a water wheel once sufficient head has developed by the tide ebbing. Interestingly there is also mention of floating tide mills utilizing the tidal currents of the Venetian lagoon in the 11th century, although the historical account is not contemporary (Minchinton, 1979).

During the twentieth century the only operational source of tidal power was from tidal barrage schemes. Such schemes are based on similar principles to tide mills except that the water power is converted to electricity via a turbine similar to those used in conventional low-head hydro schemes. According to Elliott (2004), only four significant tidal barrage schemes exist: on the Rance estuary in Brittany, France (240 MW capacity); on the Annapolis river in Nova Scotia, Canada (18 MW); on the Jangxia creek in the East China Sea (0.5 MW); and in the Kislaya Guba fjord on the Barents Sea coast of Russia (0.4 MW). Further details of the Rance estuary

[2] These figures are from the *Digest of United Kingdom Energy Statistics* (BERR, 2007a). Primary energy demand is given as 235.8 million tonnes of oil equivalent on page 27, where 1 million tonnes of oil equivalent is equal to 11.630 TWh. The total electricity demand is given on page 130.

[3] See again the *Digest*, page 27, and also BERR (2007b), which give transformation losses in electricity generation as 49.6 million tonnes of oil equivalent.

scheme are given by Elliott and by Électricité de France (EDF, 2009), a few of which we note here. It comprises 24 bulb turbines of 10 MW capacity operating in a tidal range of up to 12 m and with a typical head of 5 m. These turbines are capable of two-way operation, thus allowing generation on the flood as well as the ebb tide. They are also capable of acting as pumps in order to increase the head available; this can lead to a net power gain over a cycle as well as allowing for the generating time to be shifted. Elliott suggests that two-way operation without pumping is favoured during spring tides while one way operation with pumping is favoured with neap tides. Different figures are given by the two sources for the annual energy output: Elliott gives 480 GWh/y while the EDF website gives 600 GWh/y.

No tidal barrage schemes have been built in the UK but a number of studies have been conducted, most notably with regards to the Severn estuary. These include two Government energy papers from the 1980s: the Bondi report (Department of Energy, 1981) and the Severn Tidal Power Group (STPG) report (Department of Energy, 1989). The Bondi report favoured three potential crossing lines, one of which was between Lavernock Point near Cardiff to Brean Down near Weston-super-Mare. This option, generally known as the Cardiff-Weston Barrage, was the single option favoured by the later STPG report. In this report it was suggested that such a scheme could generate 17 TWh per year from 8640 MW of capacity using ebb generation with flood pumping. This is equivalent to just over 4% of UK electricity demand in 2007. More recently the STPG were commissioned by the Department of Trade and Industry (DTI) to conduct a definition study for a new appraisal of the project (Taylor, 2002). In addition to this report, the Sustainable Development Commission, an executive non-departmental body of the Government, produced a wider review of tidal energy in the UK, but with a strong focus on a Severn Barrage Scheme (SDC, 2007). This concluded that there was a case for a "sustainable Severn Barrage" if part of "wider and stronger" action by the Government on climate change. These two more recent reports have led the Government to undertake a feasibility study for the Severn Barrage which is currently under way (BERR, 2008, 2009).

Clearly the construction of a tidal barrage scheme will have an impact on the environment; the extent of the impact being determined at least in part by the way in which the barrage scheme is operated. The most obvious effect is that the tidal range is generally reduced. In the case of a scheme with ebb generation this will primarily be due to a higher low water level. This may adversely affect for example mud-wading birds who feed in the inter-tidal mud flats. A potentially positive effect of the reduced range is that the quantity of suspended sediment may

decrease, thus allowing sunlight to penetrate deeper in the water column and consequently increasing the biological productivity of the waters.

The other major issue related to tidal barrage schemes is the high construction cost in comparison with conventional generation. Essentially this makes the cost of electricity very sensitive to the cost of capital. This is one factor which obviously makes the project more attractive today than when last seriously investigated in the 1980s.

Where tidal barrage schemes are based on extracting the potential energy flux at sites with large tidal ranges, tidal current schemes aim to harness the kinetic energy flux at sites with strong currents. Such is the similarity with harnessing wind power that the two most prominent technologies for extracting tidal current power are based on horizontal and vertical axis turbines. Further to this apparent similarity, the aerodynamic models developed for the analysis and design of wind turbines have been applied directly to the design of tidal current turbines, and whilst there may be some differences in behaviour due to the presence of the free surface in tidal flows, tidal current turbines designed with wind turbine models have performed as predicted (Thake, 2005). Other technologies for harnessing tidal current power will be discussed below; for the present time they are included within the scope of 'tidal current turbines'.

The development of tidal current turbines can be closely linked to the commercial prospects for the technology, which has obviously influenced the availability of commercial funding, and has also dictated the availability of government funding (at least that from the UK and the EU). Such government funding has been highly significant in the majority of UK and EU based projects which have been developed from the late 1990s to date, and which will be discussed in the next section. Here we note some of the reports which have informed these funding programmes.

Within the UK the first government supported attempt to assess the magnitude of the tidal current resource and also the likely cost of electricity was in the form of the *UK Tidal Stream Review* by the Energy Technology Support Unit of the UK government (ETSU, 1993). Whilst this report concluded that the resource was considerable – up to 58 TWh/y (Blunden and Bahaj, 2007) – it suggested that it was not economically competitive (Binnie, Black and Veatch, 2001). Two later reports commissioned by the European Commission also examined tidal current power. The first of these, by the International Centre for Island Technology, based in Orkney, considered the feasibility of supplying Orkney and Shetland with power from tidal currents

(ICIT and IT Power, 1995), while the second examined the Europe-wide prospects (EC, 1996). Both of these were more favourable, suggesting lower unit costs for electricity generated (Binnie, Black and Veatch, 2001), and (it is presumed) contributed to the EU awarding grant funding to a number of tidal current projects including IT Power's 'Seaflow' horizontal axis turbine (now developed by MCT) and the vertical axis 'Kobold/Enermar' turbine of the Italian company Ponte di Archimede.

These later European reports did not apparently change the view of the UK government with regards to tidal current energy; for example, in the supporting analysis for the government energy paper *New and Renewable Energy: Prospects for the 21st century* it is stated that "the prospects for conventional tidal stream technology in the UK appear limited" (ETSU, 1999, p. 153). Conventional here means those concepts utilizing proven technology. According to Elliott (2004, pp. 239–240), two further reports which briefly examined the potential of tidal current energy (OST, 1999; RCEP, 2000), prompted the Government to commission a detailed review of tidal current energy. This review, *The Commercial Prospects for Tidal Stream Power* (Binnie, Black and Veatch, 2001), concluded that the unit costs of electricity could be lower than those projected by the *UK Tidal Stream Review* of 1993, As such the report recommended "the promotion of a prototype demonstration scheme to examine, at a realistic scale, the problems associated with constructing, installing and operating the [baseline] scheme". The baseline scheme was IT Power's Seaflow scheme, and grant funding for this was indeed given in 2001. UK Government funding for other schemes also followed.

A number of small tidal current research programmes and demonstration schemes did occur before the late 1990s, a list of which is given in *Commercial Prospects*. We discuss some of these here, giving additional references where consulted. The earliest noted is a workshop held in Palm Beach, Florida during 1973 concerning the use of the Florida current (not actually a tidal current). In the UK the General Electric Company conducted a study of tidal currents during 1976–79 but the results were never published.

One of the earliest projects which can be linked to current developments concerned the development of a vertical axis river current turbine during 1976–84. This project was run by the Intermediate Technology Development Group and then by the newly formed IT Power. An experimental raft mounted turbine was installed on the river Nile in Sudan where it was used to power an irrigation water pump. The design was later developed to use a horizontal axis turbine (Thake, 2005). A contemporary reference, which notes the applicability of the concept to tidal

currents, is found in Fraenkel and Musgrove (1979). This project was followed up in 1993–4 by a consortium of IT Power, Scottish Nuclear and the National Engineering Laboratory, who developed a 'proof of concept' horizontal axis turbine. It consisted of a 3.5 m diameter rotor suspended beneath a floating raft, this being moored to the sea bed. During testing in the Corran Narrows of Loch Linnhe in Scotland the maximum shaft power recorded was 15 kW in a current of 2.25 m/s; this would suggest an power coefficient of 0.27.

A number of experimental vertical axis turbines were constructed by Nova Energy and its successor Blue Energy during the 1980s in Canada in a collaborative research programme with the National Research Council of Canada (Blue Energy, 2009). The turbine used is called the 'Davis hydro turbine' in the Blue Energy literature, but it is understood to be no different from a conventional vertical axis turbine. Models were tested in an hydraulic laboratory test flume, in rivers, in a duct from an hydroelectric dam (with the turbine filling the duct), and in the Florida current. The efficacy of ducts surrounding the turbines in a free flow situation was also investigated. The largest model tested was installed in a duct from a hydroelectric dam and generated 70 kW.

Finally, the *Commercial Prospects* report also notes projects which have occurred in Australia, Japan, the Netherlands and Russia; in each case the experimental models which have been constructed have all had power outputs of the order of kilowatts.

1.4 Current developments

As noted above, the availability of UK and EU government funding from the late 1990s onwards has been a significant factor in the development of tidal current turbines, at least in the UK and EU. This is taken then as a convenient point at which to separate historical developments, as considered above, and current developments.

A number of sources give lists of tidal current energy projects, these including Ainsworth and Thake (2006) and Entec (2007) which list 27 and 24 projects respectively. The European Marine Energy Centre website (EMEC, 2009) lists tidal range technologies with tidal current technologies and includes a total 53 projects. Further projects, known to the author, are not included in these lists. It is clear then that it is not possible to present a complete view of tidal current energy research within the confines of a short introduction. Instead, we aim to note the following: all projects where technologies have been tested at a scale of 100s of kilowatts and

all projects which represent the most advanced development of their type. We consider these according to the device concept: horizontal axis, vertical axis, and others.

1.4.1 Horizontal axis turbines

Horizontal axis turbines represent the dominant technology for tidal current energy extraction at the present time. This is most likely due to the success of this technology for wind energy extraction; as such it is seen as the safest choice of technology for tidal currents. (We shall discuss later in this introduction why vertical axis turbines deserve re-investigation in the context of tidal currents.)

The leading developer in the UK and probably worldwide is Marine Current Turbines (MCT, 2009a). This company was set up to commercially develop the horizontal axis technology originally taken forward under IT Power. The core technology is a mono-pile mounted two-bladed horizontal axis turbine with variable pitch blades; the variable pitch blades are used to optimize the efficiency of power extraction and also to allow for operation on the flood and ebb tides. The turbine rotor and power system can be raised up the pile so that maintenance and repairs can take place above water. There is no yaw mechanism and so the technology is best suited to sites with approximately bi-directional flows. To date two large scale turbines have been installed: Seaflow and Seagen.

Seaflow consists of an 11 m diameter turbine with a rated electrical output of 300 kW (Thake, 2005; IT Power et al., 2005). It was installed in a mean water depth of 25 m approximately 1 km off Foreland Point in North Devon in 2003. The turbine is not grid connected but instead used dump load resistors installed above the sea surface on the mono-pile. It is understood that testing continues on this device. Fraenkel (2007) presents a graph of shaft power versus current speed which shows that the power coefficient is consistently within the range of 37–45%. The design efficiency, calculated from blade element momentum models, was 37%; values higher than this are, according to Fraenkel, largely due to blockage effects.

Seagen is a later development, consisting of twin 16 m diameter turbines each driving a generator with a rated output of 600 kW (Ainsworth and Thake, 2006; Fraenkel, 2007). The two turbine units are mounted at either end of a cross-arm which can be raised up the pile as with the Seaflow scheme. Again, the blades use variable pitch and there is no yaw mechanism. The principle advantage of the cross-arm arrangement is that the turbines are no longer in the

wake of the pile but instead in the much smaller wake of the streamlined cross-arm. This device was installed in Strangford Lough in Northern Ireland in 2008 and is grid connected. The rated power of 1.2 MW was achieved in December 2008 (MCT, 2009b).

A second leading horizontal axis technology is that developed by Hammerfest Strøm in Norway (Hammerfest Strøm, 2009a). This company installed a fully submerged device in 50 m deep water in Kvalsund in northern Norway in 2003; this was tested for four years and then removed. Little technical detail is provided on the website, but one source suggests that the rated power was 300 kW (Thake, 2005). In 2008 it was announced that Hammerfest Strøm would be developing a 60 MW tidal farm with Scottish Power (Hammerfest Strøm, 2009b).

There is some interest in the use of venturi ducts to increase the capture area of tidal current turbines. For example, Lunar Energy (2009) are developing a ducted horizontal axis device with fixed pitch blades capable of bi-directional operation (the structure does not yaw). A scale model of this device has been tested in a towing tank and Lunar Energy claim that the results show an increase in the power coefficient as the yaw angle is increased from 0 to 25 degrees. Such yaw angles would occur if the turbine was installed at a location where the current was not bi-directional. It is not known, however, whether these results have been corrected for blockage effects.

A final horizontal axis concept which might be mentioned is the use of co-axial contra-rotating rotors. Such a concept is being investigated by a team at the University of Strathclyde in Glasgow who have to date published results from tow tank tests (Clarke et al., 2007). The authors claim that the advantages of such a scheme are: near-zero reaction torque on the structure, near-zero swirl in the wake and high relative rotational speeds. There are of course issues related to blade-blade interaction and the cost and complexity of such a scheme.

1.4.2 Vertical axis turbines

The development of vertical axis turbines for tidal current energy extraction is less well advanced than that of horizontal axis turbines. Interestingly, what developments have taken place have been in the main overseas; the reasons for this are unknown.

The origin of the present work lies in some initial studies by Stephen Salter of the University of Edinburgh, first reported in (Salter, 1998). This paper contains a proposal for a 50 m diameter vertical axis turbine with 20 m long variable pitch blades and using a quad ring-cam hydraulic

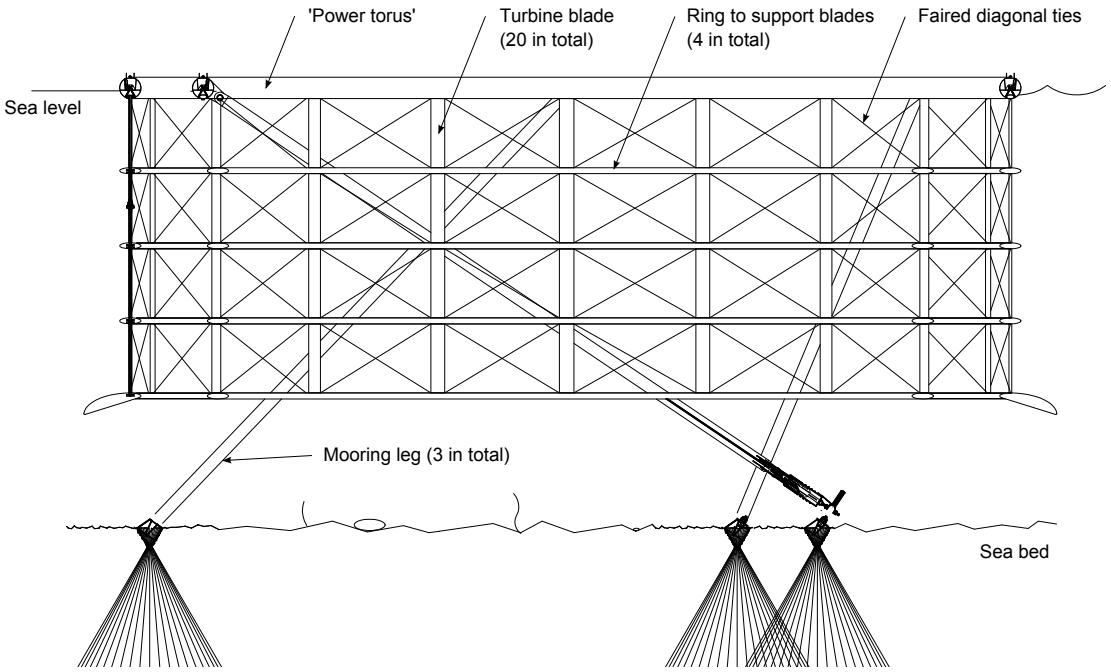

Figure 1.1: *Side view of Stephen Salter's vertical axis tidal current turbine concept, taken from (Salter, 2009) and re-labelled by the present author.*

system contained within a 'power torus' as the power take-off and radial and axial bearing. This power take-off arrangement is particularly novel and avoids the need to transmit torque from the circumference to the axis. Ideas for hydraulic power take-off systems were originally motivated by wave energy applications; see for example (Salter et al., 2002). More recent work on this vertical axis turbine concept is presented in (Salter and Taylor, 2007) and (Salter, 2009). The turbine design, figure 1.1, is similar to that presented in the 1998 paper, but the scale has increased to 140 m in diameter with 51 m long blades. Work on a variable pitch vertical axis turbine design by the company Edinburgh Designs, prompted by the work of Stephen Salter, is discussed in a later section of this chapter.

One vertical axis turbine project has already been noted, namely the EU funded Kobold/Enermar turbine of the Italian company Ponte di Archimede (2009). This turbine has a diameter of 6 m and three blades with 5 m span and 0.4 m chord (Coiro et al., 2005). A passive variable pitch system is used; this allows the blades to pitch according to the hydrodynamic forces until the blades come against end stops. It is understood that this system acts to feather i.e. reduce the angle of attack of the blades. The turbine was installed in the Strait of Messina between Sicily and mainland Italy in 2001; it lies 150 m offshore in a water depth of 20 m where the peak current is 2 m/s (Calcagno et al., 2006). According to a trade magazine report

of a conference presentation by Ponte di Archimede (IWPDC, 2008) the turbine was grid connected in 2005. The same source reports that the net 'water to wire' efficiency is about 25%.

An interesting refinement of the vertical axis concept is the use of helical blades, this being invented by Alexander Gorlov of the Northeastern University in the USA. The primary advantage of this concept is that there is simultaneously a portion of blade in every azimuthal position, meaning that the shaft torque is constant. As will be discussed below, this is not the case with non-helical blades. A paper by Gorban et al. (2001) introduces the design but is primarily concerned with a somewhat obscure (and inaccurate) method of analysing turbines which will be discussed in the *literature review* chapter. The concept is being developed by GCK Technology (2009), but little detailed information is available. Some tests on a 914 mm by 1016 mm prototype are noted. There is also some information that suggests that this concept is being pursued by the Korea Ocean Research and Development Institute KORDI (2006). Note that this concept is being developed for small (kilowatt scale) wind turbines by an apparently unrelated company in the UK (Quiet Revolution, 2009).

A number of academic research groups are known to be working on vertical axis tidal current turbines. These include groups at the University of British Columbia in Vancouver; the University of Naples (who have worked on the Kobold turbine); and the Harbin Engineering University in China (who have worked with Ponte di Archimede and Stephen Salter at the University of Edinburgh, before the time of the present author). Research from these groups is discussed in the *literature review* chapter.

1.4.3 Other concepts

A number of other concepts exist for extracting kinetic energy from tidal currents, two of which are noted here.

'Stingray' is the name of a device consisting of an oscillating hydrofoil mounted on a pivoting arm in an arrangement somewhat like a whale's tail. The hydrofoil is pitched by a set of hydraulic rams such that it causes the arm to pivot upwards and downwards in the tidal flow. Power take-off is by a second set of hydraulic rams which resist the pivoting motion of the arm. This concept was tested at a significant scale in the Yell Sound of Shetland by the Engineering Business in a series of DTI funded projects (Engineering Business, 2002, 2003, 2005). The

hydrofoil of the prototype machine had a span of 15.5 m and chord of 3 m while the arm was 11 m long and could pivot through 70 degrees. The most successful results given in the 2005 report (p. 107) suggest a cycle average hydraulic power output of 117.5 kW in a current of 2 m/s. No value for the power coefficient (as defined for turbines) is given, but one may be calculated from the information report. Taking the frontal area as $15.5\ \text{m} \times 11\ \text{m} \times 2 \sin 35^\circ = 196\ \text{m}^2$ and using all other information as directly reported leads to a power coefficient of 0.15. Such a low value may of course be explained by the experimental nature of the device. It may also be argued that as Stingray is a different device to a horizontal or vertical axis turbine and so the power coefficients cannot be compared directly; nevertheless, as the ratio of blade area to frontal area is similar to that of the Kobold turbine it would suggest that it is fair to make this comparison. Stingray is not at present being developed by the Engineering Business. A similar concept is though being taken forward by another company (Paish et al., 2007; Pulse Generation, 2009).

An alternative concept, which features the possibility of having no moving parts underwater, exists in the form of the Rochester Venturi device, invented by Geoff Rochester of Imperial College London. This device uses the pressure drop that occurs when a flow passes through a constriction to drive a secondary water or air circuit. The power take-off is from a turbine in this secondary circuit. The company HydroVenturi (2009) is developing the technology. Unfortunately no technical information has been released.

1.5 Vertical axis turbines – principle of operation

The vertical axis (wind) turbine was invented by GJM Darrieus and patented in 1931 (Darrieus, 1931). Without prior knowledge of Darrieus' work it was also conceived by South and Rangi of the National Research Council of Canada in 1968 (Paraschivoiu, 2002, p. 3). Vertical axis turbines having blades shaped as a troposkien (the shape a skipping rope assumes) are generally known as Darrieus turbines, although this name is sometimes applied to all types of vertical axis turbines. Such a shape (by definition) means that the centrifugal loads are carried as pure tension rather than as a bending stress. Other names for all types of vertical axis turbine are cross-flow and cycloidal.

Vertical axis turbines have their axes perpendicular to the direction of the oncoming flow whereas horizontal axis turbines have their axes parallel. This property means that a vertical

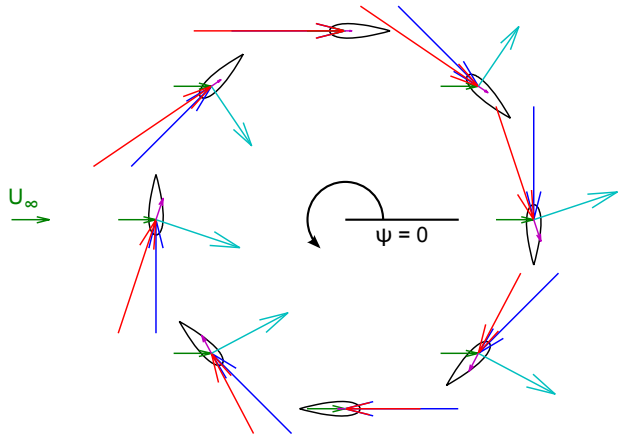

Figure 1.2: *Diagram showing velocity and force vectors for a tip speed ratio of 3 and assuming that the turbine does not affect the flow. The velocity vectors represent the ΩR (blue), flow (green), and relative (red) velocities, while the force vectors represent the lift (cyan) and drag (magenta) forces. The drag vectors are scaled by a factor of 10 relative to the lift vectors in order to make them visible. Note that the $\psi = 0$ reference is used throughout this thesis.*

axis turbine can accept an oncoming flow in a horizontal plane from any direction and therefore do not need a yaw mechanism as with horizontal axis turbines.

A key feature of a vertical axis turbine is that the angle of attack on a blade is a function of the azimuth angle of the blade. (The situation is more complicated when variable pitch is considered, but for the present time we take it that the pitch is fixed.) This is not the case for horizontal axis turbines, unless there are velocity gradients in the free stream flow. The relative flow velocity (the vector sum of the flow velocity and the reverse of the blade velocity) is also a function of the azimuth angle. These three velocities, and the lift and drag forces on the blade, are shown in figure 1.2 for a tip speed ratio ($\lambda = \Omega R/U_\infty$) of 3, while figure 1.3 shows graphically the variation in angle of attack and relative flow velocity for five different values of the tip speed ratio. Note that the azimuth angle is zero directly downstream.

Clearly the way in which the angle of attack and relative flow velocity vary with azimuth angle is a function of the tip speed ratio. For tip speed ratios less than one the angle of attack varies over the complete range 0–360° and is in effect continuously decreasing. At a tip speed ratio of exactly one the range is reduced to ±90° and there is a discontinuity at an azimuth angle of 270°; this discontinuity is physically meaningful because the relative velocity at this point is zero. For all tip speed ratios above one the range in the angle of attack becomes less than this and there is no discontinuity.

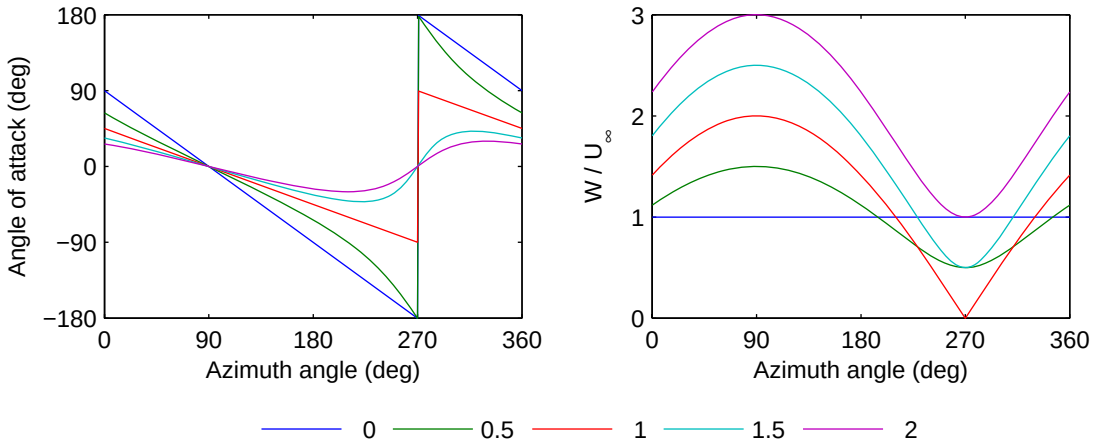

Figure 1.3: *Variation in the angle of attack and the non-dimensionalized relative flow speed (W/U_∞) with azimuth angle for five different values of the tip speed ratio. These curves are calculated on the assumption that the turbine does not affect the flow.*

Vertical axis turbines are designed to operate at tip speed ratios where the range in the angle of attack is such that the blades are never in stall; this is the case shown in figure 1.2. In this situation the lift forces are large compared to the drag forces and so a blade contributes a positive shaft torque over most of the range of the azimuth angle, therefore giving a net power output.

Note that the maximum angle of attack ($\alpha_{\max}$) and the azimuth angle (ψ) at which this occurs are given by the following closed form solutions:

$$\alpha_{\max} = \arctan\left(\frac{1}{\sqrt{\lambda^2 - 1}}\right) \qquad \psi(\alpha_{\max}) = \arcsin(1/\lambda)$$

1.6 Horizontal axis versus vertical axis and wind versus tide

Given the dominance of the horizontal axis design over the vertical axis design for large scale wind turbines, it is instructive to examine the relative merits of these two technologies for wind and to question whether, if there is a good reason for this dominance, this would also be the case for tide.

A number of authors have compared the relative merits of horizontal and vertical axis wind turbines (Döerner, 1975; Paraschivoiu, 2002; Eriksson et al., 2008), but their analyses can be somewhat partial. Nevertheless, some fundamental differences between the two technologies are, in the main, acknowledged, and these do, in the present author's view, go some way to

explaining the dominance of horizontal axis. Note that unless otherwise stated it should be taken that a 'vertical axis turbine' is a 'fixed pitch vertical axis turbine'.

One significant disadvantage of vertical axis wind turbines relative to horizontal axis wind turbines is that the peak aerodynamic efficiency occurs for a lower tip speed ratio; this in turn means increased blade area and higher gearbox and/or generator costs. The lower optimum tip speed ratio is largely due to the fact that it is not possible to optimize the pitch angle with fixed pitch vertical axis turbines, whereas it is possible to do this with fixed pitch horizontal axis turbines by introducing twist into the blade. In essence then, a fixed pitch vertical axis turbine has some of the disadvantages that one would see with a horizontal axis turbine with untwisted blades. The use of cyclical variable pitch is a potential solution to this problem for a vertical axis turbine.

The second key disadvantage of vertical axis turbines is that the blades experience cyclical aerodynamic loading due to the varying angle of attack and relative flow velocity (as shown in section 1.5). One immediate consequence of this is that of blade fatigue. A second is that for a turbine with a small number of blades (less than four) the shaft torque will vary considerably; this is often called torque ripple.

In addition to aerodynamic loads on blades there are centrifugal and gravity loads. Centrifugal loads are constant (with azimuth angle) for both horizontal and vertical axis turbines but whereas gravity loads are constant for vertical axis turbines this is not the case for horizontal axis turbines. This has been suggested as a possible upper limit to the size of horizontal axis turbines (Eriksson et al., 2008) and can therefore be seen as an advantage of vertical axis turbines.

Probably the most frequently quoted advantage of vertical axis turbines is that they are omnidirectional i.e. they can accept a freestream flow from any direction. This obviates the need for a yaw mechanism. Whilst it may be argued that yaw mechanisms are largely trouble free (not generally the view of supporters of vertical axis turbines) and that this should not be seen as a significant disadvantage of the horizontal axis type, it remains the case that the omnidirectional nature of vertical axis turbines has advantages in turbulent or rapidly varying free stream conditions.

Arguably then, two key disadvantages of vertical axis wind turbines in relation to horizontal axis wind turbines – the lower optimum tip speed ratio and the shaft torque ripple – may be

eliminated or minimized by the use of cyclical variable pitch and larger numbers of blades. Whether these innovations have not been applied to vertical axis wind turbines because of lack of investment (as argued by Paraschivoiu), or because the resulting product would be uneconomic in relation to horizontal axis turbines, is left as an open question here. Instead we look at the key differences between wind and tide, how this will influence device design, and thus whether it may favour the horizontal or vertical axis type in light of the relative merits discussed here.

In respect of turbine design drivers, Salter (1998) and others have noted some key differences between wind and tide:

- Velocities in tidal flows are lower while densities are higher.
- Cavitation sets an upper limit on the blade speed.
- Gravity loads are not a problem (they may be opposed by buoyancy).
- Tidal flows are in some places nearly bi-directional.

The fluid velocity and density affect the power density of the flow according to the law:

$$P/A = \frac{1}{2}\rho U^3 \tag{1.1}$$

Where P is the hydraulic power flow through a cross section A, and ρ and U are the density and velocity. The power density for which the blades are designed, ignoring overload conditions etc., will be that at the rated velocity (the velocity at which rated power is achieved). For wind turbines this is typically around 13 m/s (Fraenkel, 2002), but for tidal turbines it is likely to vary given the large (percentage) variation in velocity across different sites. As a guide, it is thought that a mean spring peak velocity of 2 m/s or higher is required for economic feasibility (Fraenkel, 2002) while approximately 30% of the tidal resource is found in sites with a mean spring peak velocity of over 5.5 m/s (Black and Veatch, 2005a, table 4-8, p. 28). The rated velocity will be some fraction of this. As tidal flows with a velocity of 1.4 m/s have an equivalent power density to air flows with a velocity of 13 m/s it seems likely that the design power densities will be higher. In terms of turbine design, higher power densities will lead to increased structural demands. It is not obvious whether this will favour horizontal or vertical axis.

Cavitation will limit blade speed to a value that is dependent upon depth, the blade section, and the angle of attack. For zero depth Fraenkel (2002) suggests that the limit will be around 7 m/s, but the blade section and angle of attack assumed are unknown. Considering the data in Gretton and Bruce (2005) for a series of symmetrical NACA 4-digit series foil sections, and assuming a lift coefficient of around one, suggests a broadly similar value of 8 m/s. See also Molland et al. (2004) for cavitation data. The tip speed ratio will be dictated by this maximum blade speed and the flow velocity, as above. Taking a flow velocity of 2 m/s, perhaps near the rated velocity for the more energetic sites, suggests a limiting tip speed ratio of about four. This is notably lower than the optimum tip speed ratio of a typical, modern, three-blade wind turbine, which Burton et al. (2001, p. 174) show occurring at about seven. As already noted, vertical-axis wind turbines have lower optimum speed ratio, perhaps around 5 (Paraschivoiu, 2002, chapter 7). It is though therefore that vertical axis turbines may see an advantage in this respect, or at least the disadvantage is removed.

Lower tip speed ratios will inevitable mean higher solidities. This means that either the ratio of chord length to turbine radius will increase, or the number of blades will increase. In the case of the latter this will be advantageous in reducing or nearly eliminating the shaft torque ripple found on vertical axis turbines.

A further consequence of the significantly lower blade speeds on tidal turbines will be the virtual elimination of centrifugal loads. This removes the requirement for the troposkien shaped blades found on many vertical wind turbines.

Gravity loads, noted to be an issue as the size of horizontal axis wind turbines increases, may be eliminated by making the blades neutrally buoyant. The ability to eliminate gravity loads is also an advantage when considering ducted designs.

If a tidal flow is bi-directional, or nearly so, then the yaw mechanism needed on horizontal axis wind turbines may be eliminated either by using variable pitch blades, or by using non-pitching bi-directional blades. In some respects then, this diminishes one of the major advantages of the vertical axis turbine, namely their omnidirectionality. This does remain an advantage when considering the impact of large scale turbulent structures.

One further difference between wind and tide, not noted above, is that the depth of the sea imposes an inherent limit on the diameter of a horizontal axis turbine rotor. This consideration has already lead MCT to test a twin-rotor design and a design with six rotors has been patented

(a) (b)

Figure 1.4: *Artist's impression of the Edinburgh Designs turbine concept (a) and the demonstrator turbine being commissioned (b).*

MCT (2009c). Vertical-axis turbines by comparison are not limited in diameter but are limited in blade length. Whether this limitation of the horizontal axis type will prove important is unknown at the present time.

Considering the comparison of horizontal and vertical axis turbines, and wind and tide, it is argued that where there are reasons to explain the dominance of horizontal axis for wind (other than a potential lack of investment in vertical axis) these reasons are lessened when one compares wind to tide. This provides the justification for the detailed investigation of vertical axis turbines for tidal current application.

1.7 The Edinburgh Designs turbine

The Edinburgh Designs turbine, with which this thesis is concerned, is a three blade vertical axis turbine with constant chord variable pitch blades. The objective of this prototype is to demonstrate the overall concept; especially the use of a variable pitch system which allows for the continuous and independent control of each blade. Key design parameters are given in table 1.1 and a photograph of the turbine during commissioning is shown in figure 1.4.

The variable pitch system is one where the pitch angle of each blade is specified as a function of the azimuth angle of that blade. This allows any variable pitch algorithm to be used. As will

Table 1.1: *Key design parameters for the Edinburgh Designs turbine.*

Parameter	Value
Rotor diameter (D)	2.5 m
Number of blades (N)	3
Blade profile	NACA 0024
Blade length	2.0 m
Blade chord (c)	0.2 m
Solidity (Nc/R)	0.48
Rated Power	15 kW
Rated stream speed	2.5 m/s
Rated rotational speed	54 rev/min
Maximum torque	4.0 kNm

be discussed in due course, the basic algorithm chosen limits the angle of attack on the blade so that stall is avoided.

The structural concept of the prototype resembles that of a bicycle wheel, with the blades being supported at both ends by two rims which are in turn connected to the hub with spokes. Fairings would in practice be required to reduce the parasitic drag losses from the spokes.

This prototype turbine was to have been tested by fixing it in front of a seagoing dredging barge. The turbine would then have been driven through still water by the barge at the required speed. Results from these tests would have been used in this thesis for validation of the turbine models; however, they have yet to be carried out.

1.8 Aims and objectives

The overall aim of the present work is to accurately model the hydrodynamic behaviour of the Edinburgh Designs turbine using a CFD code.

Such an aim requires further prescription and decomposition, as we discuss here. The Edinburgh Designs turbine is to be simulated for design and off-design conditions and for fixed pitch and variable pitch operation. For a given operating point, the blade loadings as a function of the blade azimuth angle are required; over a range of operating points the variation in the power coefficient with tip speed ratio is to be determined.

A commercial CFD code is to be used. This means that the model setup used in this thesis can be directly applied in industry; in essence it means that the process by which the results are produced is as important and as relevant as the results themselves. The code ANSYS CFX, hereafter CFX, was selected based on the known strengths of this code for modelling turbomachinery and free surfaces.

The problem of modelling a vertical axis turbine, complete with all structural elements, interacting with a free surface and being propelled by a barge was decomposed by considering progressive simplifications and also by considering what standard test cases could usefully inform the problem setup. Such an approach was taken to be entirely sensible practice and was subsequently found to be that suggested by the American Institute of Aeronautics and Astronautics (AIAA, 1998) who term this a 'building-block' approach. A diagram showing the different problems which could usefully be simulated, and the way in which the results of one informs the other, is given in figure 1.5.

To consider all of the problems shown in this diagram is beyond the scope of a single PhD thesis. As such the objectives of the present work were set at the simulation of three cases: turbine blades only, an oscillating hydrofoil and a hydrofoil at a fixed angle of attack.

Assessing the quality of the numerical solutions is an important part of this thesis. The process by which this is achieved is known as *verification* and *validation*. These words have specific meanings which will be introduced later in section 3.6.2; at the present juncture we note that verification refers to checking that the numerical solution procedure is correct while validation refers to the comparison of a verified numerical solution with experimental data. In the absence of experimental data to validate the turbine model, the validation of the hydrofoil simulations becomes key. This will be achieved by comparing the numerical results with published wind tunnel results. Verification will be done for all simulations, but again the building-block approach is key as this allows for the bulk of the verification work to be completed with the hydrofoil modelling.

A number of authors have already presented results from CFD simulations of vertical axis turbines, either for tidal current or wind applications. The model setups for these two cases are generally very similar, and so both are relevant when considering the novelty of the present work. Such novelty lies in the thorough verification and validation process outlined above, especially in the application of the building block approach.

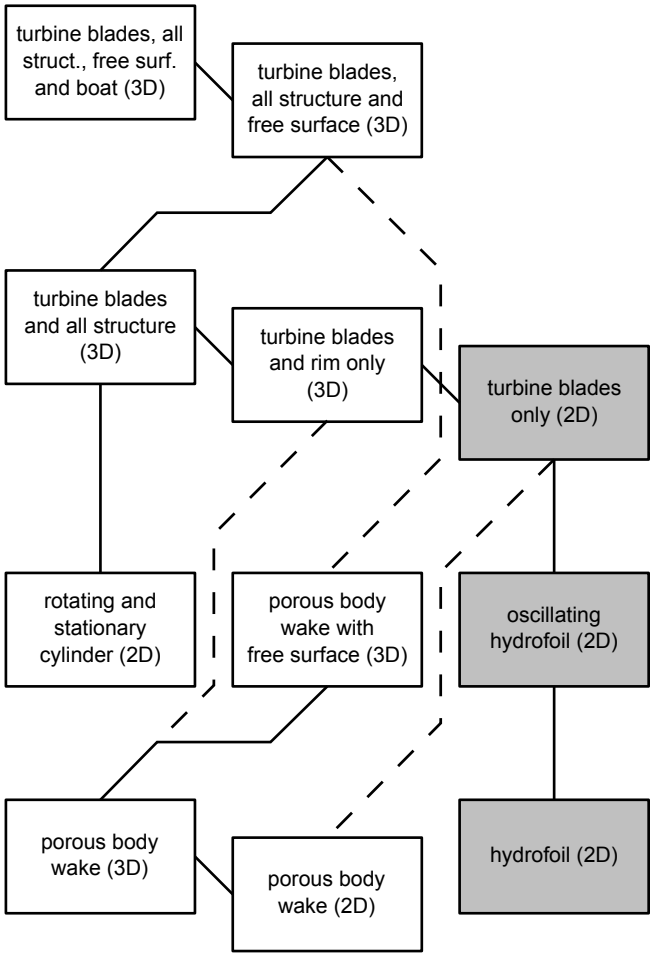

Figure 1.5: *Problem decomposition. Solid lines indicate the flow of information within a phase of validation or between two consecutive phases. Dashed lines indicate the flow of information between non-consecutive phases.*

A final aim of this thesis is to compare the results of the CFD model of the turbine with those from a blade element momentum model (hereafter blade element). Such blade element models require hydrofoil section data as an input, this being generally taken from wind tunnel results or from panel method calculations of hydrofoils. In the present work this will be taken in addition from the CFD simulations of hydrofoils performed here. These hydrofoil simulations will use the same modelling approach as the turbine simulations (or more accurately vice-versa). This allows for a novel comparison between blade element results and CFD results for the turbine. Effectively, differences in the steady state behaviour of the blade sections can be eliminated as a source of discrepancy between the two models (blade element and CFD).

To recap then, the aims are as follows:

- To verify and validate CFD simulations of a hydrofoil at a fixed angle of attack
- To verify and validate CFD simulations of an oscillating hydrofoil
- To verify CFD simulations of a vertical axis turbine in 2D
- To compare results from the CFD simulation of the turbine with blade element results of the turbine that use hydrofoil section data from the present CFD simulations

Chapter 2
Literature review

2.1 Introduction

A variety of literature were examined as part of the present work. Naturally this includes literature specifically concerned with vertical axis turbines, broadly divided into device concepts, mathematical modelling, and physical tests. Also included is literature concerned with airfoil[1] and hydrofoil sections, namely that focusing on sources of section data and previous CFD modelling work. Literature on the tidal resource were examined for the specific aim of informing the choice of inlet boundary conditions for the CFD model of the turbine and also for the more general aim of quantifying this source of sustainable energy. Other literature examined include that showing good examples of CFD practice and that presenting experimental data on the wakes behind porous objects.

2.2 Airfoil section data and modelling

A significant review was conducted of the literature on airfoil section data and the CFD modelling of such sections. The breadth of the review of section data was in response to the realization that the lift and drag coefficient data varied significantly from source to source and also due to the fact that most sources were deficient in either quality or scope. With regards to the CFD modelling of such sections, it was clear that this was a mature field (in comparison to the CFD modelling of vertical axis turbines), and that there was a lot to learn from the existing literature.

The literature consulted was primarily for airfoils at low Mach numbers ($Ma < 0.3$), as opposed to hydrofoils; this was because the majority of the literature on the section profiles of interest was for airfoils. Compressibility effects are small at these low Mach numbers and so the data were taken to be applicable (see the discussion in the sub-section below).

[1] In choosing 'airfoil' over 'aerofoil' the author has been influenced by the predominantly American literature consulted; the forbearance of readers with a particular affinity for 'aerofoil' is duly requested.

As noted in the introduction, the Edinburgh Designs turbine uses a NACA 0024 section profile. This particular profile is from the NACA 4-digit series, a description of which is given below. Whilst it was not known at the outset that this section would be used, it was thought that a symmetrical profile from this series would be used. This choice was made on the rationale of following vertical axis wind turbine parameters where appropriate (Paraschivoiu, 2002, chapter 7), and because it was known that these sections had good cavitation properties (Molland et al., 2004); in essence preliminary evidence suggested that such a choice would not be a bad one. It was also known that such profiles were frequently used for helicopter rotors (see Lednicer, 2007) and that a significant amount of section data was available.

In the sub-sections following we first introduce some basic aspects of airfoil design and behaviour before discussing the literature on section data and then that on CFD modelling.

2.2.1 Basics of airfoil behaviour and design

Airfoil section data primarily refers to measurements of the lift, drag and moment coefficients as a function of the angle of attack; these coefficients are defined in section 3.5.4. The variation in these coefficients with the angle of attack will depend upon the section profile, and also upon the Reynolds number and the Mach number[2]. An excellent introduction to many aspects of airfoil and wing behaviour is given by Anderson (2004); see also the classic reference by Abbott and von Doenhoff (1959).

One key aspect of airfoil behaviour is stall. This refers to a drop in lift and a significant increase in drag and moment with increasing angle of attack and is caused by flow separation. The nature of stall is strongly influenced by the profile of the airfoil; thinner sections will generally stall more suddenly. As with aeroplanes, stall on vertical axis turbine blades is undesirable and so its prediction is an important part of this work.

Flow separation on airfoils is controlled by boundary layer behaviour. The separation point may be located near the leading edge or towards the trailing edge and both may occur simultaneously. For two of the section profiles studied in chapter 5 (the NACA 0012 and the NACA 4412) and for angles of attack below stall this leading edge separation is controlled by a laminar boundary layer and turbulent re-attachment occurs about 1% of the chord downstream

[2]The origin of the Reynolds number and the Mach number is discussed in section 3.5

of the separation point (Gregory and O'Reilly, 1970; Hastings and Williams, 1987). This is known as a laminar separation bubble.

Given the importance of boundary layer behaviour in determining section properties it is particularly important that the boundary layer development in a wind tunnel test accurately represents that which would occur in practice. In addition to the Reynolds and Mach number scale effects already mentioned, the surface condition and the level of turbulence intensity are also important. In the context of wind tunnel tests for aeronautical applications it is primarily the surface condition that is discussed (Abbott and von Doenhoff 1959, pp. 143–148, pp. 157–175; Barlow et al. 1999, pp. 306–313). Transition strips are used to artificially induce transition to a turbulent boundary layer, thus replicating the process that would occur on a dirty wing or a wing with protuberances. Icing conditions may also be simulated in a similar manner (Gregory and O'Reilly, 1970). With regards to turbulence, the objective is to reduce the turbulence in the wind tunnel to such a level that any remaining turbulence has a negligible effect and so free flight conditions are accurately modelled (Abbott and von Doenhoff, 1959, p. 125). In the context of vertical axis turbines the level of turbulence incident on the blades will be significantly higher than that on a wing, especially during the downstream pass of the blades. As with surface roughness, high levels of incipient turbulence induce bypass transition (White, 2006, section 5.4). No research was conducted specifically on the effect of incipient turbulence on airfoil behaviour.

The drag on airfoil sections may be decomposed according to the physical phenomenon responsible. For purely subsonic flow there are two components: the skin friction drag and the pressure drag (or form drag), together known as the profile drag (Eppler 2003; Anderson 2004, p. 310). The skin-friction drag is directly due to the effect of viscosity while the pressure drag is due to the modification of the pressure field by the presence of a boundary layer or flow separation and is thus indirectly due to the viscosity. Note that Anderson attributes pressure drag to flow separation only while Eppler states that it occurs for both separated and non-separated viscous flows.

As already noted, the Reynolds number and the Mach number are the two most significant scaling parameters for airfoil behaviour. For 'low speed' flows, generally taken as encompassing Mach numbers up to around 0.3, the Mach number dependence is frequently neglected (e.g. Barlow et al., 1999, p. 13). In the same reference though it was also noted that

Table 2.1: *Changes in the lift curve slope with Reynolds and Mach numbers.*

Re (10^6)	Ma	c_{l_α}	% c_{l_α}
1	0	0.1025	–
2	0	0.1040	1.42
3	0	0.1048	2.26
10	0	0.1074	4.73
1	0.1	0.1030	0.50
1	0.2	0.1046	2.06
1	0.3	0.1074	4.83

"both the lift curve slope and maximum lift coefficient are affected by Mach numbers as low as 0.2" (Barlow et al., 1999, p. 63).

Such data (for the lift curve slope and maximum lift coefficient) are presented by McCroskey (1987) in a review of data for the NACA 0012 airfoil. It is shown that the variation in the lift curve slope with Reynolds and Mach number is given by the following equation:

$$\beta c_{l_\alpha} = 0.1025 + 0.00485 \log(\mathrm{Re}/10^6) \qquad \text{per degree} \tag{2.1}$$

where $\beta = \sqrt{1 - \mathrm{Ma}^2}$ and c_{l_α} is the lift curve slope at zero lift. Note that the Mach number scaling here is based on Prandtl-Glauert rule (Anderson, 2004, sections 5.6–5.8). Values for the lift curve slope calculated from this formula for the Reynolds numbers of interest in the present work and a range of low speed Mach numbers are shown in table 2.1. This allows some comparison of the relative effects of independent changes in the Reynolds and Mach numbers; broadly it may be concluded that the differences from an incompressible case are negligible at Mach 0.1, approximately equivalent to between a doubling and trebling of the Reynolds number at Mach 0.2 and equivalent to an order of magnitude change in the Reynolds number at a Mach number of 0.3.

No formula is given for the change in the maximum lift coefficient with Reynolds and Mach number but some data are presented. Unfortunately it is more difficult to differentiate between Reynolds and Mach number effects with this data and there is a significant amount of scatter in the low Mach number data. McCroskey's conclusion on the Mach number dependence is that it becomes increasingly significant above Ma = 0.25 where there is a monotonic decrease in the maximum lift with increasing Mach number.

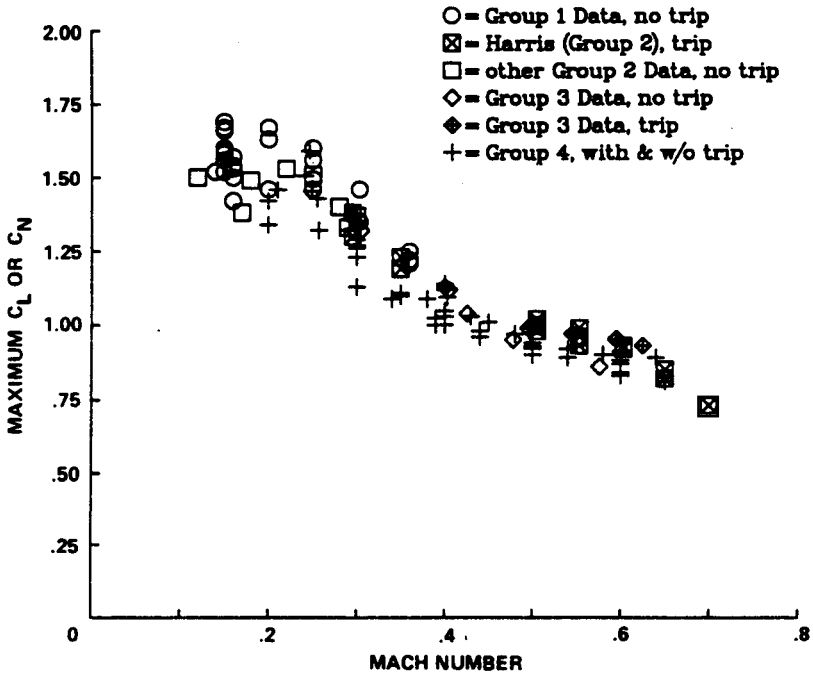

Figure 2.1: *Maximum lift versus Mach number. From McCroskey (1987).*

In the present work it was decided to concentrate on incompressible simulations and to compare the results of these directly with low speed wind tunnel tests. This was the approach taken by a number of authors (Baubeau and Latorre, 1995; Mathew et al., 2006; Mahalatkar et al., 2006) who do not mention Mach number effects. It is thought that the discrepancies that this will introduce in the comparison between CFD simulation and experiment will be smaller than many of the other error sources. Notwithstanding this, a small number of compressible flow simulations were run and will be discussed in chapter 5.

Reynolds number effects, which we have only discussed here in comparison to Mach number effects will be discussed in detail in the next sub-section.

Having introduced the basics of airfoil behaviour it remains to describe the geometry of the NACA 4-digit series profiles. These profiles were created by the National Advisory Committee for Aeronautics (absorbed into NASA with the latter's creation) during the 1930s (Jacobs et al., 1933; Abbott and von Doenhoff, 1959). The profile shape is formed by the combination of a thickness distribution and a mean or camber line. Both of these are given by simple geometric equations; the thickness distribution equation featuring a parameter determining the maximum thickness and the mean line equation featuring two parameters: the maximum ordinate of the mean line and the chordwise position of that maximum ordinate. Both of these equations were

formulated by parameterizing the geometry of a number of successful sections that had existed previously; there is thus no theoretical derivation of these equations. The 4-digit number lists the values of these parameters viz: the first digit indicates the maximum value of the mean line ordinate in per cent of the chord; the second digit indicates the distance from the leading edge to the location of maximum camber in tenths of the chord; and the last two digits indicate the section thickness in per cent of the chord. Thus the NACA 2415 section has 2 per cent camber at 0.4 of the chord from the leading edge and is 15 per cent thick.

2.2.2 Experimental measurements

As discussed above, the review of experimental measurements of section data focused on the symmetrical NACA 4-digit series. Only thicknesses of 12% or greater were of interest for structural reasons. Data were required for Reynolds numbers of the order of 1×10^6 and at low Mach numbers. Of particular interest were sources of data including tests:

- on multiple sections,
- over a wide range of the angle of attack,
- over a range of Reynolds numbers,
- with and without boundary layer trips, and
- for oscillating as well as fixed pitch.

The quality of the data reported was also examined, this being informed by a review of data for the NACA 0012 section by McCroskey (1987), discussed below.

The literature review was exhaustive only for the 0024 and 0025 sections, for which no suitable data were found; for thinner sections, sufficient data were found to make such a review unnecessary.

All of the published data thus considered suitable is listed in table 2.2. Unless otherwise stated the data includes measurements of the lift, drag and moment coefficients; some data also include measurements of the surface pressure distribution. Note also that data are not necessarily given for every combination of the angle of attack, Reynolds number etc. listed in the table.

Table 2.2: *Summary of sources of data for symmetrical NACA 4-digit series sections.*

Source	Thick (%)	α	Re (10^6)	Ma	Trip	Notes
Piziali (1994)	15	0–20°	2	0.28	yes & no	oscillating data uncorrected
McCroskey et al. (1982)	12	0–30°	1–4	0.1–0.3	yes & no	oscillating data mostly uncorrected
Sheldahl and Klimas (1981)	12	0–180°	0.35–1.76	0.07–0.21	no	corrected Re
	15	0–180°	0.35–0.70	0.07–0.18	no	corrected Re
Gregory and O'Reilly (1970)	12	0–18°	0.48–2.88	0.03–0.16	yes & no	variable roughness
Abbott and von Doenhoff (1959)	12	0–20°	3–9	< 0.17	yes & no	excessively thick trip
Critzos et al. (1955)	12	0–360°	0.5 & 1.8	< 0.15	yes & no	excessively thick trip

Most of the parameters that need to be considered when comparing wind tunnel data will be apparent from the bullet points above and the column headings in the table but two others are worthy of highlighting here: the use of corrections to account for the effects of the wind tunnel walls (in comparison to free flight) and the levels of turbulent intensity in the wind tunnel. For two-dimensional flows, corrections need to be applied to account for two distinct effects upon the flow due to the top and bottom walls (von Doenhoff and Abbott, 1947; Barlow et al., 1999):

1. The increase in the tunnel flow velocity in the vicinity of the model due to the constriction caused by the geometry of the model and by the wake created (known as solid and wake blockage), and,

2. The induced curvature of the flow.

Most of the sources listed in the table give corrected data, and further, the method by which the data is corrected appears to be traceable to Allen and Vincenti (1944) in most cases. Given that the static data of Piziali (1994) are not corrected the extent of the corrections was investigated and will be discussed below. The side walls of the tunnel will also have an effect as the boundary layers formed on these walls will cause early separation at the airfoil-wall junction; the use of corrections for this was not however investigated.

Turbulence in wind tunnels is undesirable if the tests are intended to represent free flight conditions. A correction may be applied to the test Reynolds number in order to give an 'effective' Reynolds number; this correction, a wind turbulence factor, may be found from experiments on the drag of a sphere (Jacobs and Sherman, 1937). Of the sources listed in the table, only Sheldahl and Klimas (1981) use such a correction. In other cases it is thought that the levels of turbulence in the tunnels concerned were sufficiently low to make such a correction unnecessary, although this is not always explicitly stated. Abbott and von Doenhoff (1959) do discuss this and state (p. 125–128) that the turbulent intensity in the two-dimensional low-turbulence pressure tunnel (LTPT) is "... very low, of the order of a few hundredths of 1%; and, although it is not definitely known that the remaining turbulence is negligible, the tunnel results appear to correspond closely to those obtained in flight."

We discuss below those sources listed in the table, and also those examined which are not. We begin by discussing the review of McCroskey (1987).

2.2.2.1 McCroskey (1987)

McCroskey's review examines data for the NACA 0012 section from over 40 wind tunnels, and shows that there is considerable variation in the predicted aerodynamic behaviour. Such variation, it is argued, is particularly problematic when these results are used for validating CFD simulations of airfoil behaviour. As a means of addressing this problem the review identifies and correlates the best data, thus allowing the determination of the representative behaviour of the section over a wide range of angles of attack, Reynolds numbers and Mach numbers. In particular, results are shown for the variation in:

1. Lift-curve slope,
2. Minimum drag,
3. Maximum lift-to-drag ratio,
4. Maximum lift,

each versus both Reynolds and Mach number. (Also given are results showing the variation in shock-wave position versus Reynolds number at Ma = 0.8.) Tripped and un-tripped results are shown for each of these. The comparison is limited to these results because for other quantities, such as moment coefficient and pressure distribution, there is insufficient overlap between sources.

The process of categorizing the data according to quality begins by identifying "the experiments which clearly stand out as having been conducted with the utmost care and/or as most nearly eliminating the important sources of wind-tunnel errors" (p. 3). These data are referred to as Group 1 and are used to establish curve fits for the variation in the compressibility-corrected lift-curve slope and the minimum drag (for both un-tripped and tripped cases) with Reynolds number in the subsonic regime. These are, for the lift-curve slope (as discussed above):

$$\beta c_{l_\alpha} = 0.1025 + 0.00485 \log(\mathrm{Re}/10^6) \qquad \text{per degree} \tag{2.2}$$

for the minimum drag *without* a boundary layer trip:

$$c_{d_o} = 0.0044 + 0.018\mathrm{Re}^{-0.15} \tag{2.3}$$

and for the minimum drag *with* a boundary layer trip:

$$c_{d_0} = 0.0017 + 0.91/(\log \mathrm{Re})^{2.58} \tag{2.4}$$

Comparison of the remaining data against these curve-fits allows further classification: Group 2 data are defined as those data that agree with the curve-fits for both lift and drag to within ±0.0040 for βc_{l_α} and to within ±0.0010 for c_{d_0}; Group 3 data are those that agree "well" with the curve-fits for either βc_{l_α} or c_{d_0}; Group 4 data satisfy the basic lift and/or drag criteria but otherwise have major defects, or alternatively satisfy neither criteria but cover ranges of the Mach number for which even qualitative information is helpful; a final group of data failed to satisfy any of the above criteria or offer any significant additional information and were therefore excluded. A further stage of McCroskey's filtering process is to examine the data outside of the subsonic regime, but this is of no interest here.

McCroskey's categorization was used to select the NACA 0012 data listed in table 2.2; these sources are either from Group 1 or 2. The one source listed in this table that was not assessed by McCroskey, namely Piziali (1994), was assessed in light of McCroskey's Group 1 criteria. A brief discussion of each of the sources in this table is now given.

2.2.2.2 Piziali (1994)

The data reported by Piziali include a particularly comprehensive range of oscillating pitch cases as well as quasi-static data, all of which were performed for both un-tripped and tripped boundary layers. Two points must be considered when applying the data. First, the data are un-corrected for wind tunnel effects. The effect of standard wind tunnel corrections will be examined below. Second, the lift, drag and moment data are based on integration of the surface pressure on the airfoil. This is known to give potentially inaccurate drag results for angles of attack below stall (see McCroskey et al., 1982, pp. 5–6).

2.2.2.3 McCroskey et al. (1982)

McCroskey et al. (1982) and subsequent volumes (McAlister et al., 1982; Carr et al., 1982) present data for the NACA 0012 section and seven others. The majority of the data are for a Reynolds number of 4×10^6 and for airfoils without boundary layer trips; some data exist for

other Reynolds numbers and for airfoils with boundary layer trips, but only for deep dynamic stall cases. Most of the data are uncorrected for wind tunnel effects, but some static data are presented with wind tunnel corrections according to Allen and Vincenti (1944). As with the data of Piziali, the lift, drag and moment forces are derived by integration of airfoil surface pressures. Some data are also presented for the drag as measured by a wake survey and it is shown that the total drag thus measured is lower than the pressure drag at high lift. This is noted as being fundamentally incorrect (pp. 5–6 of volume 1), but no explanation is given.

2.2.2.4 Sheldahl and Klimas (1981)

Sheldahl and Klimas present experimental data for the NACA 0009, 0012 and 0015 sections and also for a modified NACA 0012 section for the full range of the angle of attack (0–180°). Unlike any of the other data listed in table 2.2, the Reynolds numbers have been corrected by multiplying the test Reynolds number by a wind turbulence factor that ranges from 1.13 to 1.38, depending on the test Reynolds number. All of the experimental data presented have been corrected for wind tunnel wall effects according to an earlier edition of Barlow et al. (1999). The lift, drag and moment coefficients are all derived from a balance system and therefore the drag given is the total drag. Sheldahl and Klimas also present tabulated data that is a hybrid of the experimental results and results from a panel method code; this will be discussed below under *numerical modelling*.

2.2.2.5 Gregory and O'Reilly (1970)

The data of Gregory and O'Reilly are of particular interest because drag results are presented for the case of an un-tripped boundary layer and for two different thicknesses of transition strip. Unfortunately neither a lift nor a moment curve is presented for the tripped cases, but the variation in maximum lift is given. The behaviour of the laminar separation bubble near the leading edge of the airfoil in the un-tripped case is discussed and its variation with angle of attack and Reynolds number is shown. All data are again corrected but no reference is given. The lift and moment coefficients are derived from integration of airfoil surface pressures while the drag is calculated from a wake survey and is therefore the total drag.

2.2.2.6 Abbott and von Doenhoff (1959)

Abbott and von Doenhoff is a classic reference on airfoil data. The primary focus is on comparing different section profiles, mostly those from the laminar flow NACA 6-series. For symmetrical 4-digit series profiles, data are included for the 0006, 0009 and 0012 and modified versions of the 0010 and the 0012. The lift force is measured by integration of the surface pressures representing the reaction on the floor and ceiling of the tunnel, the drag force is obtained from wake survey measurements and the moment is measured using a balance. Based on a reference to von Doenhoff and Abbott (1947) for details of the tunnel it is understood that these data are corrected using the formulae of Allen and Vincenti (1944).

2.2.2.7 Critzos et al. (1955)

Besides the data of Sheldahl and Klimas, that of Critzos et al. is the only other to cover the full range of the angle of attack. Tripped data are provided at the higher Reynolds number 1.8×10^6. The lift, drag and moment are all obtained from a balance and are corrected using the formulae of Allen and Vincenti (1944).

2.2.2.8 Other data

A number of references were consulted for NACA 0024 and 0025 data but none provided data suitable for validation. One reference, Bullivant (1941), reports tests of NACA 0025 and 0035 wings in the NACA full scale tunnel; in contrast to all of the experiments discussed above this is a three-dimensional test. Whilst section data are calculated from the wing data, they were not thought suitable for a detailed validation study. Such data could perhaps be used in a blade element momentum model, but this was not pursued. Note that Goett and Bullivant (1939) provide data from similar tests of a NACA 0012 wing; this data could be compared with the true section data discussed above, thereby giving an estimate of the quality of the corrected wing data; again though, this was not pursued.

2.2.2.9 Wind tunnel corrections

All of the sources listed in table 2.2 that provide corrected data reference either Allen and Vincenti (1944) or Barlow et al. (1999), with the exception of Gregory and O'Reilly (1970) who do not provide a reference. Upon investigation it was found that the two-dimensional

corrections given in Barlow et al. (pp. 349–363) are extensively based on Allen and Vincenti who provide a summary of the key equations on (p. 179). These corrections to the Reynolds number, angle of attack, and lift, moment and drag coefficients are:

$$\mathrm{Re} = \mathrm{Re}'(1 + \Lambda\sigma + \tau c_d') \tag{2.5}$$

$$\alpha = \alpha' + \frac{57.3\sigma}{2\pi}(c_l' + 4c_m') \tag{2.6}$$

$$c_l = c_l'(1 - \sigma - 2\Lambda\sigma - 2\tau c_d') \tag{2.7}$$

$$c_m = c_m'(1 - 2\Lambda\sigma - 2\tau c_d') + c_l'\frac{\sigma}{4} \tag{2.8}$$

$$c_d = c_d'(1 - 3\Lambda\sigma - 2\tau c_d') \tag{2.9}$$

where the primed values indicate the uncorrected values. τ and σ are factors that depend on the ratio of the chord length c to the tunnel height h (assuming that the airfoil has span horizontal) and are defined as:

$$\tau = \frac{1}{4}\frac{c}{h} \tag{2.10}$$

$$\sigma = \frac{\pi^2}{48}\left(\frac{c}{h}\right)^2 \tag{2.11}$$

The remaining factor Λ depends upon the geometry of the airfoil according to an integral equation, the results of which are given by Allen and Vincenti in a table for a number of sections. For the NACA 4-digit series it appears that it may be approximated by $\Lambda \approx 2(t/c)$ within a few per cent for thinner sections and within 10% for thicknesses up to 25%.

As an example of the effect of applying corrections, the tabulated data of Sheldahl and Klimas (1981) for the NACA 0015 airfoil at a Reynolds number of 2×10^6 was used. (This data does not need correcting, but was used because it was the only data set available in tabulated form, as required for applying corrections.) The chord to height ratio was specified as 1/7, this being the ratio in the experiment of Piziali (1994) where uncorrected data is given. The uncorrected and corrected data are shown in figure 2.2, where it is clear that the effect of applying such corrections is minimal. Note that the contribution from the moment coefficient in the angle of attack correction equation 2.6 is ignored as Sheldahl and Klimas do not provide this data in

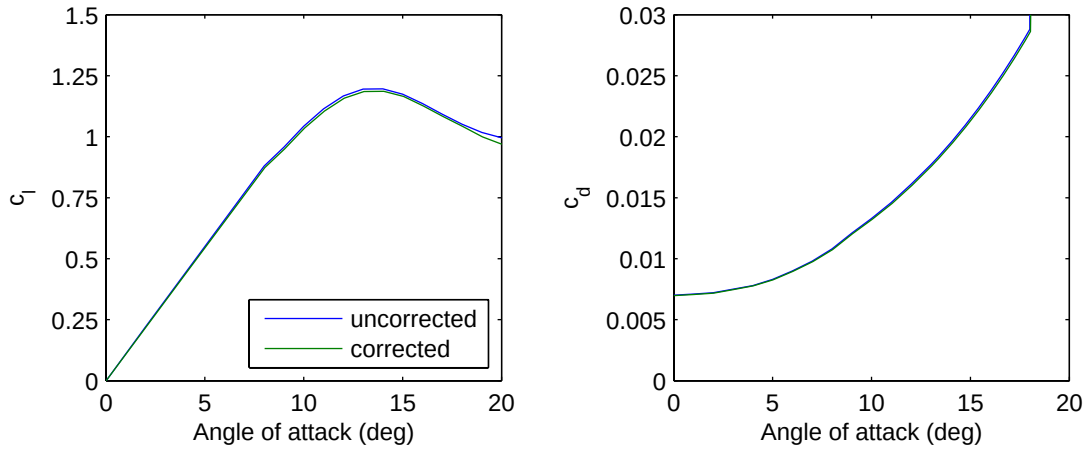

Figure 2.2: *Lift and drag coefficients from Sheldahl and Klimas (1981) for the NACA 0015 airfoil at a Reynolds number of* 2×10^6 *corrected using the equations of Allen and Vincenti (1944) for a chord to tunnel height ratio of 1/7.*

tabulated form; as the moment coefficient is much smaller than the lift coefficient in the range considered the effect will again be minimal.

2.2.3 Numerical modelling

A number of methods are available for the numerical simulation of airfoils but we discuss here only three: panel methods, Reynolds-averaged Navier-Stokes (RANS) solutions, and large eddy simulations (LES), these being listed in order of increasing complexity. The primary focus is on RANS solutions as this is the method used for turbine and airfoil simulations in the present work. Panel methods are discussed for two reasons: first, the frequently referenced source of section data by Sheldahl and Klimas (1981) includes panel method solutions, and second, a panel method solution was used in the present work to inform the specification of the RANS grid in the boundary layer and to quickly explore the effect of parameter variations such as trailing edge thickness. Large eddy simulations of airfoils were briefly researched to understand the increased computational burden relative to RANS solutions.

2.2.3.1 Panel methods

Panel methods are a type of discrete potential flow solution involving a distribution of singularity elements over the surface of the body and, in the case of airfoils, the wake (Katz and Plotkin, 1991). These singularity elements may be sources, doublets or vortices or a

combination thereof. In the case of airfoils this inviscid solution is frequently combined with an integral boundary layer solution which utilizes the inviscid pressure distribution. This boundary layer solution may be coupled to the inviscid solution in that the displacement thickness of the boundary layer can be used to update the geometry of the inviscid solution. Such viscous-inviscid coupling would involve an iteration of the two solutions.

Sheldahl and Klimas (1981) used the Profile code of Eppler and Somers (1980), often known simply as Eppler's code. This features a parabolic distribution of vortices on the panels and an integral boundary layer solution, but no viscous-inviscid coupling. The code was used by Sheldahl and Klimas to produce results for the NACA 0012, 0015, 0018, 0021 and 0025 airfoils at angles of attack from 0–27° and at Reynolds numbers from 10×10^3 to 5×10^6 (and up to 10×10^6 in the case of the NACA 0012 and 0015 airfoils); these results are reported in tabular form. The tabulated data also include results for angles of attack from 30–180° that come from the wind tunnel experiments discussed above. These high angle of attack results assume Reynolds number independence, and also section thickness independence for the thicker sections (the NACA 0015 data are used for the 0018, 0021 and 0025 sections). The data are frequently used in blade element momentum solutions of vertical axis turbines (this being the intended use) but are sometimes mistakenly referred to as being of purely experimental origin (e.g. Antheaume et al., 2008).

The panel method results for the NACA 0012 and 0015 sections show somewhat lower maximum lift coefficients than the experimental data of Sheldahl and Klimas for the Reynolds numbers which may be compared, and also a more gradual pattern of stall. For low Reynolds numbers (of the order of 10^4) the data show negative lift coefficients post-stall; Dominy et al. (2007) have expressed skepticism over this.

The tabulated data[3] for the NACA 0025 airfoil are shown in figure 2.3 for the Reynolds numbers of interest in the present work. These data will be used to produce the blade element momentum model results of chapter 4. Figure 2.4 shows the same data in an alternative form, namely as normal and tangential (to the chord) force coefficients. This form of presentation is common in the literature on vertical axis turbines as it highlights the behaviour of the useful, power generating, tangential force with the angle of attack.

[3]Manually digitized data from the tables of Sheldahl and Klimas were provided to the author by Paul Cooper of the University of Wollongong, Australia (priv. comm.). These were compared with data digitized using OCR from tables in Paraschivoiu (2002), these tables not being referenced as begin from Sheldahl and Klimas, but clearly so. The two sources were compared and all discrepancies due to errors in the manual digitization and misprints in the tables of Paraschivoiu were eliminated.

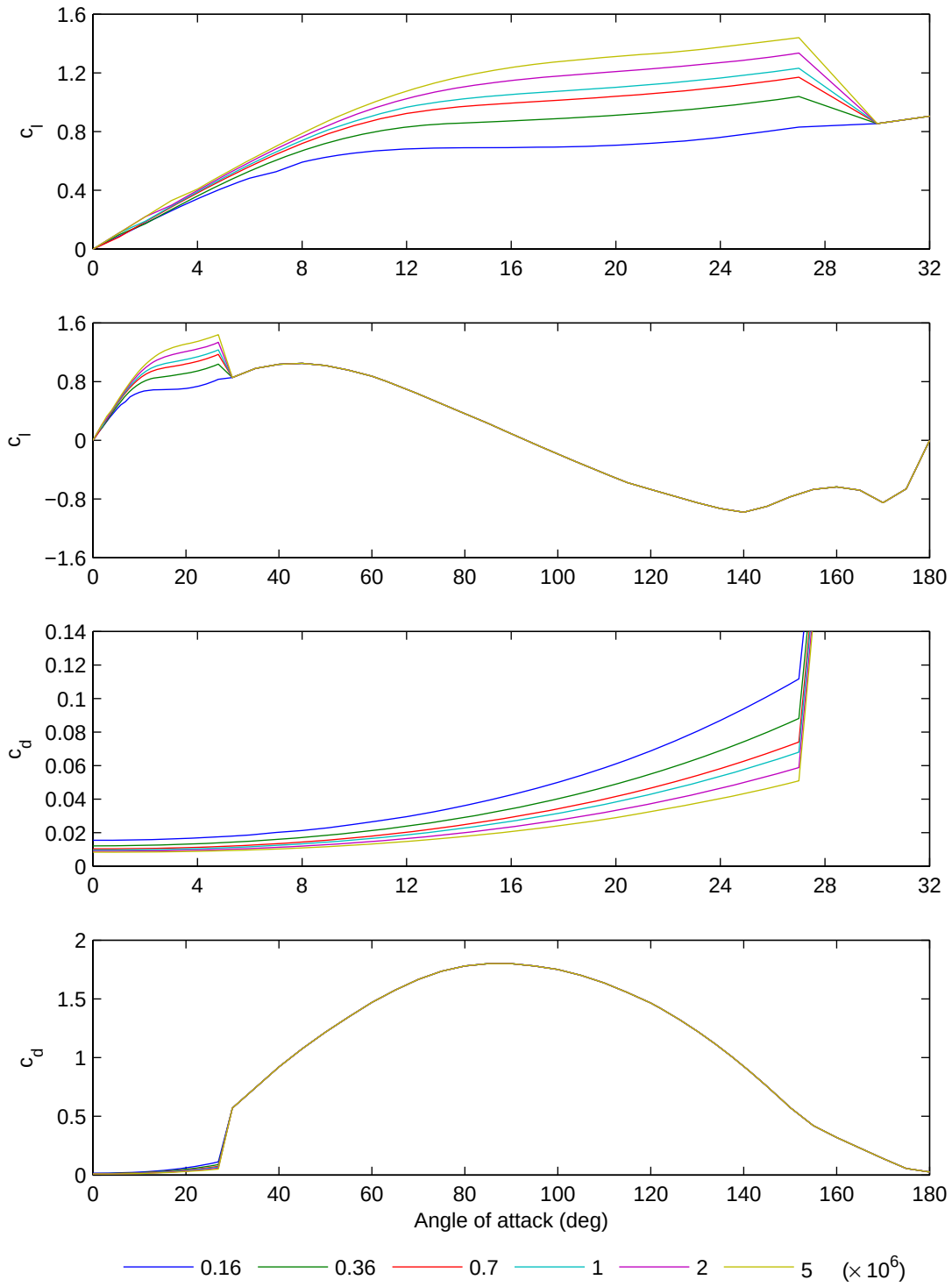

Figure 2.3: *Lift and drag coefficient data for the NACA 0025 section from Sheldahl and Klimas (1981). The Reynolds number is indicated in the legend and ranges from* 0.16×10^6 *to* 5×10^6.

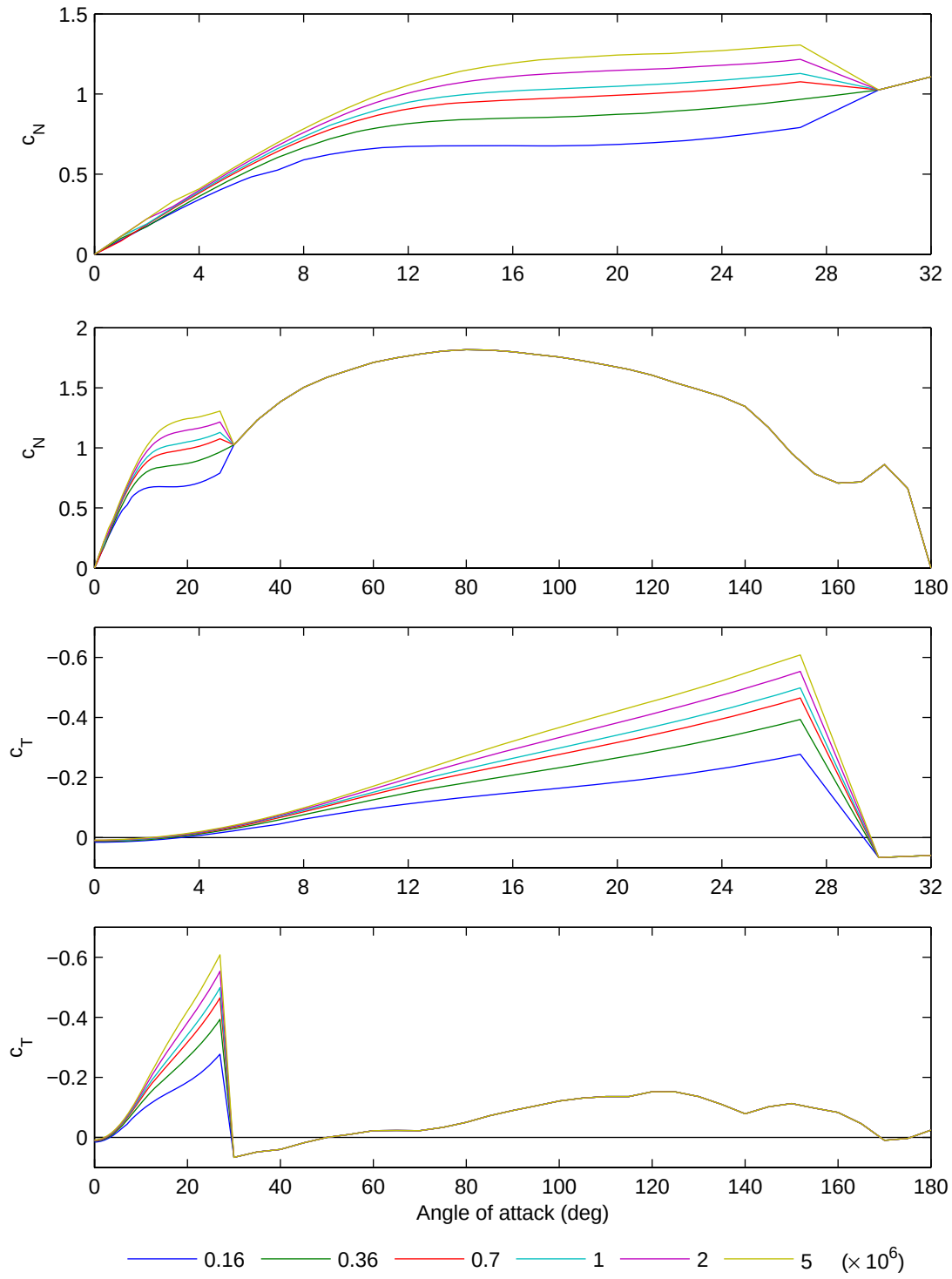

Figure 2.4: *Normal and tangential coefficient data for the NACA 0025 section from Sheldahl and Klimas (1981). The Reynolds number is indicated in the legend and ranges from* 0.16×10^6 *to* 5×10^6.

The panel method code Xfoil (Drela and Youngren, 2008) was used in the present work for reasons as noted above. Xfoil uses linear vorticity elements and includes viscous-inviscid interaction using the surface transpiration model (Drela and Youngren, 2001). This coupling permits the solution of limited regions of separation including that of laminar separation bubbles. The general methodology is described in Drela (1989b) while the boundary layer formulation and the treatment of blunt trailing edges is described in Drela and Giles (1987) and Drela (1989a) respectively. Xfoil is well known to predict stall at higher lift coefficients and at higher values of the angle of attack than shown by experiment (e.g. Molland et al., 2004; Gretton and Bruce, 2007).

2.2.3.2 RANS

The use of the RANS equations[4] for the simulation of airfoils is a mature field of research and the accompanying literature is voluminous. In reviewing this literature the clear aim was to investigate the model setups that had been used previously and the success thereof (when compared with experimental data). Of primary interest was the selection of turbulence model and the mesh definition. Concerning the mesh definition, key parameters of interest were the number of nodes on the surface of the airfoil, the non-dimensional distance to the first node from the wall (Δy^+), the number of nodes through the boundary layer, and the non-dimensional distance (L_B/c) to the far-field boundary. Sources consulted which provided at least *some* of this information are listed in tables 2.3 and 2.4 (which give an overview and details respectively); those which provided *all or most* of the required information included Zingg (1991), Ekaterinaris and Menter (1994), Haase et al. (1997) and Langtry et al. (2006) and will be discussed below.

Before proceeding to such a discussion, one characteristic of RANS and LES simulations that is listed in table 2.3 and merits note here is the treatment of transition from laminar to turbulent flow in the boundary layers. There are essentially three possibilities: first, the boundary layers may be treated as fully turbulent (forced transition at $x/c = 0$); second, the boundary layers may be treated as laminar until a certain point at which transition to turbulence is forced (this is normally achieved by 'switching off' the turbulence production until the transition point); third, transition may be allowed to occur freely, this requiring some sort of transition model. The first option is used for reasons of simplicity or when it is though that the presence of laminar

[4]The theory behind this method is discussed at length in chapter 3 and so is not discussed here.

Table 2.3: *Summary of RANS and LES simulations from the literature: Scope of simulations and results.*

Reference	Profile	α	Re	Ma[a]	Transition	Data
Langtry et al. (2006)	S809	0–20	2×10^6	I	t & b: 0 & free	c_l, c_d, c_p
Dular et al. (2005)	ALE15, ALE25	5	1.38×10^6	I	–	see note [b]
Mulvany et al. (2004)	NACA 16-series	–	8.28×10^6 1.66×10^7	I	–	c_l, c_d, c_p, c_f, b.l. profiles
Haase et al. (1997)	NACA 4412	12.49	4.17×10^6	0.18	various	c_l, c_d, c_m, c_p, c_f, b.l. profiles
Ekaterinaris and Menter (1994)	NACA 4412	13.87	1.52×10^6	0.2	–	b.l. profiles
	NACA 0015	various[c]	2×10^6	0.3	t & b: 0	c_l, c_d, c_m
	NACA 0012	$10 + 5\sin(t)$	4×10^6	0.3	t & b: 0 & [d]	
Menter (1993)	NACA 4412	13.87	1.52×10^6	I	free	c_p, b.l. profiles
Rogers et al. (1992)	NACA 4412	13.87	1.52×10^6	I	forced, various x/c	c_p, b.l. profiles, c_l vs. α
Zingg (1991, 1992)	NACA 0012	0, 6, 12	2.88×10^6	0.16	forced, $x/c = f(\alpha)$	c_d, c_{d-p}, c_{d_f}, c_l
Rhie and Chow (1983)	NACA 0012	0, 6	2.8×10^6	I	–	c_p
		6	3.8×10^5		–	c_p, b.l. profiles
	NACA 4412	13.87	1.5×10^6		–	c_p, b.l. profiles
Wang and Ostoja-Starzewski (2007)	NACA 0015	4, 8, 20	1×10^6	I	–	Cavitation
Mary and Sagaut (2002)	A-airfoil	13.3	2.1×10^6	0.15	t: free, b: forced	c_l, c_d, c_p, c_f
Weber and Ducros (2000)	A-airfoil	13.3	2.1×10^6	0.15	t: 0.12, b: 0.3	c_l, c_d, c_p, c_f, b.l. profiles

[a] 'I' indicates that the simulation is incompressible.
[b] Shedding frequency, cavity length, b.l. profiles.
[c] $4 + 4.2\sin(t)$, $11 + 4.2\sin(t)$ and $15 + 4.2\sin(t)$.
[d] Transition is specified to occur at the suction peak.

Table 2.4: *Summary of RANS and LES simulations from the literature: Turbulence models and meshing parameters. For references where more than one mesh was used the values in the table are for the mesh that was selected, with the exception of Zingg where no mesh was selected; in this case the finest mesh used is quoted. Note that question marks in parentheses indicate information that was inferred but not explicitly stated.*

Reference (/Simulation)	Profile	Turbulence model(s)[a]	Mesh	t.e.	N_x (Wake | PS | SS)	N_y	N	Δy^+
Langtry et al. (2006)	S809	SST	C	sharp	750 (75 | 300 | 300)	100	75 000	1
Dular et al. (2005)	ALE15, ALE25	RNG k-ε	C	sharp (?)	–	–	360 000	30–80
Mulvany et al. (2004)	NACA 16-series	various[b]	O-H	blunt	(S 1590)	–	208 416	2.31
Haase et al. (1997) / CASA	NACA 4412	B-L	unstr.	sharp	415	–	11 397	1
/ Dornier	NACA 4412	B-L, C-S, J-C, J-K	C	sharp	257 (33 | 97 | 97)	65	16 705	0.5
/ Saab	NACA 4412	k-ε						
Ekaterinaris and Menter (1994)	NACA 4412	B-B, S-A, k-ε, k-ω, SST	C (?)	sharp (?)	241	91	21 840	–
	NACA 0015	B-B, S-A, k-ε, k-ω, SST	C	sharp (?)	311 (45 | – | 130)	91	28 301	2
	NACA 0012	B-B, S-A	C (?)	sharp (?)	351 (– | – | 170)	91	31 941	–
Menter (1993)	NACA 4412	k-ε, k-ω, BSL, SST	C (?)	sharp (?)	241	61	14 701	–
Rogers et al. (1992)	NACA 4412	B-B, B-L	C	sharp (?)	241	63	15 183	1
Zingg (1991, 1992)	NACA 0012	B-L	C	sharp	497 (W 48, S 401)	193	92 926	0.02
Rhie and Chow (1983)	NACA 0012	k-ε	C (?)	sharp (?)	77 (S 49)	34	2618	–
			C (?)	sharp (?)	87 (S 59)	30	2610	–
	NACA 4412		C (?)	sharp (?)	95 (S 63)	31	2945	–
Wang and Ostoja-Starzewski (2007)	NACA 0015	LES	C (?)	sharp (?)	360	63	22 680	–
Mary and Sagaut (2002)	A-airfoil	LES	C-H	blunt	2761 (97 | 431 | 2049)	91	251 251	2
Weber and Ducros (2000)	A-airfoil	LES	C	sharp	499 (S 385)	65	32 435	2

[a] Abbreviations are: SST = SST k-ω; B-L = Baldwin-Lomax; C-S = Cebeci Smith; J-C = Johnson-Coakley; J-K = Johnson-King; B-B = Baldwin-Barth; S-A = Spalart-Allmaras; BSL = BSL k-ω.

[b] k-ε, realizable k-ε, k-ω, SST.

boundary layers has a negligible effect on the overall flow, while the second is normally used to match experimental measurements (in which case transition in the experiment may be either forced or free). The third option, the most complicated, is essentially used when either of the first two options are unsuitable or unavailable (due to a lack of experimental data).

The European Union funded ECARP project (Haase et al., 1997) was concerned with the assessment of turbulence models for a number of flows, including that of an airfoil at high lift. Two profiles were considered: the Aerospatiale A-airfoil and the NACA 4412. The latter was considered to be of the most relevance to the present work and is discussed in the chapter by Abbas and Cabello (1997). Quantitative assessment of the different turbulence models was achieved by comparison of the lift and drag coefficients and the separation point with the experimental measurements of Hastings and Williams (1987). Further qualitative assessment was provided by comparison of the pressure, skin friction, displacement thickness and momentum thickness distributions and the velocity and Reynolds shear stress profiles near the trailing edge.

Results as described for the NACA 4412 are provided by four partners, each using their own in-house codes, but with two of the partners using the same mesh. The partners CASA, Dornier/DASA-LM and Saab used time-marching finite volume (field) based methods, with CASA using an unstructured grid and Dornier and Saab using a common 256×64 C-grid. The fourth partner, the Technical University of Berlin (TUB) used a viscous-inviscid interaction technique, this featuring a panel method solution coupled to a finite difference boundary layer method (as distinct from the integral boundary layer methods discussed under *panel methods*).

Lift and drag coefficient results are shown in table 2.5. From these, and from the other results noted, Abbas and Cabello conclude that the Johnson-King and the SST modified k-ε model of Saab produce the best results. The Johnson-King results are shown in bold in the table and it is seen that this is the only model which predicts the drag to within 10% of the experimental value; the lift predictions are also the most accurate (alongside one of the Baldwin-Lomax/Granville model results). The other turbulence model for which the results are shown in bold is the Baldwin-Lomax model. This was used by three of the partners, two of whom used a finite volume field method and one of whom used a viscous-inviscid interaction method. In contrast to the results from the Johnson-King model, which appear nearly independent of the method used, the results from the Baldwin-Lomax model show notable differences between the two field solutions and between the field solutions and the viscous-inviscid solution. Unfortunately

Table 2.5: *Lift and drag coefficients from the ECARP study. Values are shown with the precision given in the source.*

Partner	Turbulence model	c_l	c_d	% c_l	% c_d
CASA	**Baldwin-Lomax**	**1.66**	**0.0165**	**15.4**	**-51.5**
	Baldwin-Lomax (Granville)	1.57	0.0235	9.1	-30.9
Dornier	Cebeci-Smith	1.684	0.0227	17.0	-33.2
	Cebeci-Smith (Granville)	1.696	0.0233	17.9	-31.5
	Cebeci-Smith (Granville-Goldberg)	1.694	0.0234	17.7	-31.2
	Baldwin-Lomax	**1.725**	**0.0225**	**19.9**	**-33.8**
	Baldwin-Lomax (Goldberg)	1.725	0.0225	19.9	-33.8
	Baldwin-Lomax (Granville)	1.459	0.0246	1.4	-27.6
	Baldwin-Lomax (Granville-Goldberg)	1.592	0.0245	10.6	-27.9
	Johnson-Coakley	1.607	0.0255	11.7	-25.0
	Johnson-King	**1.488**	**0.0307**	**3.4**	**-9.7**
Saab	k-ε (standard two-layer)	1.579	0.0276	9.7	-18.8
	k-ε (SST)	–	–	–	–
TUB	Cebeci-Smith	1.73	0.0207	20.2	-39.1
	Baldwin-Lomax	**1.79**	**0.0206**	**24.4**	**-39.4**
	Johnson-King	**1.43**	**0.0313**	**-0.6**	**-7.9**
	k-ε (Lien-Leschziner)	1.73	0.0185	20.2	-45.6
	k-ω BSL	1.58	0.021	9.8	-38.2
	k-ω TUB	1.58	0.024	9.8	-29.4
	k-ω (Wilcox 94)	1.56	0.023	8.4	-32.4
Experiment	–	1.439	0.034	–	–

this is not discussed by Abbas and Cabello (1997). Nevertheless, it remains clear that the average of the Johnson-King results is superior to the average of the Baldwin-Lomax results.

One aspect of the NACA 4412 simulations of the ECARP study that was not found discussed anywhere else was the inclusion of the geometry of the experimental transition strip in the numerical mesh. A study of the effect of this was conducted by Dornier on a 512×128 C-grid (this being a two times linear refinement of the 256×64 C-grid) using the Cebeci-Smith and Johnson-King turbulence models; the results from this study for the lift, drag and moment coefficients are shown in table 2.6. Clearly, for both turbulence models there is a significant increase in the accuracy of the results from the grid with the transition strip. As such the transition strip was included in all of the meshes used for the NACA 4412 simulations, other than the boundary layer mesh of TUB where the transition strip was accounted for by increasing the local Reynolds number.

Table 2.6: *Lift, drag and moment coefficients from computations with and without a transition strip from the ECARP study.*

Turbulence model	Tr. strip	c_l	c_d	c_m
Cebeci-Smith	no	1.7620	0.01795	−0.08662
Johnson-King	no	1.6083	0.02141	−0.06425
Cebeci-Smith	yes	1.6861	0.02310	−0.07627
Johnson-King	yes	1.4575	0.03158	−0.05228
Experiment	–	1.439	0.034	–

The C-grids used by Dornier were included on a CD accompanying the book (Haase et al., 1997). These were examined in detail to determine meshing parameters not discussed in the text including the leading and trailing edge spacings tangential to the wall and the growth ratios parallel and normal to the wall. The choice of these parameters was used as a basis for the grids of chapter 5.

Zingg (1991, 1992) was the only reference consulted to feature a detailed grid convergence study using Richardson extrapolation. There is significant overlap between the two papers and of all the cases studied by Zingg the three of interest in the present work are discussed in both: these three cases are all of the NACA 0012 airfoil at a Reynolds number of 2.88×10^6, a Mach number of 0.16, and at angles of attack of 0, 6 and 12 degrees. Experimental data for these cases are taken from Gregory and O'Reilly (1970).

Four 'families' of grid are used in the 92 paper, the details of which are shown in table 2.7. Taking grid A7A as the 'base' grid, N7A has fewer nodes in the wall normal direction but the same clustering, N6A has the same number of nodes as N7A but a larger normal spacing at the wall, and W7A has a redistribution of the nodes from the direction tangential to the wall to the direction normal to the wall in such a way that the total number of nodes is similar. The clustering of nodes in W7A is the same as that of A7A but for the tangential spacing at the trailing edge which is larger. In addition to these grids, coarser versions are formed by removing every second grid point to form grids labelled A7B, N7B etc. Finally, the 91 paper also uses a grid formed by removing every second grid point from A7B, this being labelled A7C.

One of the primary conclusions given by the 91 paper is that a Richardson extrapolation from medium and coarse grid solutions can be used to produce an estimate of the lift and drag coefficients that is of similar accuracy to that obtained from the fine grid solution (relative

Table 2.7: *Details of the numerical grids used by Zingg (1991, 1992).*

Grid	N_x (Wake | Surface)	N_y	Δx (l.e.)	Δx (t.e.)	Δy	Δy^+
A7A	497 (48 | 401)	193	1×10^{-4}	1×10^{-4}	1×10^{-7}	0.02
N7A	497 (48 | 401)	97	1×10^{-4}	1×10^{-4}	1×10^{-7}	0.02
N6A	497 (48 | 401)	97	1×10^{-4}	1×10^{-4}	1×10^{-6}	0.2
W7A	297 (28 | 241)	321	1×10^{-4}	1×10^{-3}	1×10^{-7}	0.02

to a solution using Richardson extrapolation from the fine and medium grids). Such a solution method potentially offers a significant reduction in computational burden.

The 92 paper includes results from the W7A grid family which are not given in the 91 paper. It is shown that the results from this family show higher predictive accuracy for the drag than from the A7A family and only negligibly higher error for the lift (less than 1 %). Accuracy is again judged from Richardson extrapolations. This would appear to stress the importance of having a large number of nodes through the boundary layer, even at the expense of reduced refinement around the body. It is also shown that for all grids the numerical error increases as the angle of attack is increased.

An analysis of the far-field boundary error is given in the 92 paper by comparing the results from grids with this boundary at 12 and 96 chord lengths from the airfoil. (All of the grids used in the resolution studies have far-field boundary at $12c$.) It is shown that the error in the drag (when comparing the $12c$ grid to the $96c$ grid) is larger than the lift and is 0% at 0°, 1.6% at 6° and 3.4% at 12°. These relatively small errors are due to the use of non-reflecting boundary conditions with a far-field circulation correction. Such boundary conditions were also used in the ECARP study where the distance to the far-field boundary was 18 chord lengths for the Dornier mesh. Note that Zingg's results from the far-field boundary study are examined further in section 3.6.4.

The paper of Langtry et al. (2006) was of particular interest in the present work, primarily because the simulations were performed in CFX using the SST k-ω turbulence model, both with and without a transition model. These simulations were of the S809 airfoil (2D) and of a wind turbine rotor which uses the S809 profile (3D). In that 2D airfoil simulations were performed as a precursor to a more complicated turbine simulation, there is a methodological similarity with the present work. The airfoil simulations are compared against wind tunnel results and Xfoil.

For angles of attack between 0 and 10 degrees there is good agreement between the transitional CFD simulations and the wind tunnel results, with the fully turbulent results over-predicting the drag over this range. Beyond this angle the agreement deteriorates with both transitional and fully turbulent results showing an over-prediction of the lift and an under-prediction of the drag, although the agreement between the transitional simulation and the wind tunnel results is somewhat better.

No grid convergence study was reported, but based on the grid parameters stated, and in comparison to the results of Haase et al. (1997) and Zingg (1991, 1992), all of which are shown in table 2.4, it is likely that the discretization error is small. Perhaps more questionable is that no study of the far-field boundary error was reported. These boundaries were placed 10 chord lengths from the airfoil, a distance which has been demonstrated by Zingg to be acceptable when non-reflecting boundary conditions with a circulation correction are used, but which will be less so when a straightforward velocity boundary condition is used. Note that this boundary condition is not specified in the paper, but was found to be the case in the electronic definition files used in the simulation and provided to the author by Florian Menter of ANSYS (priv. comm.), one of the authors of the paper.

Ekaterinaris and Menter (1994), in a frequently referenced paper (e.g. Ekaterinaris and Platzer, 1997; Cebeci et al., 2005; Spentzos et al., 2005) present simulations of oscillating airfoil flows using a number of one- and two-equation turbulence models, namely a two-layer k-ε model, the standard k-ω model, the Baldwin-Barth model, the Spalart-Allmaras model and the BSL and SST k-ω models. These results are compared with the experiments of McCroskey et al. (1982) and Piziali (1994).

It is shown that none of the models are capable of accurately predicting the two deep-stall cases (see table 2.4 for a list of cases), but that the Baldwin-Barth, Spalart-Allmaras and SST k-ω models show a significant improvement over standard two-equation models. Good predictions are given by the Baldwin-Barth, Spalart-Allmaras and SST k-ω models for the attached and light stall cases, for which the other turbulence models were not used. For the single un-tripped case, the NACA 0012 airfoil with deep stall, it is shown that even approximate modelling of the transitional flow near the leading edge significantly improves the predictive accuracy.

Some parameters are given by Ekaterinaris and Menter (1994) in relation to the unsteady solution. It is stated that simulations were run with 10 000, 16 000 and 40 000 time steps per

cycle and that identical solutions were obtained. All of the results presented in the paper were from simulations with 16 000 time steps per cycle. These numbers are though to be high given that an implicit solution was used. It is also stated that all of the presented results are from the second cycle of each simulation and that the third is 'identical' to the second.

2.2.3.3 LES

The principle of large eddy simulation is to limit the turbulence 'modelling' to the smallest eddies; this stands in contrast to the RANS approach where all scales of turbulence are modelled (Versteeg and Malalasekera, 2007). The justification for the LES approach lies in the fact that whilst the behaviour of the larger eddies tends to be more problem dependent, the smaller eddies are nearly isotropic and show a universal behaviour (at high Reynolds numbers). Thus, restricting the modelling to the smallest eddies has the potential for higher accuracy. The principal disadvantage with LES is the increased computational burden: 'proper' LES must be 3D and time dependent – although some commercial codes appear to allow for 2D time dependent simulations (Simão Ferreira et al., 2007) – and the grid aspect ratio is limited, this leading to high resolution requirements in the streamwise direction for boundary layer flows (*CFX-Solver Modelling*). Of course, if the problem under consideration is inherently 3D and time dependent and is not controlled by boundary layer effects, then LES may not be significantly more demanding then RANS.

A key reference for the LES analysis of airfoils is the LESFOIL project, sponsored by the European Union (Mellen et al., 2003). The test case for this project was the Aerospatiale A-airfoil at $\mathrm{Re} = 2 \times 10^6$ and $\alpha = 13.3°$, the same used by the ECARP project discussed above. Mellen et al. present and compare the results from seven partners who used differing approaches to the gridding, sub-grid-scale modelling, boundary layer modelling etc. and show that the results of Mary and Sagaut (2002) are the best by most measures. They conclude that:

> ... genuinely successful simulations of this type of flow [airfoils at large Reynolds number and high angles of attack] can only be achieved by using a well-resolved LES in which near-wall turbulent structures are adequately resolved and transition is properly simulated. If these demands are not met, LES is not necessarily able to improve on RANS results.

(Mellen et al., 2003, p. 580). The grid resolution required for this is shown in table 2.4, and is seen to be significantly finer in the streamwise direction than that required for successful RANS

simulations of similar problems. The same conclusion was reached by Weber and Ducros (2000) in a comparative study of Baldwin-Lomax, Spalart-Allmaras and LES simulations (referenced by Mellen et al. (2003) and consulted separately).

In the context of the present work it was felt that RANS solutions could offer results of the desired accuracy, and that this had certainly not been disproved by previous efforts. LES will be discussed again in the *further work* section of the *discussions and conclusions* chapter.

2.3 Variable pitch

Variable pitch systems for vertical axis turbines provide cyclic pitching such that the pitch angle of the blade is a function of the azimuth angle of the blade. These systems may be either *passive* or *active*. Passive systems, alternatively called self-acting systems, rely on the aero/hydrodynamic forces on the blade to cause the pitching; this is typically achieved by having the blade pitch axis near the leading edge such that the fluid dynamic fores cause the blade to feather. Active systems may be either mechanical or electro-mechanical and effectively provide a control signal.

The use of passive variable pitch for vertical axis wind turbines was considered in a PhD thesis by Kirke (1998). In this study the primary focus was on the use of variable pitch to provide the turbine with self-starting capability. (Fixed pitch vertical axis turbines are not generally self-starting, although they may self-start in a turbulent wind – see for example Dominy et al. (2007).) Passive variable pitch for wind turbines was also considered by Pawsey (2002), and, as with Kirke, there is a similar emphasis on practical passive variable pitch systems. For tidal applications, and as noted in the *introduction*, the Enermar/Kobold turbine makes use of a passive variable pitch system with end-stops (Coiro et al., 2005).

Kirke also includes a substantial literature review of previous efforts on both passive and active variable pitch concepts, showing that interest in these dates from the 1970s. One concept noted by Kirke and discussed in some detail by Pawsey is that of an active pitching system using a cam to provide a sinusoidal variation in the blade pitch angle with the blade azimuth angle, as suggested by Grylls et al. (1978). Quoting from the experimental results of Grylls et al. and using a blade element momentum analysis, Pawsey (pp. 15–21) shows that the optimum power for a given tip speed ratio depends on the amplitude of the sinusoidal pitch variation, this

optimum amplitude decreasing to zero with increasing tip speed ratio.

A number of authors have derived 'optimal' active pitch control strategies based on different assumptions and using a variety of theoretical models. Kirke lists a number of papers from the 1980s; more recently this has been considered by Kosaku et al. (2002) and Hwang et al. (2006, 2007) for wind turbines and Camporeale and Magi (2000), Salter and Taylor (2007) and Ikoma et al. (2008) for tidal turbines. Many of these authors make reference to the active pitch control of Voith-Schneider propellers, a device which is effectively a vertical axis turbine in reverse. The optimization of the pitch control for this propeller is discussed by Jürgens et al. (2007). In the view of the present author, none of the references consulted on turbine pitch control optimization present a comprehensive analysis and it is thought that there is considerable scope for further research in this area.

The primary mechanism by which variable pitch improves the performance of a vertical axis turbine is by avoiding stall. This process is neatly illustrated by Salter et al. (2002) in a discussion of variable pitch applied to Wells turbines, the aerodynamic behaviour of which is similar to vertical axis turbines. The left side of the figure shows the resultant forces on a fixed pitch blade: as the angle of attack increases the blade begins to develop useful thrust until stall at around 12 degrees where the thrust becomes negative. If instead the blade pitches to maintain a maximum angle of attack of 8 degrees, as shown in the right side of the figure, then the useful thrust continues to increase.

2.4 Mathematical models of vertical axis turbines

A number of different mathematical models have been used to predict the aerodynamic performance of vertical axis wind turbines. These models have subsequently been used to predict the hydrodynamic performance of vertical axis tidal current turbines. The complexity of each of the models broadly reflects the number of assumptions that have to be made and range from the comparatively simple blade element momentum models to complete Navier-Stokes solutions.

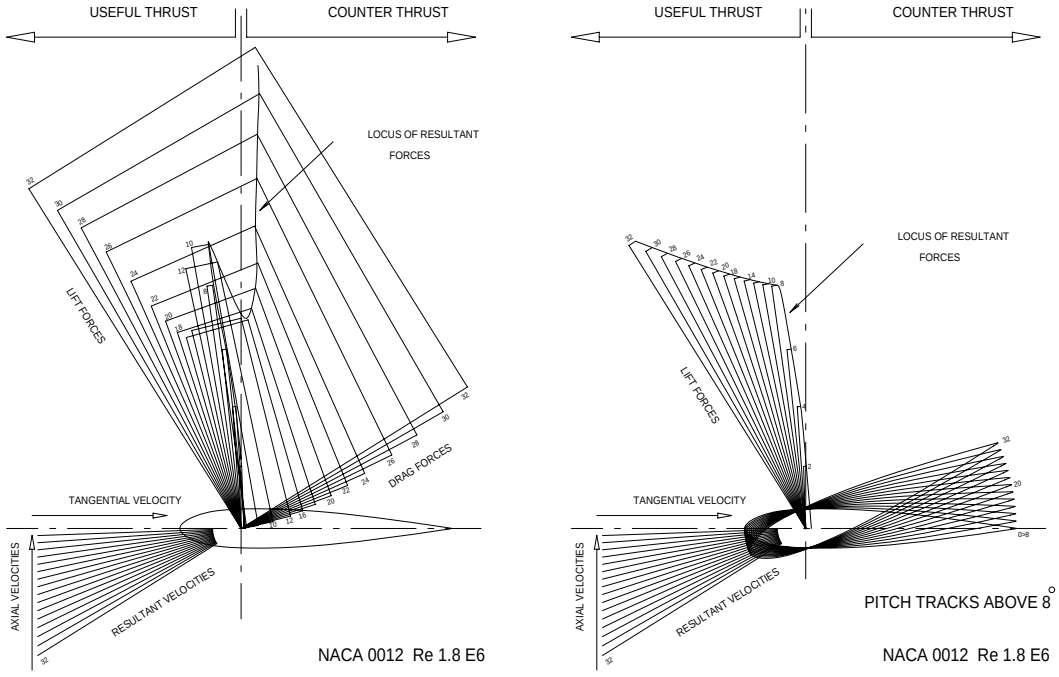

Figure 2.5: *Resultant forces on a turbine blade for fixed pitch and variable pitch operation. Figure taken from Salter et al. (2002), original source data is from Critzos et al. (1955).*

2.4.1 Blade element momentum models

Blade element momentum models involve the concept of an 'actuator disc', this representing the action of the turbine blades on the flow as a pressure drop which occurs across the disc. The pressure drop is equivalent to the streamwise force on the turbine blades divided by the area of the disc, with the forces on the turbine blades typically being calculated from airfoil section data, although basic models for the lift and drag forces are sometimes used. An iterative cycle is required because the pressure drop both determines and is determined by the velocity at the actuator disc.

Much of the terminology of the previous paragraph stems from the fact that this class of model was originally developed for 'airscrews', that is propellers and horizontal axis turbines (see for example Glauert, 1947). For these devices (airscrews) the swept area of a blade is of course a disc. Also, the term 'blade element' stems from the fact that the relative velocity at the turbine blade is a function of the radius from the axis of rotation and so it is necessary to integrate the force along the length of the blade.

For vertical axis turbines the swept area of a blade is a surface of revolution; a cylinder in the case of a straight-bladed turbine. A particle of fluid travelling 'through' the turbine will thus cross this cylinder twice: once 'upstream' and once 'downstream'. In the most basic class of blade element model (we drop 'momentum' for brevity) the velocity at the upstream and downstream intersections is taken as constant; these are known as single disc, single streamtube models and were first proposed by Templin (1974). The force is calculated by assuming that there is a blade element in each azimuthal position and integrating thus.

A refinement of the single disc, single streamtube model is the single disc, multiple streamtube model, as developed by Wilson and Lissaman (1974), Strickland (1975) and Shankar (1976), each using slightly different assumptions. In this model the velocity may vary with azimuth angle due to the multiplicity of streamtubes, but their remains a single intersection of each streamtube with an actuator disc.

The double disc, multiple streamtube model, as developed by Read and Sharpe (1980) and Paraschivoiu (1981) removes this constraint by using an upstream and a downstream disc in each streamtube. Both authors reference Lapin (1975) for the concept of using two discs. This class of model is therefore able to represent the fact that the downstream pass of the blades is in the wake of the upstream pass. The models differ in that the one of Read and Sharpe allows for streamtube expansion whereas that of Paraschivoiu does not. Given streamtube expansion, which is calculated from the conservation of mass, the upstream and the downstream 'halves' of the actuator cylinder become unequal. Later models of Paraschivoiu included streamtube expansion effects and other secondary effects; these are all documented in Paraschivoiu (2002).

The superiority of the single disc, multiple streamtube model over the single disc, single streamtube model has been shown by Strickland (1975) and Klimas and Sheldahl (1978) among others. This superiority has been judged by comparing predictions of the power coefficient from the two models with experimental data for the Sandia 2 m and 17 m diameter Darrieus turbines. Based on similar comparisons, Paraschivoiu (2002, chapter 6) has shown the superiority of double disc, multiple streamtube models over single disc, multiple streamtube models.

Klimas and Sheldahl (1978) also highlight the importance of the airfoil section data used with the blade element models. It is shown that the difference in the predicted results from the same model using different section data is comparable to that between different models using the same section data. This has also been highlighted by Tangler more recently (2002).

2.4.2 Extensions to blade element models

Various fluid dynamic effects not captured by basic blade element models may be included by the use of what might be termed 'sub-models'. Two effects which may be modelled thus are noted here: flow curvature and dynamic stall.

2.4.2.1 Flow Curvature

A blade on a vertical-axis turbine is subject to a curvilinear flow field as a result of its orbital motion. This means that the angle of attack of the blade varies along its chord. With the basic blade element momentum model we ignore this effect and take the blade angle of attack as being that at the point where the blade chord is tangent to the orbital path. It would be desirable however to account in some way for this effect within the blade element momentum model. Migliore et al. (1980) suggest the use of a conformal transformation to achieve this. The transformation is such that the curved streamlines are transformed to straight streamlines and the symmetrical foil is transformed to one having a cambered profile and set at an angle of incidence to the transformed streamlines.

2.4.2.2 Dynamic effects

When the angle of attack of an airfoil is rapidly changing, the instantaneous lift, drag and moment forces at a given angle of attack are different from those generated under steady conditions (Ekaterinaris and Platzer, 1997; Cebeci et al., 2005). The motion may be that of 'plunging' (translation normal to the chord) or pitching or a combination of the two. For pitching motions, the most commonly considered case is that of a sinusoidal oscillation about the quarter chord point. Clearly there are considerable similarities between such flows and that of a vertical axis turbine blade.

The non-dimensional number which determines the significance of these dynamic effects is the Strouhal number (see section 3.5.3); for oscillating airfoils this is defined as:

$$k = \omega c / 2U_\infty \tag{2.12}$$

where ω is the radian frequency of oscillation, c is the chord length and U_∞ is the freestream speed.

For a vertical axis turbine blade the appropriate value of U_∞ is in fact the relative flow speed, which is a function of the azimuth angle. Taking an approximate average as $U_{\infty,\,\text{blade}} = \Omega R = \lambda U_{\infty,\,\text{freestream}}$, and substituting this into the above equation we arrive at:

$$k = c/2R = \sigma/2N \tag{2.13}$$

Note how this is dependent only upon the geometry; for the Edinburgh Designs turbine, $k = 0.08$. This value is large enough for dynamic effects to be significant, and is within the range of values for which airfoil experiments were conducted by McCroskey et al. (1982, $k = 0.01$–0.2) and Piziali (1994, $k = 0.04$–0.2).

The effects of dynamic stall may be modelled, the basic idea being to calculate a corrected static angle of attack. The static airfoil behaviour at this corrected angle of attack is then used in place of true dynamic data. Paraschivoiu (2002, chapter 6) compares results from a number of dynamic stall models used with a blade element momentum model of a vertical axis turbine.

2.4.3 Vortex models

Vortex models of vertical axis turbines utilize the concept of vortex filaments, also known as lifting lines, to represent the flow field around a vertical axis turbine (Strickland et al., 1979a). The name is somewhat unfortunate in that boundary element and panel method solutions of vertical axis turbines could equally be described as vortex models; nevertheless this is the name in common usage. The basic idea is to model the production, convection and interaction of the vortex systems arising from blade elements and to use this to predict the induced velocity in the flow field. This induced or perturbation velocity is superimposed on the undisturbed flow; from this combined flow field the lift and drag forces on blade elements can be obtained using airfoil section data. The solution is progressed in time from initial conditions and predicts the time-dependent behaviour of the turbine.

Vortex models were first applied to vertical axis turbines with 2D geometry by Larsen (1975), Fanucci and Walters (1976), Holmes (1976) and Wilson (1978) and then extended to model the 3D geometry of the Darrieus turbine by Strickland et al. (1979a,b, 1981). The latter set of references include comparisons of the predicted blade forces with experimental data and show good agreement.

At the time of development, vortex models had a significant computational burden and so a class of 'fixed-wake' vortex models were developed by Wilson and Walker (1981, 1983). These combined some aspects of the vortex models noted above with blade element models. The 'original' class of vortex model is thus sometimes termed a 'free-wake' vortex model.

The accuracy of free-wake vortex models relative to double disc, multiple streamtube blade element models has been assessed by Paraschivoiu (2002, section 6.7) based on comparisons of the predicted power coefficient with experimental results for the Sandia 17 m diameter turbine. It is shown that the results are very similar when the blade element model includes either variable induction factors in each streamtube or streamtube expansion. Coiro et al. (2005) also show good agreement between blade element and vortex models but note that the blade element model fails to converge for cases with high axial induction factors.

2.4.4 Potential flow solutions

Various potential flow solutions have been presented for vertical axis wind and tidal current turbines. A few of these are listed below to highlight the different approaches:

- Gorban et al. (2001) used a modified Kirchhoff flow to model the behaviour of an actuator disc. This model does not represent the behaviour of pressure recovery in the wake of a turbine and so predicts low turbine efficiencies. It is frequently cited because it is one of the few reference points for the Gorlov helical turbine.

- Ponta and Jacovkis (2001) combined a free-vortex model in the far-field with a finite element solution for inviscid flow in the vicinity of the blades and an integral boundary layer solution. The model is validated with the experimental results of Strickland reported in Klimas (1982) – presumably those of Strickland et al. (1981) but this was not verified. The hybrid model shows improved results over the free vortex model.

- Ågren et al. (2005) present a potential flow solution using conformal mapping. Drag is not considered and the results show implausibly high performance coefficients at high tip speed ratios.

- Calcagno et al. (2006) discuss the development of a boundary element solution. Only preliminary, qualitative, results are presented.

2.4.5 CFD models

A number of authors have reported results from CFD simulations of vertical-axis wind and tidal current turbines, as listed in table 2.8. These simulations feature a number of different geometries and span a significant range of the Reynolds number. The numerical parameters used were examined to assess the quality of the results presented and to use as a basis for the CFD simulations in the present work; these are summarized in table 2.9. Clearly the reporting of these parameters is far from comprehensive, making it difficult to assess the quality of the majority of these references or to use these as a basis for the present work.

One of the most widely reported parameters is the domain extent, with many of the authors opting to position the outlet boundary 10 to 15 turbine diameters downstream of the turbine axis. Unfortunately no justification is provided in any of the references for this choice.

A number of authors state that the simulations were advanced in time until a periodic steady state was reached. Unfortunately (again) it is not stated precisely how many cycles this took, or how the attainment of the periodic steady state was assessed. This problem is not relevant to the results of Vassberg et al. (2005) which were obtained using a time spectral method.

Only one of the references, Simão Ferreira et al. (2007), reports of a verification study into either the spatial or temporal discretization; in this case, both were conducted. The spatial discretization study involved coarsening the region of the mesh nearest the blade by a factor or two linearly to reduce the number of nodes in this region by a factor of 4 (the mesh is 2D). This was repeated to obtain a third mesh. (Note that the node counts listed in table 2.9 apply to the finest mesh.) Simulations were run on these three meshes using the Detached Eddy Simulation (DES) model, a hybrid of RANS and LES approaches, and it was found that the effect on the predicted forces was small. The results from the time step refinement studies showed that a time step of $1/4°/\omega$ was suitable when the Spalart-Allmaras turbulence model was used while a time step of $1/8°/\omega$ was suitable when the DES model was used. This time step verification was assessed by qualitative comparisons of the vorticity.

A further verification exercise conducted by Simão Ferreira et al. involved assessing the effect of the iterative convergence on the high frequency (relative to the rotation frequency) oscillations predicted in the force coefficients. This study proved inconclusive.

Table 2.8: *CFD simulations of vertical axis wind and tidal current turbines presented in the literature: Scope of simulations and results.*

Reference (/Simulation)	Wind/ Tide	Profile	N	c (m)	D (m)	Nc/R	Re_c	λ	Data[a]
Klaptocz et al. (2007)	Tide	NACA 63_4-021	3	–	0.91	–	0.3×10^6 [b]	1.75–3.5	$Q = f(\psi)$, $P = f(\lambda)$
Simão Ferreira et al. (2007)	Wind	NACA 0015	1	0.05	0.4	0.25	50 000	2	F_N^+, $F_T^+ = f(\psi)$, vorticity
Hwang et al. (2006)	Wind	various[c]	4	0.22	2	0.88	0.45×10^6 [d]	1.9–2.8	$P = f(\lambda)$
Horiuchi et al. (2005) / wind tunnel	Wind	TWT11251	3	0.15	2.5	0.36	0.24×10^6 [d]	2.8 & 3.3	wake velocities
/ free stream	Wind	TWT11251	3	0.15	2.5	0.36	0.24×10^6 [d]	1.8–4.8	wake velocities
Vassberg et al. (2005) / H-type	Wind	NACA 0015	1	–	–	0.125	1×10^6	5	$C_P = f(\lambda, \sigma)$
/ H-type	Wind	WARP0015-RC8	1	–	–	0.125	1×10^6	5	$C_P = f(\lambda)$
/ Darrieus	Wind	NACA 0015	1	0.61	17	0.072	–	5	$C_P = f(\lambda)$
QinetiQ (2004)	Tide	NACA 0012	3 & 6	1 & 2	10	0.3–0.6	2×10^6	2	$F_T^+ = f(\psi)$
Ishimatsu et al. (2002)	[e]	NACA 0018, 0030	3	0.4	1	2.4	1×10^6	–	$Q^+ = f(\psi)$, efficiency[f]
Hansen and Sørensen (2001)	Wind	NACA 0015	1	0.1524	1.22	0.25	67 000	2.5	F_N^+, $F_T^+ = f(\psi)$
Paraschivoiu (2002) [g]	Wind	NACA 0015	1	0.1524	1.22	0.25	67 000	2.5	F_N^+, $F_T^+ = f(\psi)$

[a] Q is the torque; ψ is the azimuth angle; P is the power; λ is the tip speed ratio; F_N^+ and F_T^+ and the normal and tangential blade force coefficients, non-dimensionalized using the freestream velocity; Q^+ is the shaft torque coefficient, also non-dimensionalized using the freestream velocity.

[b] This is calculated by assuming that the solidity is the same as the ED turbine (0.48), therefore giving a chord length of 0.0728. $U_\infty = 1.5$ from the paper. $\lambda = 2.5$ is taken as the reference tip speed ratio.

[c] NACA 0018, 2418, 4418, 6418, 63_3-018, 63_3-218, 63_3-418, 63_3-618.

[d] Based on the middle tip speed ratio.

[e] The Application is for 'alternating flow'. Although not explicitly stated, it is understood that this alternating flow is driven by an oscillating water column type wave energy converter.

[f] An unconventional definition of efficiency is used.

[g] This reference is listed apparently out of order to reflect the fact that it is a review of previous work, namely that of Tchon (1992), Hallé (1995).

Table 2.9: *CFD simulations of vertical axis wind and tidal current turbines presented in the literature: Simulation setup.*

Reference (/Simulation)	Δ_y^+	total nodes	nodes on blade	cycles	steps/cycle	L_b/D inlet	L_b/D outlet	L_b/D side	Turbulence models[a]
Klaptocz et al. (2007)	–	–	–	–	–	5	15	5	S-A
Simão Ferreira et al. (2007)	1	1.6×10^6	3305	[b]	720–5760	10	14	1.6 [c]	S-A, k-ε, DES, LES
Hwang et al. (2006)	–	–	–	–	–	–	–	–	–
Horiuchi et al. (2005) / wind tunnel	–	–	–	[b]	–	5	15	1.1 [c]	DES
/ free stream	–	–	–	[b]	–	5	15	5	DES
Vassberg et al. (2005) / H-type	–	294 912 [d]	–		–	–	–	–	B-L
QinetiQ (2004)	–	–	–	2	–	1.6	1.6	1.6	k-ε
Ishimatsu et al. (2002)	–	889 900	–	–	–	2.1	3.1	[e]	laminar
Hansen and Sørensen (2001)	1	–	256	"some"	2000	2.5	2.5	2.5	k-ε, non-linear k-ε
Paraschivoiu (2002)	1	9615	192	1	–	11.25	11.25	11.25	laminar, C-S, J-K

[a] S-A = Spalart-Allmaras, DES = Detached Eddy Simulation, LES = Large Eddy Simulation, B-L = Baldwin-Lomax, C-S = Cebeci-Smith, J-K = Johnson-King.
[b] It is stated in the paper that a periodic steady-state is obtained.
[c] Determined by the wind tunnel walls in the validation experiment.
[d] A 192x64x24 C-grid was used for the 3D simulation.
[e] The turbine is simulated in a duct with walls at $D/2$ + blade thickness/2 + $0.025D$.

Overall, and with the notable exception of the work of Simão Ferreira et al., it was found that the literature on CFD simulations of vertical axis turbines offered little insight into the numerical parameters that should be used in the present work.

2.4.6 Coupled CFD and blade element momentum models

A number of authors have used porous cells within a CFD model to simulate the action of a turbine, with the pressure drop through these cells being determined from a blade element model. This type of hybrid model was originally proposed for vertical axis wind turbines by Rajagopalan and Fanucci (1985) and later used by Brahimi et al. (1995) and Zhang (2004) among others. It has recently been used by Antheaume et al. (2008) to simulate an isolated tidal current turbine and an array of these turbines. The advantage of this type of model is that it provides viscous simulations of the wake behaviour with comparatively few cells. As illustrated by Antheaume et al. it can also be used to predict the behaviour of arrays of turbines.

In the context of the present modelling work, these simulations provide further guidance as to the extent of the computational domain required i.e. L_b/D. Rajagopalan and Fanucci conducted a study of the effect of this distance based on the predicted power coefficient and concluded that C_P "reached its asymptotic value" at $L_b/D = 4$. Notwithstanding this oxymoron and a lack of quantification, a graph of C_P versus L_b/D in the paper shows that the stated value appears to be a reasonable approximation to the asymptotic value. No studies of this sort were conducted by Zhang or Antheaume et al. who used $L_b/D = 7.5$ and 20 respectively. For the case of the linear array simulation of Antheaume et al., the distance used was 20 array widths.

2.4.7 Free surface effects for tidal current turbines

Aerodynamic analysis methods for vertical axis wind turbines have been adopted for vertical axis tidal current turbines without modification, and indeed this is the approach taken in the present work. Research into the effect of the free surface has been limited to date, but one interesting contribution shows that it could be significant. Whelan et al. (2007) have approached the problem in 2D and modified classic actuator disc theory to include the blockage effect of the free surface and the effect of gravity. Their results show that for a blockage ratio of 0.125, equivalent to a single horizontal axis turbine in a channel of width and depth equal to $2.5D$, and at an axial induction factor of $1/3$, the turbine thrust coefficient will be increased by 28%

and the power coefficient increased by 18.7% relative to the case of a turbine in an unbounded domain.

As highlighted in the *introduction*, and especially figure 1.5, future CFD simulations of vertical axis turbines under a free surface would lead from the present work.

2.5 Physical tests of vertical axis turbines

The literature on physical tests of vertical axis wind and tidal current turbines was examined as a potential source of validation data for the mathematical modelling of the present work. The most definitive data found was that for wind turbines, as reviewed by Paraschivoiu (2002), with a significant proportion of this originating from the US Department of Energy sponsored research programmes at Sandia National Laboratories. Most references present data only for the coefficient of performance of the turbine, with a limited number presenting data for the blade forces (as a function of azimuth angle) and for the velocity in the wake of the turbine. We examine below first data from model scale tests in a tow tank and a water tunnel and then data from large scale tests in the field.

2.5.1 Experimental models

Strickland et al. (1981) describe a series of experiments on a model turbine of 1.22 m diameter conducted in the Texas Tech University towing tank. Measurements were made of the normal and tangential blade forces and the velocity profile one and two turbine diameters downstream of the axis of rotation. The turbine could be fitted with one, two or three blades, each of 9.1 cm chord and 1.1 m length, thus allowing the solidity of the turbine to be altered. The towing tank had a depth of 1.25 m, a width of 5 m and a length of 10 m. The turbine blades thus extended to within 15 cm of the bottom of the tank. In all of the tests the turbine tip speed was 45.7 cm/s giving a blade chord Reynolds number of 40 000. Three different towing speeds were used to give tip speed ratios of 2.5, 5 and 7.5.

Results are presented for five different combinations of the number of blades and the tip speed ratio, these being for one, two and three blades at a tip speed ratio of 5 and for two blades at the other two tip speed ratios (2.5 and 7.5). The results presented for the wake profile consist of the streamwise and lateral perturbation velocities one turbine diameter downstream of the axis

of rotation at six time instants for each case. Results are not presented for the wake profile at the second location.

The only data presented by Paraschivoiu (2002) that shows the development of the wake behind a turbine is that of Brochier et al. (1986). These tests were of a 12 cm diameter vertical axis turbine with 20 cm long blades and were conducted in a water tunnel with a test section of 20×20 cm. The results appear to be severely affected by blockage in that there is substantial acceleration of the flow around the sides of the turbine.

2.5.2 Large-scale devices

The most interesting data found from a large-scale test is that of Akins et al. (1987), as reported in Paraschivoiu (2002). These data are for the aerodynamic torque acting on the Sandia 17 m diameter turbine, as a function of the azimuth angle. This turbine is of a Darrieus type with a height-to-diameter ratio of 1 and was tested with many configurations of blade; the results given by Paraschivoiu (2002) are for 2 blades of 0.612 m chord and NACA 0015 profile. The rotational speed was 50.6 rev/min giving a blade chord Reynolds number of 1.25×10^6. Data are given for tip speeds of 2.87–7.93.

None of the data discussed here were considered suitable for validation of the mathematical models used in the present work. The data of Strickland et al. (1981) is suitable for validating a 2D model but is unfortunately for a low Reynolds number. Somewhat in reverse of this, the data of Akins et al. (1987) is for an appropriate Reynolds number but is for a 3D case.

2.5.3 Porous bodies

Given the lack of experimental data on the development of wakes behind vertical axis turbines, a brief investigation was made of the literature on the wakes behind porous bodies. It was thought that the behaviour in the far wake behind these objects would be qualitatively similar to that behind a turbine, at least for similar values of the Reynolds number.

Castro (1971) conducted studies of the aerodynamic behaviour of a perforated plate in a wind tunnel at Reynolds numbers of between 2.5×10^4 and 9×10^4, based on the width of the plate. The length of the plate completely spanned the wind tunnel test section and was 1/16 inch

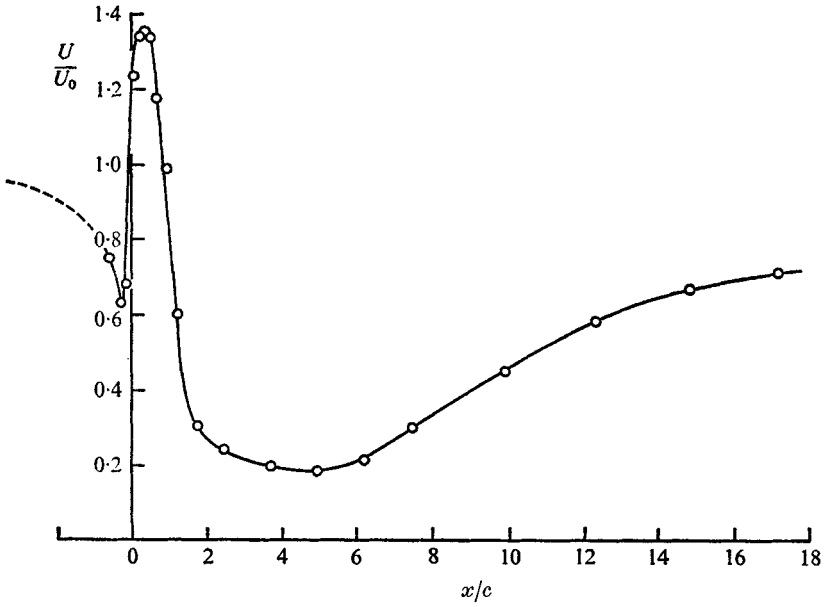

Figure 2.6: *Non-dimensionalized velocity parallel to the tunnel axis and normal to the centreline of the plate for the case of an open area to total area ratio of 0.425. Figure taken from Castro (1971).*

thick. One of the most illuminating graphs in this paper shows the velocity parallel to the tunnel axis and normal to the centreline along the same line, shown here as figure 2.6. A peak occurs immediately downstream of the plate, due to a jet of fluid coming through one of the perforations. This is followed by a decrease in the velocity to a minimum at about 5 plate widths downstream and then what appears to be asymptotic development of the wake from about 10 plate widths downstream.

Similar experiments were conducted by Huang and Keffer (1996) and Huang et al. (1996) for the case of a mesh strip at a Reynolds number of 1×10^4, again based on the width. In these papers the region from 1 to 20 plate widths downstream of the plate is identified as the "initial formation region", while that from 20 to 100 plate widths is identified as the "development stage".

Clearly the key issue in using these results to inform the design of the turbine mesh is the considerable disparity in the Reynolds number. Nevertheless, these papers suggest that the downstream boundary should be at least 10 to 20 diameters downstream of the turbine (in order to model the initial development of the wake) a distance which is broadly in accord with the better numerical studies of turbines conducted previously.

2.6 The tidal resource

An understanding of the resource is of fundamental importance for any renewable energy technology. In this section we first explain the origin of the tides and introduce terms which will subsequently be used. Second, we review assessments of the magnitude of the tidal current resource. These may be divided between those aimed at understanding the resource as an aim in itself, and those aimed at assessing the resource in the context of its use as a source of renewable energy. Third, we review literature examining the feedback effect from the extraction of tidal energy. This is a new area of research and firm conclusions are yet to emerge. Finally, we review data on turbulence in the marine boundary layer. Such data are required for use as inlet boundary conditions in the numerical model.

2.6.1 Origin and characteristics of the tides

A good introduction to the origin and characteristics of the tides is given by the Open University text *Waves, Tides and Shallow Water Processes* (1999), while a more comprehensive text is that by Pugh (1987). Here we briefly note some of the salient features of the tides, as informed by these texts.

Consider for the moment only the earth-moon system and assume spherical bodies and circular orbits. The two bodies rotate about their common centre of mass, with the centripetal acceleration of each body being produced by their mutual attraction. Importantly, for each body, every element in that body traces out a circle with the same radius. As a consequence of this, the centripetal acceleration of each element of a given body will be the same.[5]

For a particle at the centre of the earth the gravitational attraction of the moon provides exactly the force required for the acceleration. For particles nearer or further than this the attraction of the moon will be stronger or weaker respectively. Given that the centripetal acceleration required is constant there will thus be a resultant force; this is the tide generating force.

The result of this tide generating force acting on a supposed fluid covered earth is known as the equilibrium tide. This concept gives an elliptical water surface on a spherical earth, with the major axis of the ellipsoid being aligned with the centres of the earth and moon. As the earth

[5]Note that some texts do not explain this motion correctly and instead state that every element of the earth rotates about the centre of mass of the earth-moon system, resulting in a varying centripetal acceleration being required (or, as viewed from the non-inertial frame of the earth, a varying centrifugal force) e.g. Elliott (2004, p. 199).

rotates about its own axis a point on the equator will pass through approximately two high tides and two low tides per day; *approximately* because the moon has rotated about the centre of the earth-moon system in this time and so the tidal ellipsoid has also rotated. As such the actual time for a cycle of two highs and two lows is 24 hours and 50 minutes, this being known as a lunar day in an oceanographic context. This 'type' of tidal behaviour (we will note below others) is termed semi-diurnal in reference to the period being approximately half of a day.

Thus far we have considered only the action of the moon on the earth's tides. The effect of the sun on the tides is somewhat weaker, being about 0.46 times as strong as that of the moon. When combined with the effect of the moon an approximately fortnightly modulation is seen in the amplitudes of the tidal patterns discussed above. Maximum tidal ranges, known as spring tides, occur shortly after the times of a new moon and of a full moon. The minimum ranges, known as neap tides, occur shortly after the times of first and last quarter. Spring tides are larger because the tide generating forces of the moon and sun combine together, whereas neap tides are smaller because the forces are out of phase and cancel somewhat. The period from full moon to full moon is known as a synodic or lunar month and is about 29.5 days; the time from one spring tide to the next is half this i.e. about 14.8 days.

Many other aspects of the motion of the sun-earth-moon system have a significant effect on the characteristics of the tides, of which two are briefly noted here: the effect of the declination and the elliptical orbits. If the declination of either the moon or the sun is non-zero then a diurnal (i.e. once daily) tide will be introduced. This type of tide is responsible for causing the magnitudes of two successive highs (and lows) to be different. The total tidal range is largest when the declination is zero; for the sun this occurs at the equinoxes and a coincident spring tide is named an equinoctial spring tide. The elliptical nature of the moon's orbit is such that at perigee the tide generating force is 15% stronger than the mean, while at apogee it is 15% weaker. This modulates the semi-diurnal tide. The earth's orbit about the sun is less elliptical and so the effect is less significant.

2.6.2 Resource assessment

A number of estimates exist for the average tidal energy flux onto the north-west European continental shelf; this energy being dissipated by viscous friction. Blunden and Bahaj (2007), in a review of resource assessments, cite three: Flather (1976), Cartwright et al. (1980) and Egbert and Ray (2001); the paper by Flather was examined by the present author but the others

were not. Flather's estimate of 215 GW (p. 159) is the result of a two-dimensional numerical model of the region while Cartwright et al. give a value of 250 GW, this being derived from moored current metre and bottom mounted pressure transducer data. The more recent estimate of 219 ± 30 GW by Egbert and Ray is the result of an inverse model constrained by satellite altimetry data. Based on these estimates from a variety of methods it seems reasonable to conclude that the average tidal power dissipation in the waters around the British Isles is over 200 GW. This figure may be compared with that of the average primary power demand of the UK: 313 GW.[6] Clearly then there is considerable potential.

A number of reports give estimates of the 'extractable' UK tidal current energy resource, as limited by technical, economic and environmental considerations. These date back to the 1970s (see the review by Blunden and Bahaj), but we start here with two reports from the 1990s: one by the Energy Technology Support Unit of the UK government (ETSU, 1993) and a second prepared for the European Commission (EC, 1996). Details of these reports are as cited by Black and Veatch (2004) in a study for the Carbon Trust unless otherwise stated; this report will be discussed in due course and is herein referred to as 'B&V/CT Phase I'.

The ETSU 93 report included sites where the mean spring peak velocity is greater than 2 m/s, with the velocities being obtained from tidal stream atlases. Sites having water depth less than 20 m or area less than 2 km^2 were then rejected. Having identified suitable sites, the size of the turbines that could be installed was calculated based on the depths while spacing laws were applied to determine the layout. Velocities from the tidal stream atlases for a single 12.4 hour cycle were scaled according to the tidal range at Dover over a year. A single value for the velocity at a given time was used for each site i.e. no spatial interpolation was done. The power outputs from the turbines were then calculated from the velocity distribution and an assumed power curve. The resulting annual energy yield calculated was 58 TWh, equivalent to an average power output of 6.6 GW (cited in B&V/CT Phase I, p. 6).

A methodology similar to that of the ETSU 93 report was adopted by the EC 96 report. In this later report all sites with a mean spring peak velocity above 1.5 m/s were considered and sites with velocities between 1.0 and 1.5 m/s were considered on a case by case basis. The assumptions used in calculating the turbine size and spacing resulted in a lower ratio of rotor area to sea surface area to that calculated in the ETSU 93 study, as shown by Blunden and Bahaj

[6]The *Digest of United Kingdom Energy Statistics* (BERR, 2007a, p. 27) gives a figure of 235.8 million tonnes of oil equivalent for primary demand during 2007. This equates to 2742 TWh or an average power of 313 GW.

(2007). The resulting annual energy yield calculated by this study is 31 TWh/y, equivalent to an average power output of 3.5 GW (cited in B&V/CT Phase I, p. 6).

A key criticism made of the ETSU 93 and EC 96 reports by the B&V/CT Phase I and later Phase II report and summary (Black and Veatch, 2005a,b) concerns the feedback (or lack thereof) between energy extraction and the resource. Both the ETSU 93 and EC 96 reports assumed a single value of the velocity at a given time for each site; this implies that the velocity is fully 'recharged' by the time the flow reaches one turbine downstream of another. This methodology, termed the 'farm method' by Black and Veatch, was adopted from that in practice in the wind energy industry at the time, but the Phase I and II reports argued that it is not applicable to tidal energy extraction. Instead, it is argued that only a limited proportion of the 'natural' kinetic energy flux through a cross-section normal to the flow can be extracted, where natural refers to the state before energy extraction. This so called 'flux method' was independently developed by Bryden et al. (2004; 2004); the background theory given in these papers will be discussed below. The proportion of the natural kinetic energy flux which can be extracted is termed the 'significant impact factor' by Black and Veatch; this is somewhat arbitrarily defined as the proportion of energy which can be extracted without unduly affecting the flow. Values in the Phase II report (p. 20) suggest that this means a 10–15% velocity change from the natural state.

Beyond the introduction of the flux method the Phase I and II reports are similar in scope to the ETSU 93 and EC 96 reports, both being based on secondary data sources. In the Phase I report surface dimensions of the sites and velocities were taken from the ETSU 93 and EC 96 reports and a significant impact factor of 0.2 was used for all sites. The extractable resource was thus estimated at 22 TWh/y or 2.5 GW average power (Phase I, p. 6).

The Phase II report involved further investigation of the 10 most important sites identified in the Phase I report, these containing 80% of the total resource. Site widths, depths and velocities were reviewed; as noted in the Phase II report the data for the velocity are the most important owing to the cubic relationship with power. The revised velocity estimates were obtained from updated versions of Admiralty charts and tidal stream atlases (the source data for the ETSU 93 and EC 96 reports), and from the then recently published *Atlas of UK marine renewable resources* (ABPmer et al., 2004a,b), discussed below. Also updated in the Phase II report on a site by site basis were values for the significant impact factor. This remained at 0.2 for six sites (including the three most important) but was reduced to either 0.08 or 0.12 for

the other four. The basis of this appears to be a limited amount of numerical modelling and a significant amount of a priori reasoning. The resultant estimate of the extractable resource from this report is 18 TWh/y or 2.1 GW average power (Phase II p. 5).

The *Atlas of UK marine renewable resources*, herein 'Atlas 04', was produced by ABPmer et al. for the DTI. It is well described by its title, consisting as it does of geographical contour plots of quantities such as the mean peak spring and neap velocities and associated power densities. The information is from a numerical model run by the Proudman Oceanographic Laboratory with a minimum horizontal grid resolution of 1.8 km (ABPmer et al., 2004b, section 2.3). Such a relatively coarse grid scale (from the context of tidal sites of the order of kilometres or less in size) makes the data difficult to apply to site selection and assessment. An updated Atlas was produced in 2008 for what is now known as BERR (ABPmer et al., 2008a,b). This used the same horizontal grid resolution but featured enhanced vertical resolution, an improved vertical mixing scheme and more accurate treatment of the intertidal boundary (ABPmer et al., 2008b, section 2.3). The comments above for the 2004 report apply similarly.

One final report noted in passing is that produced by the consultancy Metoc (2007) as part of the Sustainable Development Commission's report *Tidal power in the UK*. This is largely a review of previous reports, but includes the results of some numerical modelling work carried out by Metoc. This consists of models of the Pentland Firth and Severn Estuary at a horizontal resolution of 1 km and of the Orkney Isles at a resolution of 200 m. The authors of the Metoc report note the importance of the grid resolution while comparing their results to those of the 2004 Atlas.

2.6.3 Feedback effects from power extraction

It is not currently known with certainty what the effect of large scale tidal current energy extraction will be on the tidal environment. Specifically, the question of how much energy may be extracted remains largely unanswered. Attempts to answer this question have to date focused on the modelling of idealized cases, as discussed here.

In one of the earlier papers in this genre Bryden and Couch (2004) consider the case of a channel linking two infinite oceans with a prescribed head difference. This is suggested as a very basic model of the behaviour of the Pentland Firth, although this comparison is only made explicit in a later paper (Couch and Bryden, 2006) discussed in due course. A one-dimensional

equation for gradually varied open channel flow (see for example White, 1999, p. 682–685), effectively a form of Bernoulli's equation, is solved numerically for two cases: with and without artificial energy extraction. The artificial energy extraction is modelled as a sink of energy at a particular node. The case with artificial energy extraction involves 10% of the kinetic energy flux through a cross-section of the channel being extracted. It is shown that this represents 8.4% of the kinetic energy flowing through the same cross section for the channel in the natural state i.e. the artificial extraction of energy has caused the volume flow rate in the channel to drop. In the vicinity of the extraction the velocity is 5.4% lower for the case with artificial energy extraction. The attractiveness of this analysis to the present author lies in its simplicity: it very obviously makes the point that we should expect tidal flows to respond differently to wind when energy is artificially extracted. See also a later paper by the same authors (Couch and Bryden, 2005) which applies a shallow water equation solver to the same problem and to a related two-dimensional case.

The case of energy extraction in the mouth of a sea loch was considered by Bryden and Melville (2004). As with Bryden and Couch (2004) the modelling was based on the equation for gradually varied open channel flow; this time a quasi-steady approach was used to simulate the response to an imposed and time dependent sea surface elevation at the open end of the sea loch. The conclusion of the authors was that the response of this system to energy extraction was notably different to that of the channel case and that it may be possible to extract 30% of the kinetic energy flux with "little" reduction in the flow speed.

An elucidation of the driving mechanisms behind five different 'types' of tidal current is given by Couch and Bryden (2006). These different types are identified as 1) offshore deep ocean currents, 2) unbounded shelf currents, 3) tidal streaming through a convergent-divergent channel, 4) hydraulic currents driven by head differences, and 5) resonant basins. The latter three types feature the high velocities that are required for economic energy extraction and some idealized cases are modelled using a shallow water equation solver. It is suggested that streaming sites have the potential for the greatest proportion of kinetic energy flux to be extracted, with a significant impact factor (as per the B&V/CT reports discussed above) of 25–30%.

Two papers by Garrett and Cummins (2004, 2005) focus on establishing the maximum amount of power which may be extracted from a bay and from a channel respectively. These cases are similar to those considered by Bryden et al. discussed above. Both papers by Garrett

and Cummins employ a 1D quasi-steady model based on the gradually varied open channel flow equations, with the flow being driven by an imposed sea surface elevation on the open boundaries. The first paper shows that tidal current energy extraction in the mouth of the bay could harvest up to 76% of the maximum theoretically possible with a single operation barrage type scheme. This maximum is calculated by assuming that all of the water in the bay at the natural high tide is impounded and used to generate all of the energy at the natural low tide i.e. the full head range is used. For this case of maximum tidal current energy extraction the tidal range in the bay is reduced to 74% of the natural range. It is shown that if this were to be judged environmentally unacceptable it would be possible to maintain 90% of the natural range in the bay without significantly reducing the energy generated. It is also argued by the authors that the kinetic energy flux in the mouth of the bay is not an especially useful measure of the tidal energy potential for this case.

The second paper by Garrett and Cummins looks at energy extraction in a tidal channel and shows that the maximum average power that may be generated is between 20% and 24% of the product of the peak tidal pressure head and the peak undisturbed volume flow rate. The range of estimates is produced by the assumptions made about the background i.e. natural energy losses in the channel. Whilst the presentation of results differs between the papers of Bryden et al. and Garrett and Cummins the results do seem broadly comparable in that a tidal channel driven by a head difference is more sensitive to energy extraction than a sea loch type environment.

An alternative perspective on the impact of tidal current energy extraction is provided by Salter and Taylor (2007). The approach taken in this paper involves estimating the so called bottom friction losses and examining the ratio of these losses to the power extracted by turbines completely filling the channel cross section. When common terms are eliminated this ratio is LC_D/ZC_P, where L is the length of the channel, C_D is the bottom drag coefficient, Z is the depth and C_P is the power coefficient of the turbine. Salter and Taylor calculate the value of this ratio to be 14 for the Pentland Firth based on a length of 23 km, a drag coefficient of 0.017, a depth of 70 m and a turbine power coefficient of 0.4. In an analogy with electrical circuit theory it is argued that under these conditions the channel would act as a high impedance source and the effect of power extraction on the tidal environment would be minimal. As such the authors argue that the B&V/CT resource assessment based on the flux method may be an underestimate. Salter and Taylor also give an estimate of the bottom friction power dissipation in the Pentland Firth as 53 GW based on the above length and drag coefficient and a width of 10 km and a velocity of 3 m/s.

Whilst not being based on hydrodynamic modelling of tidal flows, the paper of Salter and Taylor is an interesting contribution to the debate. One concern the present author has with the estimate is the value of the bottom drag coefficient used. The value of 0.017, taken from a paper by Campbell et al. (1998), is somewhat higher than that commonly used. Flather's (1976) modelling of tidal flows on the north-west European continental shelf used values of 0.005 and 0.006. A paper by Rippeth et al., discussed in the next sub-section, calculated a value of 0.005. All of these drag coefficients are used with the depth average velocity. Pugh (1987, p. 238) states that drag coefficients may be between 0.003 and 0.005 based on the velocity 1 m above the sea bed. Assuming a seventh power law turbulent boundary layer profile or similar we would expect Pugh's drag coefficients to be higher than those based on the depth average. We thus may expect Salter and Taylor's impedance and power dissipation to be reduced. Note that all of the drag coefficient values stated here are based on the engineering definition of the drag coefficient (see for example White, 1999, p. 297). The definition used in the oceanographic community (see for example Pugh, 1987, p. 238) is such that engineering drag coefficients are double the oceanographic drag coefficients. The drag coefficients found in Flather (1976), Pugh (1987), Campbell et al. (1998) and Rippeth et al. (2002) are thus half the values stated here.

2.6.4 Turbulence in the marine boundary layer

Data on the turbulence intensity and length scale in tidal flows is required for the boundary conditions to the CFD model. The tidal environment in which turbines would be installed (typically having spring currents of 2 m/s or higher) are extreme and only a limited amount of preliminary observational data exists from the nascent marine energy industry. See for example, Norris and Droniou (2007) who report observational measurements from a site with spring currents of 3.5 m/s. Data for less extreme tidal environments (spring currents up to around 1 m/s) is however available from the well established oceanographic community; for example (Baumert et al., 2005).

A classic paper by Soulsby (1977) presents measurements of the horizontal and vertical components of velocity made with electromagnetic current meters. The location is in Start Bay, southwest England (near Dartmouth) where the water depth is 14 m. The data consist of ensemble averages of U, $\sqrt{\overline{u'^2}}$, $\sqrt{\overline{v'^2}}$ and $\overline{u'v'}$ at two heights from the sea bed: 30 cm and 140 cm (y/δ = 0.02 and 0.1 respectively). The direction of the U-velocity is aligned with the mean flow.

Table 2.10: *Mean velocity and turbulent stresses as presented by Soulsby (1977) (left column) and these values non-dimensionalized using a calculated free stream velocity of* 65.1 cm/s *(right column).*

Values from Soulsby	Normalized values
$U = 54.7$ cm/s	$U/U_\infty = 0.84$
$\sqrt{\overline{u'^2}} = 8.6$ cm/s	$\sqrt{\overline{u'^2}} \,/\, U_\infty = 0.13$
$\sqrt{\overline{v'^2}} = 4.4$ cm/s	$\sqrt{\overline{v'^2}} \,/\, U_\infty = 0.068$
$\overline{u'v'} = 12.3$ cm^2/s^2	$\overline{u'v'} \,/\, U_\infty^2 = 0.0029$

The ensemble averaged data given by Soulsby for a height of 140 cm from the sea bed are displayed in the left column of table 2.10. The velocity U_∞, taken to occur on the sea surface, has been calculated by the present author by assuming a logarithmic velocity profile (such velocity profiles are applied to the marine boundary layer – see the paper by Rippeth et al. (2002), discussed below). Values for the RMS velocity fluctuations and the turbulent shear, normalized by U_∞, are shown in the right column. The fluctuation in the streamwise component is seen to be quite high – 13%.

The Edinburgh Designs turbine is a floating device with 2 m long blades and so the mid-span of the blade will be 1 m from the sea surface. In order to estimate the extent of the turbulent fluctuations at this position in the water column, we turn to the measurements made by Klebanoff (1955) on a flat-plate boundary layer in a wind tunnel (figure 2.7). It can be seen that at $y/d = 0.1$ the streamwise velocity fluctuation is about 7% – approximately half the value recorded by Soulsby in the marine boundary layer. Whilst the absolute values of the turbulent stresses varies between the two flows, the ratios between the stresses remain similar: $\sqrt{\overline{u'^2}}/\sqrt{\overline{v'^2}} \sim 2$ and $\sqrt{\overline{u'^2}}/(\overline{u'v'} \,/\, U_\infty) \sim 45$ for both flows. This similarity is despite the considerable difference in the Reynolds number between the two flows – $\mathrm{Re}_\delta = 1.6 \times 10^7$ for the tidal flow and $\mathrm{Re}_\delta = 7.3 \times 10^4$ for the flat plate boundary layer. It is thus argued that the behaviour of the turbulent stresses though the flat-plate boundary layer shown in figure 2.7 will be similar for the marine boundary layer, and so we may use this to calculate approximate values for the turbulent stresses near the sea surface. For example, at $y/\delta = 0.9$ in the marine boundary layer (taking δ as the depth) we would estimate the RMS fluctuation in the U velocity as about 2%. Assuming isotropic turbulence ($\overline{u'^2} \approx \overline{v'^2} \approx \overline{w'^2}$) gives $Tu = 2\%$.

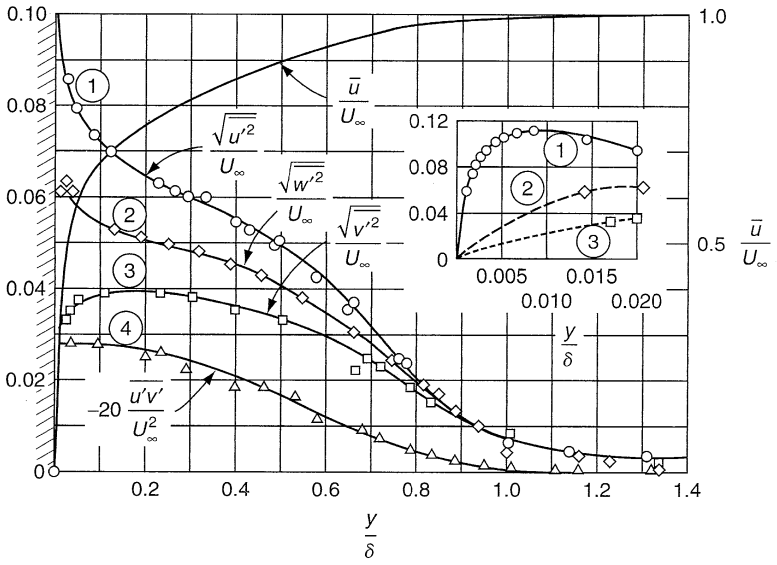

Figure 2.7: *Measurements of the turbulent stresses* $\sqrt{\overline{u'^2}}/U_\infty$ ①, $\sqrt{\overline{w'^2}}/U_\infty$ ②, $\sqrt{\overline{v'^2}}/U_\infty$ ③, *and* $\overline{u'v'}/U_\infty^2$ ④, *and the mean velocity* $\bar{u}/U_\infty$ *(un-numbered) in a flat-plate boundary layer at* $\mathrm{Re}_x \approx 10^7$. *Values for the turbulent stresses are taken from the left y-axis while values for the mean velocity are taken from the right y-axis. Note also that the turbulent shear stress is multiplied by* −20. *The data are originally from Klebanoff (1955) while the graph is taken from White (2006, p. 404).*

Soulsby's paper also presents a spectral analysis of the three turbulent stresses discussed above. This shows that at a height of 140 cm above the sea bed, the peaks in the energy spectra of u' and v' and the cospectra of $u'v'$ all occur at wavenumbers of between 0.36 m^{-1} and 0.7 m^{-1}. This corresponds to length scales of between 18 m and 36 m. Soulsby also plots the spectra at a height of 30 cm above the sea bed and shows that the peaks in each of the three spectra occur at approximately the same value of the non-dimensionalized wavenumber $k^* = ky$ for the two positions. This would suggest that the turbulent length scales at the sea surface would be between 180 m and 360 m.

A more recent paper by Rippeth et al. (2002) reports acoustic Doppler current profiler (ADCP) data from the Menai Strait (between the isle of Anglesey and mainland Wales). The peak spring velocity reported is about 1.2 m/s while the mean depth is 15 m and the range at spring is 5 m. Unfortunately this paper does not present any values for the velocity fluctuations or any spectral information, but instead shows the Reynolds stress in the along-channel direction, $\tau_{yx} = \rho\overline{u'v'}$. Values are given throughout the water column. For a surface velocity of about 1 m/s, the Reynolds stress at mid-depth is approximately 1 Pa.

In order to relate the Reynolds stress to the turbulent intensity, we must make some approximations. We again look at the flat-plate boundary layer measurements of Klebanoff (1955). We make two approximations about the behaviour of the fluctuating velocities in the middle of the boundary layer ($y/\delta = 0.5$). First, isotropic turbulence, and second:

$$\frac{\sqrt{\overline{u'^2}}}{U_\infty} \approx 40 \frac{\overline{u'v'}}{U_\infty^2} \tag{2.14}$$

Applying the two approximations in the equations defining the turbulent kinetic energy and the turbulent intensity we arrive at:

$$Tu = 40 \frac{\overline{u'v'}}{U_\infty^2} = 40 \frac{\tau_{yx}}{\rho U_\infty^2} = 4\% \tag{2.15}$$

where we have taken $\tau_{yx} = 1$ Pa, $\rho = 1 \times 10^3$ kg/m^3, and $U_\infty = 1$ m/s. This is approximately the same level of turbulence intensity shown in the Klebanoff data. A value for the turbulence intensity at mid-depth may be estimated from the Soulsby measurements at around 8%.

One explanation which may be readily offered for why the Soulsby data shows such high levels of turbulence intensity is the condition of the sea bed at the measurement location. It is noted that the sand on the sea bed is both rippled and formed into sand waves 50–100 cm high and 7–10 m in wavelength. Given that the measurement data is for heights above the sea bed of 30 cm and 140 cm, it is likely that the flow is strongly influenced by the condition of the bed.

Recent unpublished data from an ADCP device in the Falls of Warness in Orkney gives turbulence intensity values around 8% (Ian Bryden, University of Edinburgh, priv. comm.). This turbulence intensity value is derived directly from the velocity measurements and therefore does not rely upon the assumptions made in the present author's analysis of published data. It would suggest the values that have been derived here are sensible.

Chapter 3
Theory

This chapter presents theory relevant to the understanding and use of a commercial CFD code. As such both the theory of the governing physical equations and the numerical solution are discussed.

3.1 Basic fluid dynamics theory

The basic equations of fluid flow are three conservation laws:

1. Conservation of mass (continuity)
2. Conservation of momentum (Newton's second law)
3. Conservation of energy (first law of thermodynamics)

3.1.1 Conservation of mass

The conservation of mass for a compressible fluid may be stated as:

$$\frac{\partial \rho}{\partial t} + \nabla \cdot (\rho \mathbf{u}) = 0 \tag{3.1}$$

For the case of an incompressible fluid this simplifies to:

$$\nabla \cdot \mathbf{u} = 0 \tag{3.2}$$

3.1.2 Conservation of momentum

Newton's second law states that the rate of change of momentum of a system is equal to the sum of the forces on the system. For a fluid system, this may be stated as:

$$\rho \frac{D\mathbf{u}}{Dt} = \nabla \cdot \tau_{ij} \tag{3.3}$$

where the left hand side of the equation uses the particle derivative:

$$\frac{D}{Dt} = \frac{\partial}{\partial t} + (\mathbf{u} \cdot \nabla) \tag{3.4}$$

The stress tensor τ_{ij} may be split into pressure and viscous terms:

$$\tau_{ij} = -p\delta_{ij} + \tau^{v}_{ij} \tag{3.5}$$

where δ_{ij} is the Kronecker delta function ($\delta_{ij} = 1$ if $i = j$ and $\delta_{ij} = 0$ if $i \neq j$). Substitution of this into the momentum equation (3.3) gives:

$$\rho\frac{D\mathbf{u}}{Dt} = -\nabla p + \nabla \cdot \tau^{v}_{ij} \tag{3.6}$$

If the viscous stresses are assumed to be linearly related to the strain rates, i.e. the fluid is Newtonian, then the following deformation law may be derived, as first given by Stokes in 1845:

$$\tau_{ij} = -p\delta_{ij} + \mu\left(\frac{\partial u_i}{\partial x_j} + \frac{\partial u_j}{\partial x_i}\right) + \delta_{ij}\lambda\nabla \cdot \mathbf{u} \tag{3.7}$$

The coefficient of bulk viscosity (λ) is often assumed to be related to the (ordinary) coefficient of viscosity by Stokes' hypothesis (1845):

$$\lambda + \frac{2}{3}\mu = 0 \tag{3.8}$$

Such an assumption may indeed be incorrect (see White, 2006, p. 67), but it is rarely important given that $\nabla \cdot \mathbf{u}$ is usually very small (and indeed zero in incompressible flows). White notes two exceptions to this: normal shock waves and sound-wave absorption and attenuation. The term $\delta_{ij}\lambda\nabla \cdot \mathbf{u}$ is not included by default in the CFX solver (CFX-Solver Theory, p. 73).

Substitution of equation 3.7 into 3.3 results in the famous Navier-Stokes equations applicable to compressible viscous flow:

$$\rho\frac{D\mathbf{u}}{Dt} = -\nabla p + \frac{\partial}{\partial x_j}\left[\mu\left(\frac{\partial u_i}{\partial x_j} + \frac{\partial u_j}{\partial x_i}\right) + \delta_{ij}\lambda\nabla \cdot \mathbf{u}\right] \tag{3.9}$$

If we assume that both density and viscosity are constant we arrive at the much simpler equation:

$$\rho\frac{D\mathbf{u}}{Dt} = -\nabla p + \mu\nabla^2\mathbf{u} \tag{3.10}$$

Note the use of the vector Laplacian in the final term.[1]

For the case of incompressible fluids, equation 3.10 coupled with the continuity equation 3.2, may be solved for the velocity and pressure. If the temperature field is required, then this may subsequently be solved using the energy equation described in the next section. Similarly for the case of compressible flow under isothermal conditions the mass and momentum equations may again be solved separate from the energy equation. This case would require a relation between the density and the pressure e.g. the ideal gas law (see later). For all other cases where the density and/or the viscosity is related to the temperature the energy equation is coupled with the mass and momentum equations.

3.1.3 Conservation of energy

The first law of thermodynamics states that the rate of change of energy of a system is equal to the rate of heat addition to the system plus the rate of work done on the system. Stated mathematically for a fluid system, we have the energy equation:

$$\rho\frac{DE}{Dt} = \nabla\cdot(k\nabla T) - \nabla\cdot(p\mathbf{u}) + \frac{\partial(u_i\tau^v_{ij})}{\partial x_j} \tag{3.11}$$

where E is the specific energy of a fluid. As used here, this is the sum of the internal (thermal) energy e and the kinetic energy $\frac{1}{2}u_iu_i$ i.e. $E = e + \frac{1}{2}u_iu_i$. The above equation also incorporates Fourier's law for the heat conduction term.

In CFX, the energy equation is used in either of two alternative forms: as the 'total energy' equation (actually the total enthalpy) or the thermal energy equation. Considering first the total enthalpy equation, taking the definitions of the static and total enthalpy:

$$h = e + p/\rho \quad \text{and} \quad h_0 = h + \frac{1}{2}(u_iu_i) \tag{3.12}$$

[1]The vector Laplacian is defined as $\nabla^2\mathbf{u} \equiv \nabla(\nabla\cdot\mathbf{u}) - \nabla\times(\nabla\times\mathbf{u})$. In Cartesian coordinates this reduces to $\nabla^2\mathbf{u} = \nabla^2u\,\mathbf{i} + \nabla^2v\,\mathbf{j} + \nabla^2w\,\mathbf{k}$

and the definition of the specific energy E, we have:

$$h_0 = E + p/\rho \tag{3.13}$$

Substitution of the above into equation 3.11 yields after some rearrangement the total enthalpy equation:

$$\frac{\partial(\rho h_0)}{\partial t} + \nabla \cdot (\rho h_0 \mathbf{u}) = \nabla \cdot (k \nabla T) + \frac{\partial p}{\partial t} + \frac{\partial(u_i \tau^v_{ij})}{\partial x_j} \tag{3.14}$$

The thermal energy equation is derived by deducting from the energy equation (3.11) an equation for the kinetic energy. This kinetic energy equation is found by taking the scalar product of the velocity and the momentum equation (3.3) to give:

$$\rho \frac{D[\frac{1}{2}(u_i u_i)]}{Dt} = -\mathbf{u} \cdot \nabla p + \mathbf{u} \cdot \nabla \cdot \tau^v_{ij} \tag{3.15}$$

Subtracting equation 3.15 from 3.11 yields the thermal energy equation:

$$\rho \frac{De}{Dt} = \nabla \cdot (k \nabla T) - p \nabla \cdot \mathbf{u} + \tau^v_{ij} \frac{\partial u_i}{\partial x_j} \tag{3.16}$$

The implementation of this equation in CFX neglects the term $p\nabla \cdot \mathbf{u}$, which will be non-zero in variable density flows. Different results will thus arise from use of the thermal energy equation versus the total enthalpy equation. The *CFX-Solver Theory Guide* suggests use of the thermal energy equation for low speed flows where compressibility effects are minimal. It is also suggested for cases where the total enthalpy equation may experience robustness issues due to the pressure transient and the p/ρ contribution to enthalpy.

3.1.4 Secondary thermodynamic properties and equations of state

For the case of a non-isothermal flow of a compressible fluid we have five coupled equations with seven independent variables (ρ, u_1, u_2, u_3, p, h, T), assuming that k and μ are constant. Two additional equations are thus required (provided no further independent variables are introduced). Many models are available for these additional equations; the one selected for the compressible cases of chapter 5 is that of an ideal or perfect gas with constant specific heat.

The ideal gas law is:

$$p = \rho R T \tag{3.17}$$

where R is the gas constant. This is related to the universal gas constant $\bar{R}$ with:

$$R = \bar{R}/M \tag{3.18}$$

where M is the molar mass of the gas.

The assumption of constant specific heat (at constant pressure) gives:

$$h = c_p T \tag{3.19}$$

from which it follows that the specific heat at constant volume, c_v, and the ratio of the specific heats, γ will also be constant. Two relations concerning these quantities are stated here for reference:

$$c_p = c_v + R \quad \text{and} \quad \gamma = \frac{c_p}{c_v} \tag{3.20}$$

3.2 Turbulence

The most basic description of turbulence is that of random fluctuations in the flow variables. Beyond this, a number of general features may be highlighted:

- *Three-dimensionality*. Turbulence is always three-dimensional, even if the mean flow is two-dimensional.
- *Unsteadiness*. Turbulent flows are inherently unsteady, again, even if the mean flow is steady.
- *Unpredictability*. Two flows starting with slightly (infinitesimally) different conditions will develop differently.
- *Broad spectrum*. Turbulent fluctuations occur over a range of time and length scales, with the range of scales increasing with the Reynolds number.
- *Coherent structures*. Rotational flow structures termed 'eddies' are readily observable in turbulent flow. Such eddies are found in a variety of flow-specific (super-) structures for which a detailed terminology exists.

The broad range of scale is an important aspect of turbulence and is related to the way in which kinetic energy in the mean flow is dissipated by turbulence. The largest turbulent eddies have

length and velocity scales of the same order as those of the mean flow and are responsible for the transfer of kinetic energy from the mean flow to turbulence. Through a variety of processes including vortex stretching (whereby the eddies become longer axially and shorter radially) energy is transferred to smaller scales. At the smallest scales, called the Kolmogorov microscales, the Reynolds number of the eddy is approximately one and so there is viscous dissipation of the turbulent kinetic energy. This process is termed the turbulent energy cascade.

3.2.1 Mathematical description

Standard mathematical descriptions of turbulence begin with the concept of the Reynolds decomposition. This splits the instantaneous value of a flow variable ϕ into the sum of a steady mean component Φ and a time varying fluctuating component ϕ' with zero mean value:

$$\phi(t) = \Phi + \phi'(t) \tag{3.21}$$

where:

$$\Phi = \frac{1}{\Delta t} \int_0^{\Delta t} \phi(t)\, \mathrm{d}t \tag{3.22}$$

The choice of the time interval Δt is significant. In theory we should have $\Delta t \to \infty$ but this is not practical and indeed the selection of Δt to be 'longer' than the time scales associated with the largest eddies (t_1) gives meaningful results. This definition is sufficient for steady mean flows. For unsteady mean flows it must also be the case that Δt is 'shorter' than the time scales associated with the unsteadiness of the mean flows (t_2). Wilcox (1998, pp. 32–3) suggests that t_1 and t_2 must differ by 'several' orders of magnitude.

One-half of the sum of the variances of the fluctuating velocity components is interpreted as the kinetic energy per unit mass contained in turbulence, or turbulence kinetic energy:

$$k = \frac{1}{2}\left(\overline{u'^2} + \overline{v'^2} + \overline{w'^2}\right) \tag{3.23}$$

A further useful quantity derived from the variances of the velocity fluctuations is the turbulence intensity. This is the square root of the mean of the fluctuating velocity variances,

non-dimensionalized by a reference mean flow velocity:

$$Tu = \frac{\left(\frac{2}{3}k\right)^{1/2}}{U_{\text{ref}}} \tag{3.24}$$

If we assume isotropic turbulence, $\overline{u'^2} = \overline{v'^2} = \overline{w'^2}$, then the meaning of the turbulence intensity is clearer:

$$Tu = \frac{\sqrt{\overline{u'^2}}}{U_{\text{ref}}} \tag{3.25}$$

i.e. it is equal to the RMS of a given fluctuating component.

3.2.2 The Reynolds-averaged Navier-Stokes equations

Classical approaches to modelling turbulence begin with substitution of the Reynolds decomposition for each of the relevant flow variables into the (instantaneous) conservations equations, followed by time-averaging of the equations. The process of time-averaging, being an integral operation, is of course linear and commutative with differentiation. A few important results governing the time-averaging of a scalar quantity $\phi = \Phi + \phi'$ and its product with a second scalar quantity $\psi = \Psi + \psi'$ are:

$$\overline{\Phi} = \Phi \qquad \overline{\phi'} = 0 \qquad \overline{\Phi\Psi} = \Phi\Psi \qquad \overline{\Phi\phi'} = 0 \qquad \overline{\phi'\psi'} \neq 0 \tag{3.26}$$

To derive the time-averaged mass and momentum equations for an incompressible fluid with constant viscosity we first substitute:

$$\mathbf{u} = \mathbf{U} + \mathbf{u}' \qquad u = U + u' \qquad v = V + v' \qquad w = W + w' \qquad p = P + p' \tag{3.27}$$

into equations 3.2 and 3.10. Taking and then propagating the time-average we derive the continuity equation for the mean flow:

$$\nabla \cdot \mathbf{U} = 0 \tag{3.28}$$

and the time-averaged momentum equation:

$$\rho\frac{D\mathbf{U}}{Dt} + \rho\frac{\partial}{\partial x_j}(\overline{u_i' u_j'}) = -\nabla P + \mu\nabla^2\mathbf{U} \tag{3.29}$$

collectively known as the Reynolds-averaged Navier-Stokes (RANS) equations.

Equations 3.28 and 3.29 differ from what would be achieved with a naïve substitution of $u = U$ into equations 3.2 and 3.10 (i.e. assuming that the latter equations applied directly to the mean flow) by the addition of a term involving the product of two fluctuating velocities. This term is associated with convective momentum transfer due to the turbulent eddies, and its action is that of an additional stress, termed the Reynolds stress.

Reflecting its action as a stress, the term conventionally appears on the right hand side of the equation:

$$\rho\frac{D\mathbf{U}}{Dt} = -\nabla P + \nabla\cdot\tau_{ij} \tag{3.30}$$

where

$$\tau_{ij} = \mu\left(\frac{\partial U_i}{\partial x_j} + \frac{\partial U_j}{\partial x_i}\right) - \rho\overline{u_i' u_j'} \tag{3.31}$$

As with the Newtonian viscous stress, the Reynolds stress consist of three normal stresses:

$$\tau_{xx}' = -\rho\overline{u'^2} \qquad \tau_{yy}' = -\rho\overline{v'^2} \qquad \tau_{zz}' = -\rho\overline{w'^2}$$

and three shear stresses:

$$\tau_{xy}' = \tau_{yx}' = -\rho\overline{u'v'} \qquad \tau_{xz}' = \tau_{zx}' = -\rho\overline{u'w'} \qquad \tau_{yz}' = \tau_{zy}' = -\rho\overline{v'w'}$$

The normal stresses are intrinsically non-zero because they consist of squared velocity fluctuations. As the shear stresses consist of correlations between velocity components, they would be zero if the fluctuations were independent. Due to the coherent structure of turbulent eddies this is not the case and the turbulent shear stresses are usually large compared to the viscous stresses in turbulent flows.

Unlike the Navier-Stokes equations for incompressible flow which consist of four equations in four unknowns and are therefore closed, the RANS equations are not closed due to the addition of six unknowns in the form of the Reynolds stresses. Two approaches exist to develop a closed system of equations. First, the Reynolds stresses may be related to the mean flow gradients,

with or without the addition of conservation equations for additional variables; so-called eddy viscosity models. Second, we may develop conservation equations for the Reynolds stresses, the solution of which generally involves further conservation equations for additional variables; so-called Reynolds stress equation models. In this work we use the former approach, the theoretical basis of which is outlined in the next section.

3.2.3 The Boussinesq approximation

Eddy viscosity turbulence models such as the mixing length, k-ε and k-ω models begin with Boussinesq's assumption of 1877 that the Reynolds stresses are proportional to the mean flow gradients:

$$\tau'_{ij} = -\rho\overline{u'_i u'_j} = \mu_t\left(\frac{\partial U_i}{\partial x_j} + \frac{\partial U_j}{\partial x_i}\right) - \frac{2}{3}\rho k\delta_{ij} \tag{3.32}$$

where $k = \frac{1}{2}\left(\overline{u'^2} + \overline{v'^2} + \overline{w'^2}\right)$ is the turbulent kinetic energy per unit mass.

The first term on the right hand side is analogous to the viscous stress τ^v_{ij}, with the turbulent viscosity μ_t replacing the molecular viscosity μ. Note that whilst the turbulent viscosity has the same units as the molecular viscosity, it is not a fluid property, varying instead with the flow conditions and geometry. The second term on the right hand side involves the Kronecker delta δ_{ij} and the turbulent kinetic energy k. This term ensures that the formula gives the correct result for the normal Reynolds stresses. The necessity of this term is best illustrated by calculating and then summing the three normal stresses in the case of incompressible flow:

$$\begin{aligned}
\tau'_{xx} = -\rho\overline{u'^2} &= 2\mu_t\left(\frac{\partial U}{\partial x}\right) - \frac{2}{3}\rho k \\
\tau'_{yy} = -\rho\overline{v'^2} &= 2\mu_t\left(\frac{\partial V}{\partial y}\right) - \frac{2}{3}\rho k \\
\tau'_{zz} = -\rho\overline{w'^2} &= 2\mu_t\left(\frac{\partial W}{\partial z}\right) - \frac{2}{3}\rho k
\end{aligned}$$

$$\tau'_{xx} + \tau'_{yy} + \tau'_{zz} = -\rho(\overline{u'^2} + \overline{v'^2} + \overline{w'^2}) = -2\rho k$$

In the summation, the terms involving μ_t sum to zero due to the continuity equation, and thus without the kinetic energy term we would incorrectly have the sum of the three normal stresses equalling zero. With this term we have the correct result where the sum is equal to minus twice the turbulent kinetic energy per unit volume.

Despite the sound physical reasoning for the term $\frac{2}{3}\rho k\delta_{ij}$, it is not included by default in the momentum equation in the CFX-Solver (CFX-Solver Theory, p. 73). (It is however included in the production terms in the turbulent quantity conservation equations.) Substitution of equation 3.32 into 3.29 yields the momentum equation to be solved:

$$\rho\frac{D\mathbf{u}}{Dt} = -\nabla p + \frac{\partial}{\partial x_j}\left[\mu_{\text{eff}}\left(\frac{\partial u_i}{\partial x_j} + \frac{\partial u_j}{\partial x_i}\right)\right] \tag{3.33}$$

where the effective viscosity is the sum of molecular and turbulent viscosities: $\mu_{\text{eff}} = \mu + \mu_t$. With the Boussinesq approximation, the closure problem thus becomes that of finding the solution for the turbulent viscosity.

3.2.4 Mixing length models

For simple two-dimensional thin shear layer flows with slow changes in the flow direction the production of turbulence is everywhere in balance with its dissipation. Such flows include wakes, jets, mixing layers and boundary layers, all in isolation from each other and from other flow features. For these flows it is possible to specify the turbulent viscosity using a mixing length model such as Prandtl's:

$$\mu_t = \rho\ell_m^2\left|\frac{\partial U}{\partial y}\right|$$

where the mixing length ℓ varies with the flow type. For flat plate boundary layer flows the following values are commonly used:

$\ell_m = \kappa y[1 - \exp(-y^+/26)]$	in the viscous sublayer and log-law layer ($y/\delta < 0.22$), and
$\ell_m = 0.09\delta$	in the outer layer ($y/\delta > 0.22$)

The above equations allow the turbulent viscosity to be calculated from existing quantities, i.e. the mean flow field, without recourse to further conservation equations. It is thus referred to as a zero-equation model.

For flows where the transport of turbulence is significant, for example recirculating flows, the mixing length model will give inaccurate results. In such cases we need to form conservation equations for one or more turbulent quantities in order to accurately model turbulence.

3.2.5 Governing equation for the turbulent kinetic energy

A common choice of variable for which a conservation equation may be written is the turbulent kinetic energy. An equation for this is derived by taking the scalar product of the fluctuating velocity vector with the Navier-Stokes equations and then subtracting from this the scalar product of the fluctuating velocity vector with the RANS equations. After substantial re-arrangement we obtain:

$$\underbrace{\frac{\partial(\rho k)}{\partial t}}_{\text{(I)}} + \underbrace{\nabla\cdot(\rho k\mathbf{U})}_{\text{(II)}} = \underbrace{\nabla\cdot(-\overline{p'\mathbf{u}'}}_{\text{(III)}} + \underbrace{2\mu\overline{\mathbf{u}'s'_{ij}}}_{\text{(IV)}} - \underbrace{\frac{1}{2}\rho\overline{u'_i\cdot u'_i u'_j})}_{\text{(V)}} - \underbrace{2\mu\overline{s'_{ij}\cdot s'_{ij}}}_{\text{(VI)}} - \underbrace{\rho\overline{u'_i u'_j}\cdot S_{ij}}_{\text{(VII)}}$$

In words:

Rate of change of turbulent kinetic energy k	+	Transport of k by convection	=	Transport of k by pressure	+	Transport of k by viscous stress	+	Transport of k by Reynolds stress	+	Rate of dissipation of k	+	Rate of production of k

Referring to ρ, U and k as 'knowns' (they are of course what we want to calculate), and using the Boussinesq approximation to relate the quantity $\rho\overline{u'_i u'_j}$ in the production term to the mean flow velocity we are left with four unknown terms (III-VI).

Terms III-V, which represent transport/diffusion processes, are usually modelled using the gradient-diffusion hypothesis. See the model k-equation in the next section.

Term VI, representing the viscous dissipation of turbulent kinetic energy, is normally written as the product of the density ρ and the rate of dissipation of turbulent kinetic energy per unit mass ε, thus:

$$\varepsilon = 2\nu\overline{s'_{ij}\cdot s'_{ij}} \tag{3.34}$$

There are two approaches to the calculation of the dissipation (ε). First, it may be modelled and calculated from the turbulent kinetic energy and a mixing length. This is the approach taken in one-equation models based on the turbulent kinetic energy. Such models are completed by the calculation of the turbulent viscosity, also from k and ℓ_m (but in a different combination).

The second approach is to develop a conservation equation for the dissipation, as is the case in the k-ε turbulence model.

3.2.6 The k-ε turbulence model

The k-ε model is termed a two-equation turbulence model as it involves the solution of conservation equations for two turbulence quantities, i.e. k and ε. The model k-equation (3.35) is developed from the exact turbulent kinetic energy equation, with the gradient diffusion hypothesis modelling three unknown transport/diffusion terms, and using the Boussinesq approximation for the production term. Whilst an exact conservation equation may also be developed for ε it does not in fact form a useful starting point for the model equation; as such the model equation (3.36) is best viewed as being entirely empirical.

$$\frac{\partial(\rho k)}{\partial t} + \nabla \cdot (\rho k \mathbf{U}) = \nabla \cdot \left[\frac{\mu_t}{\sigma_k} \nabla k \right] + \mathcal{P} - \rho\varepsilon \tag{3.35}$$

$$\frac{\partial(\rho \varepsilon)}{\partial t} + \nabla \cdot (\rho \varepsilon \mathbf{U}) = \nabla \cdot \left[\frac{\mu_t}{\sigma_\varepsilon} \nabla \varepsilon \right] + C_{\varepsilon 1} \frac{\varepsilon}{k} \mathcal{P} - C_{\varepsilon 2} \rho \frac{\varepsilon^2}{k} \tag{3.36}$$

with:

$$\mathcal{P} = 2\mu_t S_{ij} \cdot S_{ij} \tag{3.37}$$

Note that the production term does not include the turbulent kinetic energy term which appears in the Boussinesq approximation.

Completing the model, and from dimensional analysis, the turbulent viscosity is calculated from k and ε as:

$$\mu_t = \rho C_\mu \frac{k^2}{\varepsilon} \tag{3.38}$$

The model constants are:

$$C_\mu = 0.09, \quad \sigma_k = 1.0, \quad \sigma_\varepsilon = 1.3, \quad C_{\varepsilon 1} = 1.44, \quad C_{\varepsilon 2} = 1.92 \tag{3.39}$$

This is the standard k-ε model. In the CFX solver a slightly modified version is used:

$$\frac{\partial(\rho k)}{\partial t} + \nabla \cdot (\rho k \mathbf{U}) = \nabla \cdot \left[\left(\mu + \frac{\mu_t}{\sigma_k} \right) \nabla k \right] + \mathcal{P} - \rho\varepsilon \tag{3.40}$$

$$\frac{\partial(\rho \varepsilon)}{\partial t} + \nabla \cdot (\rho \varepsilon \mathbf{U}) = \nabla \cdot \left[\left(\mu + \frac{\mu_t}{\sigma_\varepsilon} \right) \nabla \varepsilon \right] + C_{\varepsilon 1} \frac{\varepsilon}{k} \mathcal{P} - C_{\varepsilon 2} \rho \frac{\varepsilon^2}{k} \tag{3.41}$$

$$\mathcal{P} = 2\mu_t S_{ij} \cdot S_{ij} - \frac{2}{3}(3\mu_t \nabla \cdot \mathbf{U} + \rho k) \nabla \cdot \mathbf{U} \tag{3.42}$$

This features two differences. First, the molecular viscosity is included in the gradient-diffusion term in both the k- and ε-equations. This modification is usually made to allow the k-ε model to be applied at grid points within the viscous sublayer of boundary layers. However, wall damping functions must also be added to the model to allow its use in the viscous sublayer, and these are not present in the CFX implementation. Reflecting this, the k-ε model can only be used in CFX in conjunction with wall functions (discussed later).

Second, the production term features two extra terms. These will only be active in compressible flow due to the divergence of the velocity. One of the terms, $\frac{2}{3}\rho k\nabla\cdot\mathbf{U}$, is from the Boussinesq approximation. The second, $\frac{2}{3}(3\mu_t\nabla\cdot\mathbf{U})\nabla\cdot\mathbf{U}$, is a modification to account for the phenomenon of 'frozen stress' across a shock (AEA Technology, 2002). The frozen stress refers to the fact that the Reynolds stresses do not change as rapidly as the mean flow across a shock. Note that the definition of the production in equation 3.42 is also that used in the k-ω models in CFX.

The values of the constants used in the CFX implementation of the k-ε model are the same as those in the standard model described above.

3.2.7 The Wilcox k-ω turbulence model

Of the many two-equation turbulent models proposed most use k as one of the variables, but choice of the second variable is more diverse. Next to ε, the most prominent is ω, the dissipation per unit kinetic energy, often called the turbulence frequency. It is defined as $\omega = \varepsilon/(\beta^* k)$ where β^* is a constant. Such a choice of variables was originally proposed by Kolmogorov (1942) and Prandtl (1945). The version implemented in CFX is that due to Wilcox (1988, 1993), for which the relevant equations and constants are given below

$$\mu_t = \rho\frac{k}{\omega} \tag{3.43}$$

$$\frac{\partial(\rho k)}{\partial t} + \nabla\cdot(\rho k\mathbf{U}) = \nabla\cdot\left[\left(\mu + \frac{\mu_t}{\sigma_k}\right)\nabla k\right] + \mathcal{P} - \beta^*\rho k\omega \tag{3.44}$$

$$\frac{\partial(\rho\omega)}{\partial t} + \nabla\cdot(\rho\omega\mathbf{U}) = \nabla\cdot\left[\left(\mu + \frac{\mu_t}{\sigma_\omega}\right)\nabla\omega\right] + \gamma_1\frac{\omega}{k}\mathcal{P} - \beta_1\rho\omega^2 \tag{3.45}$$

$$\sigma_k = 2.0, \quad \sigma_\omega = 2.0, \quad \gamma_1 = 5/9 = 0.556, \quad \beta_1 = 0.075, \quad \beta^* = 0.09 \tag{3.46}$$

The primary advantage of the k-ω model over the k-ε is in its ability to be applied throughout the boundary layer without the use of wall damping functions. For such boundary layer flows, and especially adverse pressure gradient boundary layer flows, its superiority over the k-ε model has been shown by e.g. Wilcox (1993).

The primary *dis*advantage of the k-ω model relates to the specification of the freestream value of ω. A small but arbitrary value for this must be assumed, and Menter (1992a) has shown that the subsequent results are overly dependent upon the choice.

3.2.8 The Baseline (BSL) k-ω turbulence model

Noting the complementary strengths and weaknesses of the k-ε and k-ω models, Menter (1993, 1994) pragmatically suggested a hybrid model. This uses Wilcox's k-ω model within the boundary layer and a transformation of the k-ε model into a k-ω model outside of the boundary layer. The transformation of the k-ε model is achieved by substitution of $\varepsilon = \beta^* k\omega$ in the k and ε model equations. Besides differences in the model coefficients, the only difference between the transformed equations and those of the Wilcox model is an extra cross-diffusion term appearing in the ω-equation. The new model equations for k and ω are derived by multiplying the Wilcox k-ω equations by a function F_1 and the transformed k-ε equations by $(1 - F_1)$, and adding both together. The function F_1 is designed such that it is one in the viscous sublayer and zero outside of the boundary layer; the blending takes place in the wake region of the boundary layer.

Wilcox k-ω model:

$$\frac{\partial(\rho k)}{\partial t} + \nabla \cdot (\rho k \mathbf{U}) = \nabla \cdot \left[\left(\mu + \frac{\mu_t}{\sigma_{k1}} \right) \nabla k \right] + \mathcal{P} - \beta^* \rho k \omega \tag{3.47}$$

$$\frac{\partial(\rho \omega)}{\partial t} + \nabla \cdot (\rho \omega \mathbf{U}) = \nabla \cdot \left[\left(\mu + \frac{\mu_t}{\sigma_{\omega 1}} \right) \nabla \omega \right] + \gamma_1 \frac{\omega}{k} \mathcal{P} - \beta_1 \rho \omega^2 \tag{3.48}$$

Transformed k-ε model:

$$\frac{\partial(\rho k)}{\partial t} + \nabla \cdot (\rho k \mathbf{U}) = \nabla \cdot \left[\left(\mu + \frac{\mu_t}{\sigma_{k2}} \right) \nabla k \right] + \mathcal{P} - \beta^* \rho k \omega \tag{3.49}$$

$$\frac{\partial(\rho \omega)}{\partial t} + \nabla \cdot (\rho \omega \mathbf{U}) = \nabla \cdot \left[\left(\mu + \frac{\mu_t}{\sigma_{\omega 2}} \right) \nabla \omega \right] + \gamma_2 \frac{\omega}{k} \mathcal{P} - \beta_2 \rho \omega^2 + 2\rho \frac{1}{\sigma_{\omega 2} \omega} \nabla k \nabla \omega \tag{3.50}$$

BSL model:

$$\frac{\partial(\rho k)}{\partial t} + \nabla \cdot (\rho k \mathbf{U}) = \nabla \cdot \left[\left(\mu + \frac{\mu_t}{\sigma_k} \right) \nabla k \right] + \mathcal{P} - \beta^* \rho k \omega \tag{3.51}$$

$$\frac{\partial(\rho \omega)}{\partial t} + \nabla \cdot (\rho \omega \mathbf{U}) = \nabla \cdot \left[\left(\mu + \frac{\mu_t}{\sigma_\omega} \right) \nabla \omega \right] + \gamma \frac{\omega}{k} \mathcal{P} - \beta \rho \omega^2 + 2(1 - F_1) \rho \frac{1}{\sigma_{\omega 2} \omega} \nabla k \nabla \omega \tag{3.52}$$

The compact description of the BSL model in equations 3.51 and 3.52 is achieved by calculating the 'constants' $\phi = \sigma_k, \ldots$ in the new model from those in the Wilcox model ($\phi_1 = \sigma_{k1}, \ldots$) and those in the transformed k-ε model ($\phi_2 = \sigma_{k2}, \ldots$) according to:

$$\phi = F_1 \phi_1 + (1 - F_1) \phi_2 \tag{3.53}$$

The blending function is defined as:

$$F_1 = \tanh(\arg_1^4) \tag{3.54}$$

$$\arg_1 = \min \left[\max \left(\frac{\sqrt{k}}{\beta^* \omega y} \;\middle|\; \frac{500\nu}{y^2 \omega} \right) \;\middle|\; \frac{4\rho k}{CD_{k\omega} \sigma_{\omega 2} y^2} \right] \tag{3.55}$$

$$CD_{k\omega} = \max \left(2\rho \frac{1}{\sigma_{\omega 2} \omega} \nabla k \nabla \omega \;\middle|\; 10^{-10} \right) \tag{3.56}$$

The set of constants (ϕ_1) from the Wilcox k-ω model are:

$$\sigma_{k1} = 2.0, \quad \sigma_{\omega 1} = 2.0, \quad \gamma_1 = 5/9 = 0.556, \quad \beta_1 = 0.075, \quad \beta^* = 0.09 \tag{3.57}$$

The set of constants (ϕ_2) from the transformed k-ε model are:

$$\sigma_{k2} = 1.0, \quad \sigma_{\omega 2} = 1/0.856 = 1.168, \quad \gamma_2 = 0.44, \quad \beta_2 = 0.0828, \quad \beta^* = 0.09 \tag{3.58}$$

3.2.9 The shear stress transport (SST) k-ω turbulence model

The shear stress transport (SST) model incorporates the BSL turbulence model with the addition of a function to limit the turbulent shear stress (Menter, 1994). The origins of this model lie in the observation that when applied to boundary layer problems, one of the major differences between eddy-viscosity and full Reynolds stress models is that the latter account for the effect of

the transport of the principal turbulent shear stress $\tau'_{xy} = -\rho\overline{u'v'}$. The importance of modelling such an effect has been demonstrated by the success of the Johnson-King (JK) model.

The JK model is a transport equation for the turbulent shear stress that is based on Bradshaw's assumption that the shear stress in a boundary layer is proportional to the turbulent kinetic energy:

$$\tau'_{xy} = \rho a_1 k \tag{3.59}$$

with a_1 being a constant. By comparison, in two-equation models, the shear stress is calculated from the Boussinesq assumption:

$$\tau'_{xy} = \mu_t \frac{\partial U}{\partial y} \tag{3.60}$$

As described by Menter (1992b), the latter may be re-written as:

$$\tau'_{xy} = \rho \sqrt{\frac{\text{Production}_k}{\text{Dissipation}_k}}\, a_1 k \tag{3.61}$$

where:

$$\text{Production}_k = 2\mu_t S_{ij} \cdot S_{ij} = \mu_t \left(\frac{\partial U}{\partial y}\right)^2 \tag{3.62}$$

In the case of adverse pressure gradient boundary layer flows, the experimental measurements of Driver (cited by Menter, 1994) show that the ratio of production to dissipation may be significantly greater than one. Thus (3.60) leads to an overprediction of τ relative to (3.59). For the case of production = dissipation, equations 3.59 and 3.60 are equivalent if $a_1 = \sqrt{C_\mu} = 0.3$. (Note that CFX uses $a_1 = 0.31$.)

In order to satisfy (3.59) within the framework of an eddy-viscosity model, the eddy viscosity is calculated as:

$$\nu_t = \min\left(\frac{k}{\omega} \,\middle|\, \frac{a_1 k}{S F_2}\right) \tag{3.63}$$

This equation thus uses Bradshaw's assumption $\tau'_{xy} = \rho a_1 k$ to limit the eddy viscosity via the term $a_1 k/(S F_2)$ in the equation above. This term uses an invariant measure of the shear strain rate $S = \sqrt{2 S_{ij} S_{ij}}$, with $S = \partial U/\partial y$ for boundary layer flows, and the function F_2 that is one in boundary layers and zero outside. The blending function ensures that the original formulation $\nu_t = k/\omega$ is used outside of boundary layers where Bradshaw's assumption does not necessarily hold. It is similar to the function F_1 used in the BSL model and is defined as:

$$F_2 = \tanh(\arg_2^2) \tag{3.64}$$

$$\arg_2 = \max\left(\frac{2\sqrt{k}}{\beta^*\omega y} \,\middle|\, \frac{500\nu}{y^2\omega}\right) \tag{3.65}$$

3.2.10 Modelling flow near the wall

Two approaches exist to the modelling of turbulent boundary layers, these being separated by the resolution required in the near-wall computational grid and by the boundary conditions applied for the velocity or wall shear stress. The first may be termed the 'low Reynolds number' approach, in which the first grid point from the wall (point P) must be in the viscous sublayer (with $y_P^+ < 2$) and where the velocity boundary condition is $\mathbf{U}_w = 0$. The second may be termed the 'high Reynolds number' or wall function approach, in which the first grid point from the wall must be outside the viscous sublayer (with $y_P^+ > 35$), and where we prescribe the wall shear stress based on the velocity at point P using the log-law. The primary benefit of the wall function approach lies in the reduced computational burden; in the case of the k-ε model it also obviates the need for wall damping functions in the model equations. With the low Reynolds number approach there exists the potential for greater accuracy. We discuss first the wall function approach, then a blended high/low Reynolds number approach, both as implemented in CFX for k-ω based models. Only the velocity boundary condition is discussed; limited details of the boundary conditions for k and ω are given in the *CFX-Solver Theory Guide*.

3.2.10.1 Wall functions

As stated above, the wall function approach is based on the universal behaviour of attached near-wall flows. Within the overlap region of the boundary layer $35 < y^+ < 350$, corresponding roughly to the range $0.02 < y/\delta < 0.2$, the famous log-law applies:

$$\frac{U}{u_\tau} = \frac{1}{\kappa}\ln\left(\frac{y u_\tau}{\nu}\right) + B \tag{3.66}$$

with the friction velocity u_τ defined:

$$u_\tau = \sqrt{\frac{\tau_w}{\rho}} \tag{3.67}$$

and where U is the velocity tangential to the wall at a distance y normal to the wall and τ_w is the wall shear stress. Commonly used values for the constants κ and B are 0.41 and 5 respectively. Different values for B apply to rough walls.

Unfortunately equation 3.66 does not apply to separating flows, where both U and τ_w tend to zero. As suggested by Launder and Spalding (1974), two modifications are made. First, an alternative velocity scale u_τ^* is used in the logarithm instead of u_τ:

$$u_\tau^* = C_\mu^{1/4} k^{1/2} \tag{3.68}$$

This is closely related to the assumptions behind the shear stress limiter in the SST k-ω turbulence model discussed above. As shown there, if production and dissipation of turbulent kinetic energy are equal then the turbulent shear stress is given by: $\tau_x y' = \rho\sqrt{C_\mu}k$. Thus, $u_\tau^* = u_\tau$ if it is also assumed that the wall shear stress is equal to the turbulent shear in the logarithmic portion of the boundary layer; the frequently quoted experimental results of Klebanoff (1955) show that this is valid. The advantage of using u_τ^* as a velocity scale is that it is never zero.

The second modification is to calculate the wall shear stress from:

$$\tau_w = \rho u_\tau^* u_\tau \tag{3.69}$$

The purpose of this modification is to make the wall shear stress go to zero linearly with the wall tangential velocity U, as suggested by experiment. (Without this modification, the behaviour is quadratic.) The log-law thus becomes:

$$\frac{U}{(\tau_w/\rho)} u_\tau^* = \frac{1}{\kappa} \ln\left(\frac{y u_\tau^*}{\nu}\right) + B \tag{3.70}$$

Equation 3.70 is implemented in CFX as a 'scalable' wall function with two further modifications. First, the value of y used is based on one quarter of the distance from the wall to the near wall grid point. According to the *CFX-Solver Theory Guide* this is done to achieve 'an optimum performance in terms of accuracy and robustness'. Second, the value of y^* ($= y u_\tau^*/\nu$) used in the logarithm is limited to a lower value of 11.06. This allows the wall function approach to be used with arbitrarily fine grids.

3.2.10.2 Blended high/low Reynolds number formulation

The CFX-Solver includes an 'automatic' near wall treatment for k-ω based models. As with the wall function formulation, the wall shear stress is calculated from:

$$\tau_w = \rho u_\tau^* u_\tau \tag{3.71}$$

but here the values of u_τ^* and u_τ are both blended between sublayer and log-law relations:

$$u_\tau = (u_{\tau_{\text{sub}}}^4 + u_{\tau_{\text{log}}}^4)^{1/4} \tag{3.72}$$

$$u_\tau^* = (u_{\tau_{\text{sub}}}^{*4} + u_{\tau_{\text{log}}}^{*4})^{1/4} \tag{3.73}$$

with:

$$u_{\tau_{\text{sub}}} = u_{\tau_{\text{sub}}}^* = \sqrt{\nu U / y} \tag{3.74}$$

The log-law velocity scales $u_{\tau_{\text{log}}}$ and $u_{\tau_{\text{log}}}^*$ are defined as per the wall function approach, but that the value of y used is the distance from the wall to the near wall grid point rather than one quarter thereof.

3.2.11 The decay of inlet turbulence

In the absence of mean velocity gradients the production of turbulence will be zero and any existing turbulence will decay. For external flow problems this is the case from the inlet to 'near' the object, 'near' being no more than about one characteristic length (hydrofoil chord or turbine diameter) upstream. Given the necessity of placing the freestream boundaries a significant number of characteristic lengths (of the order of tens) away from the hydrofoil or turbine, the turbulence levels incident on the object can be significantly different from those specified at the inlet.

An analytical solution for the decay of inlet turbulence can be developed from the model equations used in the simulation; such a solution is here developed for the k-ω model. Assuming that the gradient diffusion of k and ω is negligible, and making the substitution $U = \mathrm{d}x/\mathrm{d}t$ the model equations reduce to:

$$\frac{\mathrm{d}k}{\mathrm{d}t} = -\beta^* \omega k \tag{3.75}$$

$$\frac{\mathrm{d}\omega}{\mathrm{d}t} = -\beta_1 \omega^2 \tag{3.76}$$

Integration of equation 3.76 and specification of the boundary condition $\omega = \omega_{\mathrm{in}}$, $t = 0$, yields:

$$\omega = \frac{\omega_{\mathrm{in}}}{1 + \beta_1 \omega_{\mathrm{in}} t} \tag{3.77}$$

Substitution of this equation into 3.75 followed by integration and specification of the boundary conditions $k = k_{\mathrm{in}}$, $t = 0$ then yields:

$$k = k_{\mathrm{in}}(1 + \beta_1 \omega_{\mathrm{in}} t)^{\frac{-\beta^*}{\beta_1}} \tag{3.78}$$

Taking the timescale as $t = x/U_\infty$, where x is the distance from the inlet, and utilizing the definitions of the turbulence intensity and the turbulent viscosity, we arrive at:

$$Tu = \sqrt{Tu_{\mathrm{in}}^2 \left(1 + \frac{3\,\rho\, U_\infty\, x \beta_1\, Tu_{\mathrm{in}}^2}{2\,\mu(\mu_{t_{\mathrm{in}}}/\mu)}\right)^{\frac{-\beta^*}{\beta_1}}} \tag{3.79}$$

This form is useful because it incorporates the two turbulence variables specified as inlet conditions in the CFD simulations of later chapters, namely Tu and μ_t.

3.3 CFX discretization and solution theory

Analytical solutions to the Navier-Stokes equations exist for only the simplest of cases. For practical cases then a numerical solution is required, the subject of this section.

3.3.1 The finite volume method

CFX is a finite volume method which utilizes finite element shape functions for the discretization of some terms. As will be discussed in due course, other significant features of the solver are an implicit formulation and the use of a co-located grid.

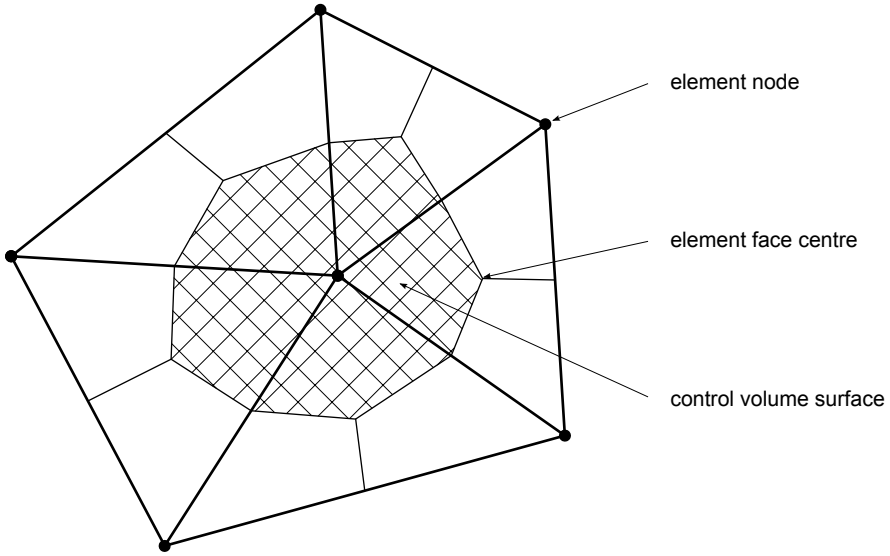

Figure 3.1: *Mesh elements and a control volume surface for a 2D mesh. Adapted from the* Solver Theory *guide.*

We consider here the discretization of the integral mass and momentum conservation equations for a non-deforming control volume:

$$\frac{\mathrm{d}}{\mathrm{d}t}\int_{\mathcal{V}} \rho \,\mathrm{d}\mathcal{V} + \int_{\mathcal{S}} \rho U_j \,\mathrm{d}\mathcal{S}_j = 0 \tag{3.80}$$

$$\frac{\mathrm{d}}{\mathrm{d}t}\int_{\mathcal{V}} \rho U_i \,\mathrm{d}\mathcal{V} + \int_{\mathcal{S}} \rho U_j U_i \,\mathrm{d}\mathcal{S}_j = -\int_{\mathcal{S}} P \,\mathrm{d}\mathcal{S}_j + \int_{\mathcal{S}} \mu_{\mathrm{eff}} \left(\frac{\partial U_i}{\partial x_j} + \frac{\partial U_j}{\partial x_i}\right) \mathrm{d}\mathcal{S}_j + \int_{\mathcal{V}} S_{M_i} \,\mathrm{d}\mathcal{V} \tag{3.81}$$

where $\mathcal{V}$ and $\mathcal{S}$ denote volume and surface regions of integration respectively. Note that these are the RANS equations, hence the effective viscosity. These equations may be derived in this form either from first principles or by integrating the differential equations presented in preceding sections over a volume and using Gauss' divergence theorem to convert some volume integrals into surface integrals. The condition of non-deforming control volumes is necessary for the time derivative to be moved outside of the volume integral in the unsteady terms.

The control volumes are formed around mesh element nodes, as shown in figure 3.1. Volume integrals in the transient and source terms are approximated as the product of the nodal value and the volume of the surrounding control volume. An exception to this occurs for some source terms where it is necessary to use shape functions to approximate the values on a per-sector basis. Surface integral terms are discretized by approximating values at integration points.

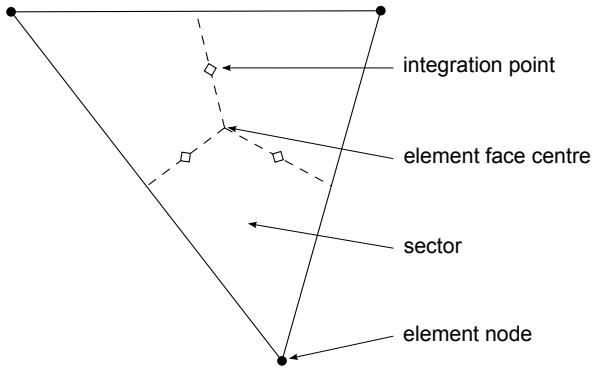

Figure 3.2: *Mesh element. Adapted from the* Solver Theory *guide.*

These integration points may be located at the centre of each surface segment, as shown in figure 3.2, or where the surface intersects an element edge. This choice is discussed in the next section.

The semi-discrete form of the integral mass and momentum equations becomes:

$$\mathcal{V}\,\frac{\rho^{n+1/2}-\rho^{n-1/2}}{\Delta t}+\sum_{ip}(\rho U_j \Delta \mathcal{S}_j)_{ip} \tag{3.82}$$

$$\mathcal{V}\,\frac{(\rho U_i)^{n+1/2}-(\rho U_i)^{n-1/2}}{\Delta t}+\sum_{ip}\dot{m}_{ip}(U_i)_{ip}=-\sum_{ip}(P\Delta \mathcal{S}_i)_{ip}+\sum_{ip}\left(\mu_{\text{eff}}\left(\frac{\partial U_i}{\partial x_j}+\frac{\partial U_j}{\partial x_i}\right)\Delta \mathcal{S}_j\right)_{ip}+S_{M_i}\mathcal{V} \tag{3.83}$$

where the subscript ip denotes evaluation at an integration point and the summations are over all integration points of a control volume. The general form of the transient terms shows that values must be estimated for half of a time step forwards and backwards of the current time step (n). The discrete mass flow through a control volume surface is given by:

$$\dot{m}_{ip}=(\rho U_j \Delta \mathcal{S}_j)_{ip} \tag{3.84}$$

As the solution is implicit a number of terms must be linearized, namely the mass flow term in the continuity equation (in the case of compressible flow), and the convection and diffusion terms in the momentum equation. The convection and diffusion terms are linearized by using old values for the mass flow rate and the viscosity respectively. The treatment of the mass flow term is discussed later under 'compressibility'.

Before discussing the discretization of particular terms, two general features of the CFX

formulation are discussed: shape functions and the Rhie and Chow interpolation strategy used to prevent 'checkerboard' oscillations on the co-located grid.

3.3.2 Shape functions

Finite element shape functions are used to approximate solution variables and geometric quantities at integration points from the values stored at the nodes. The variation of a quantity ϕ within an element is calculated from:

$$\phi = \sum_{i=1}^{\text{nodes}} N_i \phi_i \tag{3.85}$$

where N_i is the shape function for node i and ϕ_i is the value of ϕ at node i. The tri-linear shape functions for a hexahedral element (figure 3.3) are:

$$\begin{aligned}
N_1(s,t,u) &= (1-s)(1-t)(1-u) \\
N_2(s,t,u) &= s(1-t)(1-u) \\
N_3(s,t,u) &= st(1-u) \\
N_4(s,t,u) &= (1-s)t(1-u) \\
N_5(s,t,u) &= (1-s)(1-t)u \\
N_6(s,t,u) &= s(1-t)u \\
N_7(s,t,u) &= stu \\
N_8(s,t,u) &= (1-s)tu
\end{aligned}$$

Shape functions may also be used to evaluate spatial derivatives at a point within the element:

$$\left.\frac{\partial \phi}{\partial x}\right|_{ip} = \sum_{i=1}^{\text{nodes}} \left.\frac{\partial N_i}{\partial x}\right|_{ip} \phi_i \tag{3.86}$$

The cartesian derivatives of the shape functions are calculated from their local derivatives using the Jacobian transformation matrix:

$$\begin{bmatrix} \frac{\partial N}{\partial x} \\ \frac{\partial N}{\partial y} \\ \frac{\partial N}{\partial z} \end{bmatrix} = \begin{bmatrix} \frac{\partial x}{\partial s} & \frac{\partial y}{\partial s} & \frac{\partial z}{\partial s} \\ \frac{\partial x}{\partial t} & \frac{\partial y}{\partial t} & \frac{\partial z}{\partial t} \\ \frac{\partial x}{\partial u} & \frac{\partial y}{\partial u} & \frac{\partial z}{\partial u} \end{bmatrix}^{-1} \begin{bmatrix} \frac{\partial N}{\partial s} \\ \frac{\partial N}{\partial t} \\ \frac{\partial N}{\partial u} \end{bmatrix}$$

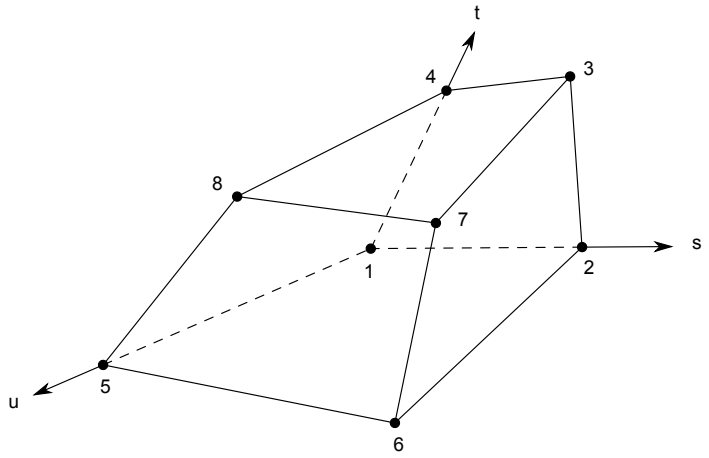

Figure 3.3: *Hexahedral element. Figure adapted from the* Solver Theory *guide.*

As noted earlier, the integration point may be at the centre of each integration point surface ('tri-linear' interpolation) or where the integration point surface intersects the element edge ('linear-linear' interpolation). Whilst the former gives an estimate of higher order accuracy, the latter improves the robustness of the formulation when the element aspect ratio becomes large or as the elements become skewed. The default choice in CFX is to use linear-linear interpolation for the pressure gradient and diffusion terms.

3.3.3 The Rhie-Chow interpolation method

CFX uses a co-located (non-staggered) grid and so the control volumes are identical for all transport equations. It is well known that the use of such a grid layout can lead to checkerboard oscillations in the pressure field, most obviously because the momentum equations are insensitive to a node to node pressure difference when a central difference scheme is adopted for the pressure gradient term. The solution adopted in CFX is an extension of that first suggested by Rhie and Chow (1983). The basic idea is to calculate the convecting velocity at each integration point via a momentum-like equation and introduce there a sensitivity to the node to node pressure difference. Such a calculation is used for the convecting velocity in all transport equations.

As a brief example of this concept, consider the case of a steady, inviscid, incompressible, one-dimensional flow. The control volume layout is as shown in figure 3.4. The momentum

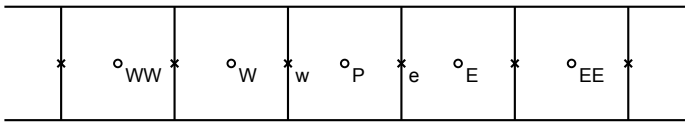

Figure 3.4: *One-dimensional control volume layout. Upper case letters refer to nodes while lower case letters refer to integration points.*

conservation equation for the control volume around node P can be written as:

$$A_P\, U_P = \left(\sum_{nb} A_{nb} U_{nb}\right)_P - \mathcal{V}\left(\frac{\partial p}{\partial x}\right)_P \tag{3.87}$$

where the subscript nb refers to nodes neighbouring node P. For convenience in the following derivation, introduce symbols d and $\hat{U}$ where:

$$d_P = -\frac{\mathcal{V}}{A_P} \tag{3.88}$$

and:

$$\hat{U}_P = \frac{1}{A_P}\left(\sum_{nb} A_{nb} U_{nb}\right)_P \tag{3.89}$$

such that the control volume momentum equation can be written as:

$$U_P = d_P\left(\frac{\partial p}{\partial x}\right)_P + \hat{U}_P \tag{3.90}$$

An equation for the integration point e in the same form would be:

$$U_e = d_e\left(\frac{\partial p}{\partial x}\right)_e + \hat{U}_e \tag{3.91}$$

We now approximate the terms $\hat{U}_e$ and d_e in equation 3.91 by an average of the equivalent terms from the surrounding nodal control volume equations:

$$\hat{U}_e = \frac{1}{2}(\hat{U}_P + \hat{U}_E) \tag{3.92}$$

$$d_e = \frac{1}{2}(d_P + d_E) \tag{3.93}$$

and substitute, thus:

$$U_e = \frac{1}{2}(\hat{U}_P + \hat{U}_E) + \frac{1}{2}(d_P + d_E)\left(\frac{\partial p}{\partial x}\right)_e \tag{3.94}$$

The difficulty with equation 3.94 is that the connectivity of the nodal velocities is large and complicated when $\hat{U}_P$ and $\hat{U}_E$ are expanded. To reduce this we rearrange equation 3.90 as:

$$\hat{U}_P = U_P - d_P\left(\frac{\partial p}{\partial x}\right)_P \tag{3.95}$$

and substitute into equation 3.94 to give:

$$U_e = \frac{1}{2}(U_P + U_E) + \frac{1}{2}(d_P + d_E)\left(\frac{\partial p}{\partial x}\right)_e - \frac{1}{2}\left[d_P\left(\frac{\partial p}{\partial x}\right)_P + d_E\left(\frac{\partial p}{\partial x}\right)_E\right] \tag{3.96}$$

which can be approximated as:

$$U_e = \frac{1}{2}(U_P + U_E) + \frac{1}{2}(d_P + d_E)\left\{\left(\frac{\partial p}{\partial x}\right)_e - \frac{1}{2}\left[\left(\frac{\partial p}{\partial x}\right)_P + \left(\frac{\partial p}{\partial x}\right)_E\right]\right\} \tag{3.97}$$

We thus have an equation for the integration point velocity which features not only the average of the surrounding nodal velocities, but a number of pressure gradients including most importantly the local node to node pressure difference. Insight into the influence of these pressure gradient terms is gained by substituting equation 3.97 into the continuity equation.

For the one-dimensional incompressible case considered the continuity equation reduces to:

$$U_e - U_w = 0 \tag{3.98}$$

which becomes after substitution of equation 3.97:

$$U_E - U_W + \frac{\mathcal{S}}{2\dot{m}}(-p_{WW} + 4p_W - 6p_P + 4p_E - p_{EE}) = 0 \tag{3.99}$$

where central difference approximations have been used for all pressure gradient terms. Some rearrangement of equation 3.99 yields:

$$\frac{U_E - U_W}{2\Delta x} + \frac{\Delta x^3 \mathcal{S}}{4\dot{m}}\left(\frac{-p_{WW} + 4p_W - 6p_P + 4p_E - p_{EE}}{\Delta x^4}\right) = 0 \tag{3.100}$$

The leading term in this equation is a central difference approximation to a first derivative of

the velocity while the second term is a central difference approximation to a fourth derivative of pressure. Equation 3.100 thus represents a discretization of the following equation:

$$\frac{\partial U}{\partial x} + \frac{\Delta x^3 \mathcal{S}}{4\dot{m}} \frac{\partial^4 p}{\partial x^4} = 0 \tag{3.101}$$

which can be compared to the differential form of the continuity equation for this case:

$$\frac{\partial U}{\partial x} = 0 \tag{3.102}$$

The pressure gradient terms which feature in the calculation of the integration point velocities are thus seen to introduce a pressure term into the continuity equation, the effect of which is to prevent a checkerboard pressure field. As the pressure term is multiplied by Δx^3 relative to the mass flow term, the correct differential form of the continuity equation is quickly recovered.

3.3.4 Transient term

The second order backward Euler scheme is used to discretize the transient term in CFX. The start and end of time step values are approximated as:

$$(\rho\phi)^{n-1/2} = (\rho\phi)^{n-1} + \frac{1}{2}((\rho\phi)^{n-1} - (\rho\phi)^{n-2}) \tag{3.103}$$

$$(\rho\phi)^{n+1/2} = (\rho\phi)^{n} + \frac{1}{2}((\rho\phi)^{n} - (\rho\phi)^{n-1}) \tag{3.104}$$

Substituting these values into the semi-discrete approximation used in equations 3.82 and 3.83 gives:

$$\mathcal{V}\,\frac{(\rho\phi)^{n+1/2} - (\rho\phi)^{n-1/2}}{\Delta t} = \frac{\mathcal{V}}{\Delta t}\left(\frac{3}{2}(\rho\phi)^{n} - 2(\rho\phi)^{n-1} + \frac{1}{2}(\rho\phi)^{n-2}\right) \tag{3.105}$$

3.3.5 Convection term

It has already been noted that the convection term in the momentum equation is linearized by using the old mass flow rates. To complete the discretization of this term the integration point value of the quantity being convected, that is the given component of velocity, must be approximated in terms of the nodal values. We use ϕ here to refer to the given component of velocity. All of the convection schemes implemented in CFX can be cast in the form:

$$\phi_{ip} = \phi_{up} + \beta \nabla\phi \cdot \Delta\mathbf{r} \tag{3.106}$$

where ϕ_{up} is the value at the upwind node, β is a blending value which may be either constant or variable depending on the scheme, and $\Delta\mathbf{r}$ is the vector from the upwind node to the integration point; the location at which $\nabla\phi$ is calculated also depends upon the scheme.

For a first order upwind scheme $\beta = 0$ while for a central difference scheme $\beta = 1$ and $\nabla\phi$ is calculated at the integration point. Broadly speaking, the former is diffusive but robust while the latter is less of both but may introduce non-physical oscillations where there is rapid solution variation.

The scheme used in the current work is the so called 'high resolution scheme'. This computes β locally to be as close as possible to one without introducing oscillations, and $\nabla\phi$ at the upwind node. It is both accurate and bounded.

3.3.6 Compressibility

For compressible flows the mass flow term in the continuity equation is non-linear. The discretization of this term is made as implicit as possible in each time step by the use of a Newton linearization:

$$(\rho U_j)^n = \rho^n U_j^o + \rho^o U_j^n - \rho^o U_j^o \tag{3.107}$$

where the superscripts n and o refer to new and old values respectively. The two terms on the RHS involving new values correspond to pressure/density coupling and pressure/velocity coupling. The latter term, $\rho^o U_j^n$, is discretized in the same manner as for incompressible cases and thus incorporates the Rhie and Chow terms. The treatment of the former, $\rho^n U_j^o$, depends upon the Mach number.

3.3.7 The coupled solution

The system of linear equations which arise from an implicit finite volume discretization may be written as:

$$\sum_{nb \text{ of } i} A_i^{nb} \phi_{nb} = b_i \tag{3.108}$$

where ϕ is the solution, A represents the coefficients of the equations, b is the right hand side, i is the number of the control volume, and nb means neighbour but also includes the central coefficient and solution at the i location. For the discrete solution of an uncoupled scalar equation such as enthalpy each entry A_i^{nb}, ϕ_{nb} and b_i is a single number. For the coupled 3D mass-momentum equation set they are a 4 by 4 matrix or a 4 by 1 vector and may be expressed as:

$$A_i^{nb} = \begin{bmatrix} A_{uu} & A_{uv} & A_{uw} & A_{up} \\ A_{vu} & A_{vv} & A_{vw} & A_{vp} \\ A_{wu} & A_{wv} & A_{ww} & A_{wp} \\ A_{pu} & A_{pv} & A_{pw} & A_{pp} \end{bmatrix}_i^{nb} \qquad \phi_{nb} = \begin{bmatrix} u \\ v \\ w \\ p \end{bmatrix}_{nb} \qquad b_i = \begin{bmatrix} b_u \\ b_v \\ b_w \\ b_p \end{bmatrix}_i \tag{3.109}$$

The first subscript in the A_i^{nb} matrix and the subscript in the b_i vector refer to the equation being solved i.e. u, v and w for the x-, y- and z-momentum equations and p for the continuity equation (which includes the pressure due to the Rhie and Chow interpolation). The second subscript in the A_i^{nb} matrix refers to the variable that the coefficient is multiplying. The full matrix of coefficients a thus becomes a (4 × nodes) by (4 × nodes) matrix while ϕ and b become (4 × nodes) by 1 vectors.

The full equation set is solved with the same treatment for all rows i.e. there is no discrimination between mass and momentum equations. According to Raw (1996) the advantages of such an approach are "robustness, efficiency, generality and simplicity" while the principal drawback is the higher memory requirements.

3.3.8 The iterative solution method

The linear system of equations described in the previous section could in principle be solved using a direct method such as Gaussian elimination. In practice this is computationally far too expensive and so iterative methods are used. Indeed, iterative methods are well suited to the solution of the discretized mass and momentum equations because of the process of linearization: some form of iteration will always be required. This linearization iterative cycle is referred to as the 'inner' loop; the 'outer' loop refers to the process of evolving steady state solutions in time.

CFX uses a multigrid accelerated Incomplete Lower Upper (ILU) factorization technique to solve the linear equation system. The multigrid method involves the use of solutions on a series of coarser grids to speed up the solution on the original (fine) grid. It is based on the observation that iterative methods such as ILU factorization are efficient at reducing errors in the solution which occur with a wavelength of the order of the grid spacing, but very slow in reducing errors with a wavelength larger than this. The same error that has a long wavelength on the fine grid thus has a (relatively) short wavelength on the coarse grid.

Four choices are pertinent to all multigrid methods: the coarsening algorithm, the method by which the fine grid solution is applied to the coarse grid ('restriction') and vice-versa ('prolongation'), the cycle type, and the factorization scheme. These are discussed below. Note that much of the detail in this section is from Raw (1996).

3.3.8.1 Coarsening algorithm

It has already been noted that iterative solvers preferentially reduce short wavelength errors. When applied to multi-dimensional problems a further aspect of the behaviour of iterative solvers is that they will preferentially reduce errors in the 'large coefficient' direction. Such anisotropic coefficients can result from anisotropic grids or the flow being aligned with the grid. The Algebraic Multigrid (AMG) coarsening algorithm, as used by CFX, is based on coarsening the grid in the large coefficient direction. The number of volumes that are merged during each coarsening operation is a parameter of the algorithm; Raw (1996), in discussing the implementation in an antecedent of CFX (TASCflow), states that the AMG algorithm is specified to merge between a minimum of 9 and a maximum of 13 volumes into each 'block'.

3.3.8.2 Restriction and prolongation operators

Having defined a hierarchy of grids it is next necessary to specify how the coarse grid equations are created and how their solution is used to reduce the long wavelength errors on the finer grids. The technique used by CFX for this is known as Additive Correction Multigrid (ACM) and is conceptually very simple: the 'blocks' of the coarser grids are used to define finite volumes for which the conservation equations are expressed. Restriction thus involves using the fine grid solution in the coarse grid conservation equations. Prolongation meanwhile involves applying

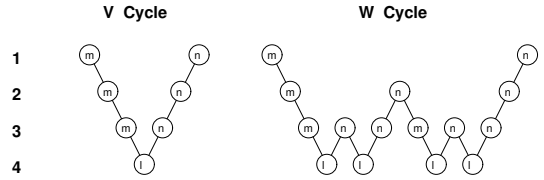

Figure 3.5: *V and W cycles. Figure from Raw (1996).*

the correction to the coarse grid solution for a given block to every fine grid control volume contained in that block.

3.3.8.3 Cycle type

The order in which the solver uses different grid levels may be either flexible, in that it is determined by the residuals in the developing solution, or fixed. The fixed cycle type is normally used with either a 'V' or a 'W' pattern figure 3.5. With the V-cycle each grid level is visited consecutively proceeding downwards until the coarsest level then upwards to the finest. This cycle is repeated until the target residual reduction is achieved. With the W-cycle, as a grid level is visited on the way up, the direction is reversed one time before it is allowed to continue up. The W-cycle has been found to be the most effective for the solution of the coupled mass-momentum equations (Raw, 1996).

3.3.8.4 Factorization algorithm

As noted, CFX uses an Incomplete Lower Upper (ILU) factorization. In the context of a multigrid method this is often referred to as a relaxation scheme. The version of the ILU method implemented involves only modifying coefficients on the main diagonal; this is done to reduce the memory requirements.

One feature of the algorithm is that in the limit of strong coefficients in one direction, it approaches the exact Tri-Diagonal Matrix Algorithm (TDMA). This is the case irrespective of node numbering (i.e. equation ordering). Such a feature means that the ILU factorization is particularly well suited to use with the Algebraic Multigrid method. In essence then, the Algebraic Multigrid method allows the efficiency of the ILU method in this context to be fully exploited.

3.4 Boundary conditions

The boundary conditions specified should be sufficient to ensure a unique solution. For all of the CFD simulations of later chapters this was essentially achieved by specifying a velocity at the inlet and a (static) pressure at the outlet. This section notes in more detail those boundary conditions used.

3.4.1 Inlet

The inlet boundary condition involves specification of the values of the velocity components and turbulence quantities, and, in the case of compressible flow simulations, the density and (static) temperature. Most of the CFD simulations of later chapters were performed with the SST k-ω turbulence model; values for k and ω were specified indirectly by specifying the turbulence intensity Tu and the eddy viscosity ratio μ_t/μ.

3.4.2 Outlet

For the outlet boundary the (static) pressure was specified. Two variants of this exist: either the pressure is forced to be constant across the entire outlet or it is allowed to vary such that the mean is the value specified.

3.4.3 Opening

An opening boundary condition is specified when the direction in which the fluid crosses the boundary is to be determined as part of the solution. The specific option used was 'static pressure for entrainment'. This involves specification of the static pressure, with the given value applying both as an inlet and an outlet value. With this option the velocity gradient normal to the boundary is constrained to be zero.

3.4.4 Symmetry plane

A symmetry plane boundary condition imposes constraints which mirror the flow about the plane. The constraints are on the velocity normal to the boundary and the gradient of scalar quantities normal to the boundary, all of which are set to zero.

Two symmetry planes are used in all of the CFD simulations in this thesis to create a 2D flow within the framework of a 3D solver.

3.5 Dimensional analysis and scaling

The non-dimensional numbers relevant to the present work are listed in this section.

3.5.1 Reynolds number

The Reynolds number is relevant to all viscous flow phenomena and is given by:

$$Re = \frac{\rho U L}{\mu} \tag{3.110}$$

For airfoil problems the velocity scale is taken as the free stream velocity and the length scale as the chord length giving:

$$Re_c = \frac{\rho U_\infty c}{\mu} \tag{3.111}$$

3.5.2 Mach number

The Mach number is relevant to compressible flow and is given by:

$$Ma = \frac{U}{a} \tag{3.112}$$

where a is the speed of sound:

$$a = \sqrt{\gamma R T} \tag{3.113}$$

For air ($\gamma = 1.4$, R = 287 J/kg $\cdot$ K) at 298 K, $a = 346$ m/s. Note that the definition of the Mach number incorporates the ideal gas law, but that this does not affect its general validity.

3.5.3 Strouhal number or reduced frequency

The Strouhal number is relevant to oscillating flows. It may be determined by non-dimensionalizing an equation describing the cyclical, time dependent behaviour of some

quantity. For the case of the harmonically oscillating angle of attack on an airfoil described by:

$$\alpha = \alpha_1 \cos \omega t \tag{3.114}$$

if we non-dimensionalize with $t^* = t/(L/U)$ we arrive at:

$$\alpha = \alpha_1 \cos\left(\frac{\omega L}{U} t^*\right) \tag{3.115}$$

where the argument to the cosine contains the Strouhal number:

$$\mathrm{St} = \omega L/U \tag{3.116}$$

For oscillating airfoils and hydrofoils this number is termed the 'reduced frequency' and the symbol k is used. As with the Reynolds number the chord length and free stream velocity are used for the length and velocity scales. Most authors, e.g. McCroskey et al. (1982, p. ix) and Piziali (1994, p. 2), introduce a factor of 2 in the denominator, thus giving:

$$k = \omega c/2U_\infty \tag{3.117}$$

This is the definition used in the current work.

3.5.4 Force and moment coefficients for airfoil sections

If the force, F on a body depends only on the body length, stream velocity, fluid density and fluid viscosity:

$$F = f(L, U, \rho, \mu) \tag{3.118}$$

then we may use Buckingham pi theorem (or another method) to show that:

$$\frac{F}{\rho U^2 L^2} = g\left(\frac{\rho U L}{\mu}\right) \tag{3.119}$$

where g is a function. The left hand side is termed the force coefficient while the non-dimensional term on the right hand side is of course the Reynolds number. For an airfoil we are interested in the non-dimensional forces causing lift L and drag D. These are defined as:

$$c_l = \frac{L}{\frac{1}{2}\rho U_\infty^2 cS} \tag{3.120}$$

$$c_d = \frac{D}{\frac{1}{2}\rho U_\infty^2 cS} \tag{3.121}$$

where S is the wing span. A moment coefficient may also be derived. This is:

$$c_m = \frac{M}{\frac{1}{2}\rho U_\infty^2 c^2 S} \tag{3.122}$$

The moment coefficient is defined as positive for 'pitch up'. More formally, if we consider a right-hand coordinate system with x- and y-axes aligned with the drag and lift vectors respectively, then the moment is positive in the sense of a negative (clockwise looking towards the origin) rotation of the z-axis.

Note that lowercase letters are used for the 'c' of the coefficient and the associated subscript. This is the convention for section i.e. 2D characteristics. For wing i.e. 3D characteristics, uppercase letters are used.

In analysing vertical axis turbines it is helpful to consider the forces normal and tangential to the blade chord (as opposed to normal and tangential to the freestream velocity in the case of lift and drag). The subscripts N and T are used for these coefficients, which are non-dimensionalized in the same manner as the lift and drag.

3.6 Errors and uncertainty in CFD modelling

There are many sources of error and uncertainty in a CFD simulation, the categorization of which is generally agreed upon. Also agreed upon are the rudiments of a methodology for assessing and where possible minimizing these errors, known as verification and validation. All of the terms, error, uncertainty, verification and validation have specific meanings which will be introduced below.

General CFD textbooks such as Versteeg and Malalasekera (2007, chapter 10) and Ferziger and Peric (2002, pp. 34–35, 329–341) cover this subject, while a more specific reference is that by Roache (1998). There is also a specific guide to the verification and validation methodology

from the American Institute of Aeronautics and Astronautics (AIAA, 1998), and a more general guide to CFD best practice from a European research community (Casey and Wintergerste, 2000); these are referred to below as the AIAA and ERCOFTAC[2] guides respectively. Finally, there may be code-specific guidelines included in the user documentation; for CFX these are included in the *Reference Guide*.

3.6.1 Categorization of errors and uncertainties

The AIAA guide makes a distinction between error and uncertainty; as simplified slightly in the ERCOFTAC guide, this is:

> *Error*: A recognized deficiency that is not due to lack of knowledge.
>
> *Uncertainty*: A potential deficiency that is due to a lack of knowledge.

Error may be subdivided into acknowledged errors and unacknowledged errors. For example discretization error is acknowledged whereas a coding error is not. This classification is relevant to the treatment of errors and uncertainties. Whereas errors can generally be eliminated with the current level of knowledge, uncertainties by definition cannot.

3.6.1.1 Model error/uncertainty

Modelling errors are defined as the difference between the actual flow and the exact solution to the conservation equations. They arise, essentially, because the equations are wrong. The most significant errors in this category are generally a result of turbulence modelling assumptions, for example it is well known that the standard k-ε model will give inaccurate predictions for flow separation determined by boundary layer behaviour in an adverse pressure gradient. These may or may not be due to a lack of knowledge and so they may be errors or uncertainties.

3.6.1.2 Discretization error

Discretization errors are defined as the difference between the exact solution of the conservation equations and the exact solution of the algebraic equation system. It is due to the terms

[2]European Research Community on Flow, Turbulence and Combustion

neglected when, for example, using finite differences to represent exact derivatives. The error will reduce to zero as the grid spacing and time step decrease, the rate at which this occurs being determined by the order of the finite difference approximation. The reduction in spatial discretization error is known as grid convergence.

3.6.1.3 Iteration error

Iteration errors are defined as the difference between the exact and iterative solutions of the algebraic equation system. The significance of this error is readily investigated by monitoring the variation in the solution with the reduction in the equation residuals. Note that it is often called convergence error, but this term is avoided here because of the ambiguity with what might be termed grid convergence error.

3.6.1.4 Round-off errors

Real numbers can of course only be stored with a finite level of precision. This is generally either 'single' i.e. 32 bit or 'double' i.e. 64 bit in industrial CFD codes, giving approximately 7 and 16 decimal digits of precision respectively. Round-off errors are significant when calculating small differences between large numbers and so floating point arithmetic operations should be arranged to avoid this. An example of this is the use of gauge pressure in calculations instead of the absolute pressure.

All CFD simulations in later chapters were run in double precision because of concerns about the accuracy of geometric calculations. Unfortunately these calculations are done in the specified run precision of the solver (single or double) and it is not possible to perform this calculation as a double precision operation before truncating. In the case of the turbine mesh the range of scale is from the order of microns (smallest edge length) to hundreds of metres (domain width) and so larger than single precision.

3.6.1.5 Far-field boundary error

For external flow problems the far-field boundary must be placed a sufficiently large distance, L_b, from the body of interest such that the free stream boundary condition applied is appropriate.

Some error will of course always be introduced though. This error source is not singled out by all authors, but is by Roache (1998, section 2.10).

The mathematical treatment of the free stream boundary condition will affect the distance L_b that is required to reduce the error to a given tolerance. In comparison to general purpose CFD codes such as CFX, specialized external aerodynamics codes feature free stream boundary conditions which allow the distance L_b to be smaller for the same error tolerance.

3.6.1.6 Application uncertainty

This includes uncertainties introduced by simplification of the geometry or boundary conditions. Some authors include this in modelling error/uncertainty.

3.6.1.7 User errors

User errors do of course occur.

3.6.1.8 Code errors

Code errors can often be difficult to find; Roache (1998) gives a salutary example. They can be detected by verification and validation against an analytical solution.

3.6.2 Verification and validation

Verification and validation refer to two phases in assessing the quality of a CFD model. Such a quality assessment is mandatory for the publication of CFD results in many journals. See for example the editorial policy statements concerning this quoted by Roache (1998). The broadly agreed definitions of these terms, taken from the AIAA guide, is:

> *Verification*: The process of determining that a model implementation accurately represents the developer's conceptual description of the model and the solution to the model.
>
> *Validation*: The process of determining the degree to which a model is an accurate representation of the real world from the perspective of the intended uses of the model.

These definitions have been expressed somewhat more tersely by Roache (1998, p. 23) as:

> *Verification*: Solving the equations right.
>
> *Validation*: Solving the right equations.

The processes involved in each of these two phases are discussed below.

It is also worth mentioning *calibration* here. This can be used to mean one of two quite different things, depending on the text. The AIAA guide defines calibration as:

> *Calibration*: The process of adjusting numerical or physical modelling parameters in the computational model for the purpose of improving agreement with experimental data.

whereas the ERCOFTAC guide defines calibration as:

> *Calibration*: Procedure to assess the ability of a CFD code to predict global quantities of interest for specific geometries of engineering design interest.

The word is not used in the present work, first because no calibration in the AIAA sense was performed, and second because the present author sees no significant distinction between calibration in the ERCOFTAC sense and validation.

3.6.2.1 Verification

Verification primarily involves assessing the error due to insufficiently fine spatial and temporal discretization, insufficient iterative convergence and programming errors. From the perspective of a user of an industrial CFD code, programming errors are not specifically checked for. For external flow problems the far-field boundary error is also investigated in the framework of verification.

The spatial discretization error is assessed by performing the simulation on a series of grids of different resolutions, this process being commonly known as a grid convergence study. It is possible to estimate the solution on a grid with zero grid spacing – the exact solution – from solutions on two grids using Richardson extrapolation. The spatial discretization error for

a given grid may therefore be determined. This method is discussed below in section 3.6.3. Richardson extrapolation may also be used to estimate the temporal discretization error and the far-field boundary error, although in the present work it is not used to estimate the temporal discretization error. Section 3.6.4 discusses the application of Richardson extrapolation to the estimation of far-field boundary error.

The extent of iterative convergence can be assessed by looking at some measure of the equation residuals, namely the differences between the left and right hand sides of the algebraic equation system. The CFX solver gives a normalized value of the maximum and RMS residuals for each of the conservation equations being solved. Limited details of the normalization procedure are given in the *Theory guide* (p. 296), while the *Modelling guide* (pp. 391–2) and the *Reference guide* (p. 100) give some guidance as to the significance of the values.

Whilst reducing the RMS residuals for all equations to less than 1×10^{-6} strongly suggests that the solution is tightly converged, i.e. there is negligible iterative error, the reverse is not necessarily true. This is the case when there are a small number of nodes with high residuals, the presence of which does not affect an integral quantity of interest. Iterative convergence can be demonstrated by plotting the variation of the integral quantity with time step and residual level.

3.6.2.2 Validation

Validation involves comparing the results of a *verified* simulation with experimental data in order to assess the modelling error.[3] This may be difficult if the problem under consideration is particularly complex and the experimental data is limited; in addition the application uncertainty may be significant. Under these circumstances the AIAA guide recommends a 'building block' approach to validation, and thus also verification.

The strategy of this building block approach is to progressively decompose the complete system into subsystem cases, benchmark cases and finally unit problems, as indicated in figure 3.6. Each level is characterized by the complexity of the flow physics and geometry; in addition

[3] In some cases the results of a Navier-Stokes-based CFD simulation may be compared with an analytical solution that is not derived from the Navier-Stokes equations. If this analytical solution is known to accurately represent reality then such a comparison would fall within the gamut of validation. An example of such an analytical solution would be one based on the Rankine-Hugoniot conditions which describe the behaviour of shock waves in supersonic compressible flow.

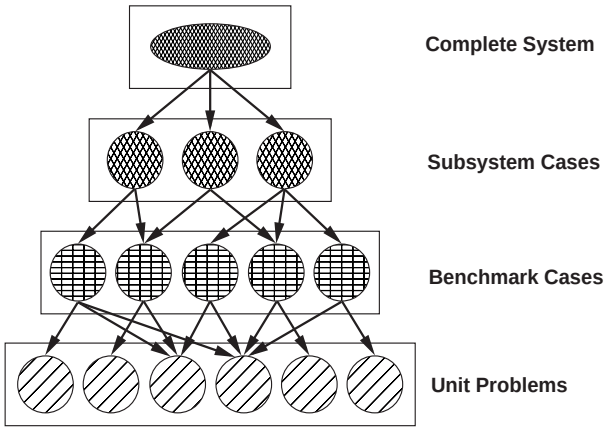

Figure 3.6: *Validation phases. Taken from the AIAA guide (figure 4).*

the quality and extent of experimental data will likely be related to the level. The *complete system* will feature many interacting flow features and experimental data may be very limited. The *subsystem case* is the first level of simplification, perhaps achieved by removing some components from the complete system. This will limit the complexity, but nevertheless the flow physics being simulated will closely resemble that of the full system. The experimental data at this level will be somewhat more comprehensive than that for the complete system. *Benchmark cases* involve a more significant simplification, with specific hardware being fabricated to represent key features of each subsystem case. The aim at this level is to study the interaction between two flow physics features, and to have comprehensive experimental data to compare with. The final simplification is to a *unit problem*, which will only contain a single flow physics feature. This is likely to be a standard test case and an analytical solution may be available. The experimental data will be comprehensive and will have low uncertainty.

The complete system in the current work is Edinburgh Designs' variable pitch vertical axis turbine. In addition to the turbine blades, the shaft, spokes and rim of the supporting structure are either partially or fully immersed. There is also the interaction with the free surface to consider, and, in the context of sea trials, the presence of the barge. The present work is limited to the simulation of one subsystem of the above case, and the benchmark case and unit problem below this. This subsystem case is a 2D representation of the turbine blades themselves. This removes all of the supporting structure (sadly necessary in the real world) and the presence of the free surface and the barge. The benchmark case is an oscillating airfoil/hydrofoil, for which a significant amount of experimental data is available. This removes

the complexity of the curved path of the turbine blade, and its interaction with the turbine wake. The experimental data includes lift, drag and moment force coefficients and surface pressure coefficients. Finally, the unit problem considered is a foil at a fixed angle of attack. This removes the time dependence from the solution. The experimental data available for this problem is particularly comprehensive and includes in addition to the lift, drag, moment and pressure coefficients, measurements of the boundary layer profiles. Such data is of low uncertainty; in particular the drag coefficient has significantly lower uncertainty than with the oscillating case due to the method of measurement (see section 2.2.2).

In order to perform a complete system simulation it would be desirable to simulate a number of other subsystem cases, benchmark cases and unit problems. A full breakdown of this is given in figure 3.7. Some discussion of these other cases will be provided in the *further work* section of chapter 8.

One aspect of this building block approach to validation has not yet been discussed, namely the way in which it relates to the verification work. Such verification studies as described above can consume a significant amount of CPU time if conducted on the complete system case. With the building block approach, comprehensive verification studies can be performed on the unit problem and benchmark cases relatively quickly. These results can then be used to inform the numerical parameters required for the problem setup of the subsystem and complete system cases. Even when verification is required for the more complicated cases, the results from the less complicated cases will likely guide the choice of the new parameter values, reducing the time taken for verification.

3.6.3 Estimating the spatial discretization error

A well developed method for estimating the spatial discretization error is given by Roache (1998) and by NPARC[4] (2008). This is based around the use of Richardson extrapolation and is described below.

[4]The National Project for Application-oriented Research in CFD; a partnership between NASA and the US Air Force, with additional involvement from Boeing.

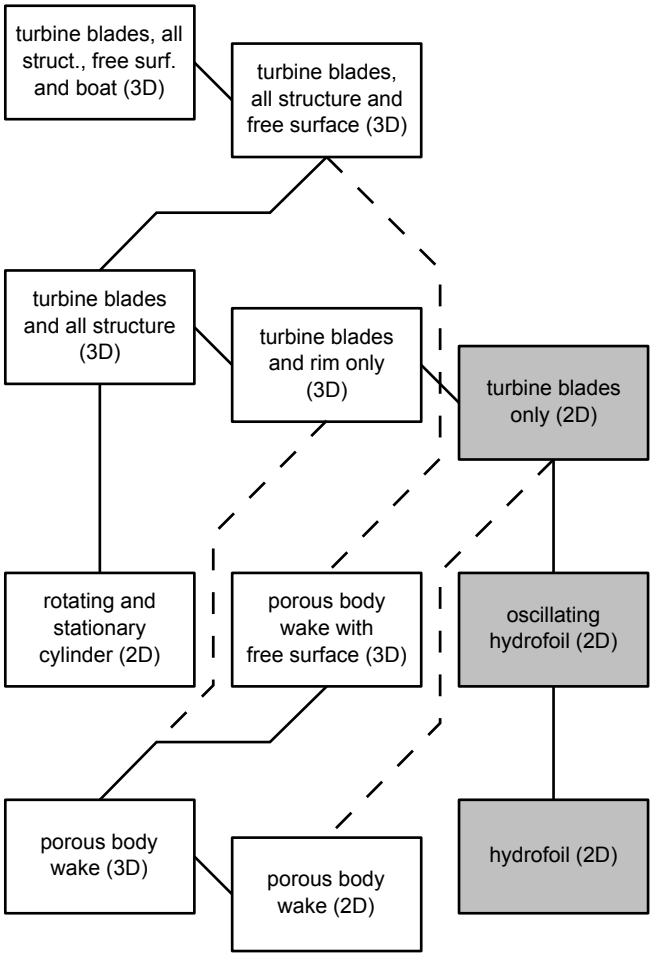

Figure 3.7: *Validation problems relevant to the present work. This diagram shows four validation phases as per the AIAA guidelines, but with the addition of a hierarchy within each phase. Solid lines indicate the flow of information within a phase or between two consecutive phases. Dashed lines indicate the flow of information between non-consecutive phases.*

3.6.3.1 Richardson extrapolation

Richardson extrapolation is a method for obtaining a higher-order estimate of the continuum value of a quantity from a series of lower-order discrete values. The discrete solutions for a quantity f are assumed to have a series representation:

$$f = f_{exact} + g_1 h + g_2 h^2 + g_3 h^3 + \cdots \tag{3.123}$$

where h is the grid spacing and the functions g_1, g_2, etc. are independent of the grid spacing. With a second-order method $g_1 = 0$.

If we have two discrete solutions f_1 and f_2 on two different grids with discrete spacings h_1 (fine grid) and h_2 (coarse grid) then we can write out two equations for the above series representation. We solve one equation for g_2, substitute this into the second and solve for f_{exact}. Omitting third and higher order terms, the result is:

$$f_{exact} \cong f_1 + \frac{f_1 - f_2}{r^2 - 1} \tag{3.124}$$

where $r = h_2/h_1$ is the grid refinement ratio.

The Richardson extrapolation can be generalized to p^{th} order methods as:

$$f_{exact} \cong f_1 + \frac{f_1 - f_2}{r^p - 1} \tag{3.125}$$

The quantity f for which Richardson extrapolation is to be used can be a primary variable at a grid point, or an integral quantity such as drag. Where f is an integral quantity, the methods used in the evaluation must be of equal or higher order to order of the solution (e.g. if the solution is second-order then second or higher order quadratures must be used when calculating forces.)

3.6.3.2 Richardson extrapolation as an error estimator

In equation 3.125 the correction to the fine grid solution f_1 can be seen to be an estimator of the error in the fine grid solution. We express this as the estimated fractional error E_1 for the fine grid solution:

$$E_1 = \frac{\varepsilon}{r^p - 1} \tag{3.126}$$

$$\varepsilon = \frac{f_2 - f_1}{f_1} \tag{3.127}$$

The estimated fractional error E_1 is an ordered error estimator, and a good approximation to the discretization error of the fine grid solution if that solution is of reasonable accuracy i.e. $E_1 \ll 1$. It is a significantly more informative measure of the error that ε, which does not take into account either r or p. (ε could be made artificially small by selecting a grid refinement ratio r close to 1.) Like any relative error indicator, the value of E_1 will become meaningless if f_1 is zero or very small relative to $f_2 - f_1$.

3.6.3.3 Grid convergence index for the fine grid solution

Whilst the error estimator E_1 is based on sound theory, it does not provide a bounded estimate of the error. Roache (1998) suggests that it is equally probable that E_1 be optimistic as conservative, i.e. just as likely that the actual error be greater than E_1 as less than E_1. What is desired in the reporting of CFD calculations, Roache argues, is not a true 'error bound', but an 'error band', that is a tolerance on the accuracy of the solution which may be exceeded, but in which there is 'some practical level of confidence'.

For this Roache points to the use of the ε of equation 3.127 when reporting results obtained using a grid doubling and a verified second-order code. For this particular situation there is general acceptance that ε *does* provide a reasonable error band. Observe that for $r = 2$ and $p = 2$, E_1 is only 1/3 of ε.

The grid convergence index is a means of relating the ε obtained from a grid convergence study with any r and p to the epsilon that would be expected from a grid convergence study of the same problem and with the same fine grid but with $r = 2$ and $p = 2$. The GCI is defined as being equivalent to the value of ε that would produce the same E_1 with $r = 2$ and $p = 2$ as the value of E_1 calculated with the actual values for ε, r and p from grid convergence study. It is expressed as:

$$\mathrm{GCI}_{fine} = F_s \frac{|\varepsilon|}{r^p - 1}, \quad F_s = 3 \tag{3.128}$$

It is seen that for the case of a grid doubling ($r = 2$) with a second-order method ($p = 2$) the denominator is equal to 3, and we obtain GCI = $|\varepsilon|$ as intended. If the coefficient F_s is chosen as equal to 1 then GCI = E_1 for any r and p. In this sense F_s can be seen as a 'factor or safety' on the Richardson error estimator E_1.

3.6.3.4 Grid convergence index for the medium grid solution

If we are performing a three grid convergence study then there are two ways we can calculate a grid convergence index for the medium grid solution. Firstly, we can use the same equation as for the fine grid GCI (equation 3.128), but the f_1 and f_2 solutions are now the medium and coarse solutions whereas previously they were the fine and medium solutions.

Secondly, we can use the 'coarse' grid GCI. This would be the only option in a two-grid study, hence why it is termed 'coarse':

$$\mathrm{GCI}_{coarse} = r^p \mathrm{GCI}_{fine} \tag{3.129}$$

Checking the ratio between the GCI_{coarse} calculated in these two ways is a further check on the solution being in the asymptotic range. The ratio should be close to unity.

3.6.3.5 Choice of the factor of safety

Roache (1994) originally recommended use of the value $F_s = 3$ in the definition of the GCI. Subsequently (Roache, 1998) it was decided that $F_s = 3$ gave an overly conservative estimate for the error in grid convergence studies using three or more grids to experimentally determine the observed order of convergence p. In this instance a value of 1.25 is now recommended as being adequately conservative.

3.6.3.6 Calculation of the observed order of convergence

Using solutions from three grids with constant grid refinement ratio $r = r_{12} = r_{23}$, the order of convergence can be calculated directly:

$$p = \ln\left(\frac{f_3 - f_2}{f_2 - f_1}\right) / \ln(r) \tag{3.130}$$

This equation is again derived from the series representation (equation 3.123) for the discrete solution of a quantity f. In deriving the Richardson extrapolation we used two solutions of this equation to eliminate the function g in the leading error term. In this instance we use three solutions of the equation to again eliminate g in the leading error term and also the f_{exact}.

The NPARC guidelines suggest that the observed order of convergence is often less than the theoretical order of convergence due to such factors as boundary conditions and grid stretching. Conversely, David Ingram of the University of Edinburgh (priv. comm.) has indicated that 'super-linear' convergence, i.e. observed order of accuracy higher than theoretical, can be seen in the numerical solution of non-linear equations such as the Navier-Stokes.

3.6.3.7 Calculating grid spacing and stretching ratios for refined grids

All of the C-grids used in the modelling of the hydrofoil exploit non-uniform grid spacing in order to minimize the spatial discretization error. The grid spacing is specified along block edges by setting the first element edge length and the growth ratio, with the growth being controlled by simple geometric progression. Such a grid is termed a 'compound interest grid' in Ferziger and Peric (2002, section 3.3.4). When such a grid is refined by a factor R we want every R^{th} node on the new grid to correspond to a node on the old grid. We also want the growth ratio to be uniform on the new grid.

This can be calculated by starting from the general equation for the sum of a geometric series:

$$S = \frac{a(1 - r^n)}{1 - r} \tag{3.131}$$

where S is the cumulative distance, a is the first spacing along an edge and r is the stretching ratio. From this it can be readily shown that:

$$r_2 = r_1^{1/R} \tag{3.132}$$

and:

$$a_2 = a_1 \frac{1 - r_1^{1/R}}{1 - r_1} \tag{3.133}$$

where a_1 and r_1 are the first spacing and stretching ratio on the first grid, a_2 and r_2 are the first spacing and stretching ratio on the second grid, and R is the ratio of the number of cells (along the edge) in the second grid to the first grid. Thus $R > 1$ if the second grid is finer than the first. Note that these formulas apply equally to non-integer grid refinement.

3.6.4 Estimating the far-field boundary error

For external flow problems the question arises as to where to specify the outer computational boundary, i.e. the 'far-field' boundary. Clearly this must be placed a sufficient distance from the body (around which we are simulating the flow) such that the error introduced by the boundary is small.

Roache (1998, section 6.10) shows that, as with the spatial discretization error, Richardson extrapolation can be used to estimate the error; Roache demonstrates this by analysing the subsonic airfoil computations of Zingg (1992).

Table 3.1: *Drag and lift coefficients, Richardson extrapolations and errors therefrom. Coefficients from Zingg (1992, table 8, case 3), analysis due to Roache (1998).*

Grid (L_b/c)	c_d	c_l	% c_d	% c_l
12	0.01349	1.3139	−3.9174	0.23905
24	0.01376	1.3121	−1.9943	0.10172
96	0.01397	1.3111	−0.4986	0.02543
RE 24-96	0.01404	1.3108	–	–

The results of Zingg that are analysed are those for a NACA 0012 airfoil at $\alpha = 12°$, Re $= 2.88 \times 10^6$, Ma $= 0.16$. The computations are from three grids having far-field boundaries at 12, 24 and 96 chord lengths from the airfoil. The grids with boundaries at 24 and 12 chord lengths were generated by removing the outer grid lines from the grid with boundaries at 96 chord lengths, thus the spatial discretization in the common regions is the same. Characteristic boundary conditions with a circulation correction are applied at the far-field boundary.

Unfortunately the three grids used by Zingg do not have a consistent change in the distance to the far-field boundary and so it is not possible to directly calculate the observed order of convergence. Instead, first-order behaviour is assumed in the Richardson extrapolation, which is calculated from the results with $L_b/c = 24$ and 96. Roache then calculates the errors for each grid and for each extrapolated value (table 3.1). Finally, Roache calculates an R value for two pairs of grids, $L_b/c = 12$ and 24 and $L_b/c = 24$ and 96, where:

$$R = r^p = \frac{f_0 - f_2}{f_0 - f_1} \tag{3.134}$$

Calculations by the present author show that R value calculated for the grids with $L_b/c = 24$ and 96 is 4. Indeed it should be, because we have effectively gone full circle. It is believed Roache's results here are erroneous and due to a rounding error in the calculation.

We may calculate a p value based on the grids with $L_b/c = 12$ and 24 and the Richardson extrapolation (not done by Roache). This gives $p = 1.23$ for the lift coefficient and $p = 0.97$ for the drag coefficient. Clearly the drag coefficient shows almost exact first-order convergence with the inverse distance to boundary, while the lift coefficient shows slightly higher than first-order. It is believed that this demonstrates well Roache's observation.

3.7 Bibliographic note

The most general theory discussed in this chapter is not specifically referenced and comes from a number of sources. That in the *basic fluid dynamics theory* section is informed by White (2006) and Versteeg and Malalasekera (2007). For the *turbulence* section the preceding references along with Ferziger (2005), Pope (2008) and Wilcox (1998) are relevant. The two sections *CFD discretization and solution theory* and *boundary conditions* draw again from Versteeg and Malalasekera as well as Ferziger and Peric (2002). The general scaling laws are informed by White (1999, 2006). All theory for the CFX solver comes from either (CFX-Solver Theory) or (CFX-Solver Modelling).

Chapter 4
Blade element momentum models

4.1 Introduction

Blade element momentum models are a standard design and analysis tool in the wind energy industry and have been adopted for use in the nascent tidal energy industry (e.g. Garrad Hassan, 2009). A description of the blade element momentum model used in the present research is presented in this chapter, as well as results from this model. These results serve as an introduction to the operational principles of a vertical-axis turbine. Also included in this chapter is a description of the non-dimensional parameters used to describe vertical axis turbines, with which we begin.

4.2 Turbine parameters

4.2.1 Tip speed ratio and solidity

Two non-dimensional parameters are commonly used to describe the rotational speed and geometry of vertical axis turbines. The first, the tip speed ratio λ, is the ratio of the blade speed to the wind speed:

$$\lambda = \Omega R / U_\infty \tag{4.1}$$

For vertical axis turbines with constant R this ratio is unambiguous; in other cases the maximum value of R is usually used. The second parameter, the solidity σ, describes the geometry of the turbine and is the ratio of the blade area to the frontal area of the turbine. In the present work the following definition is used:

$$\sigma = Nc/R \tag{4.2}$$

The definition $\sigma = Nc/(2R)$ is also sometimes used.

These two parameters are also used to describe horizontal axis turbines; the definition of the tip speed ratio is the same, but that of the solidity differs.

4.2.2 Coefficients of power, torque and thrust

The coefficients of power, torque and thrust are defined as:

$$\text{power coefficient} \quad C_P = \frac{\text{power}}{\frac{1}{2}\rho U_\infty^3 A} \tag{4.3}$$

$$\text{torque coefficient} \quad C_Q = \frac{\text{torque}}{\frac{1}{2}\rho U_\infty^2 AR} \tag{4.4}$$

$$\text{thrust coefficient} \quad C_T = \frac{\text{thrust}}{\frac{1}{2}\rho U_\infty^2 A} \tag{4.5}$$

Note that $C_P = C_Q\lambda$.

In the context of blade element models, specification of the tip speed ratio and the solidity provides sufficient information to allow the calculation of the power, torque and thrust coefficients if one assumes a blade chord Reynolds number. Blade element models thus neglect any effect due to the number of blades (other than the change in chord Reynolds number).

4.2.3 Blade force and moment coefficients

In analysing the forces on blades we make use of the following non-dimensional coefficients:

$$F_N^+ = \frac{F_N}{\frac{1}{2}\rho U_\infty^2 cL} \tag{4.6}$$

$$F_T^+ = \frac{F_T}{\frac{1}{2}\rho U_\infty^2 cL} \tag{4.7}$$

$$M^+ = \frac{M}{\frac{1}{2}\rho U_\infty^2 c^2 L} \tag{4.8}$$

The non-dimensional blade forces and moment are similar to the coefficients of normal and tangential force and the coefficient of moment; the difference is that the definitions above use the turbine freestream speed as the velocity scale whereas the normal, tangential and moment coefficients use the freestream speed seen by an airfoil. In the context of a turbine this is the relative flow speed. Whilst this is known in the blade element model (it is part of the calculation process) it is not generally known in the case of experiment or CFD (its value is approximated in chapter 7).

The non-dimensionalized shaft torque is defined as:

$$Q^+ = \frac{Q}{\frac{1}{2}\rho U_\infty^2 cRL} \tag{4.9}$$

and is used for analysis of the instantaneous shaft torque. This differs from M^+ in that we use $c\,R$ for the length^2 scale as opposed to c^2. Note that it also differs from the torque coefficient C_Q which is reserved for the cycle-average shaft torque. The rationale behind the definition of Q^+ is that, for the case of a fixed pitch turbine with the blade chord line normal to the radius at the quarter chord point:

$$Q^+ = F_T^+ + M^+ c/R \tag{4.10}$$

and with F_T significantly larger than M we have $Q^+ \sim F_T^+$.

4.3 A description of the model

The blade element momentum model of a vertical axis turbine described by Sharpe (1990) has been programmed in Matlab by the present author. A code listing is provided in appendix A. The theory behind the model is outlined below using notation similar to that used in the Matlab code.

This model considers the interaction between multiple streamtubes and an actuator cylinder of unit depth, as formed by a straight-bladed vertical axis turbine. Further, the model allows for the expansion of the streamtubes as the velocity reduces from the upstream 'half' to the downstream 'half' of the actuator cylinder (such 'halves' are not equal). Other more basic models exist which make progressively more assumptions (no streamtube expansion, only a single disc instead of a cylinder, and only a single streamtube) but these were not employed.

4.3.1 Preliminaries

Three right-hand Cartesian coordinate systems are used in the blade element model. These are shown in figure 4.1. First, the 'Flow' c.s. is aligned with the streamlines such that $U_x \geq 0$ and $U_y = 0$. The subscripts x and y are associated with this system. Second, the 'Rotating' c.s is aligned with the blade's orbital path. Here we use the subscripts ϑ and r; these indicate the directions in a polar coordinate system. The angle from the x-axis of the Flow c.s. to the ϑ-axis of the Rotating c.s. is θ, which is positive for an anti-clockwise rotation. Third, the

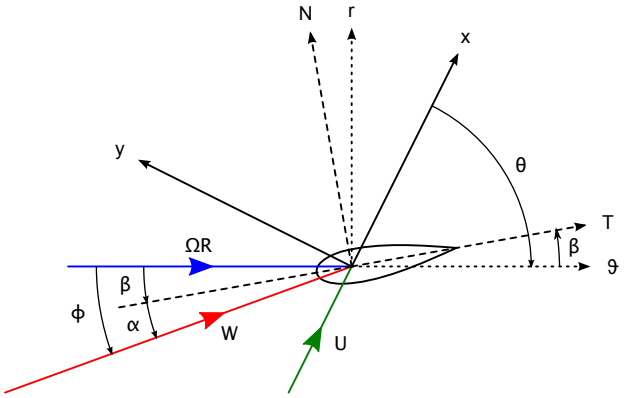

Figure 4.1: *Diagram showing the orientation of the velocity vectors ΩR, U and W and the three coordinate systems x-y, ϑ-r and T-N used in the blade element model. For the case shown in the diagram the blade is at $\psi \sim 30°$ while $\beta = 10°$ and $\alpha = 10°$. The angle θ is negative at this position.*

'Blade' c.s. is aligned with the rotating and pitching blade. As is common in the literature on vertical-axis turbines we use the subscripts T and N to indicate directions tangential and normal to the blade's chord line. The angle from the ϑ-axis of the Rotating c.s. to the T-axis of the Blade c.s. is the pitch angle β, which is again positive for an anti-clockwise rotation. The familiar angle of attack α is then the angle of the relative flow vector W in the Blade c.s.

4.3.2 Momentum theory

The standard actuator disc theory first developed by Rankine and Froude is applied to each intersection of a streamtube with the actuator cylinder. The area of each actuator disc is taken to be the area of the actuator cylinder segment normal to the streamtube.

One key assumption is that for each streamtube there is full recovery of the static pressure in the wake behind the upstream disc before the downstream disc.

The velocity at the upstream disc is:

$$U_x^{\uparrow} = U_\infty(1 - a^{\uparrow}) \tag{4.11}$$

while the velocity midway between the upstream and downstream discs is:

$$U_x^{|} = U_\infty(1 - 2a^{\uparrow})$$

which, as already noted, assumes that the static pressure at this point is equal to the freestream static pressure.

The force exerted on the fluid by the upstream disc is therefore:

$$\widetilde{F_x^{\uparrow}} = 2A^{\uparrow}\rho U_{\infty}^2(1-a^{\uparrow})a^{\uparrow}$$

Note that this is a time averaged force.

At the downstream disc the velocity is:

$$U_x^{\downarrow} = U_x^{|}(1-a^{\downarrow}) \tag{4.12}$$

while in the far wake downstream of the turbine the velocity is:

$$U_x^{\Downarrow} = U_x^{|}(1-2a^{\downarrow})$$

Thus the force exerted by the downstream disc on the fluid is:

$$\widetilde{F_x^{\downarrow}} = 2A^{\downarrow}\rho U^{|2}(1-a^{\downarrow})a^{\downarrow}$$

4.3.3 The Betz limit

Utilizing the equations for the behaviour of a single actuator disc, it may be readily shown that there is a theoretical maximum value of the power coefficient:

$$C_{P,\max} = 16/27 = 0.593 \tag{4.13}$$

which occurs for an axial induction factor $a = 1/3$. This limit is known as the Betz limit after the aerodynamicist Albert Betz, although the work of Lanchester and Joukowsky should perhaps also be acknowledged in the name (van Kuik, 2007). Whilst it has been shown that there are effects which may increase or decrease the maximum power coefficient in practice (Inglis, 1979; Sharpe, 2004; Xiros and Xiros, 2007), these effects are generally small and the basic principle of the Betz limit is withheld.

4.3.4 Blade element theory

In calculating and analysing the forces on a vertical-axis turbine blade it is helpful to begin by converting the coefficients of lift and drag to coefficients of normal and tangential force. This is determined by rotating the coordinate system:

$$\begin{pmatrix} c_T \\ c_N \end{pmatrix} = \mathbf{R}(-\alpha) \begin{pmatrix} c_D \\ c_L \end{pmatrix}$$

where $\mathbf{R}$ is the rotation matrix:

$$\mathbf{R}(-\alpha) = \begin{bmatrix} \cos(-\alpha) & \sin(-\alpha) \\ -\sin(-\alpha) & \cos(-\alpha) \end{bmatrix}$$

If we know the relative flow velocity, W, and the angle of attack, α, then we can calculate the instantaneous force on the blade in the Blade coordinate system as:

$$\mathbf{F}_{TN} = 0.5\rho W^2 c \begin{pmatrix} c_T \\ c_N \end{pmatrix}$$

which, in the Flow coordinate system is:

$$\mathbf{F}_{xy} = \mathbf{R}(-(\theta + \beta))\mathbf{F}_{TN}$$

A time averaged force is required for the application of actuator disc theory. This can be calculated by substituting the true chord length with a 'time averaged' chord length, which represents the amount of blade that is, on average, in a given streamtube. This can be equally considered as a spatially averaged chord length. The two chord lengths are related by the following equation:

$$\tilde{c} = \frac{Nc\delta\psi}{2\pi} \tag{4.14}$$

where $\delta\psi$ is the angle subtended by the intersection of the streamtube with *either* the upstream or downstream halves of the actuator cylinder. Physically, the product Nc represents the total amount of blade-chord over 360° while the fraction $\frac{\delta\psi}{2\pi}$ is the proportion of the total circumference occupied by the streamtube/actuator cylinder intersection. The ratio $\tilde{c}/c$ will thus be equal to the ratio of the time averaged force to the instantaneous force.

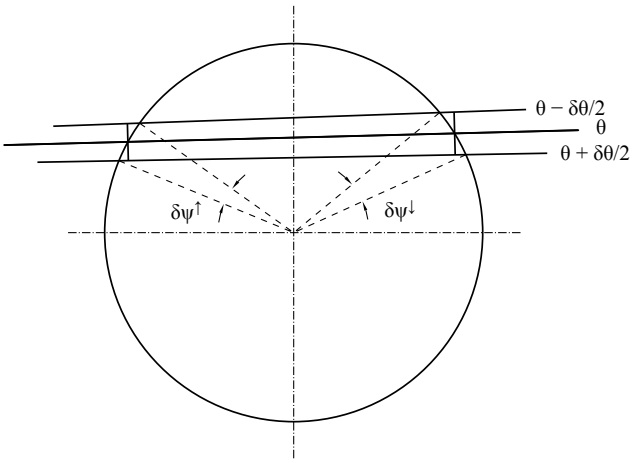

Figure 4.2: *Streamline and streamtube geometry.*

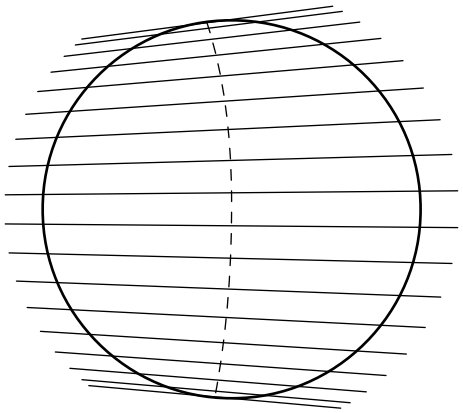

Figure 4.3: *Streamline diagram showing expansion of the streamtubes. 18 streamtubes were used in the calculation. The case shown is that of the Edinburgh Designs turbine with fixed pitch and at a tip speed ratio of 2.6.*

We can relate the area of the actuator disc (upstream or downstream) to the angle $\delta\psi$ by the following equation:

$$A = R\delta\psi|\sin\theta| \tag{4.15}$$

Using equations 4.14 and 4.15 we arrive at an equation for the time averaged force (upstream or downstream):

$$\widetilde{\mathbf{F}}_{\mathbf{xy}} = \frac{\tilde{c}}{c}\mathbf{F}_{\mathbf{xy}} = \frac{NA}{2\pi R|\sin\theta|}\mathbf{F}_{\mathbf{xy}} \tag{4.16}$$

$\widetilde{F}_x$ is the force that we want to equate with the rate of change of momentum in the streamtube.

This leads to the following two equations:

$$a^{\uparrow}(1-a^{\uparrow}) = \frac{N}{2\pi R|sin\theta|}\frac{1}{2\rho U_{\infty}^{2}}F_{x}^{\uparrow} \tag{4.17}$$

$$a^{\downarrow}(1-a^{\downarrow}) = \frac{N}{2\pi R|sin\theta|}\frac{1}{2\rho U^{|2}}F_{x}^{\downarrow} \tag{4.18}$$

Note that the cross-sectional area of the streamtube does not feature in these equations. These equations must be iterated, beginning with an initial guess for $a^{\uparrow}$ and $a^{\downarrow}$, because the forces on the streamtube, $F_x^{\uparrow}$ and $F_x^{\downarrow}$, are functions of both the relative flow velocity, W, and the angle of attack, α, which depend upon the axial induction factors.

The relative flow vector is calculated as:

$$\mathbf{W}_{\vartheta r} = \begin{pmatrix} \Omega R + U_{\vartheta} \\ U_r \end{pmatrix}$$

with:

$$\mathbf{U}_{\vartheta r} = \mathbf{R}(\theta)\mathbf{U}_{xy}$$

where $\mathbf{U}_{xy}$ is calculated for either the upstream or the downstream disc from equation 4.11 or 4.12 respectively.

The relative flow angle ϕ is readily calculated as:

$$\tan\phi = W_r/W_{\vartheta}$$

and so for a known pitch angle β we can calculate α:

$$\alpha = \phi - \beta$$

4.3.5 Force normal to the streamline

Equations 4.17 and 4.18 specify the velocity change tangential to a streamline due to the force exerted on the fluid by the upstream and downstream halves of the actuator cylinder. The forces normal to the streamlines, which would cause the streamlines to be curved, are however neglected in the model.

4.3.6 Integrated forces and torques

In order to calculate the torque and thrust on the turbine we need to calculate the areas of the actuator discs, $A^{\uparrow}$ and $A^{\downarrow}$. We can do this now that we know the velocities at the actuator cylinder.

From the continuity equation we have:

$$A^{\uparrow}U_x^{\uparrow} = A^{\downarrow}U_x^{\downarrow}$$

If we assume that the streamlines are straight then:

$$\theta^{\uparrow} = -\theta^{\downarrow} = \theta$$

This assumption also leads to the following relation:

$$\delta\theta = \delta\psi^{\uparrow}/2 + \delta\psi^{\downarrow}/2$$

which can be shown using basic geometry.

Substituting the above three equations into equation 4.15 for the actuator disc area, we arrive at the following expressions for the upstream and downstream areas:

$$A^{\uparrow} = \frac{2U_x^{\downarrow}}{U_x^{\uparrow} + U_x^{\downarrow}} R|\sin\theta|\delta\theta \qquad A^{\downarrow} = \frac{2U_x^{\uparrow}}{U_x^{\uparrow} + U_x^{\downarrow}} R|\sin\theta|\delta\theta \tag{4.19}$$

Now that the actuator disc areas are known we can calculate the thrust force on the turbine by summing the time averaged forces of equation 4.16:

$$\text{Thrust} = \sum_{\text{streamtubes}} \widetilde{F_x^{\uparrow}} + \widetilde{F_x^{\downarrow}}$$

This summation is not strictly correct because the streamlines are not parallel and so the streamwise forces cannot properly be added. Nevertheless, for cases with a limited amount of streamtube expansion it serves as a good approximation.

The instantaneous and time averaged torque can be calculated from the forces. If the contribution from the pitching moment is neglected then:

$$Q = -F_\vartheta R$$
$$\widetilde{Q} = -\widetilde{F}_\vartheta R$$

with the negative sign giving the torque the correct sign in a right-handed coordinate system. Note that this equation applies when, for a blade pitch angle of 0°, the blade chord line is tangential to the blade orbital path at the quarter chord point.[1]

As with thrust we may now calculate the average torque on the whole turbine:

$$\bar{Q} = \sum_{\text{streamtubes}} \widetilde{Q}^{\uparrow} + \widetilde{Q}^{\downarrow}$$

from which the power can be found (power = $\bar{Q}\Omega$).

4.3.7 Streamtube expansion

The equations already developed for calculating the actuator disc areas also allow the calculation of the azimuth angles, ψ, at which the streamtubes intersect the blade orbit. Equating equations 4.15 and 4.19:

$$A^{\uparrow} = R\delta\psi^{\uparrow}|\sin\theta| = \frac{2U_x^{\downarrow}}{U_x^{\uparrow} + U_x^{\downarrow}} R|\sin\theta|\delta\theta$$

$$A^{\downarrow} = R\delta\psi^{\downarrow}|\sin\theta| = \frac{2U_x^{\uparrow}}{U_x^{\uparrow} + U_x^{\downarrow}} R|\sin\theta|\delta\theta$$

gives:

$$\delta\psi^{\uparrow} = \frac{2U_x^{\downarrow}}{U_x^{\uparrow} + U_x^{\downarrow}}\delta\theta$$

$$\delta\psi^{\downarrow} = \frac{2U_x^{\uparrow}}{U_x^{\uparrow} + U_x^{\downarrow}}\delta\theta$$

[1] In Sharpe (1990) the model is applied to a fixed-pitch vertical-axis wind turbine having the blade chord line tangential to the blade orbital path at the half chord point. In this instance there will be a contribution to the shaft torque from the radial force equal to $-F_r\, c/4$. More subtly, the angle of attack calculated would apply at the half chord point, illustrating an ambiguity in the model.

In summing the streamtube angles $\delta\psi$ it is assumed that the stream*line* for which $\theta = 0$ crosses the blade orbit at $\psi = 0$.

4.3.8 θ-angles of the streamtubes

A streamtube is defined as a closed collection of streamlines, which are not necessarily parallel. The blade element momentum model of a vertical-axis turbine described here considers the interaction of a multitude of streamtubes with the turbine. For each streamtube we must specify the angle, θ, at which the streamtube crosses the blade orbital path. Clearly this will vary over the streamtube; as such we consider it to be the angle at which the central streamline in the streamtube crosses the blade orbital path. Thus if we specify 18 streamtubes, the streamtube angles, θ, will be $5°, 15°, \ldots, 175°$.

4.3.9 Implementation of variable pitch

As previously noted, the variable pitch strategy employed in the present work is to limit the angle of attack based on an assumed velocity field. This assumed velocity field is specified by two parameters: the velocity reduction ratios for the upstream and downstream halves of the cylinder i.e. $U_x^{\uparrow}/U_\infty$ and $U_x^{\downarrow}/U_\infty$. A limiting angle of attack is specified separately for the upstream and downstream halves of the cylinder, thus four parameters in total completely specify the variable pitch algorithm. In effect this produces a function $\beta = f(\psi, \lambda)$. As this function is in terms of the azimuth angle ψ, this angle must be calculated using the equations of section 4.3.7 during each iteration (for the axial induction factor). In contrast, for the case of fixed-pitch, it is only necessary to calculate the streamtube azimuth angles at the end of the iterative solution.

4.3.10 Selection of the number of streamtubes

The number of streamtubes is the sole discretization parameter in the present blade element model. In general, we would expect the solution accuracy to increase with an increase in the number of streamtubes. Whilst this is the case for small numbers of streamtubes i.e. 2, 4, 8, 16, there is a problem in the prediction of the axial induction factor when larger numbers of streamtubes are used. The problem occurs first for the streamtube for which $\theta \to 0$ (as $\Delta\theta \to 0$), and stems from equation 4.17. In essence, as the number of streamtubes increases,

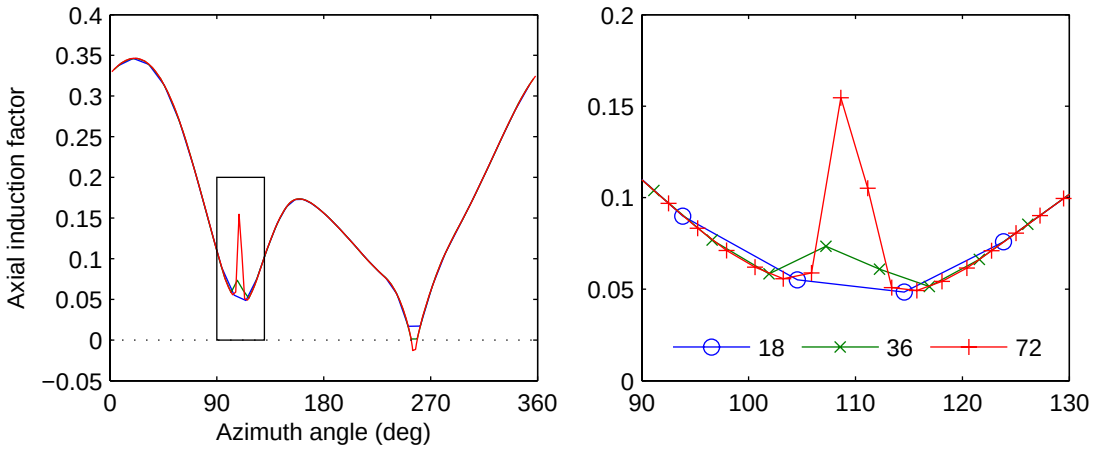

Figure 4.4: *The effect of the number of streamtubes on the axial induction factor for the Edinburgh Designs turbine with fixed pitch and at a tip speed ratio of 2.4 (with $U_\infty = 2.5$ m/s). The boxed region in the left graph shows the area of the detail shown in the right graph. Markers are omitted for the lines in the left graph.*

the cross-sectional area of this streamtube tends to zero as $\sin\theta$ whereas the force (which is purely the drag force at this point) remains finite.

Example results for the Edinburgh Designs turbine operating at fixed pitch are shown in figure 4.4. As can be seen, for an azimuth angle of around 110 degrees, corresponding to $\theta = 0°$, there is a sharp and localized increase in the axial induction factor. Based on these results, 18 streamtubes were selected for subsequent calculations; this was approximately the largest number of streamtubes for which there is no localized increase in the axial induction factor around $\theta = 0°$.

Surprisingly, no mention of this problem is given in Sharpe (1990), who appears to have used 18 streamtubes (this is not stated, but is implied from a diagram showing the streamlines). Sharpe's model has been implemented in an Excel spreadsheet by Paul Cooper of the University of Wollongong, Australia, for the analysis of wind turbines, who advised that he had not observed the problem discussed here (priv. comm.). A copy of his spreadsheet was kindly provided for verification of the present author's Matlab implementation. Cooper's formulation uses 180 streamtubes, but ignores the outermost two (for which $\theta = 0$ and 180°) in the calculations. It was discovered that the problem of a localized maximum in the axial induction factor around $\theta = 0°$ was not significant for the turbine geometry and operating conditions simulated by Paul Cooper, but was so for those of the present study.

4.4 Results

Results from the blade element model for the Edinburgh Designs turbine are now presented. All results were produced using the airfoil section data of Sheldahl and Klimas (1981) for the NACA 0025 airfoil. Primarily we are interested in comparing the performance of this turbine for fixed and variable pitch operation, with the variable pitch operation being based on limiting the angle of attack according to an assumed velocity field. The parameters for this variable pitch operation are maximum angles of attack of 8 degrees upstream and 10 degrees downstream, and assumed velocity ratios of 0.85 upstream and 0.7 downstream. The maximum angle of attack is set lower upstream with the intention of leaving more kinetic energy in the flow for extraction during the downstream pass, the result of which is a smoother shaft torque output. Results are also presented for the case of a turbine with four blades, and for the case of a turbine with variable pitch operation based on the true velocity field.

4.4.1 Turbines with three and four blades and with fixed pitch and variable pitch using an assumed velocity

We first look at the results for the power, torque and thrust coefficients as shown in figure 4.5. Using variable pitch increases the maximum power coefficient somewhat and increases the tip speed ratio at which this occurs. For the three blade variable pitch case the maximum C_P is 0.4998 at a tip speed ratio of 2.7 versus 0.4794 at a tip speed ratio of 2.34 for the fixed pitch case. Perhaps more significant than the increase in $C_{P_{\max}}$ is the fact that the C_P-curve is broader for the case of variable pitch operation. This is important because it is unlikely that the freestream speed and therefore the tip speed ratio will be known with accuracy during operation. Results for the four blade case differ from the three blade case only due to the drop in the blade chord Reynolds number, as discussed above. Such a drop becomes insignificant at the higher tip speed ratios shown. The obvious kink in the C_P-curve for the fixed pitch case at a tip speed ratio of 2 is due to the airfoil section data. Below this tip speed ratio the angle of attack exceeds 27 degrees, at which point the lift and drag curves are themselves kinked (figure 2.3). As was discussed in section 2.2.2.4, this is due to the fact that numerical data are used for angles of attack up to and including 27 degrees while experimental data are used for 30 degrees and above.

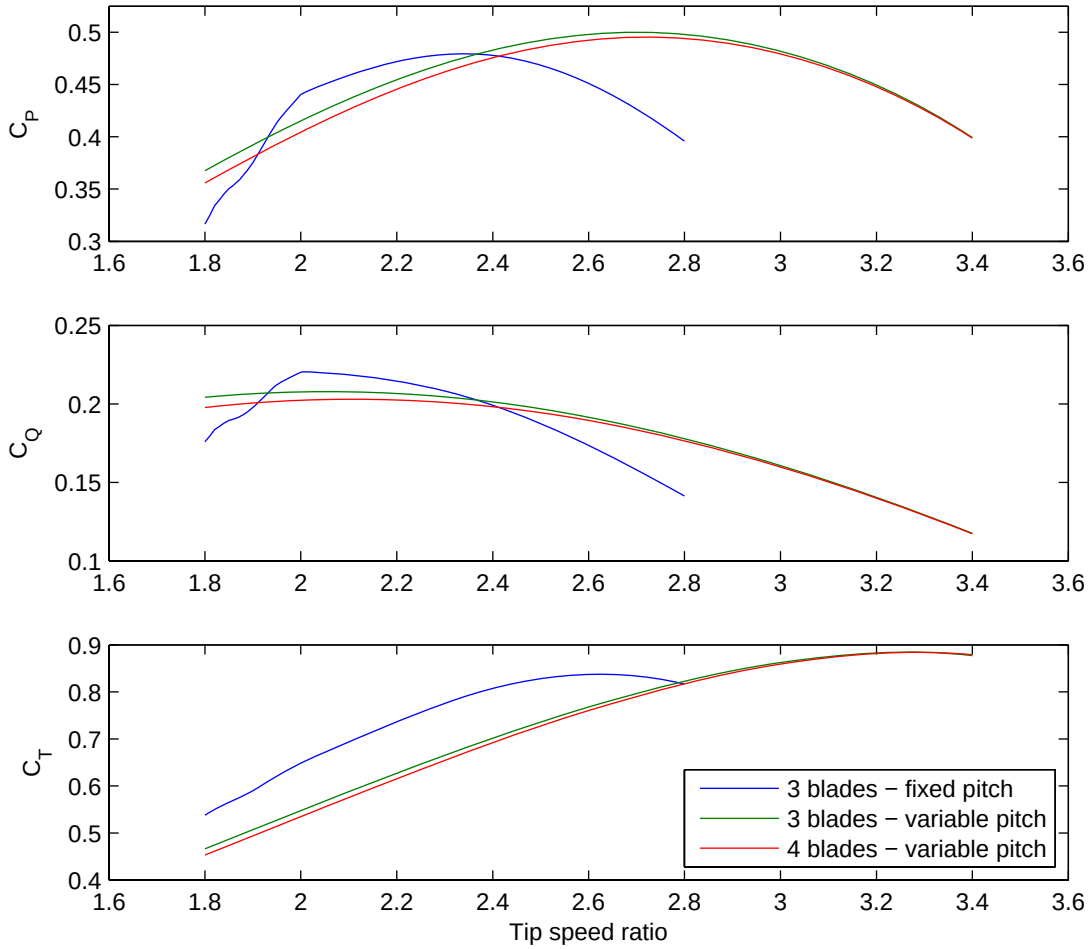

Figure 4.5: *Coefficients of power, torque and thrust versus tip speed ratio for three different configurations.*

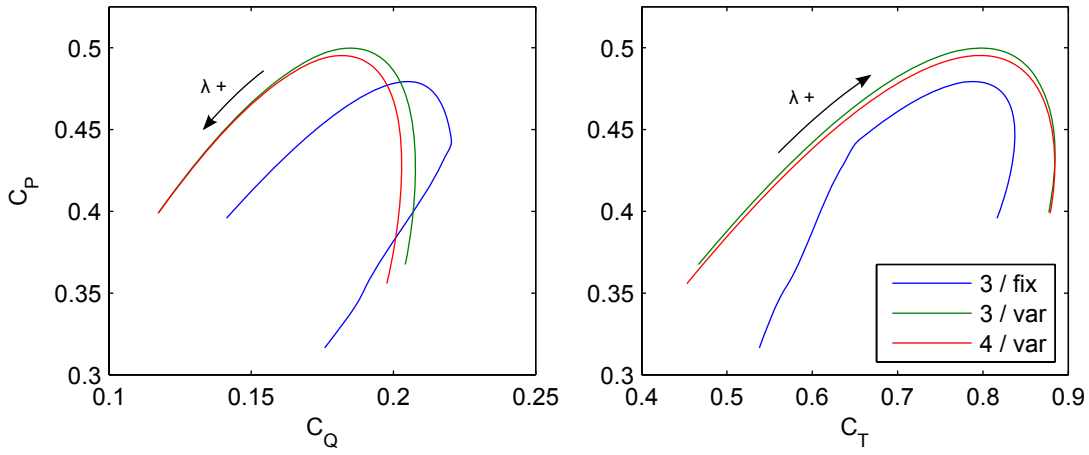

Figure 4.6: *Coefficient of power versus those of torque (left) and thrust (right) for three different configurations (as figure 4.5). The arrows labelled λ+ indicate the direction of increasing tip speed ratio.*

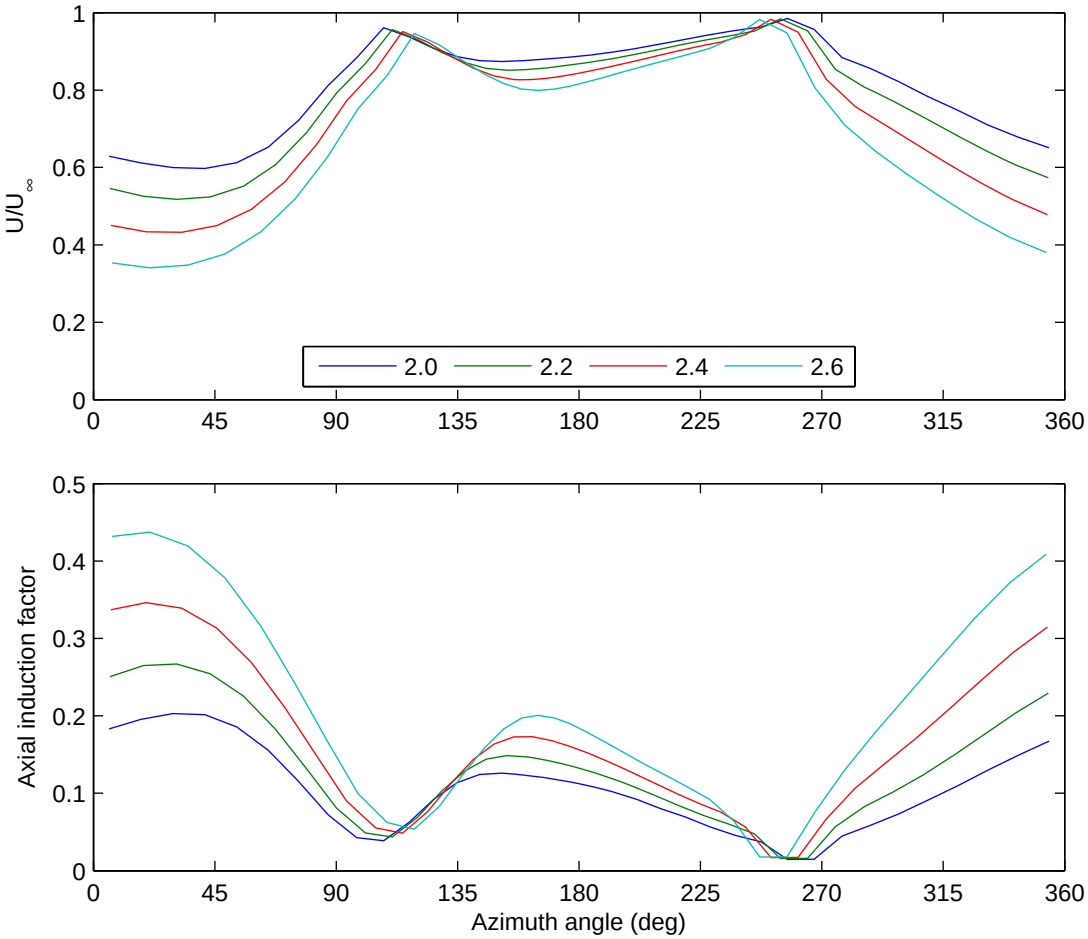

Figure 4.7: *Velocity in the freestream direction and axial induction factor versus azimuth angle for the case of fixed pitch.*

The value of the torque and thrust coefficients are of interest because the cost of the device is likely to be more strongly related to these than to the power coefficient. A useful method of interpreting this is to plot the power coefficient against the torque coefficient and the thrust coefficient, figure 4.6. These graphs should be interpreted loosely along the lines of a plot of drag versus lift for an airfoil, except that we are looking for the maximum ratio rather than the minimum. Clearly the variable pitch case is superior on both measures (C_P vs. C_Q and vs. C_T), although the former suggests an operating point with a higher tip speed ratio than that at $C_{P_{\max}}$ while the latter ratio suggests one below.

Graphs showing the variation of the velocity at the actuator cylinder and the induction factor, both versus azimuth angle, are given in figures 4.7 and 4.8. Both cases apply to the Edinburgh Designs geometry i.e. three blades; the former for fixed pitch and the latter for variable. Results

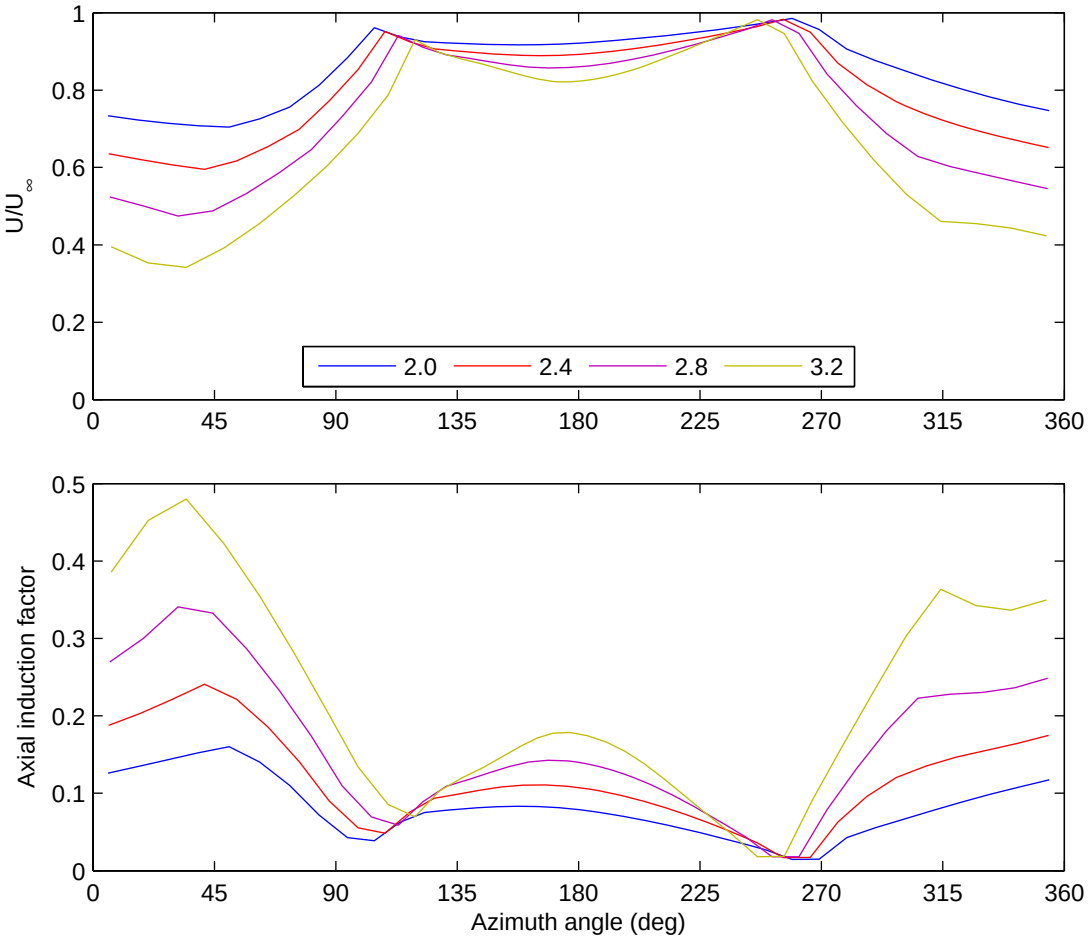

Figure 4.8: *Velocity in the freestream direction and axial induction factor versus azimuth angle for the case of variable pitch.*

are not presented for the four blade variable pitch case as they are essentially the same as with the three blade variable pitch case. Whilst there is some redundancy in presenting both the velocity at the disc and the induction factors (from which the velocity is derived) each highlights a different aspect of the data; specifically, the velocity plots are used to evaluate the accuracy of the assumptions made about the velocity field for the variable pitch algorithm, while the axial induction factor best illustrates the individual behaviour of the upstream and downstream sides of the actuator cylinder. Note that the colours used for the line series are consistent for both figures i.e. the blue and red lines are for tip speed ratios of 2.0 and 2.4 in both figures.

The clear trend shown in both figures is that of a greater velocity reduction with increasing tip speed ratio. Such a trend has of course already been shown by the near-monotonic increase in the thrust coefficient with tip speed ratio for the range of values of interest. Given this

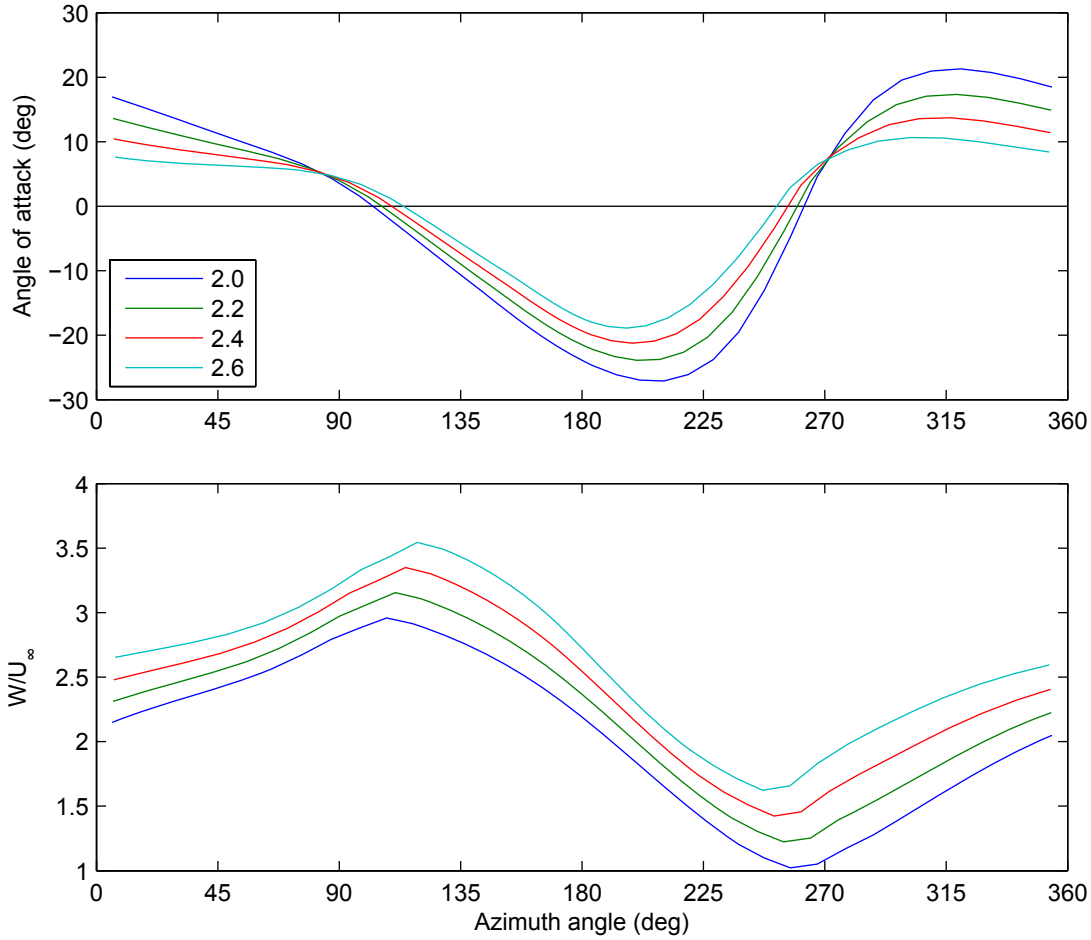

Figure 4.9: *Angle of attack and relative velocity variation with azimuth angle for the case of fixed pitch.*

trend, and the variation in the velocity at the disc with azimuth angle, the use of a constant assumed velocity ratio for the variable pitch algorithm is a significant approximation. Some of the variation with azimuth angle is though captured by the use of separate ratios for the upstream and downstream halves of the cylinder. The assumed ratios of 0.85 and 0.7 are most accurate for the two lowest tip speed ratios shown in figure 4.8. The consequence of assuming a higher ratio is to more severely limit the angle of attack and so is conservative in terms of avoiding stall. A more detailed discussion of this will be given later.

Figures 4.9 and 4.10 show the angle of attack and relative flow speed versus azimuth angle for fixed pitch and variable pitch operation of the three blade turbine. In the latter case the pitch angle is also shown. For the fixed pitch case some differences between the predictions of the blade element model and the values shown in figure 1.3 (which assumed that the turbine did

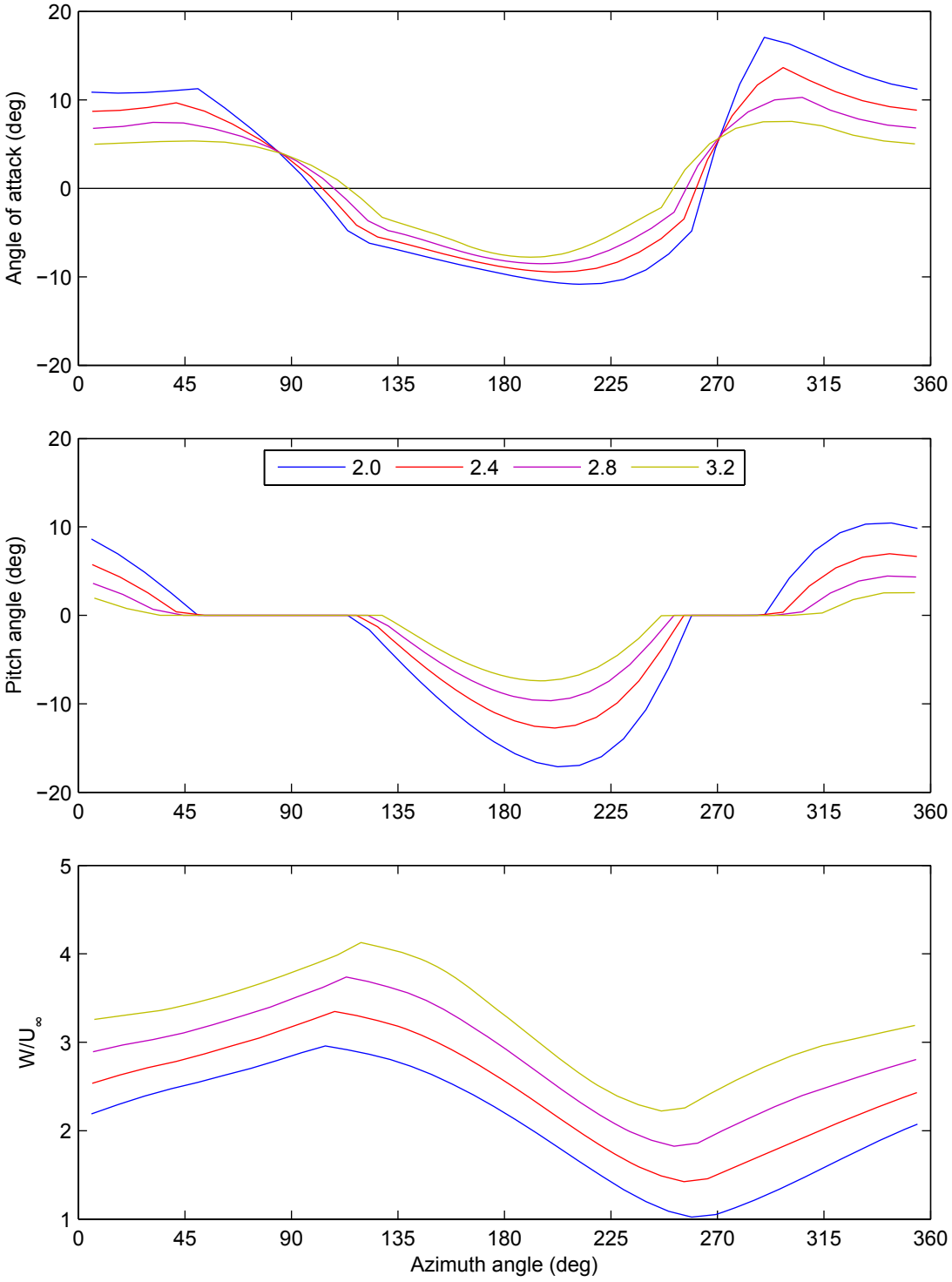

Figure 4.10: *Angle of attack, pitch angle and relative velocity variation with azimuth angle for the case of variable pitch.*

not interfere with flow) may be usefully highlighted. For the angle of attack the maximum and minimum values are not symmetric about zero degrees in the blade element results. Instead, the magnitude of the maximum value is lower as this occurs during the downstream pass where the flow velocity is lower due to the influence of the upstream pass. In effect the 'local' tip speed ratio is higher. Also, the azimuth angles at which $\alpha = 0°$ are not constant with tip speed ratio and equal to 90° and 270°. This arises in the blade element model due to streamtube expansion. The pattern of relative flow speed versus azimuth angle is now more like a triangular wave than a sine wave due to the variation in flow speed with azimuth angle.

With the variable pitch algorithm and parameters employed, and for the tip speed ratios shown, there is a clear change in the pattern of angle of attack versus azimuth angle. At the lowest tip speed ratio, 2.0, the angle of attack is being limited by feathering for the majority of the cycle and the form of the curve tends towards that of a square wave. For this tip speed ratio and the next lowest there is an apparent failure of the variable pitch algorithm for azimuth angles around 290 degrees. This is due to the 'true' velocity ratio at this point (~ 0.9, see figure 4.8) being significantly higher than the assumed velocity ratio (0.7), and highlights the limitation of assuming a constant velocity ratio for the upstream and downstream halves of the actuator cylinder.

Of prime interest in the analysis of vertical axis turbines is the tangential force coefficient. For a fixed pitch turbine with the blade chord line normal to the radius at the quarter chord point, the tangential force is the only (shaft) torque generating force. The contribution from the moment about the quarter chord point is small and is ignored in the present analysis. Note that the direction of the y-axis in the graph of the tangential force coefficient is reversed – this is so that negative values which produce useful (positive) shaft torque are at the top. The pattern shown in figure 4.11 is typical and shows that the tangential force has two minima per revolution at around 0 degrees and 180 degrees. Also shown are the two maxima just after 90 degrees and just before 270 degrees; at these points the angle of attack passes through zero and so the tangential force is equal to the drag force. The shaft torque is of course composed of the sum of the forces on all the blades and so can be smoother. This will be examined shortly.

For the variable pitch case, figure 4.12, the pattern for the tangential force is quite different. In particular the minima near 180 degrees is smaller in magnitude. At this point though the blade pitch angle is non-zero and so the normal force will also contribute to the shaft torque.

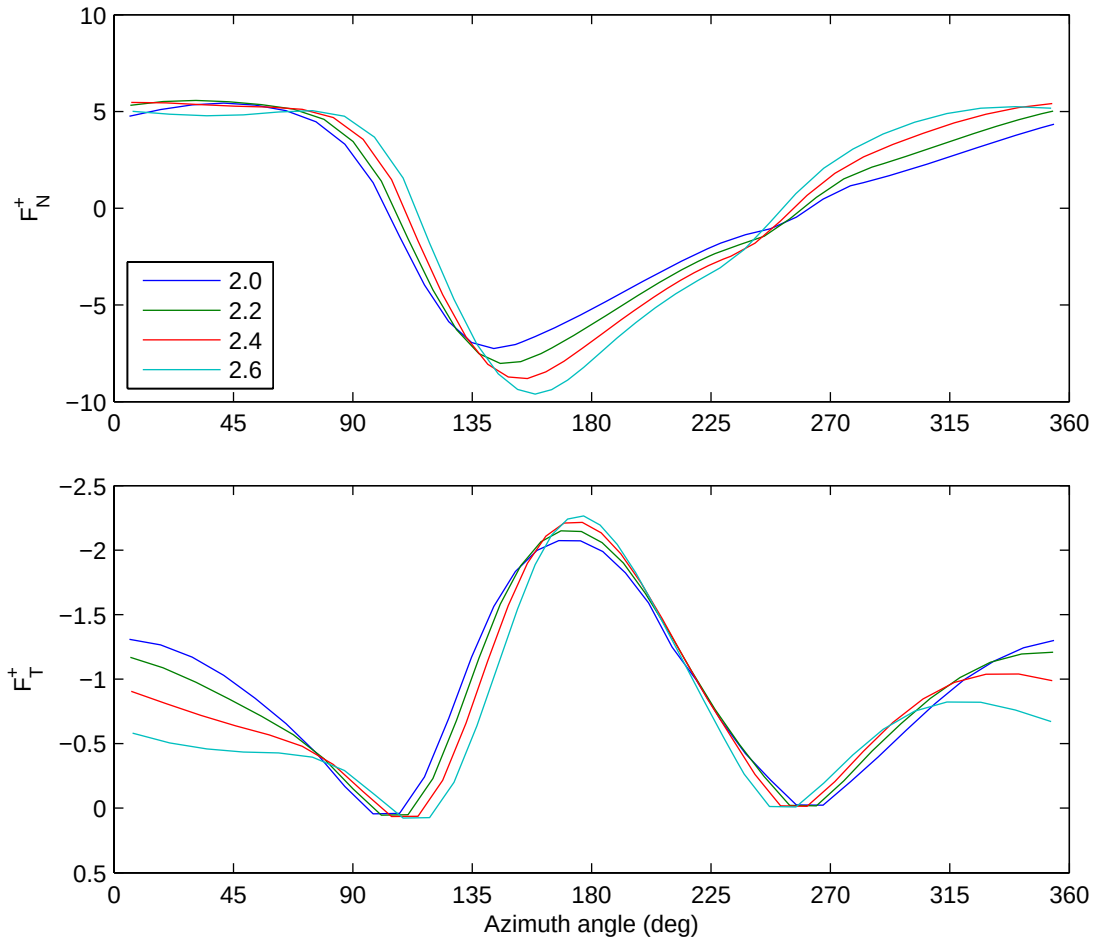

Figure 4.11: *Normal and tangential force coefficients on a blade versus azimuth angle for the case of fixed pitch.*

The total shaft torque versus azimuth angle for configurations of three blades with fixed and variable pitch and four blades with variable pitch is shown in figure 4.13. The azimuth angle corresponds to that of one of the blades on the turbine. For a configuration with three blades (either fixed or variable pitch) there is a significant variation with azimuth angle. In both cases an increasing tip speed ratio makes the shaft torque more peaky. The case with four blades (and variable pitch) is interesting. At the two lowest and the one highest tip speed ratios there is again significant (although less) variation with azimuth angle. For a tip speed ratio of 2.8 though this variation is much reduced.

Figure 4.14 shows the contribution to the shaft torque from each of the blades as well as the sum for one tip speed ratio for each of the three blade cases. The azimuth angle is that of blade A in both graphs. In both cases the peaks in the total shaft torque correspond to a peak in

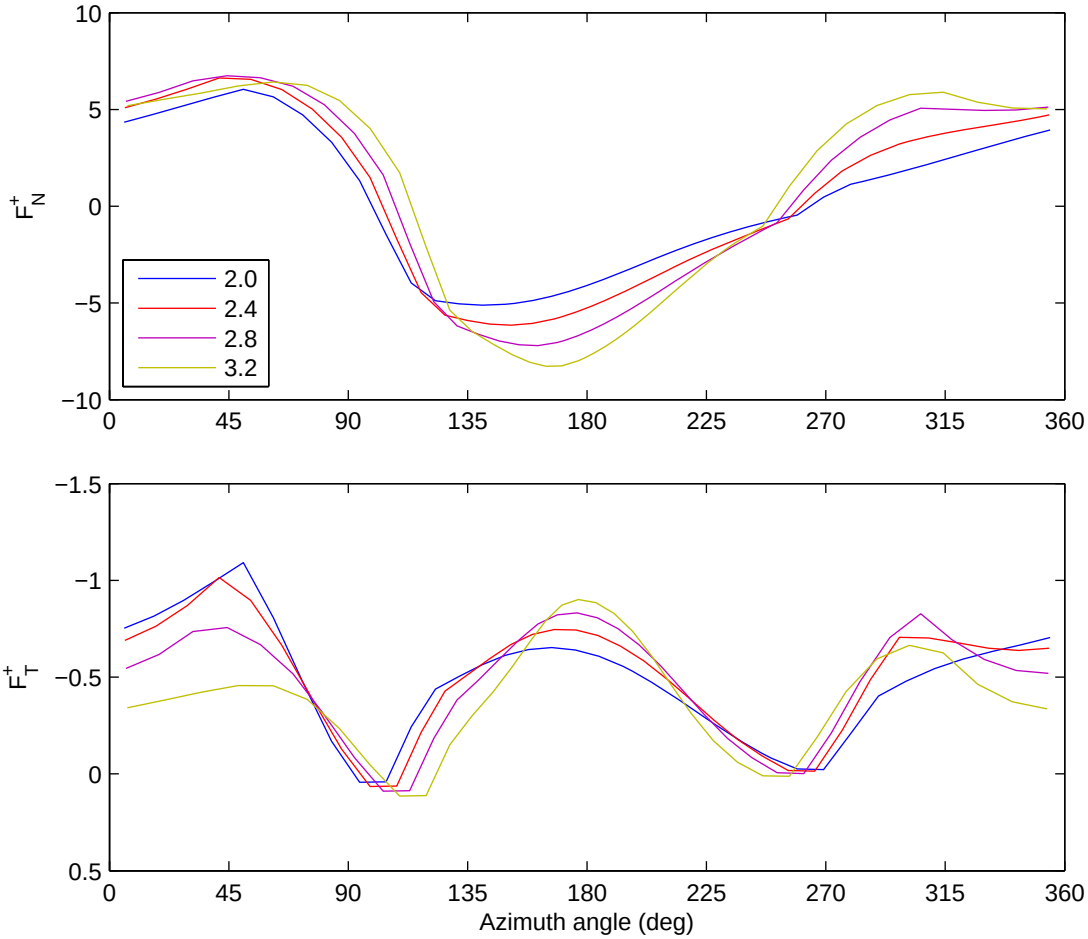

Figure 4.12: *Normal and tangential force coefficients on a blade versus azimuth angle for the case of variable pitch.*

the contribution from one of the blades. It is suggested that the use of a variable pitch strategy which limited the upstream angle of attack to a lower value than that in the current variable pitch case (8°) may make it possible to almost eliminate the variation in the total shaft torque for a three blade turbine.

Equivalent graphs are given in figure 4.15 for two tip speed ratios of the four blade variable pitch case. These are shown to illustrate the fact that small changes in the shapes of the curves for individual blades can have a significant impact on the total shaft torque.

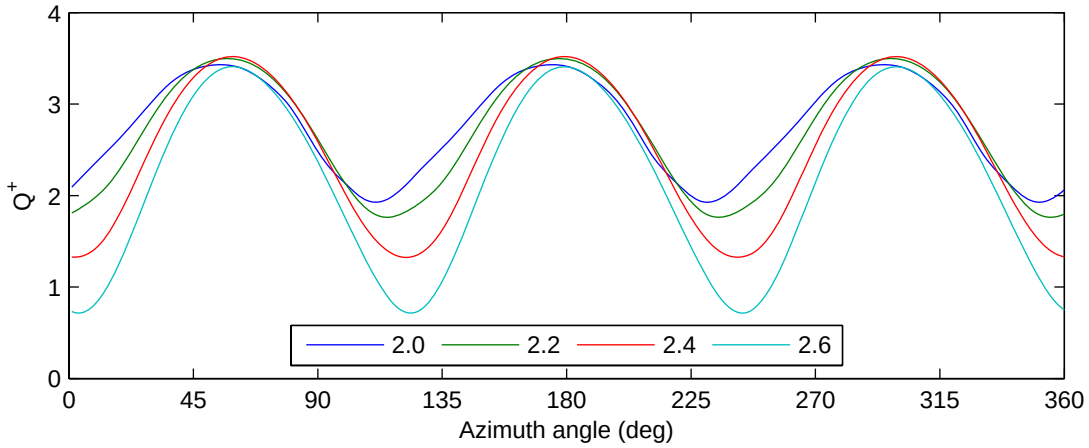

(a) Three blades, fixed pitch.

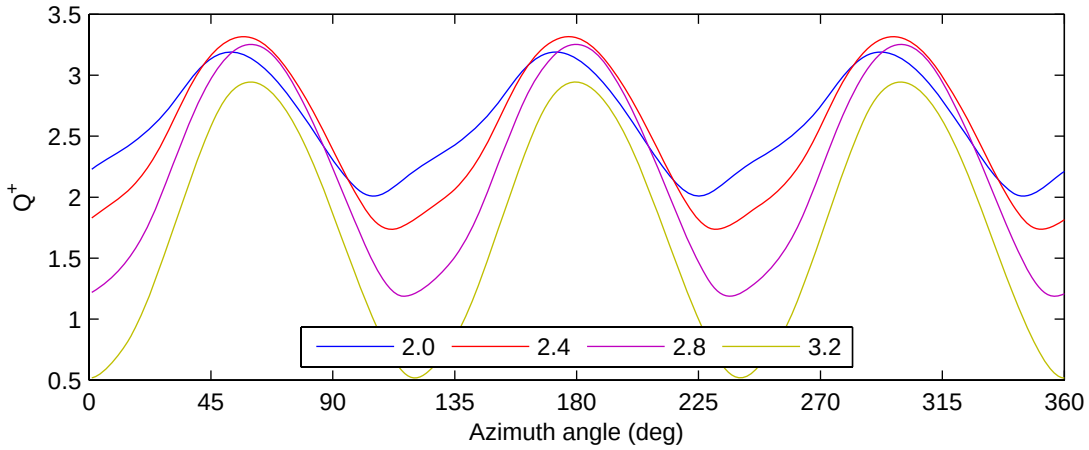

(b) Three blades, variable pitch.

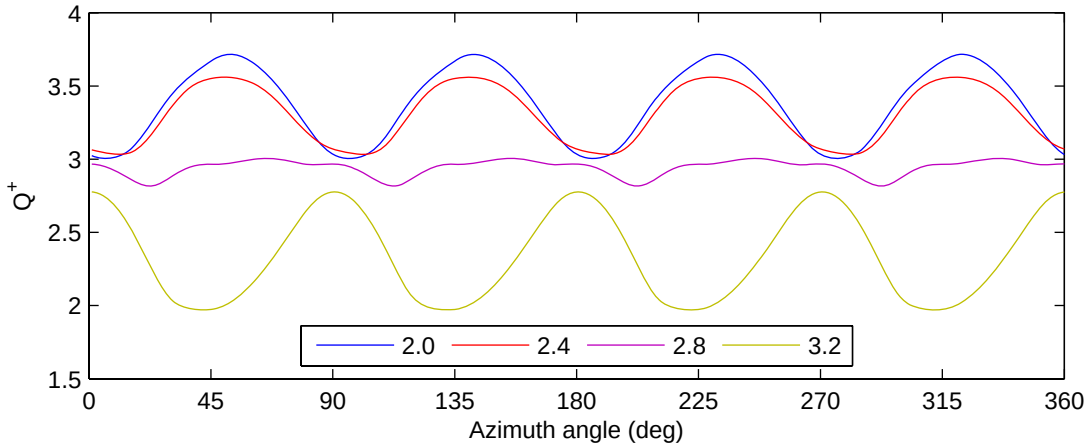

(c) Four blades, variable pitch.

Figure 4.13: *Non-dimensionalized shaft torque versus azimuth angle of blade A for various configurations as indicated by the sub-captions.*

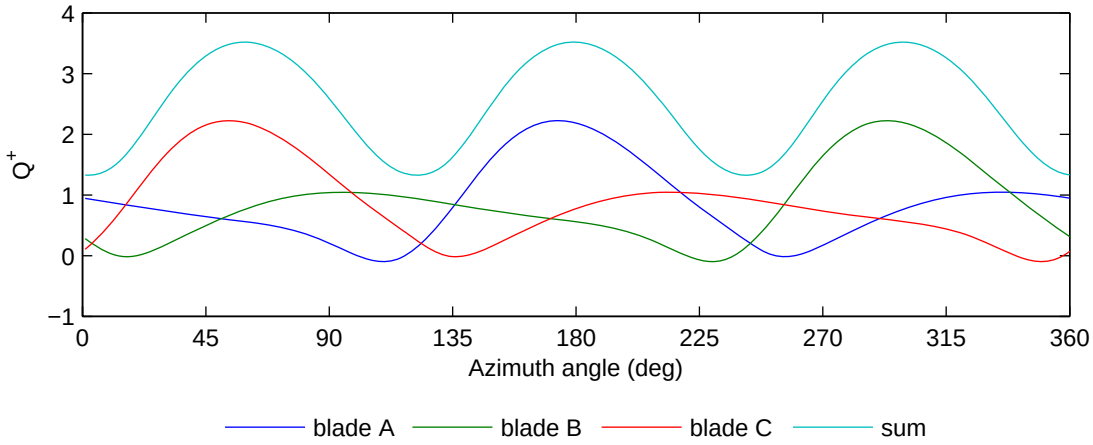

(a) Three blades, fixed pitch, $\lambda = 2.4$.

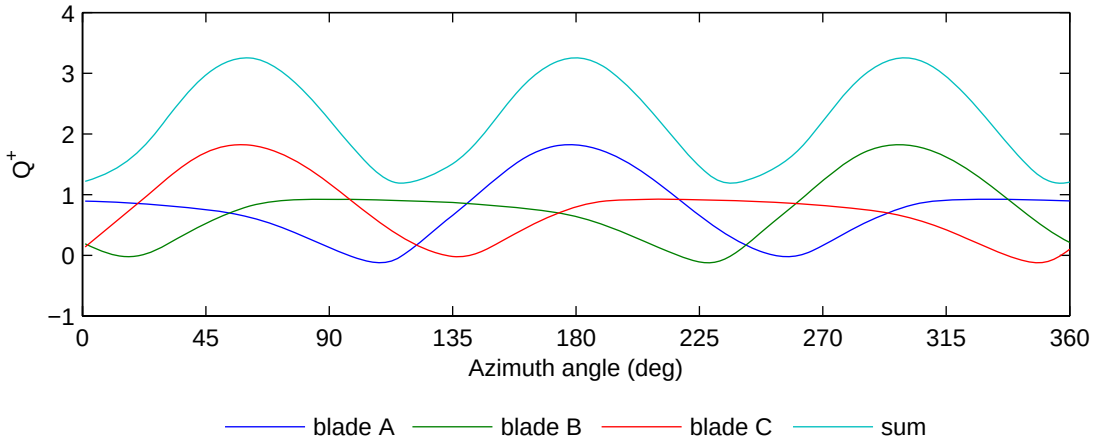

(b) Three blades, variable pitch, $\lambda = 2.8$.

Figure 4.14: *Non-dimensionalized shaft torque due to individual blades and the sum thereof for various configurations as indicted by the sub-captions.*

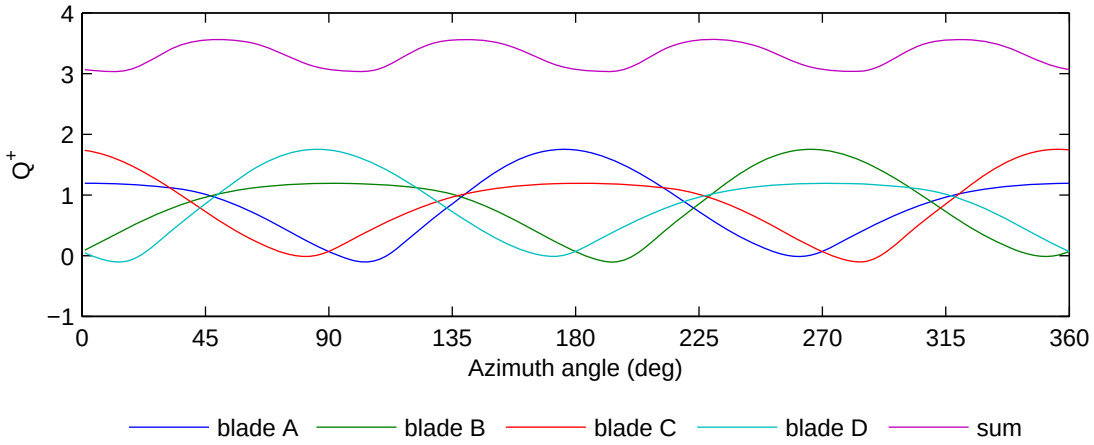

(a) Four blades, variable pitch, $\lambda = 2.4$.

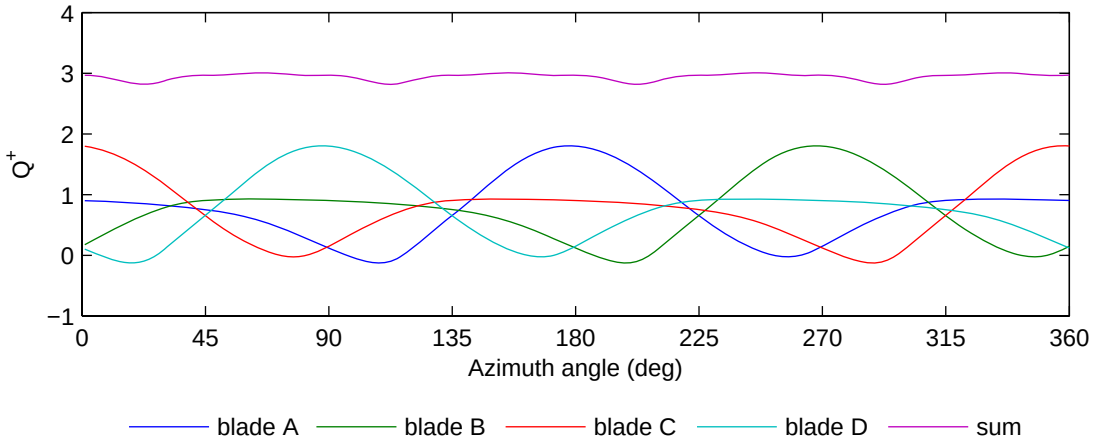

(b) Four blades, variable pitch, $\lambda = 2.8$.

Figure 4.15: *Non-dimensionalized shaft torque due to individual blades and the sum thereof for various configurations as indicted by the sub-captions.*

4.4.2 Variable pitch based on the true velocity field

The variable pitch results of the previous section were based on an assumed velocity field – as must be used when the velocity field is not known. In the case of the blade element model the velocity field is however known. As such we present results here for variable pitch operation based on the true velocity field, for the case of the three blade turbine.

Considering the results for the power coefficient, figure 4.16, we may judge the variable pitch strategy based on an assumed velocity field to be preferable. Whilst there is a slight increase in the maximum power coefficient for variable pitch operation based on the true velocity field ($C_{P_{\max}} = 0.5008$ at $\lambda = 2.64$ versus $C_{P_{\max}} = 0.4998$ at $\lambda = 2.7$), the most significant trend is that the C_P curve becomes less broadly peaked. As discussed, this is likely to lead to lower energy capture in practical operation given the uncertainty about the tip speed ratio.

The angle of attack and pitch angle versus azimuth angle are shown in figure 4.17 for the two variable pitch algorithms. For the assumed velocity strategy there is a more significant limiting of the angle of attack during the downstream pass, and a wider period of limiting during the upstream pass. It is though that the former is primarily due to an incorrect assumption about the flow velocity at the downstream half of the cylinder (see figure 4.8), while the latter is primarily due to the assumed velocity field not taking into account streamtube expansion, as the assumed velocity at the upstream half of the cylinder is quite accurate (again, see figure 4.8). Such trends become more significant as the tip speed ratio increases.

Whilst the two variable pitch algorithms for which results are presented here both use limiting angles of attack of 8 degrees upstream and 10 degrees downstream, the angle of attack is in effect limited to lower values in the case of the assumed velocity strategy due to the values of the velocity ratio used. Given the way in which this shifts the peak of the C_P-λ curve to a higher tip speed ratio, it is suggested that it may be possible to produce an almost flat peak in the C_P-λ curve by decreasing the limiting angle of attack as the tip speed ratio is increased. As the selection and tuning of variable pitch strategies is not the focus of this thesis, further calculations were not run.

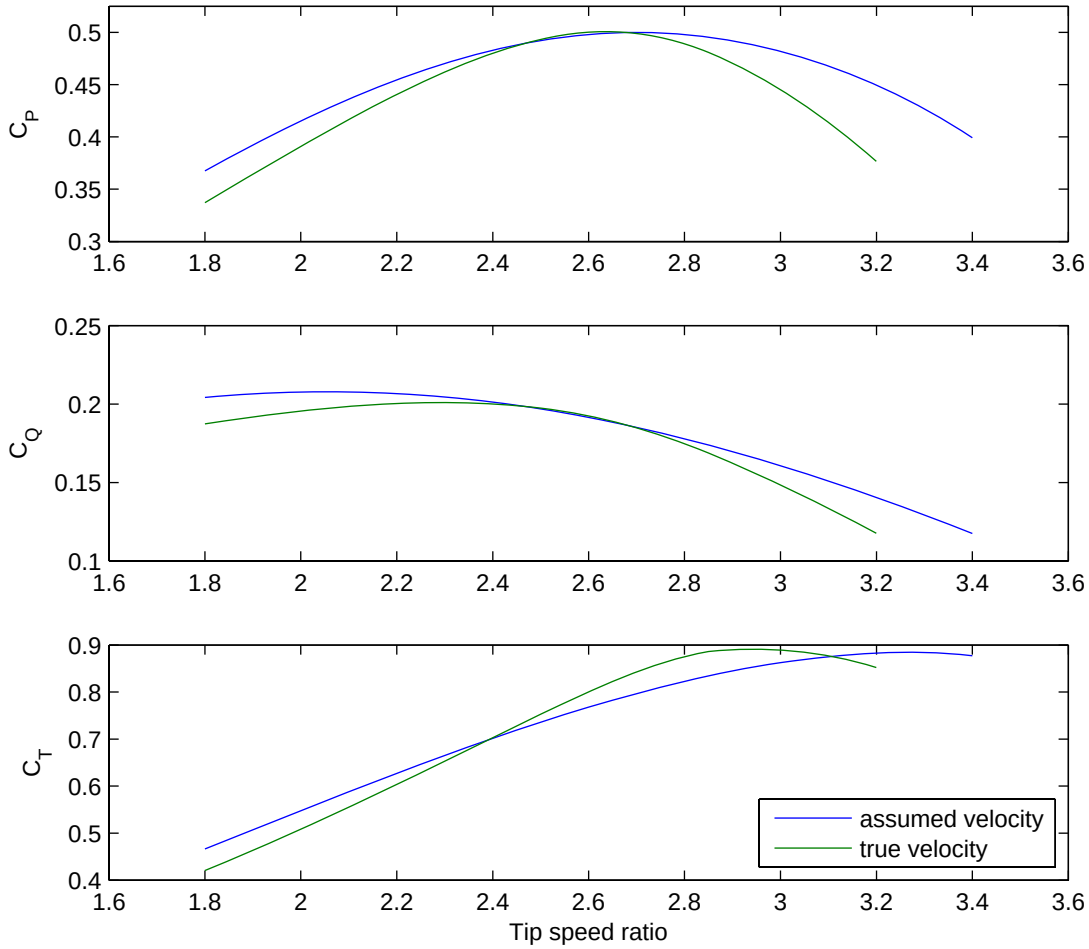

Figure 4.16: *Coefficients of power, torque and thrust versus tip speed ratio for the case of variable pitch based on an assumed velocity field and variable pitch based on the true velocity field.*

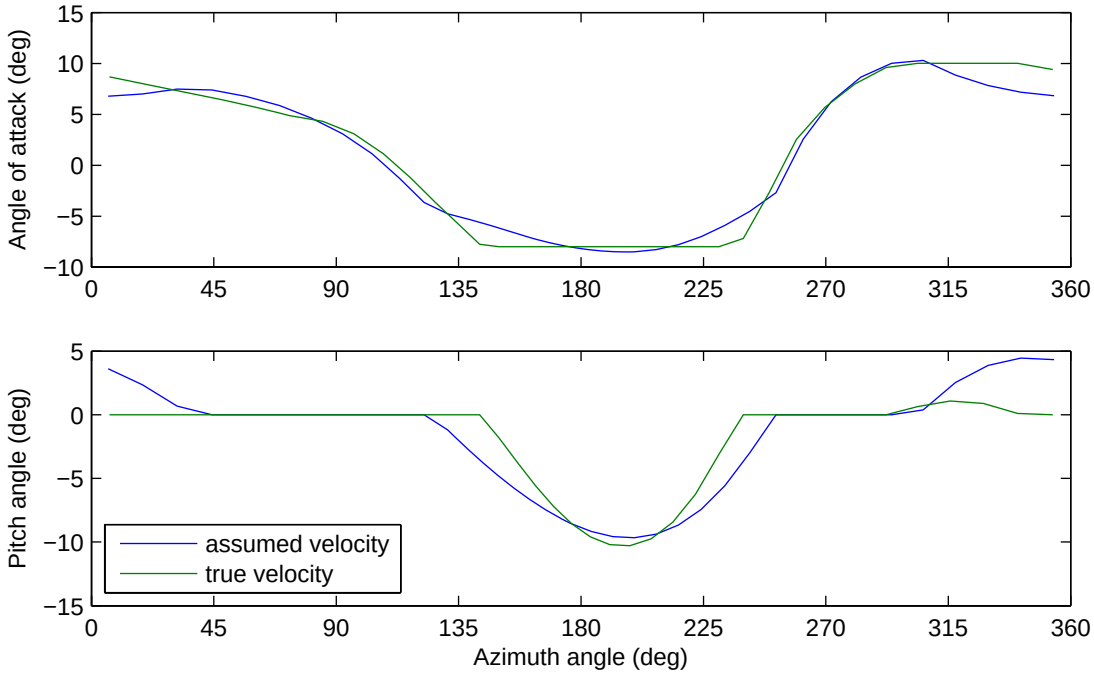

Figure 4.17: *Angle of attack and blade pitch angle versus azimuth angle at a tip speed ratio of 2.8 for the case of variable pitch based on an assumed velocity field and variable pitch based on the true velocity field.*

4.5 Chapter conclusions

A description of a blade element momentum model for a vertical axis turbine has been presented in this chapter. This model is able to capture many of the flow features associated with vertical axis turbines – primarily the fact that the downstream pass of the blades is through fluid which is in the wake of the upstream pass of the blades, and the fact that the axial induction factor varies with azimuth angle – and offers calculation times of less than one second for a single operating point (as programmed in Matlab and run on a contemporary laptop computer having a dual-core 1.2 GHz processor). The results of this model are known to be acceptably accurate within certain boundaries (Sharpe, 1990; Paraschivoiu, 2002), namely for operating points where the effects of dynamic stall are limited and where the induction factor is low. Results presented here, using the airfoil section data of Sheldahl and Klimas (1981), have been used to outline the basic hydrodynamic behaviour of vertical axis turbines, and will be compared with the results from CFD simulations in a later chapter.

Chapter 5

The CFD analysis of airfoils

5.1 Introduction

The study of isolated airfoils forms a significant proportion of the work in this PhD thesis and it is the author's contention that this is a necessary step in the modelling of a turbine geometry such as a vertical-axis turbine.

This study looks at airfoils operating under steady state conditions (i.e. fixed pitch and fixed inlet conditions) and also the case of a sinusoidally oscillating airfoil. The flow-field about the latter will be similar to that about a vertical axis turbine blade. Such studies are made because the verification of a complete vertical axis turbine simulation would be problematic, and because there is no data set suitable for model validation.

Whilst primarily being a verification and validation exercise, the steady state airfoil section data generated can be used in the blade element model, thus allowing us to neatly compare the two turbine models. It is believed that any differences then resulting between the two models will be due to assumptions made in the blade element model about the behaviour of the *turbine* as opposed to the behaviour of the *blades*. Two exceptions to this are the effects of dynamic stall and flow curvature, the significance of which will be estimated.

The *airfoil* simulations presented in this chapter are directly applicable to vertical axis *tidal current* turbines because we are concerned with low Mach number cases for which air can be accurately modelled as an incompressible fluid. Thus, for the same Reynolds number an airfoil simulation performed with air at constant density should give *exactly* the same predictions for the lift, drag and moment coefficients as a simulation of an hydrofoil in water (also modelled as constant density). The small number of compressible computations presented in this chapter (section 5.2.9 only) are relevant to the validation, and demonstrate the validity of the assumption of incompressibility.

5.2 The NACA 4412 airfoil

The NACA 4412 section was selected as the starting point for the present verification and validation study on airfoils primarily because it has been the subject of previous numerical studies at relevant values of the angle of attack, Reynolds number and Mach number. In particular, it was studied as part of the ECARP project (Haase et al., 1997), discussed in section 2.2.3.2, from which the numerical grid was available (from a CD provided with the book). This provided an excellent starting point for the design of the numerical grid used in the work presented in this chapter.

Validation data used in the ECARP study came from the wind tunnel experiment of Hastings and Williams (1987). The physical conditions of this experiment were an angle of attack of 12.15°, a Reynolds number of 4.17×10^6 and a Mach number of 0.18. This angle of attack is just below the point of maximum lift. In the ECARP study the angle of attack was corrected for wind tunnel effects to 12.49° and the airfoil was de-cambered by 0.28%. The corrected conditions were used in the present study.

No specific details are given for the characteristics of the turbulence in the wind tunnel used for the Hastings and Williams experiment; instead it is stated that the flow quality is "excellent". As a reference point Abbott and von Doenhoff (1959, p. 125) state that the turbulence level in the two-dimensional low-turbulence pressure tunnel is "very low, of the order of a few hundredths of 1%". It is assumed here that excellent means something similar to very low.

In the experiment, transition of the boundary layer is fixed using transition bands consisting of 0.28 mm ballotini (glass beads) attached by a thin layer of adhesive. On the upper surface, the transition band extends 30 mm along the airfoil contour from the leading edge (to $0.014c$ along the chord line), while on the lower surface the band extends from $0.10c$ to $0.11c$.

This is a challenging test case for numerical analysis because of the number of flow features that are shown in the experimental data. Near the leading edge there is a laminar separation bubble which is followed by turbulent reattachment. At the trailing edge there is a second area of recirculation.

Based on the results of Zingg (1991), it is believed that the errors calculated for this test case will serve as an upper bound on the errors that would be found in simulations at lower angles of attack.

Experimental values for the lift and drag coefficients are given as 1.439 and 0.034 in the ECARP study. Hastings and Williams however give a value of 1.46 for the lift coefficient but do not quote a value for the drag coefficient; instead, values are given for the momentum thickness at six wake locations. Using values for θ, U_e and H at the final wake location ($x/c = 1.35$) and employing the Squire-Young formula (Eppler, 2003) to evaluate the momentum thickness of the wake at downstream infinity:

$$\theta_\infty = \theta\left(\frac{U_e}{U_\infty}\right)^{\frac{H+5}{2}}$$

gives $c_d = 2\theta_\infty = 0.0345$. It thus seems likely that the ECARP study also used the Squire-Young formula to evaluate the drag. The reason for the lift coefficient given by the ECARP study being different from that reported in the Hastings and Williams paper is unknown.

5.2.1 Specification of the geometry

As already noted, it was possible to obtain the numerical grid used in the ECARP study and thus the geometry of the airfoil section. As is common in numerical studies of airfoils, the precise geometry of the NACA 4412 section was altered to create a sharp trailing edge suitable for meshing with a C-grid. This was achieved by altering the shape of the lower surface of the airfoil between the point of maximum thickness and the trailing edge. The modification allowed for a 'smooth geometry distribution – with respect to the second derivative' (Abbas and Cabello, 1997). Exact details of the modification are not given. For the other 4-digit series NACA airfoils studied later in this chapter (0012, 0015 and 0024) similar modifications were made, except that both upper and lower surfaces were altered between the point of maximum thickness ($x/c = 0.3$) and the trailing edge. This modification used a $\sin^3$ function:

$$\Delta y_{\text{mod}} = \frac{\Delta y_{\text{t.e.}}}{2}\sin^3\left(\left(\frac{x/c - 0.3}{0.7}\right)\left(\frac{\pi}{2}\right)\right) \tag{5.1}$$

where Δy_{mod} is the magnitude by which y-coordinates were altered on the top and bottom surfaces and $\Delta y_{\text{t.e.}}$ is the thickness of the trailing edge.

Some basic calculations were performed using Xfoil (see section 2.2.3.1) to investigate the effect of a blunt versus sharp trailing edge on the zero-lift drag coefficient for the NACA 0012 airfoil at $\text{Re} = 2.88 \times 10^6$ (one of the validation cases later in this chapter). Using 140 panel

nodes, and specifying transition at $x/c = 0.01$, gives $c_{d_0} = 0.00922$ in the case of a blunt trailing edge, and $c_{d_0} = 0.00916$ in the case of a sharp trailing edge. Such small differences are not significant.

The nodal coordinates from the airfoil surface were read into the CAD program Rhinoceros and used to define a cubic interpolated curve (spline) through the points. This curve was then exported in the igs file format for import into the meshing program ICEM. Care was taken to ensure that the generated mesh respected the smooth geometry of the airfoil (based on the radius of curvature) at the end of these operations. Initially this was found not to be the case. It was subsequently discovered that the default behaviour of the ICEM program is to create a faceted geometry based on the splines imported from the igs file, onto which the generated mesh is projected. To obtain a smooth geometry it is necessary to instruct the meshing program to project the mesh onto the spline curves instead.

5.2.2 Generation of the grids

Whilst a C-grid is in essence a single block structure, it was found that it was not possible to do this in ICEM for the reason that at least three blocks are required around bodies (in this case the airfoil). Further, it was found that it was necessary to use a multitude of blocks around the airfoil in order to ensure that the grid lines 'normal' to the wall were indeed geometrically normal to the wall, as recommended by the *CFX Reference Guide* and ERCOFTAC guidelines. The multi-block structure arrived at is shown in figure 5.2. Six blocks were used immediately around the airfoil, extending to $x/c = 0.1$. These are referred to as the 'boundary layer' blocks. Outside of these blocks, two blocks continue the wall normal grid lines to the far-field, while a further two blocks are used downstream of the airfoil.

The grid spacings along block edges were specified using either 'geometric' or 'bi-geometric' growth laws. Both laws require the number of nodes along the edge; in addition the former law requires the specification of the spacing at one end of the edge while the latter requires the specification of the spacing and the stretching ratios at both ends of the edge. The parameters used in the creation of the 'medium' grid are displayed in table 5.1, with some key parameters chosen in bold. In essence, the design of the grid is driven by the selection of the along the wall and wall normal spacings at the leading and trailing edge and the accompanying stretching ratios. The stretching ratios were selected to be generally 1.05 along the wall, and 1.2 in the wall normal direction.

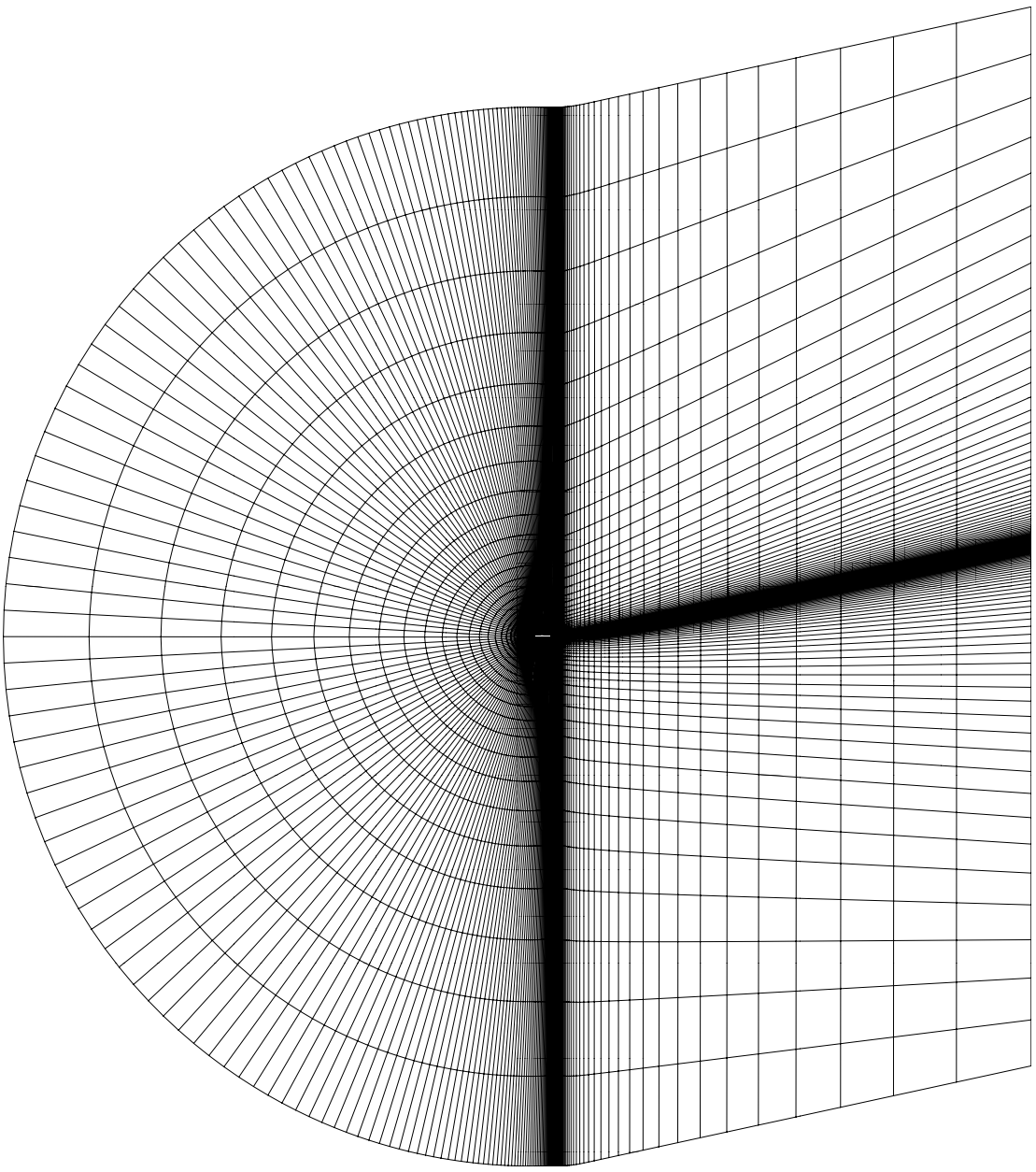

Figure 5.1: *View of the medium C-grid.*

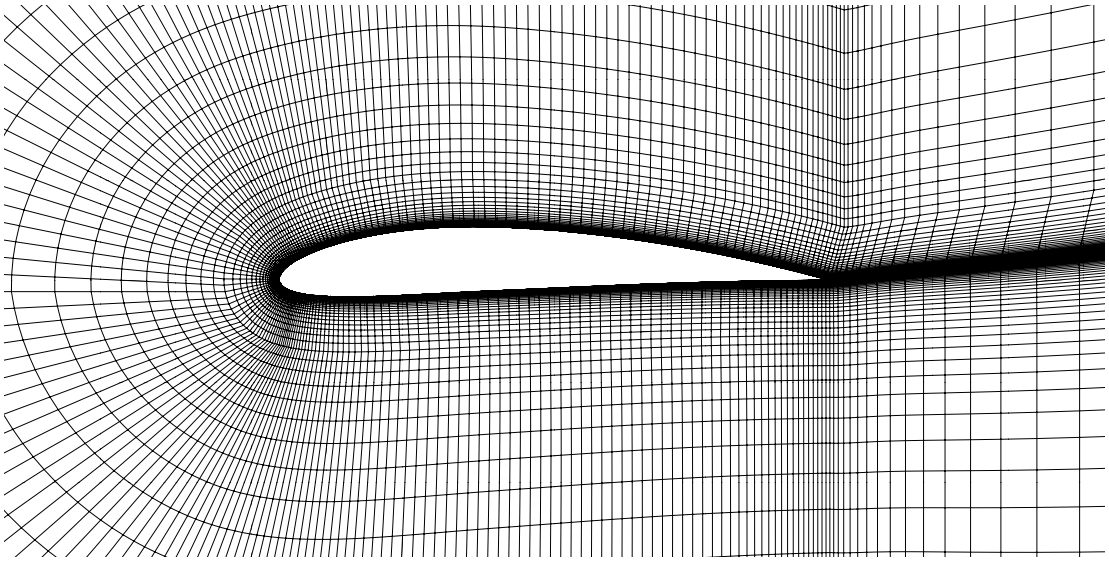

(a)

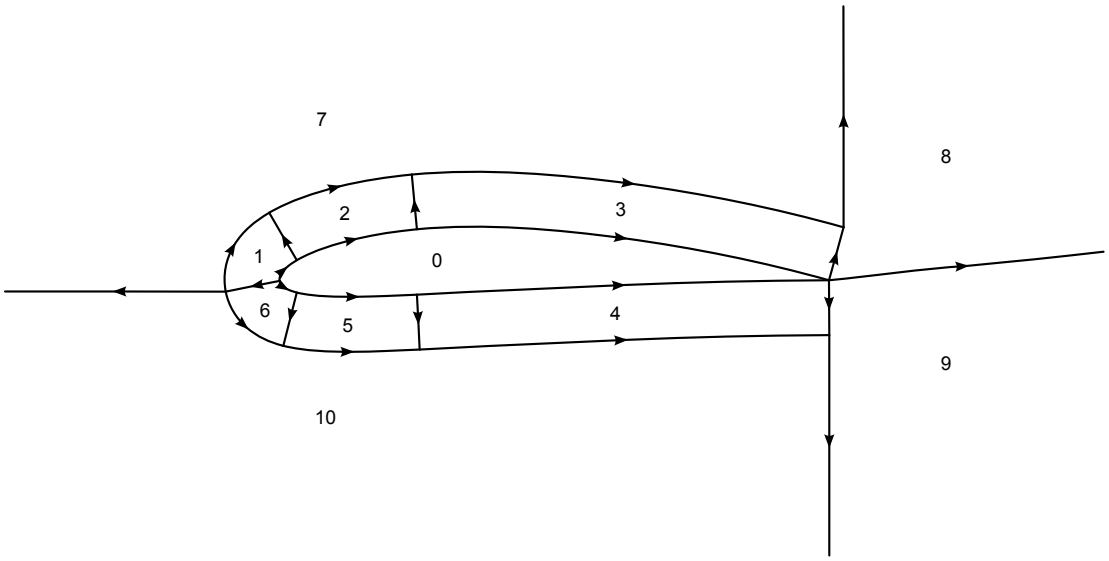

(b)

Figure 5.2: *View of the medium C-grid (a) and the block structure used to create the grid (b) in the vicinity of the airfoil.*

Table 5.1: *Block edge parameters used in constructing the medium C-grid. Edges are identified by the blocks that they separate – see figure 5.2. Element sizes were specified using either 'geometric' or 'bi-geometric' spacings. In the former case the growth ratio along the edge is constant and the ratio is displayed at the end of the edge for which the spacing was specified. Note that some edges are not included in the table; the edge parameters for these are to be inferred from those that are specified by assuming that the grid were symmetrical.*

Adjoining blocks (numbers and descriptions)			n	Δx_a	r_a	Δx_b	r_b
Wrap-around direction grid lines							
0	1	Fore-top b.l. – airfoil	23	**0.0014**	1.0464	0.00363	–
0	2	Mid-top b.l. – airfoil	29	0.0038	1.0515	0.0148	–
0	3	Aft-top b.l. – airfoil	49	0.0156	1.05	**0.007**	1.05
1	7	Fore-top b.l. – top outer	23	0.0119	–	0.005	1.04
2	7	Mid-top b.l. – top outer	29	0.005	1.0451	0.0164	–
3	7	Aft-top b.l. – top outer	49	0.0164	1.05	0.00726	1.05
7	FF	Top outer – far-field	99	1	0.992	0.00726	1.065
8	9	Top wake – bottom wake	37	0.007	1.188	2.89	–
8	FF	Top wake – far-field	37	0.007	1.188	2.89	–
0	6	Fore-bottom b.l. – airfoil	23	0.0014	1.0234	0.00227	–
0	5	Mid-bottom b.l. – airfoil	29	0.00232	1.0795	0.0183	–
0	4	Aft-bottom b.l. – airfoil	49	0.0186	0.996	0.007	1.05
6	10	Fore-bottom b.l. – bottom outer	23	0.012	–	0.0035	1.06
5	10	Mid-bottom b.l. – bottom outer	29	0.0035	1.062	0.0179	–
4	10	Aft-bottom b.l. – bottom outer	49	0.0179	1.024	0.00706	1.05
Wall normal grid lines							
1	6	Fore-top b.l. – fore-bottom b.l.	53	$\mathbf{2 \times 10^{-6}}$	1.193	0.0162	–
1	2	Fore-top b.l. – mid-top b.l.	53	2×10^{-6}	1.193	0.0162	–
2	3	Mid-top b.l. – aft-top b.l.	53	4×10^{-6}	1.175	0.0149	–
3	8	Aft-top b.l. – wake	53	$\mathbf{1 \times 10^{-5}}$	1.151	0.0131	–
7	10	Top outer – bottom outer	31	0.0193	1.193	3.24	–
7	8	Top outer – wake	31	0.0151	1.205	3.4	–
8	FF	Wake – far-field	83	0.001	1.0967	1.76	–

5.2.3 Boundary conditions and fluid models

For the grid convergence and boundary error studies, boundary conditions were applied as follows: on the inlet the velocity was specified as 64.4 m/s with turbulent intensity of 0.3% and an eddy viscosity ratio of 10; on the outlet the average static pressure was specified as 0 Pa, relative to the reference pressure of 1 atm; no-slip walls were specified for the airfoil surface; and a symmetry boundary condition was specified on the 'front' and 'back' faces. The inlet turbulence parameters were chosen to give a turbulent intensity of 0.1% near the leading edge of the airfoil, based on a distance of 20 chord lengths from the inlet to the leading edge of the airfoil. Clearly the intensity immediately ahead of the airfoil will therefore vary in the boundary error study. Thus, following the grid convergence and boundary error studies, an investigation was made into the effect of the inlet turbulence levels, the results of which influenced subsequent investigations; see section 5.2.6.

The fluid was specified as air with constant density in all studies other than that into the effect of compressibility (section 5.2.9). Values specified for the density and viscosity were $\rho = 1.185\ \mathrm{kg/m^3}$ and $\mu = 1.831 \times 10^{-5}\ \mathrm{kg/(m \cdot s)}$. (These are the default values in CFX for air at 25 °C.)

5.2.4 Grid convergence study

The strict verification methodology proposed by Roache (1994, 1998) and endorsed by e.g. NPARC (2008) is adopted for the study of the spatial discretization error, commonly referred to as a grid convergence study. A series of five grids were used in the study, each having a linear refinement ratio of $\sqrt{2}$ from the next. As the grids are two-dimensional this means that each refinement doubles the number of nodes.

Three grids of constant refinement ratio are required to calculate the observed order of convergence, p, necessary for the Richardson extrapolation or for the calculation of the grid convergence indices. Thus with five grids – termed extra-coarse, coarse, medium, fine and extra-fine – it is possible to perform four studies, incorporating the results from:

- Medium, coarse and extra-coarse grids,
- Fine, medium and coarse grids,

Table 5.2: *Lift, drag and moment coefficients from the five grids. The 'RE ef-f' results were obtained by Richardson extrapolation from the extra-fine and fine grid solutions. The percentage changes are from these extrapolated results.*

Grid	c_l	c_d	c_m	% c_l	% c_d	% c_m
Extra-coarse	1.5332	0.02826	−0.06215	−4.82	21.42	−12.13
Coarse	1.5756	0.02530	−0.06652	−2.19	8.71	−5.96
Medium	1.5933	0.02404	−0.06839	−1.10	3.30	−3.32
Fine	1.6034	0.02361	−0.06969	−0.47	1.43	−1.47
Extra-fine	1.6077	0.02342	−0.07027	−0.20	0.62	−0.65
RE ef-f	1.6110	0.02327	−0.07073	–	–	–

- Extra-fine, fine and coarse grids, and
- Extra-fine, medium and extra-coarse grids (with grid refinement ratio of 2).

The drag, lift and moment coefficients predicted from the five grids are shown in table 5.2 and figure 5.3 along with the Richardson extrapolation from the extra-fine and fine grids (which uses p (ef-f-m) – see table 5.4). This Richardson extrapolation is considered to give the best estimate of the continuum value of the coefficients. It might be argued that a Richardson extrapolation based on the extra-fine and medium grids would give a better estimate of the continuum value given the larger refinement ratio r, but Roache (1998, p. 124) has shown this not to be the case.

Also shown in table 5.2 are the percentage errors for the results from the five grids from the given Richardson extrapolation. It can also be seen that the errors in the drag coefficients are consistently around three times higher than the error for the lift coefficient on the same grid. Such a trend is not unusual; the results of Zingg (1991) for a NACA 0012 airfoil at $\mathrm{Re} = 2.88 \times 10^6$, $\mathrm{Ma} = 0.16$, $\alpha = 12^\circ$ show errors in the drag coefficient an order of magnitude higher than the errors in the lift coefficient for the each of the five grids used. The errors are relative to a Richardson extrapolation.

Table 5.3 shows the grid convergence indices derived from the four studies. Also shown is the ratio $\mathrm{GCI}_{23}/r^p\mathrm{GCI}_{12}$; a value close to one indicates that the solutions are in the asymptotic range. The subscripts 1, 2 and 3 refer to the three grids used in each study, where 1 is the finest. We obtain three grid convergence indices for each of the coefficients for the medium grid from the complete study. These values are printed in bold in the table and can be compared with the errors from the Richardson extrapolation value for the medium grid shown in table 5.2. The

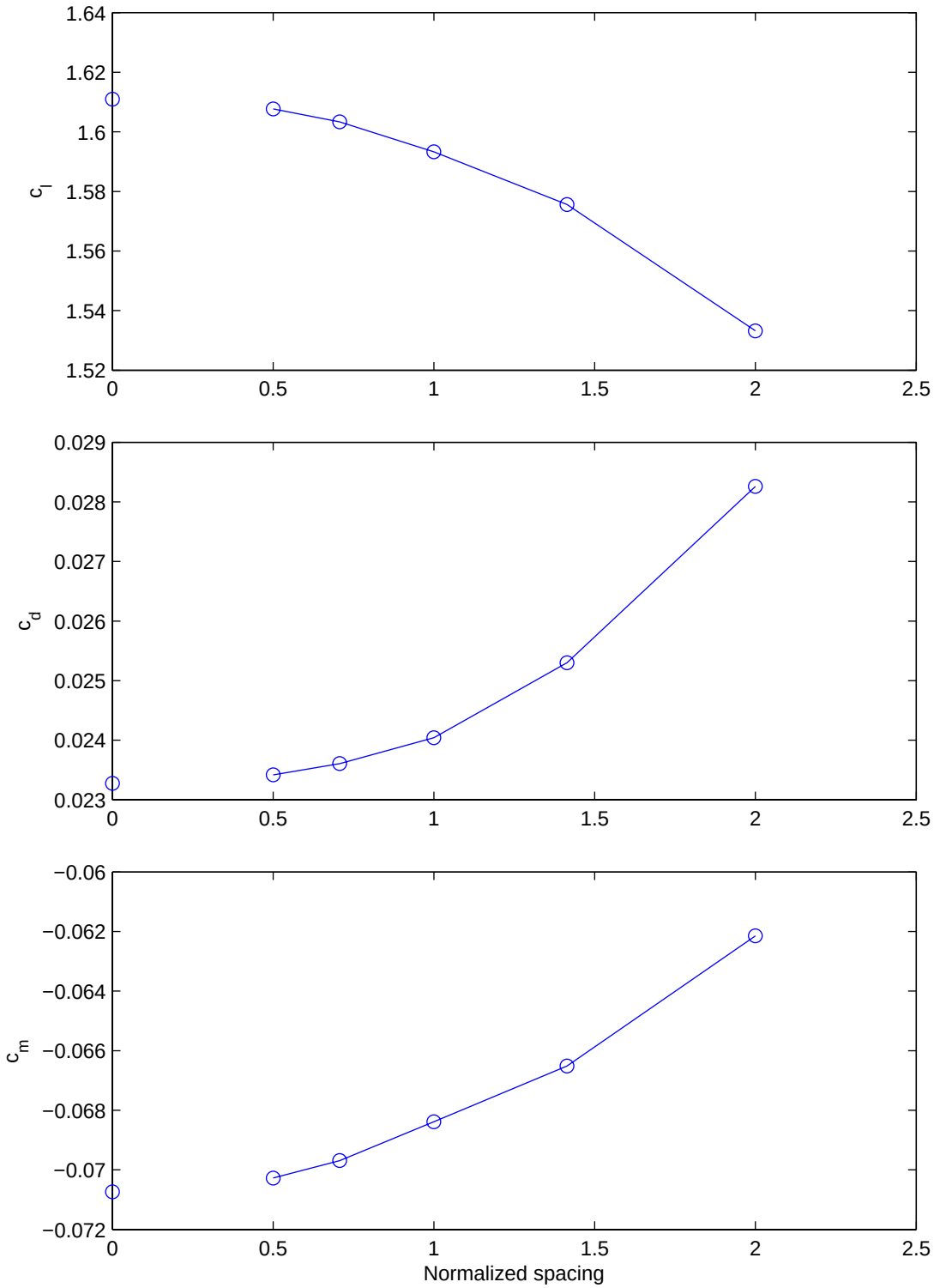

Figure 5.3: *Convergence of lift, drag and moment coefficients with decreasing grid spacing.*

Table 5.3: *Grid convergence indices for the lift, drag and moment coefficients. Also shown are the ratios* $\mathrm{GCI}_{23}/r^p\mathrm{GCI}_{12}$.

		c_l	c_d	c_m			
GCI c-ec	p (m-c-ec)	2.41	10.81	6.13			
GCI m-c		**0.99**	**4.83**	**2.55**	1.011	0.950	1.028
GCI m-c	p (f-m-c)	**1.84**	**3.46**	**8.00**			
GCI f-m		1.04	1.22	5.50	1.006	0.982	1.019
GCI f-m	p (ef-f-m)	0.59	1.76	1.86			
GCI ef-f		0.25	0.77	0.82	1.003	0.992	1.008
GCI m-ec	p (ef-m-ec)	**1.49**	**3.81**	**4.95**			
GCI ef-m		0.35	0.58	1.46	1.009	0.974	1.028

Table 5.4: *Observed order of convergence for lift, drag and moment coefficients.*

	c_l	c_d	c_m
p (m-c-ec)	2.52	2.47	2.45
p (f-m-c)	1.62	3.06	1.03
p (ef-f-m)	2.44	2.41	2.35
p (ef-m-ec)	2.06	2.76	1.72
$\bar{p}$	2.67	2.16	1.89

grid convergence index is intended to provide a conservative estimate of the error, and so we would hope to see that the GCIs are greater than the errors from the Richardson extrapolation values. We see this to be the case for all of the drag GCIs, but not for the lift and moment GCIs computed from the medium and coarse grids with p (m-c-ec).

The observed order of convergence values p for each of the coefficients and each of the grids are shown in table 5.4; a mean value for each coefficient is also presented. Clearly these is some variability in the observed order of convergence. Interestingly there also appears to be a correlation between higher than average observed order of convergence for the drag coefficients and lower than average observed order of convergence for the lift and moment coefficients. Such variation in the observed order of convergence for different quantities is seen in a paper by Richmond-Bryant (2003), which presents a verification study of the flow about a circular cylinder at Re = 5232. Whilst the solution is calculated to be globally convergent it is shown that it is not locally convergent for all degrees of freedom at 19% of the sampling points.

The reason behind the observed order of convergence varying is unknown, but two possible explanations are offered. First, there may be a 'switch' that is activated in the code when Δy_1^+

is below a certain threshold which would cause the modelling to change. Thus the model used on the extra-fine, fine and medium grids may be different from that used on the coarse and extra-coarse grids. In such a case the only truly valid p value would be that calculated from the extra-fine, fine and medium grids. Alternatively, it may be that there is a certain flow feature that is not resolved by the coarse and extra-coarse grids. The effect would be the same as that of a change in the modelling.

Based upon the criteria of the maximum spatial discretization error for either the drag or the lift coefficient being less than 5%, the evidence from the Richardson extrapolation error comparison and the calculation of the grid convergence indices would strongly suggest the use of the medium grid. We are less concerned with the prediction of the moment coefficient as the moment on a blade does not significantly influence the power generated by a vertical axis turbine.

5.2.5 Distance to far-field boundary study

An estimate of the error introduced by the position and specification of the far-field boundary can also be calculated from a Richardson extrapolation. This has been shown by Roache (1998, section 6.10) in his analysis of the results of Zingg (1992). Roache found the error to be ordered by approximately $1/L_b$, where L_b is the distance to the far-field boundary i.e. $r = L_{b_1}/L_{b_2}$ and $p = 1$. See section 3.6.4 of the present work.

In the present study, four different grids were used having L_b/c equal to 10, 20, 40 and 80. All grids used the same spatial discretization and thus the grids with $L_b/c = 40$, 20 and 10 can be thought of as being progressively cropped from the grid with $L_b/c = 80$. The spatial discretization is that of the medium grid of the previous section.

Values for the observed order of convergence p for each of the coefficients were calculated from the three smallest grids ($L_b/c = 10$, 20 and 40) and the three largest grids ($L_b/c = 20$, 40 and 80) and are shown in table 5.6. A Richardson extrapolation of each of the coefficient results from the two largest grids was then calculated with the p values calculated from the three largest grids. These are shown in table 5.5 along with the percentage errors from the extrapolated values.

The patterns shown in the present results are broadly similar to those of Zingg's results as shown by Roache (see table 3.1). Most obviously, for a grid with a similar distance to the

Table 5.5: *Lift, drag and moment coefficients from the four grids having different distance to far-field boundary. The 'RE 40-80' results were obtained by Richardson extrapolation from the grids having 40 and 80 chord lengths distance to their respective boundaries. The percentage changes are from these extrapolated results.*

Grid (L_b/c)	c_l	c_d	c_m	% c_l	% c_d	% c_m
10	1.5887	0.02638	−0.06090	−0.74	26.24	1.90
20	1.5933	0.02404	−0.06839	−0.46	15.06	1.13
40	1.5968	0.02261	−0.06817	−0.24	8.18	0.81
80	1.5986	0.02182	−0.06801	−0.12	4.44	0.58
RE 40-80	1.6006	0.02090	−0.06762	–	–	–

Table 5.6: *Observed order of convergence for drag, lift and moment coefficients (distance to boundary study).*

	c_l	c_d	c_m
p (10-20-40)	0.41	0.70	1.26
p (20-40-80)	0.94	0.88	0.48
$\bar{p}$	0.67	0.79	0.87

far-field boundary, the errors from the extrapolated values are significantly higher in the present work. For example, for the results of Zingg, the errors in the lift and drag values on the grid with $L_b/c = 12$ are 0.24 and −3.92% respectively whereas in the present research, and on the grid with $L_b/c = 10$ the errors are −0.74 and 26.24% for lift and drag. This may readily be attributed to the different far-field boundary conditions employed: whereas Zingg uses characteristic boundary conditions with a circulation correction, the present work does not.

Despite the large differences in the magnitudes of the errors, the observed orders of convergence are comparable, but lower, to those of Zingg. The drag coefficient shows convergence with the most consistent observed order, perhaps because the errors are the largest. This consistency gives increased confidence in the drag value extrapolation.

As with the study of the spatial discretization, the criteria for selecting a grid is that the relative error from the Richardson extrapolation is less than 5% for the lift and drag coefficients. In this case the selection is clearly determined by the accuracy of the drag predictions and dictates the use of the grid with $L_b/c = 80$.

Table 5.7: *The effect of turbulence intensity on the aerodynamic coefficients.*

Tu_{inlet} (%)	μ_t/μ	Tu (%)	c_l	c_d	c_m	% c_l	% c_d	% c_m
0.3	10	0.05	1.5986	0.02182	−0.06801	–	–	–
0.3	40	0.10	1.5980	0.02186	−0.06794	−0.04	0.18	−0.11
3	120	0.20	1.5971	0.02193	−0.06785	−0.09	0.51	−0.24

5.2.6 Inlet turbulence levels

Given the uncertainty associated with specifying levels of inlet turbulence in a CFD simulation it is clearly necessary to conduct a sensitivity study – the object of the current section.

As noted in section 5.2.3, the simulations in the previous two sections used a turbulence intensity of 0.3% and an eddy viscosity ratio of 10 for turbulence parameters at the inlet boundary condition. For the mesh with far-field boundary at $80c$, used herein, this gives a turbulent intensity immediately ahead of the airfoil of 0.05% according to equation 3.79. Two alternative pairs of values were specified for the turbulent intensity and the eddy viscosity ratio: first, $Tu_{inlet} = 0.3\%$ and $\mu_t/\mu = 40$, which gives $Tu = 0.1\%$ immediately ahead of the airfoil, and second, $Tu_{inlet} = 3\%$ and $\mu_t/\mu = 120$, which gives $Tu = 0.2\%$ immediately ahead of the airfoil. It is believed that this range of turbulence intensity values is broadly representative of the range of conditions that would be experienced between different wind tunnels.

The effect of turbulence intensity on the aerodynamic coefficients is shown in table 5.7. Clearly the effect is much less significant than that of either the spatial discretization or the distance to the far-field boundary. It may be noted that the drag increases slightly as the turbulence intensity increases; this is the trend that we would expect to see.

Values for the turbulent intensity and the eddy viscosity ratio equal to 0.3% and 40 respectively were selected.

5.2.7 Geometrically modelled transition strip

As noted above, transition in the Hastings and Williams experiment was fixed using transition bands consisting of 0.28 mm ballotini. In explaining the initially poor comparison between numerical and experimental results, the conclusion of the ECARP study was that transition was 'over-fixed' i.e. too much turbulence was introduced by the boundary layer trip. As a result, the geometry of the airfoil in the numerical model of the ECARP study was modified to include the

Table 5.8: *The effect of including the geometry of the transition strip in the numerical model.*

Tr. strip	c_l	c_d	c_m	% c_l	% c_d	% c_m
no	1.5980	0.02186	−0.06794	–	–	–
yes	1.5880	0.02253	−0.06666	−0.63	3.02	−1.89

experimental transition strip. See table 2.6 in the literature review section for the results from the ECARP study.

The effect of the inclusion of the geometry of the transition strip was also examined in the present study, the results of which are shown in table 5.8. The effect on the drag is most significant, but considerably less so than that observed in the ECARP study. It is possible that this is due to the fact that the comparison shown in table 5.8 is based on results from the medium grid having 284×90 cells, whereas in the ECARP study this comparison was based on results from a grid having 512×128 cells. Thus a very fine grid is perhaps needed to well resolve the effect of such a transition strip.

For the present work, it was decided to continue the research using the grid without the geometrically modelled transition strip. This decision was based on the observation that most numerical studies of airfoil performance do not include transition strips in the mesh, and the observation that the effect is minimal.

5.2.8 Spalart-Allmaras turbulence model

An investigation was made into the use of the Spalart-Allmaras turbulence model, a beta feature of CFX-11. Initially, two simulations were run having $\tilde{\nu}/\nu = 0.01$ and 0.1 respectively. These were found to fail with a linear solution error after 23 and 29 iterations respectively.

One option in the model formulation in CFX is the ability to change the velocity gradient norm used in both the production and destruction terms. By default, the vorticity is used ($\sqrt{2\Omega_{ij}\Omega_{ij}}$), but the strain rate ($\sqrt{2S_{ij}S_{ij}}$), or a hybrid of the vorticity and the strain rate, may be used. Two simulations were successfully run with the strain rate option and having the inlet values of $\tilde{\nu}$ as used previously. In both cases the equation residuals failed to reduce as far as with the k-ω SST model; the largest equation residual was that in the U-momentum equation and having an RMS value of around 6×10^{-5}, achieved after 700–800 iterations (the simulations being run for a total of 2000 iterations).

Table 5.9: *The effect of the choice of turbulence model.*

Turbulence model	Inlet b.c.s	c_l	c_d	c_m
Spalart-Allmaras	$\tilde{\nu}/\nu = 0.01$	1.6543	0.02076	−0.07682
Spalart-Allmaras	$\tilde{\nu}/\nu = 0.1$	1.6543	0.02077	−0.07682
k-ω SST	$Tu = 0.3\%$, $\mu_t/\mu = 40$	1.5980	0.02186	−0.06794
Experiment		1.46	0.0345	–

The results from the two successful runs with the Spalart-Allmaras turbulence model are shown in table 5.9. Clearly the choice of inlet conditions for the Spalart-Allmaras model makes little difference. Relative to the results from the k-ω SST turbulence model, the results from the Spalart-Allmaras turbulence model show higher lift, lower drag and a more negative pitching moment. Interestingly, this is the same trend seen when refining the grid or increasing the distance to the far-field boundary (with the k-ω SST model). In comparison to the experimental results for the lift and drag, the results from the k-ω SST model are the best.

The above results show the k-ω SST turbulence model to be somewhat better than the Spalart-Allmaras model for this test case. Based on this, and the suggestion by Versteeg and Malalasekera (2007, p. 90) that the S-A model "lacks sensitivity to transport processes in rapidly changing flows" (as is the case with the flow through a vertical axis turbine), it was decided to continue with the use of the k-ω SST model.

5.2.9 Compressibility model

Low speed flows are often treated as incompressible, with a commonly accepted limit of Ma $\leq$ 0.3 (e.g. White, 1999, p. 221). It is ambiguous, however, as to whether the Mach number limit applies to the free stream speed, or to the maximum speed found anywhere in the flow field. Often these will not be greatly different, but for airfoils at angles of attack near maximum lift the low pressure suction peak can be significant. In the present work, the results show $c_{p_{\min}} \approx -6$ and thus:

$$\mathrm{Ma}_{\max}/\mathrm{Ma}_\infty = U_{\max}/U_\infty = \sqrt{1 - c_{p_{\min}}} = 2.6 \tag{5.2}$$

The experiment of Hastings and Williams (1987) was conducted at a free stream Mach number of 0.18, thus having a maximum Mach number of 0.47. Given that compressibility effects could be significant at this Mach number, simulations were run to investigate the three compressibility

Table 5.10: *The effect of the compressibility model on the lift, drag and moment.*

Compressibility	c_l	c_d	c_m	% c_l	% c_d	% c_m
Incompressible	1.5977	0.02206	−0.06811	–	–	–
Isothermal	1.5680	0.02264	−0.06349	−1.86	2.63	−6.78
Thermal energy	1.5664	0.02269	−0.06331	−1.96	2.86	−7.05
Total energy	1.5524	0.02262	−0.06331	−2.84	2.54	−7.05
Experiment	1.46	0.0345	–			

models available in CFX: isothermal, thermal energy and total energy (see section 3.1.3 for details of the thermal energy equation).

In the simulations, the fluid was specified as air using the ideal gas model and having a molar mass of 28.96 kg/kmol and a specific heat capacity at constant pressure of 1.0044×10^3 J/kg · K. Using the ideal gas laws $R = \bar{R}/M$ and $\gamma = c_p/c_v = c_p/(c_p - R)$ yields $R = 287$ J/kg · K and $\gamma = 1.4$. The inlet temperature was specified as 25 °C and therefore $\rho = p/(RT) = 1.185$ kg/m^3. The Reynolds number was 4.17×10^6 as before and so the Mach number is 0.186. (Note that this is slightly higher than the value of 0.18 quoted in Hastings and Williams, perhaps due to a different temperature being assumed.)

The results for the lift, drag and moment coefficients from the three compressible simulations are shown in figure 5.4 along with the results from an incompressible simulation having the same grid and boundary conditions. All three compressible simulations show oscillations in the aerodynamic coefficients, and it appears that the lift, drag and moment are phased such that maximum lift, minimum drag and maximum (smallest in magnitude) moment occur simultaneously. This may be the result of an underlying unsteadiness in the compressible flow solution, or, alternatively or additionally, the result of the far-field boundary conditions reflecting pressure oscillations in the solution. The oscillations are also seen in the residuals (figure 5.5), where the frequency appears to be double that of the force and moment coefficients.

Based on the assumption that the oscillations in the forces and moments have a period of 300 iterations, average values were calculated over the interval of 1701–2000. These are shown in table 5.10 along with the incompressible solution. In general, all of the compressible solutions are alike; the exception being the total energy solution for the lift. The most significant difference, in percentage terms relative to the incompressible solution, is for the moment coefficient. This difference (for the moment) is comparable to that seen between the coarse grid solution and the Richardson extrapolation (see table 5.2). Differences for the lift and drag

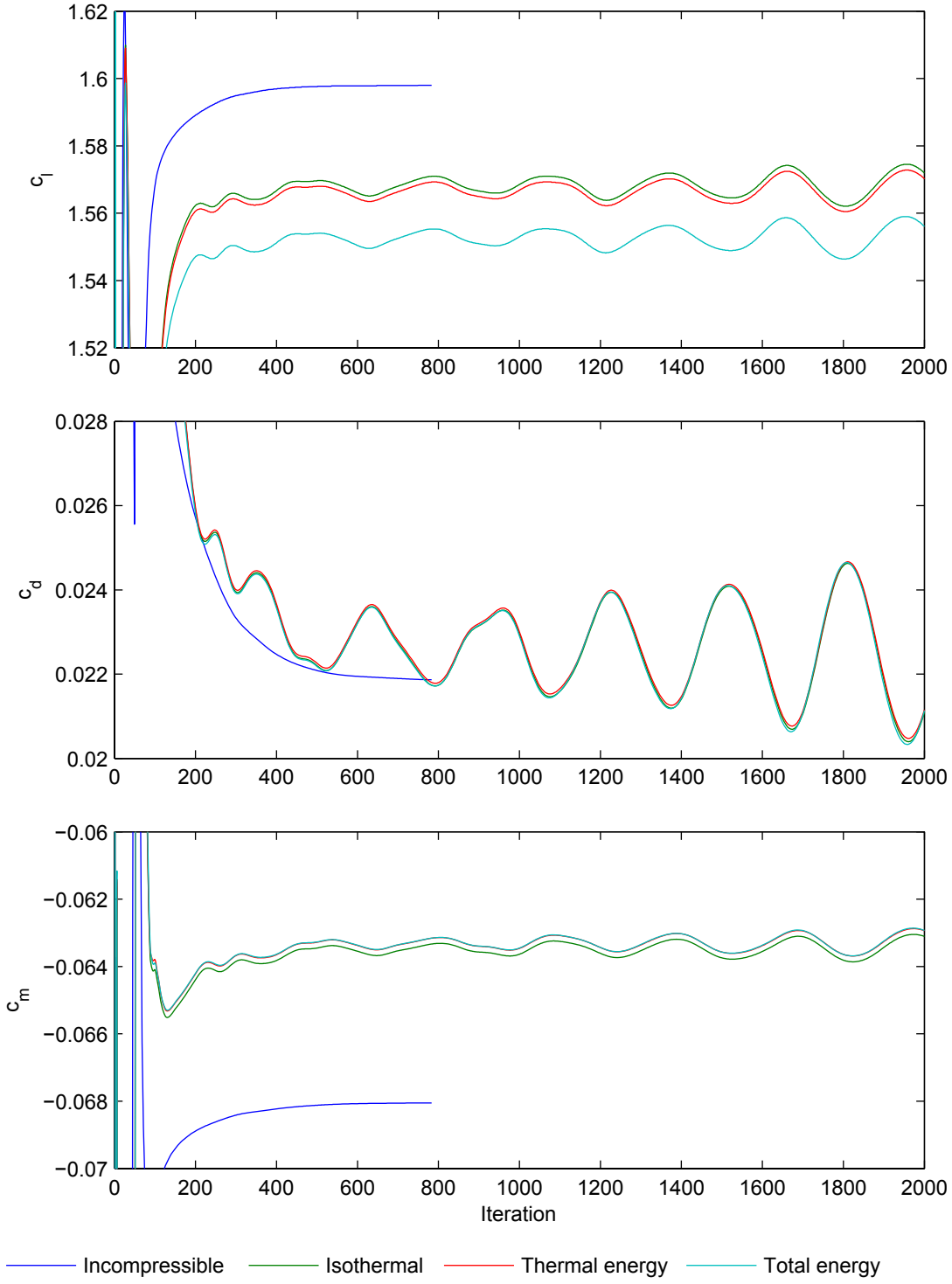

Figure 5.4: *The effect of four compressibility models on the aerodynamic coefficients.*

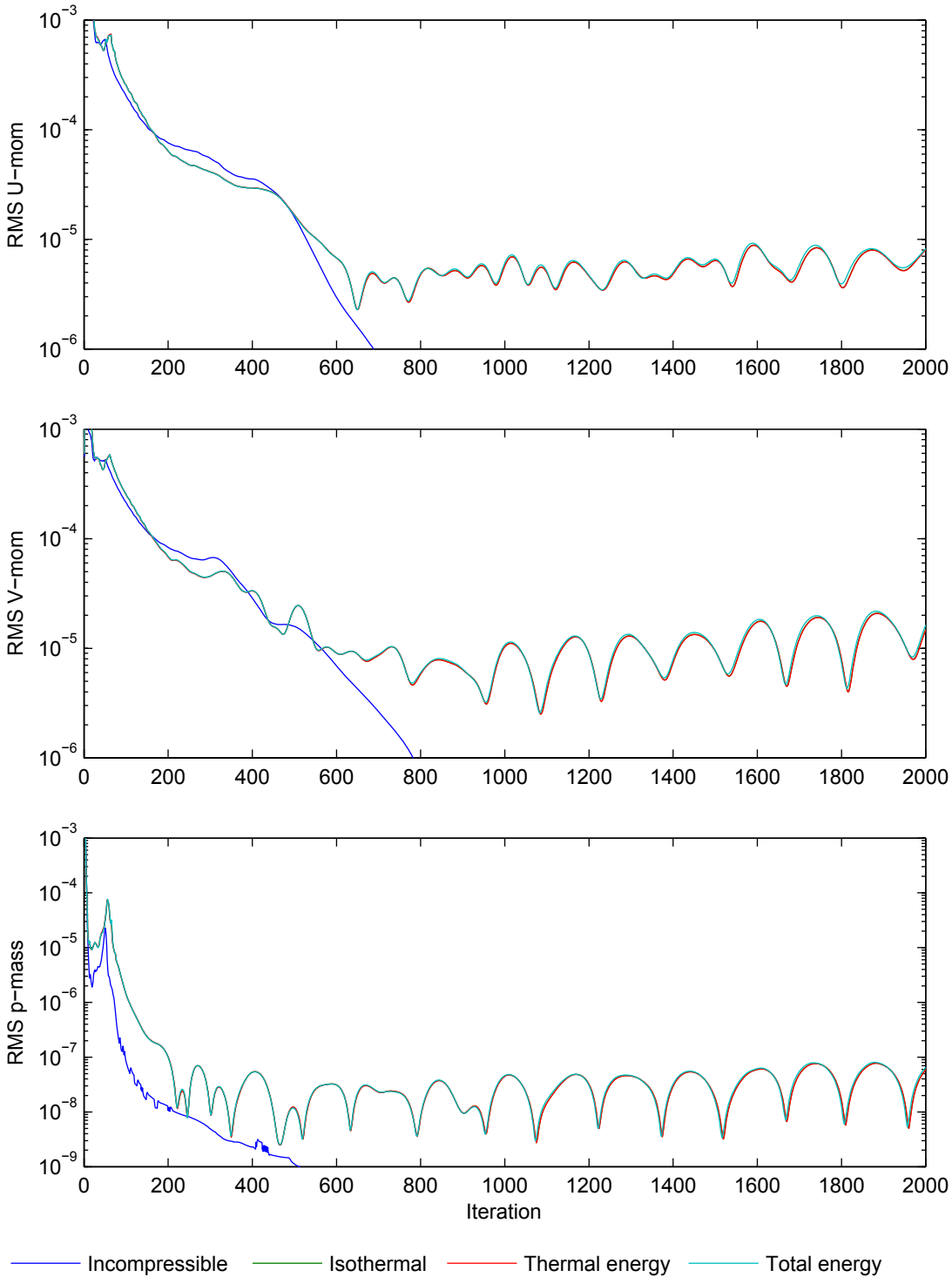

Figure 5.5: *The momentum and pressure equation residuals versus iteration number for the four compressibility models.*

are all less than 3%. In comparison to the experimental results it will be seen that as the model complexity increases (incompressible – isothermal – thermal energy – total energy) the agreement with experiment improves. The exception to this is with the total energy solution for the drag coefficient which is slightly 'worse' than the thermal energy solution. Drag values for the compressible solutions should be treated with some caution though, given the relatively large magnitude of the oscillations.

5.2.10 Specification of the grid in the wake

All of the grids discussed above used the results of a preliminary simulation to orientate the mesh in the wake behind the airfoil. Specifically, the grid line in the 'wrap-around' direction that forms the surface of the airfoil follows in the wake the dividing streamline from the preliminary simulation (we term this the dividing grid line). This ensures that the tightly spaced grid lines in the boundary layer on the airfoil surface continue downstream in the correct position to best capture the high velocity gradients in the wake. Such a grid is tailored to the flow field at a specific angle of attack and is therefore less suited to the simulation of oscillating airfoils considered later in this chapter, and indeed to the flow around turbine blades. The purpose of the present section is to investigate the design of a grid that is not tailored to a specific angle of attack.

Given that the angle of attack of a vertical axis turbine blade will oscillate about 0 degrees, it was believed that the dividing grid line should be orientated with the extension of the chord line in the wake. It was also believed that it would be beneficial to 'fan-out' the (wrap-around) grid lines in the wake. The latter was parameterized by specifying the grid spacing normal to the dividing grid line. This is labelled Δy_1 based on boundary layer notation.

In the reference tailored grid (medium resolution, far-field at $80c$) the spacing Δy_1 increases from 10 μm at the trailing edge of the airfoil to 4 mm at the far-field. New grids were generated with the dividing grid line orientated with the chord and having different values for the spacing Δy_1 at the far-field. Values of 4, 16, 64, 256 and 1024 mm were used.

For all of the new grids, the difference in the results for the force and moment coefficients from the reference grid was less than 1%. The only exception was the moment coefficient on the grid with $\Delta y_1 = 1024$ mm at the far-field where the difference was approximately 2%. From this we may conclude that the force and moment coefficient results are not especially sensitive to the

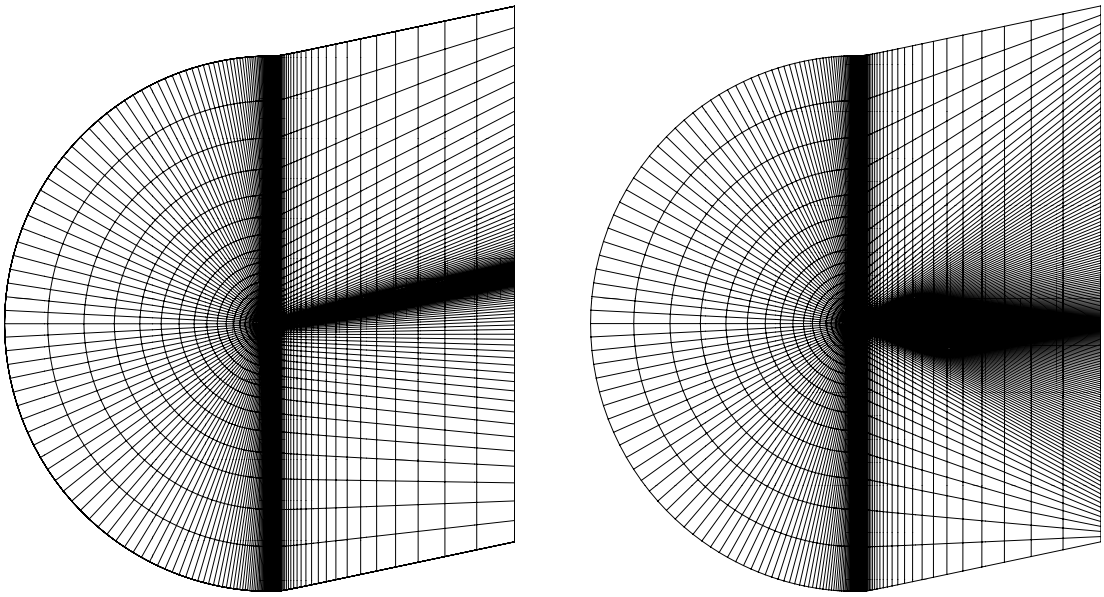

Figure 5.6: *Comparison of the reference tailored grid (a) and the grid with* $\Delta y_1 = 256$ mm *(b).*

grid spacing and orientation in the wake.

The equation residuals did however vary between grids and there are shown in figure 5.7. Only two solutions reached the target of reducing all RMS equation residuals below 1×10^{-6}; these were the solution on the reference grid, and the solution on the grid with $\Delta y_1 = 256$ mm at the far-field. Broadly, as the spacing Δy_1 at the far-field was increased or decreased from the value of 256 mm, the residuals increased. Based on this pattern of residual convergence it was concluded that the '256 mm' grid was the optimum and so this was adopted for investigations at different angles of attack.

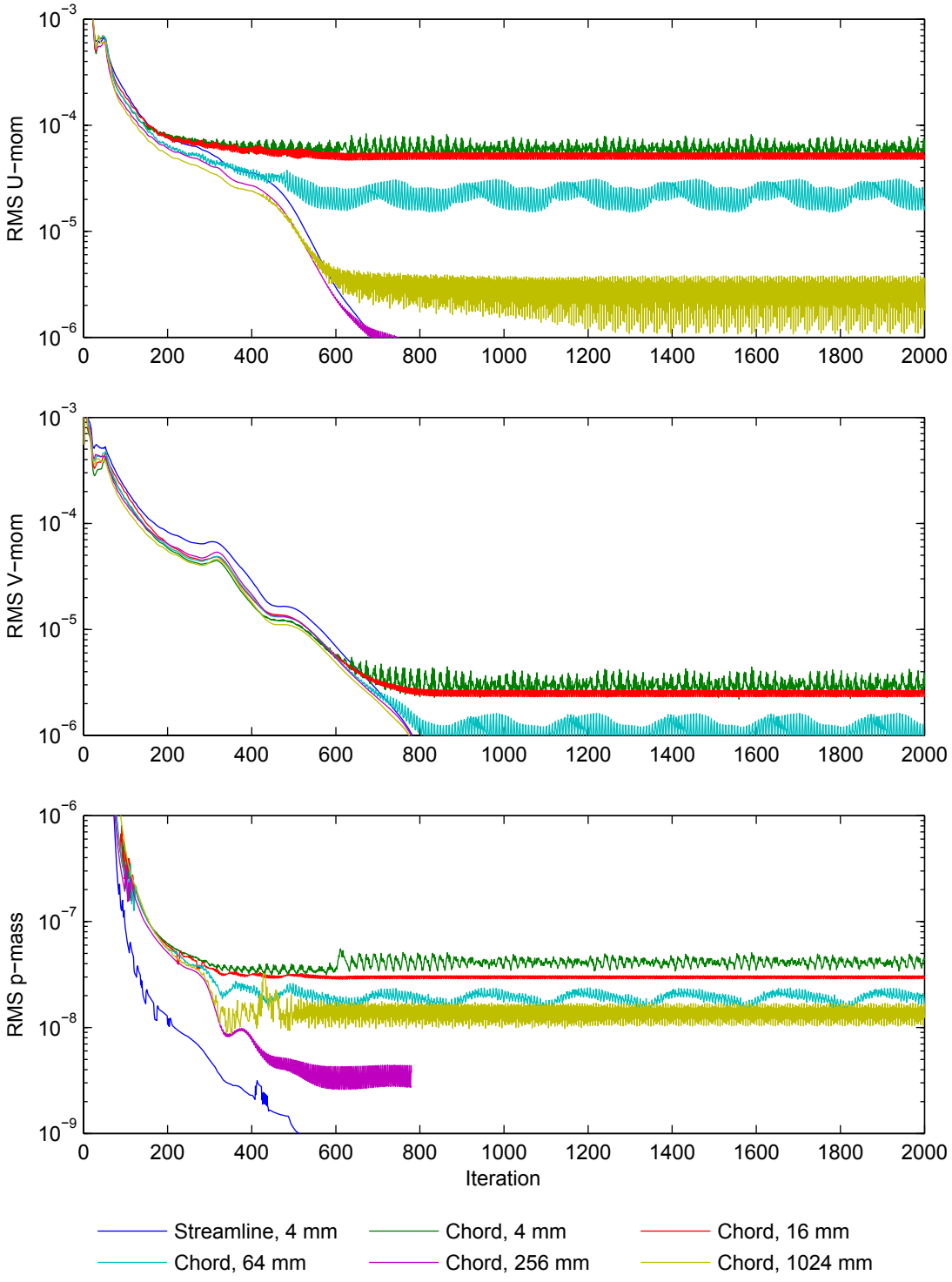

Figure 5.7: *The momentum and pressure equation residuals versus iteration number for grids having different spacing in the wake.*

5.3 The NACA 0012 airfoil

Having completed a verification and validation study for the simulation of the steady state flow about the NACA 4412 airfoil at a single angle of attack, we turn to the simulation of the NACA 0012 airfoil. This airfoil has been chosen for study because of the wealth of steady state experimental data, and the existence of oscillating airfoil data from McCroskey et al. (1982). This oscillating airfoil data set has been used in previous numerical studies, for example Ekaterinaris and Menter (1994); Tuncer et al. (1995).

Prior to performing steady state simulations on this geometry, some preliminary computations were made for an oscillating case using a C-grid, as outlined in section 5.5.1. These simulations highlighted a problem with the use of a moving inlet boundary in CFX, the solution to which was to move to a two-domain grid. In this topology an inner domain surrounding the airfoil rotates within a stationary outer domain, to which the inlet boundary is applied. As it was desired to relate as directly as possible the steady state results to the oscillating results, this two-domain grid was used for all of the steady state computations (after some initial comparisons between the C-grid and the new two-domain grid). The design of this new grid is now discussed.

5.3.1 The design of the two-domain grid

In developing a new two-domain grid it was desired to preserve as much as possible the structure of the existing C-grid in order that the verification studies previously conducted would be applicable to the new grid. Clearly the most significant constraint is that there must be a circular interface with centre at the quarter chord point between the inner and outer domains. The radius of this interface must be greater than $0.75c$ (i.e. the trailing edge of the airfoil) and slightly less than the $80c$ distance to the far-field boundary. We do however want to pick a value that would allow the inner domain to be used as part of the turbine mesh. This limits the radius to a small number of chord lengths, the upper limit being slightly less than $R\sin(\pi/N)/c$ (as shown by some elementary geometry). For the Edinburgh Designs turbine with $R = 1.25$ m, $N = 3$ and $c = 0.2$ m this gives $5.4c$. A value somewhat less than half of this, $2c$, was chosen.

If we use a circular far-field boundary for the outer domain then an O-grid is an obvious choice. For the inner domain we wish to preserve the C-grid immediately around the airfoil and match this to an O-grid at the domain interface. This was achieved with the block structure shown in

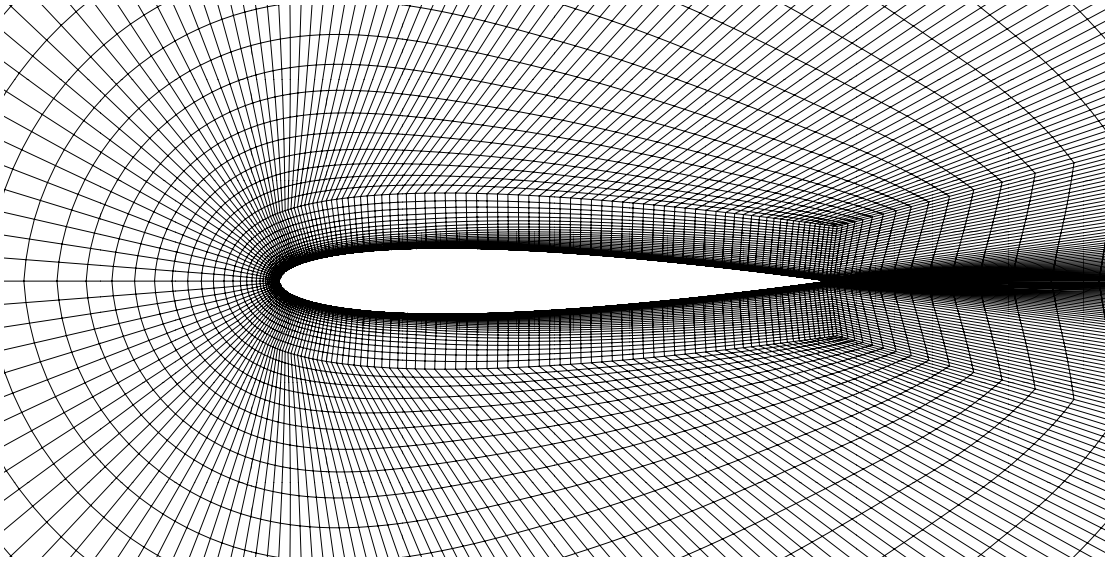

(a)

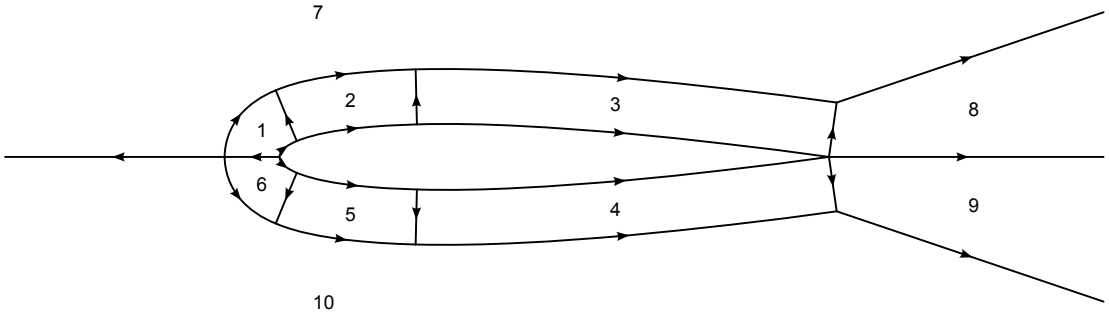

(b)

Figure 5.8: *View of the medium O-C-grid (a) and the block structure used to create the grid (b) in the vicinity of the airfoil.*

figure 5.8, henceforth referred to as an O-C-grid. In this grid the blocks immediately around the airfoil (1–6) remain as a C-grid while the outer blocks (7–10) form an O-grid around the C-grid. Note that the block structure appears very similar to that of the C-grid shown in figure 5.2; the key difference is that, whereas in the C-grid the two edges separating blocks 3 and 7 from block 8 forms one side of block 8, these two edges form two sides of block 8 in the O-grid.

The edge parameters for the boundary layer blocks (1–6) in the O-C-grid remained as for the C-grid with the exception of that on the edge separating blocks 3 and 8. Here, the spacing at the wall (start of the edge) remained the same, but the parameterization was changed to

bi-geometric to allow the specification of the spacing at the end of the edge. A smaller value of Δx_b was chosen to reduce the growth (contraction) ratio between blocks 3 and 7.

For the edges on the outer boundary of the inner domain at $r = 2c$ (not shown in figure 5.8b), the spacing and growth ratios were chosen to resemble the values in the C-grid at this point. Particular attention was focussed on the choice of the parameters on the outer edge of block 8, and also the length of this edge. For a given value of Δy_1 (notation as per section 5.2.3), chosen to be $(1.25/80) \times 256$ mm = 4 mm, and a given number of cells (52), the length of the edge is determined by the growth ratio. There are two competing influences in the choice of this. First, for an outer O-grid where the radial grid lines match those of the inner grid for a 'pitch' angle of 0 degrees, a larger expansion ratio will give a greater mismatch across the interface between inner and outer domains when the pitch angle is non-zero. Second, a larger growth ratio and therefore larger edge length reduces the skew of cells in block 7 near the junction of blocks 3, 7 and 9. Based on these influences, a value of 1.03 was chosen for the growth ratio. For pitch angles up to 10 degrees the jump in cell edge length across the interface is less than three, while the level of skew in the cells in block 7 was judged to be acceptable. Views of the grid for two different pitch angles (0 and 10 degrees) are shown in figure 5.9.

Note that the interface between inner and outer domains is dealt with using the 'General Connection' interface model in CFX. This model is suitable for connecting non-matching grids with hanging nodes, as described above, and also for modelling a transient sliding interface, as is required for the oscillating airfoil simulations of section 5.5.

5.3.2 Verification of the O-C-grid and the iterative convergence

In order to verify the new O-C-grid structure a series of steady-state simulations were performed on both the new grid and the previously verified C-grid (as adapted to the NACA 0012 geometry – see section 5.5.1). These simulations were of the NACA 0012 airfoil at angles of attack of $0, 4, \ldots, 20$ degrees and for a Reynolds number of 4×10^6. For the O-C-grid simulations the inner domain was fixed relative to the outer domain such that the pitch angle was zero; the case of non-zero pitch angle is discussed in section 5.3.2.1. All simulations were run until the RMS residual decreased to 1×10^{-6} or for a maximum of 1000 iterations.

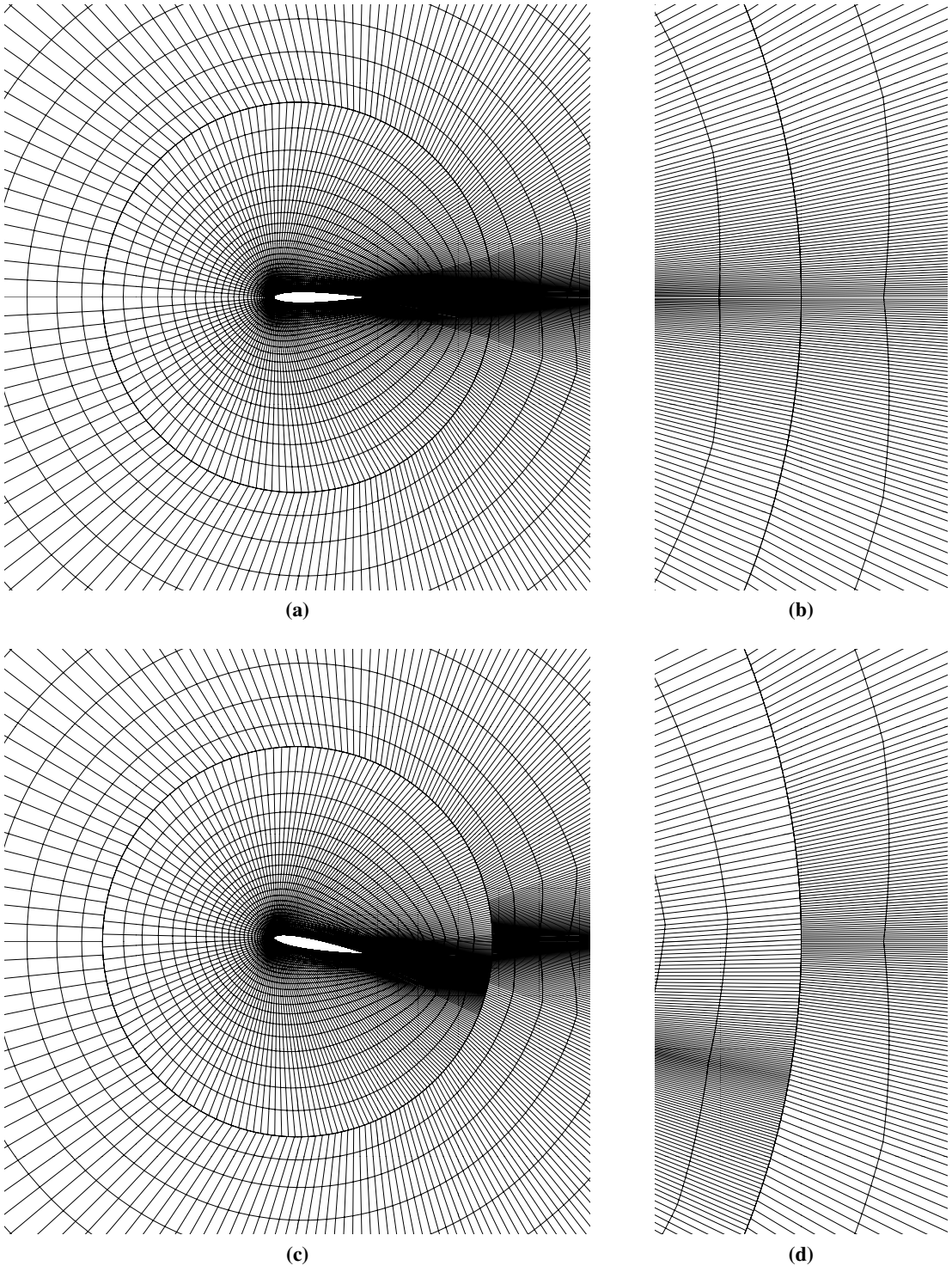

Figure 5.9: *View of the inner and outer domains of the medium O-C grid. The top two views show the case where the inner domain is aligned with the outer domain and there is a one-to-one correspondence between nodes across the interface, while the bottom two views show the case where the inner is rotated by 10 degrees relative to the outer. Views (b) and (d) are details of (a) and (c) respectively, the scale being enlarged by a factor of four.*

Table 5.11: *Comparison of the results for the lift, drag and moment coefficients at six different angles of attack from the C- and O-C-grids. Final values are used for angles of attack of* $0, 4, \ldots, 16$ *degrees, while an average over the final 100 iterations is used for the results at 20 degrees.*

	c_l		c_d		c_m				
α	C	O-C	C	O-C	C	O-C	% c_l	% c_d	% c_m
0	0.0000	0.0000	0.00881	0.00865	0.00000	0.00000	–	−1.82	–
4	0.4326	0.4342	0.00950	0.00933	0.00265	0.00255	0.37	−1.79	−3.77
8	0.8498	0.8540	0.01194	0.01163	0.00668	0.00636	0.49	−2.60	−4.79
12	1.2249	1.2312	0.01738	0.01687	0.01421	0.01376	0.51	−2.93	−3.17
16	1.4751	1.4928	0.03103	0.02986	0.02624	0.02544	1.20	−3.77	−3.05
20	0.7643	0.7768	0.23689	0.24916	−0.06891	−0.07470	1.64	5.18	8.40

The results of this comparison are shown in table 5.11. Of most relevance are the results at an angle of attack of 12 degrees given that the verification results for the C-grid were for an angle of attack of 12.49 degrees (albeit for a different section). The difference from the C-grid is seen to be about 0.5% for the lift coefficient and about 3% for the drag and moment coefficients. This is broadly similar to the difference seen between the medium C-grid and the Richardson extrapolation estimate for the NACA 4412 results (table 5.2), and is thus seen as acceptable. For smaller angles of attack, the differences between the C- and O-C-grids are similar but smaller, the trend being monotonic for lift and for drag for angles of attack excluding zero degrees. At the largest angle of attack, 20 degrees, the solution was oscillatory with a period of around 17 iterations. As such a mean over the final 100 iterations was taken. The differences between the grids are somewhat larger – not unexpected given that this angle of attack is greater than the stall angle.

The pattern of iterative convergence for the O-C-grid solution was examined in detail. Figure 5.10 shows the reduction of the RMS residual with iteration number. Only the solution for an angle of attack of 8 degrees reaches the target of 1×10^{-6}, while the solution for 12 degrees shows a relatively high RMS residual of around 1×10^{-4} in the U-momentum equation. Thus, where it was previously shown (section 5.2.10) that the RMS residuals could be reduced, apparently by the selection of an optimum grid (based on simulations at a constant angle of attack), the present results show that these residuals are dependent upon the angle of attack. Whilst it would not be surprising to see some dependence on the angle of attack, we might expect to see a more progressive trend.

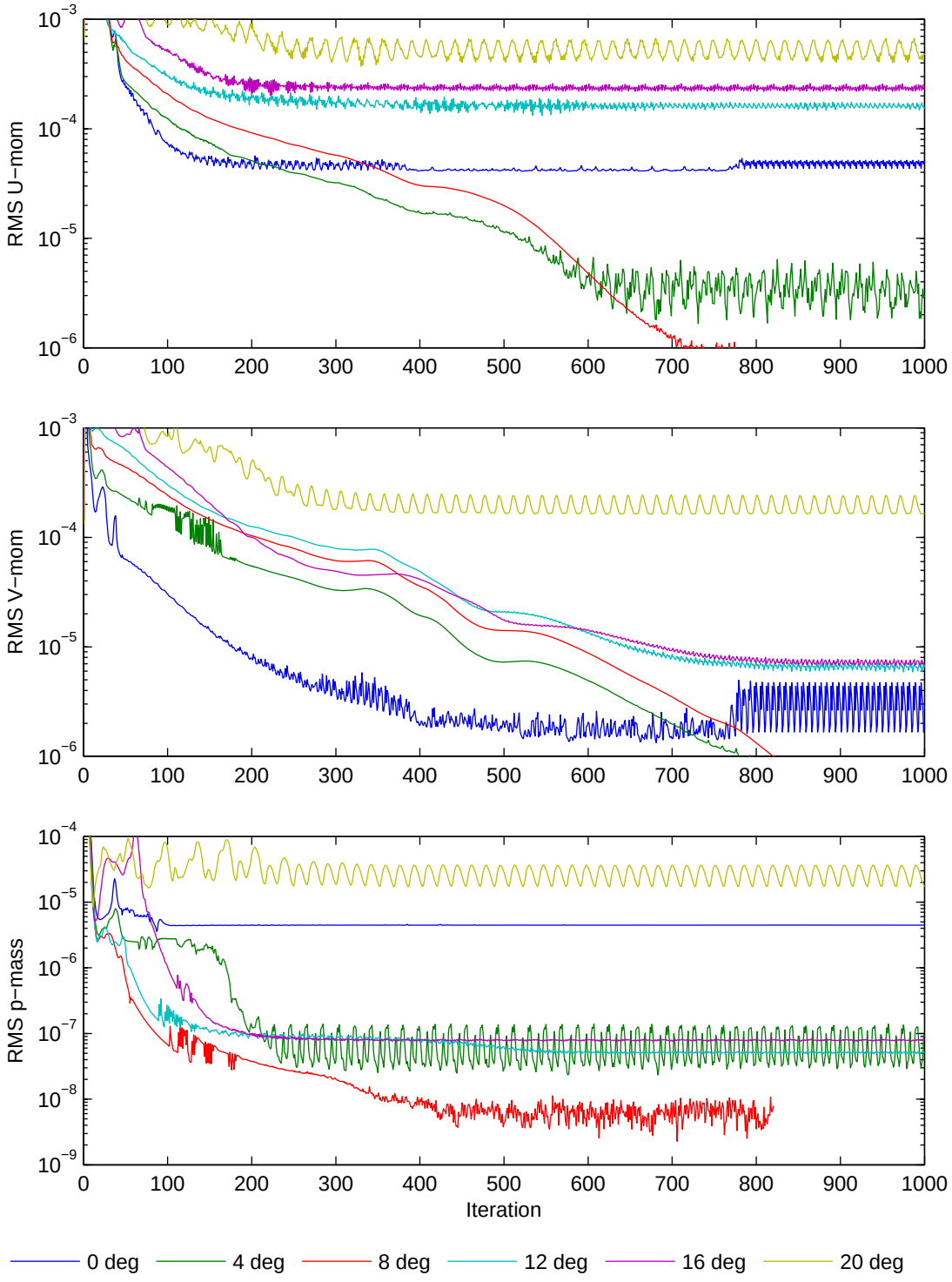

Figure 5.10: *RMS residuals for simulations of the NACA 0012 on the O-C-grid at a Reynolds number of* 4×10^{-6}.

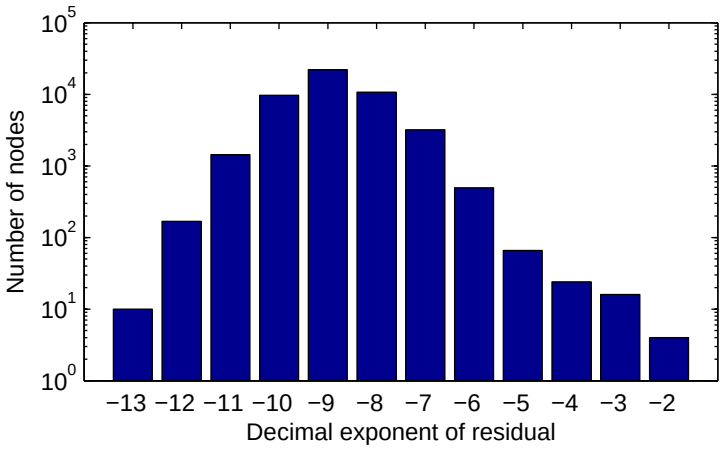

Figure 5.11: *Bar graph of the U-momentum equation residuals.*

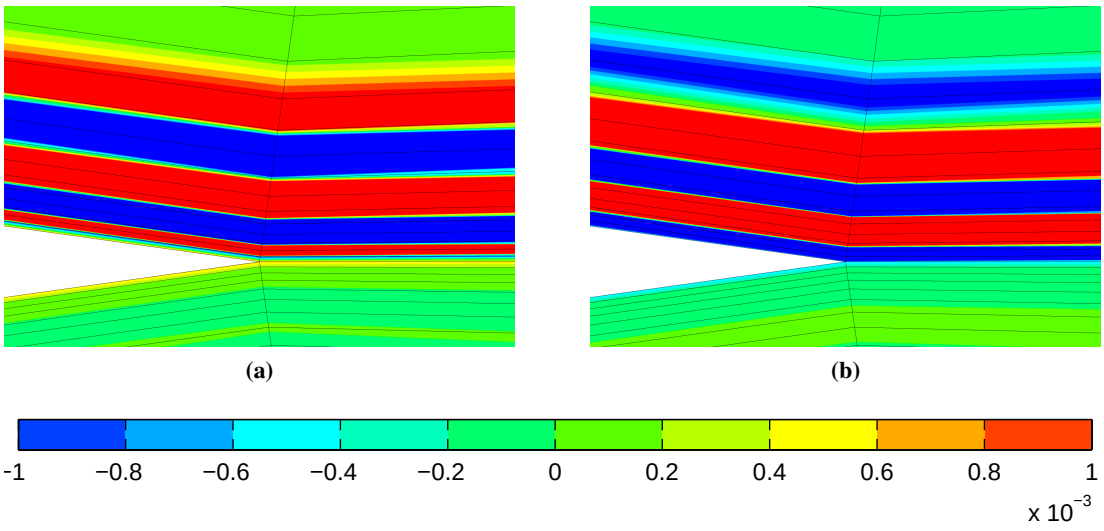

Figure 5.12: *U-momentum equation residuals on the front (a) and back (b) planes.*

A bar graph of the U-momentum equation residuals for the 12 degrees solution is shown in figure 5.11. It is readily seen that the number of nodes where the equation residual is 'high' (taken as orders of 10^{-3} and 10^{-2}) is very small: 16 and 4 respectively, out of a total of 47880. All of these nodes were found to be located at the trailing edge of the airfoil. Contour plots of the U-momentum equation residuals on the front and back faces of the grid are shown in figure 5.12. Interestingly the sign of the residual oscillates in the direction normal to the foil and from the front to the back faces of the grid. We may question whether these high residuals are due to an underlying physical driver or whether they are a purely numerical artefact. The most likely physical cause is a Kelvin-Helmholtz instability, as the nodes concerned are at the centre of volumes which encompass the interface between the fluid streams that have passed

above and below the airfoil. No serious investigation of this was conducted. In the context of the present research we are primarily concerned with whether the high residuals affect the results for the force and moment coefficients. This question was answered by further analysis of the results presented in section 5.2.10. It was found that on the 'non-optimal' grids, the high residuals were confined to a small number of nodes at the trailing edge; despite these high residuals, the force and moment results were within 1% of the results from the 'optimal' grid.

The iterative convergence of the force and moment coefficients is examined in figure 5.13 for five values of the angle of attack (the solution for $\alpha = 20^\circ$ behaved differently and is discussed separately). Errors relative to the final value are plotted versus iteration number, and U- and V-momentum equation residuals. We define the target as reducing the error in any of the coefficients at any of the angles of attack considered to less than 5%. When examining the errors plotted against iteration number, it is immediately clear that the slowest convergence is that in the drag coefficient, and especially for angles of attack of 8, 12 and 16 degrees. Approximately 300 iterations are required to reach the error target. Plotted against the V-momentum equation residuals, the picture is again relatively clear: the residual needs to be reduced to below between 5×10^{-5} and 7×10^{-5} (depending upon the angle of attack) for the error to be reduced to less than 5%. Looking at the error plotted against the U-momentum equation residuals, it would not seem to be possible to define a single target value that would ensure acceptable iterative convergence for all angles of attack. This is a direct result of the high but localized residuals in the solutions at angles of attack of 12 and 16 degrees.

As noted above, the solution for an angle of attack of 20 degrees was oscillatory, almost certainly due to stall. After around 400 iterations the oscillations in the aerodynamic coefficients remained considerable: approximately ±8% for the lift, ±5% for the drag, and ±25% for the moment. As such a 100 iteration prior moving average was calculated, the error in which from the final instance (the mean over iterations 901–1000) is shown in figure 5.14. This shows that the moving average largely eliminates the oscillation and that an asymptotic value is achieved after around 400 iterations.

Based on the above analysis, it was decided to run all subsequent steady state simulations for 500 iterations in order to effectively eliminate iterative convergence error. The extra computational burden is not significant for these steady state simulations.

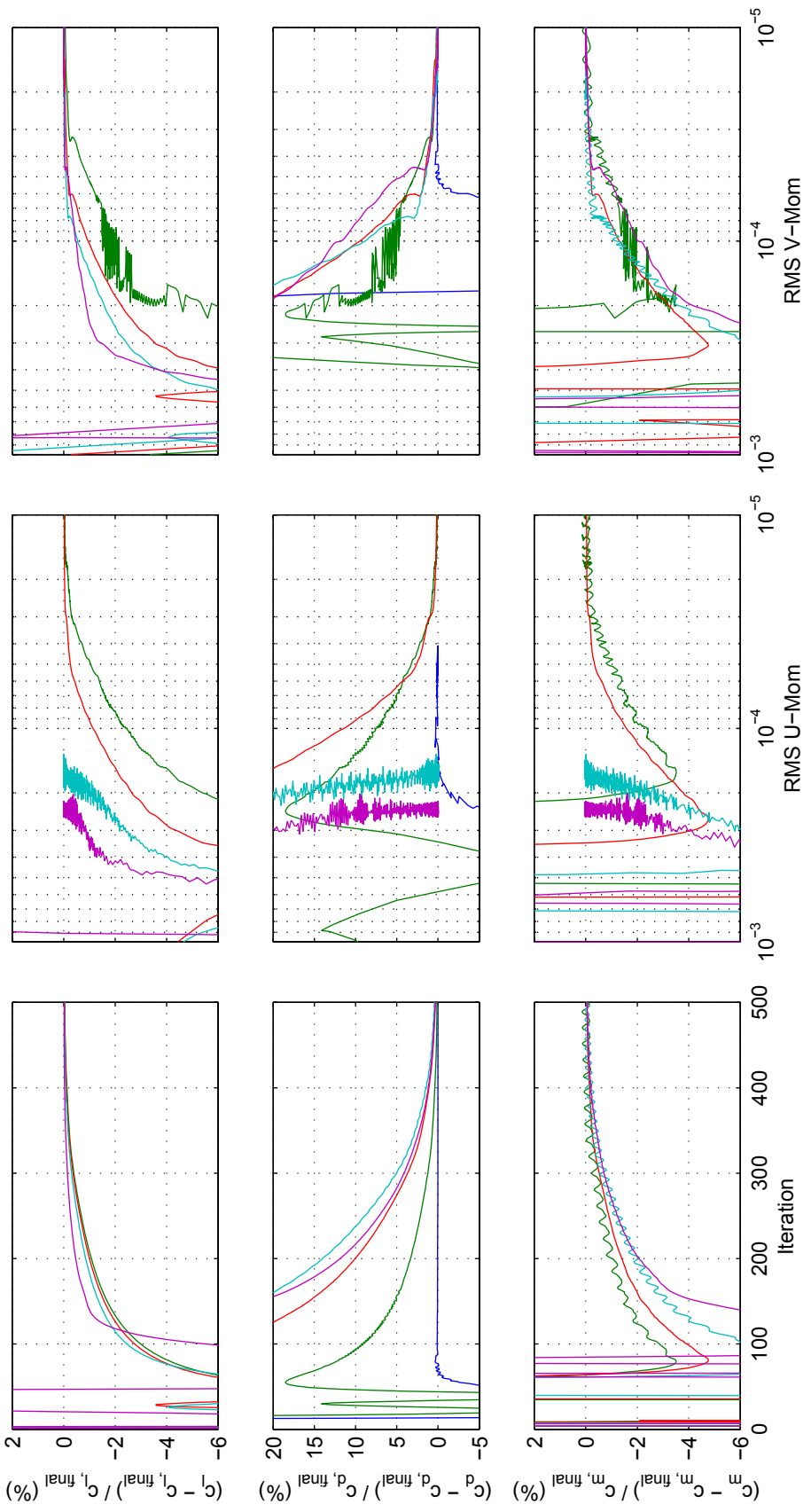

Figure 5.13: *Errors in the predicted coefficients relative to the final value for a given simulation. All simulations are of the NACA 0012 on the O-C-grid at a Reynolds number of* 4×10^{-6}.

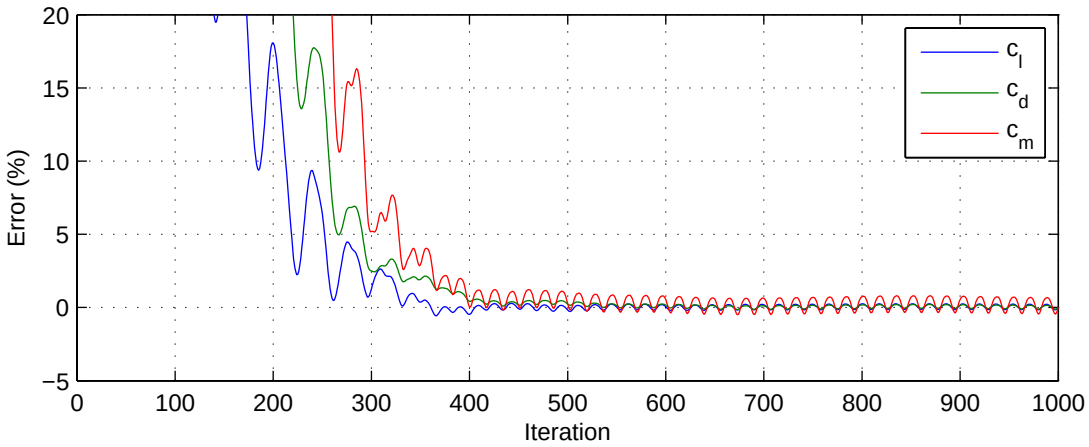

Figure 5.14: *Errors in the predicted coefficients for an angle of attack of 20 degrees. All values (including the reference) are 100 iteration prior moving averages.*

5.3.2.1 Non-zero pitch angle on the O-C-grid

As noted at the start of the present sub-section, all of the O-C-grid based simulations discussed above were for the case of the inner domain being fixed relative to the outer domain at a pitch angle of zero degrees. In order to investigate the error introduced by having a non-zero pitch angle (such that the inner and outer domain grids are non-matching) a series of simulations were run where the outer domain was fixed relative to the free stream direction, in which case the pitch angle is equal to the angle of attack.

It was found that, for a given angle of attack, the differences in the predicted lift, drag and moment coefficients were less than 1% in all but three cases, these being c_m at $\alpha = 4°$, and c_d and c_m at $\alpha = 20°$. In these cases the errors were similar to or smaller than those between the C-grid and the O-C-grid. The solution fields were also examined for non-physical behaviour (i.e. oscillations) in the vicinity of the interface; these were found to be negligible. Finally, the pattern of iterative convergence and the distribution of residuals at the final iteration were found to be the same as for the cases with zero pitch angle i.e. there are no elevated residuals associated with a non-matching domain interface. From this study it was concluded that the use of non-matching grids does not introduce significant errors.

5.3.3 Validation of steady state simulations

Having concluded the verification of the O-C-grid we next discuss a series of validation simulations. The validation is against experimental data from the reports listed in table 5.12.

Table 5.12: *Summary of NACA 0012 section data*

Data set	Re (10^6)	Trip?	Remarks
Gregory and O'Reilly (1970) Data available: c_l, c_d, c_m, c_p	1.44, 2.88	yes & no	Tripped and un-tripped data
Sheldahl and Klimas (1981) Data available: c_l, c_d, c_m	0.35–1.76	no	NACA 0015 data
McCroskey et al. (1982) Data available: c_l, c_d, $c_{d\text{-}p}$, c_m	4	no	Oscillating airfoil data

Each data set was chosen to allow a specific comparison to be made; briefly, the data of McCroskey et al. (1982) contains static and dynamic results, the data of Gregory and O'Reilly (1970) contains untripped and tripped results, while the data of Sheldahl and Klimas (1981) also includes results for the NACA 0015, for which validation simulations were also conducted. These three data sets were introduced in section 2.2.2.

The experimental data of McCroskey et al. (1982) is for a Reynolds number of 4×10^6 and includes data for both the pressure drag and the total drag (based on a wake survey). Figure 5.15 shows a comparison with CFD results in the range $0 \leq \alpha \leq 20$, where CFD calculations were made for angles of attack of $0, 2, \ldots, 10, 11, \ldots, 20$. Regarding the experimental data, it should be noted that for angles of attack of 8 degrees and above below stall, the pressure drag (which does not include the contribution from skin friction) incorrectly exceeds the total drag. This was noted by McCroskey and is discussed in section 2.2.2. Comparing the present results to those of McCroskey, the general pattern is that of the CFD simulations predicting the occurrence of stall at higher values of the angle of attack and for higher values of the lift coefficient; a not unexpected result for RANS based simulations. One positive aspect of agreement is that the relatively sudden nature of stall on the NACA 0012 airfoil is reproduced. In comparing the results for the drag coefficient it is especially important to remember that we are comparing a fully turbulent CFD simulation to an untripped experiment. An analysis of the zero-lift i.e. minimum drag values from all of the validation cases is given later in this section.

A comparison with the experimental results of Gregory and O'Reilly (1970) is shown in figures 5.16, 5.17 and 5.18 for the lift, drag and moment respectively. As with the comparison with the results of McCroskey, the general pattern is one of the CFD results showing stall to occur at a higher angle of attack, although there is better agreement in this case, at least for the higher Reynolds number. For the drag coefficient results it is interesting that at low values of

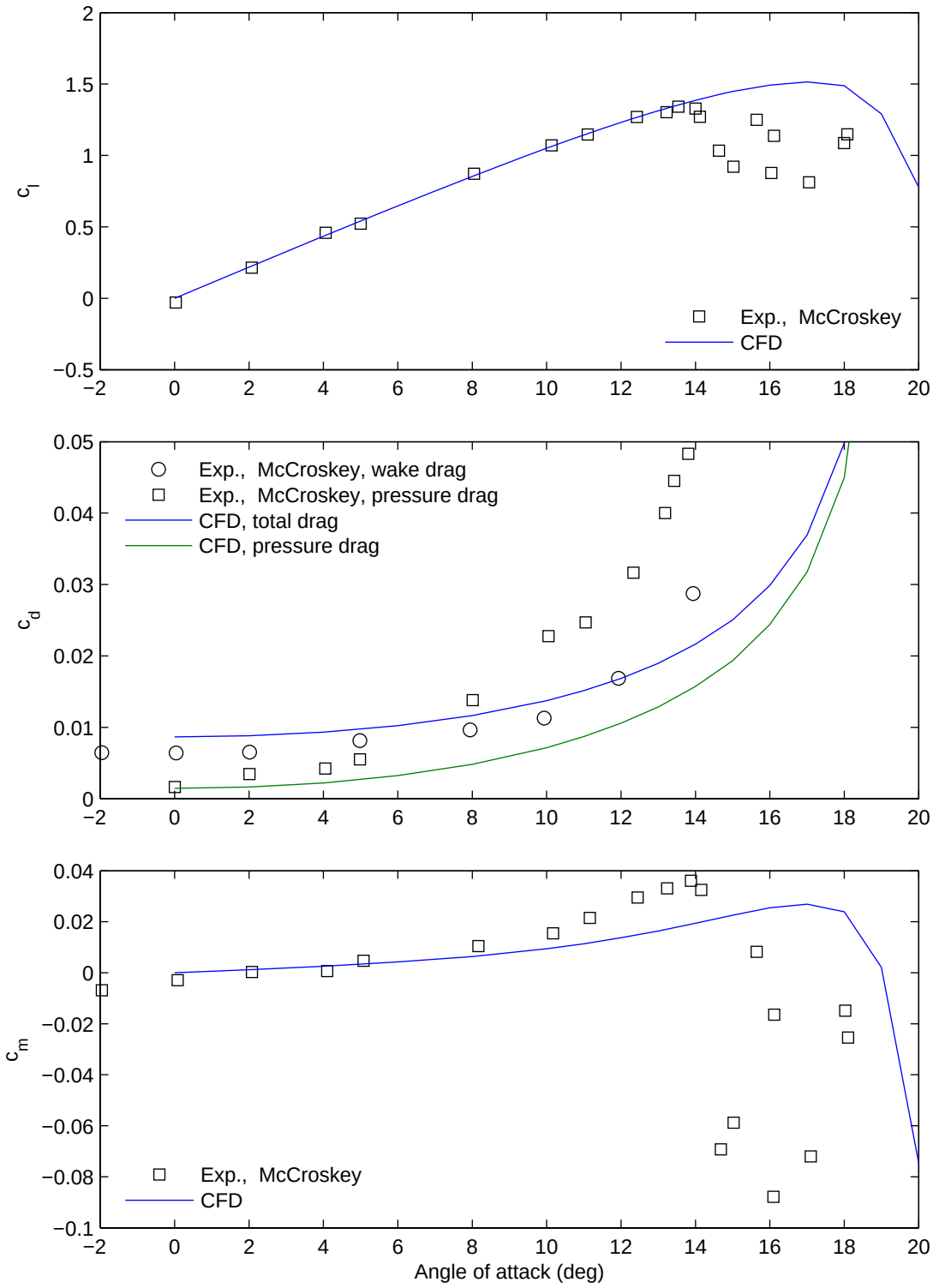

Figure 5.15: *Validation with the results of McCroskey et al. (1982, figure 16, pp. 67–8).*

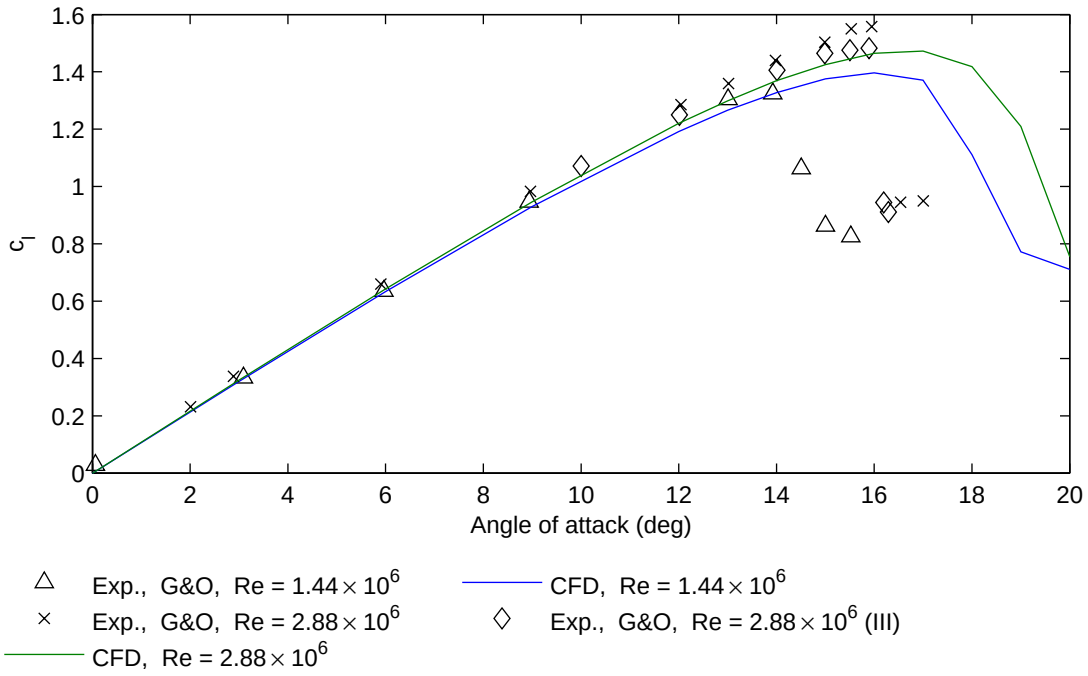

Figure 5.16: *Validation with the results of Gregory and O'Reilly (1970) for the lift coefficient.*

the lift coefficient the agreement is best with the tripped data of Gregory and O'Reilly, whereas for higher values of the lift coefficient the agreement is best with the untripped experimental data. It is tempting to speculate that the use of transition bands in an experimental context has a more profound impact on the airfoil performance that simply altering the nature of the boundary layer, but no discussion of this was found in the literature studied.

Sadly Gregory and O'Reilly do not present data on the effect of boundary layer trips on the lift and moment curves; the only information presented is for the maximum lift coefficient. This shows the expected decrease with the addition of transition bands (and a decrease from the smaller to the larger ballotini). Abbott and von Doenhoff (1959) present a c_l-α curve, but only for a Reynolds number of 9×10^6. The trend shown is a considerable drop in the maximum lift coefficient, from about 1.6 to 1.0, with the accompanying angle decreasing from about 16 degrees to 12. It has been observed (McCroskey, 1987) that an excessively thick trip was used in the experiment; thus the data may not be entirely representative. Nevertheless it is clear that for fully turbulent CFD results which overestimate the maximum lift in comparison to untripped experimental data, the agreement with tripped experimental data will be poorer.

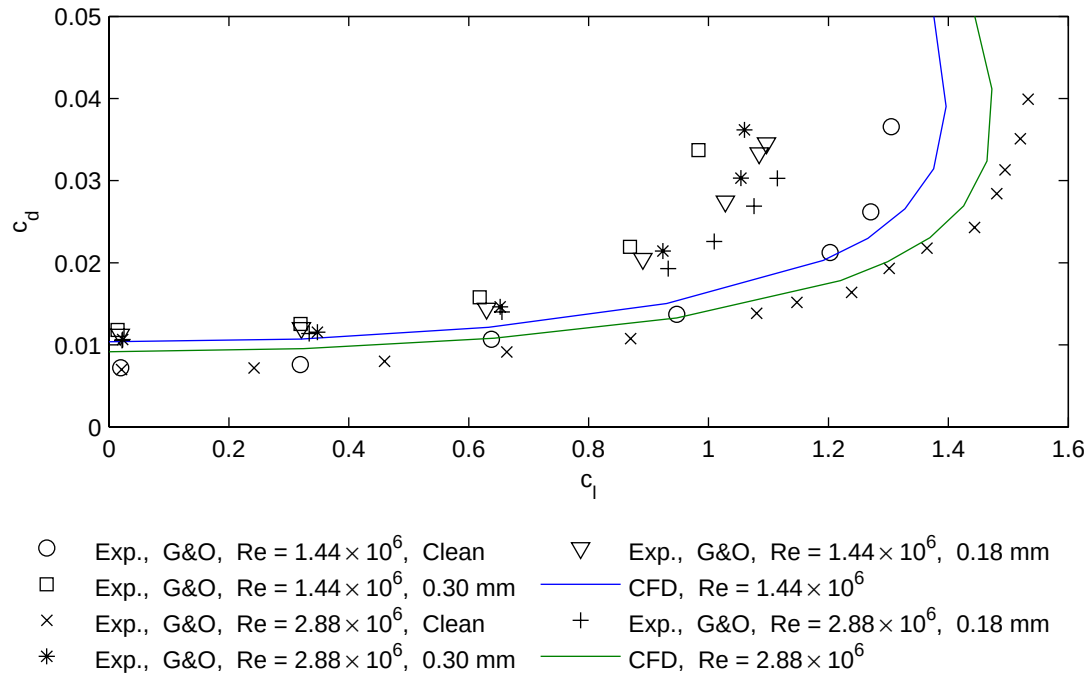

Figure 5.17: *Validation with the results of Gregory and O'Reilly (1970) for the drag coefficient.*

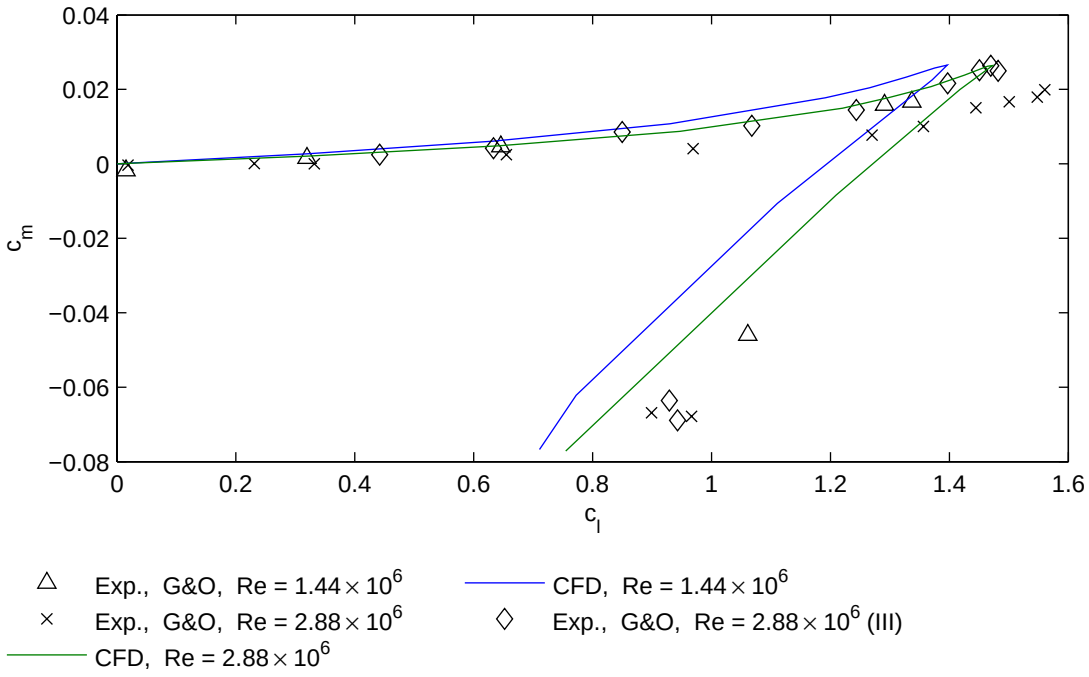

Figure 5.18: *Validation with the results of Gregory and O'Reilly (1970) for the moment coefficient.*

The final steady state validation case is the results of Sheldahl and Klimas (1981). As previously stated, the prime reason for the inclusion of this case is that Sheldahl and Klimas also present results for the NACA 0015 airfoil. This therefore allows us to see whether the accuracy of the CFD results is related to the airfoil section being studied, as was found to be the case, for example, by Bertagnolio et al. (2001). Two further reasons for the inclusion of this comparison are, one, that it extends the range of Reynolds numbers for which the present simulation setup is validated, and two, that Sheldahl and Klimas give data for a Reynolds number very similar to that of Gregory and O'Reilly (1.76×10^6 and 1.44×10^6 respectively). The results are shown in figure 5.19. It would appear that the trend observed with the Gregory and O'Reilly validation case whereby the agreement between CFD and experiment is better for higher Reynolds numbers is also in evidence here: for a Reynolds number of 1.76×10^6 the CFD results overpredict the stall angle by about 2 degrees (similar to comparison with the Gregory and O'Reilly results) whereas at a Reynolds number of 0.7×10^6 the CFD results overpredict by about 3–4 degrees.

Given that only one of the experimental data sets used in the validation cases above presents data from a tripped case, some further investigations into the effect of boundary layer trips on the drag coefficient were conducted. McCroskey's (1987) analysis of a range of experimental data for the NACA 0012 airfoil includes formulae for the effect of the Reynolds number on the minimum drag coefficient for untripped and tripped cases. These formulae are presented in section 2.2.2.1. Minimum drag values calculated using these formulae are compared with the results of the CFD calculations and the experimental data used in the validation in table 5.13. The agreement between the present CFD results and McCroskey's formula for tripped experiments is excellent, with the relative error being less than 1% for the results at the two highest Reynolds numbers, rising to 6% for the lowest Reynolds number. It will be seen that the minimum drag value from the tripped cases of Gregory and O'Reilly is higher than that given by McCroskey's formula.

Briefly, the validation of the steady-state CFD simulations of the NACA 0012 airfoil show the following:

- For the lift, the agreement with untripped experimental results is excellent for low angles of attack/low lift coefficients. The CFD results tend to overpredict the maximum lift and the angle at which this occurs. The agreement with tripped experimental results will be poorer, but is not known in detail.

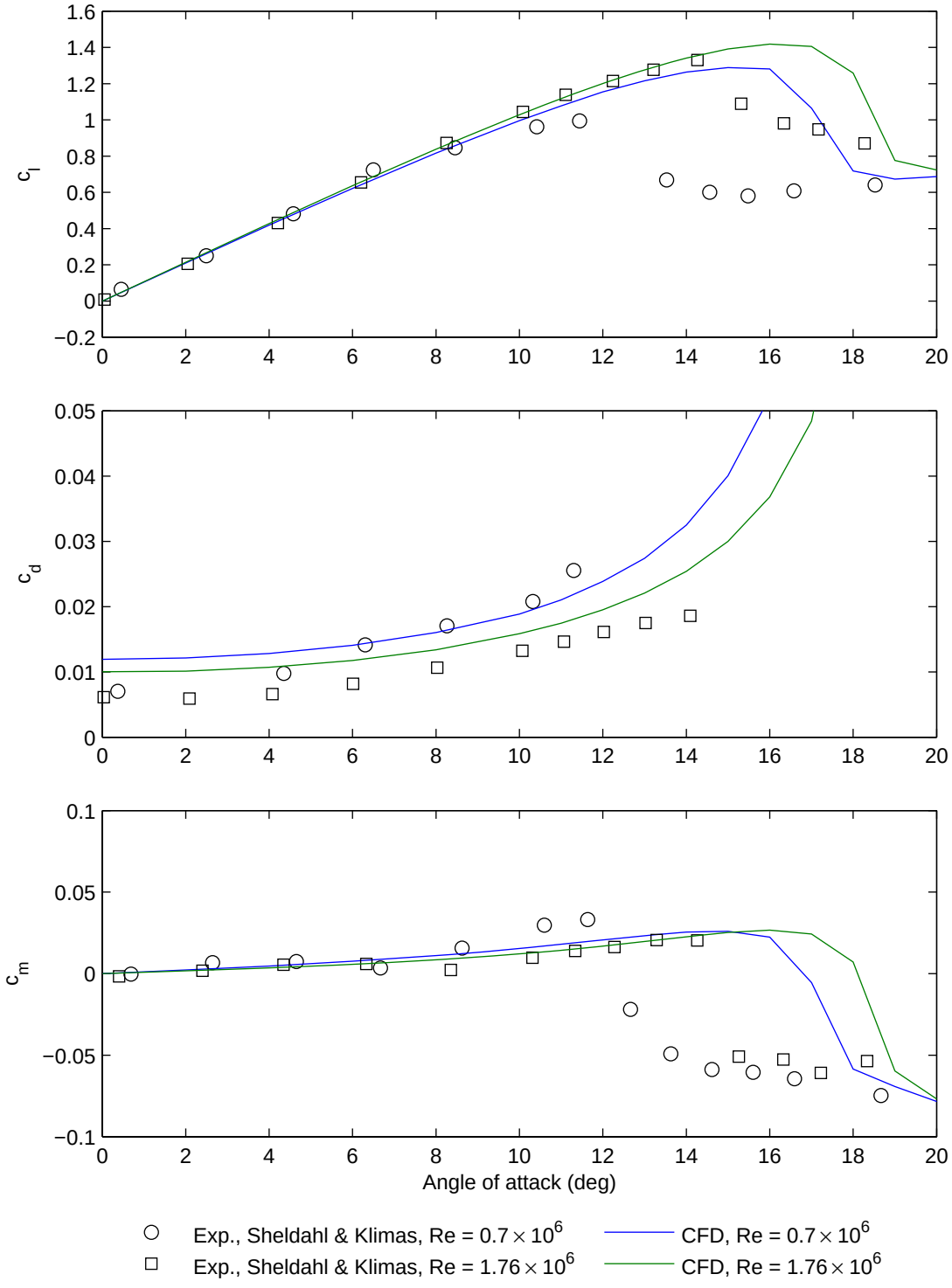

Figure 5.19: *Validation with the results of Sheldahl and Klimas (1981).*

Table 5.13: *Zero-lift drag coefficient for the NACA 0012 section.*

	Reynolds number (10^6)				
Data set	0.7	1.44	1.76	2.88	4
CFD	0.01193	0.01037	0.01000	0.00917	0.00865
G & O'R	–	0.00721	–	0.00701	–
G & O'R (0.18 mm)	–	0.01125	–	0.01055	–
G & O'R (0.30 mm)	–	0.01182	–	0.01066	–
S & K	0.00701	–	0.00610	–	–
McCroskey et al. (1982)	–	–	–	–	0.00641
McCroskey (1987)	0.00679	0.00655	0.00648	0.00633	0.00624
McCroskey (1987) (tripped)	0.01127	0.01006	0.00976	0.00909	0.00869

Note: For the experimental data the values given in the table are from digitized graphs. The data point used is not always at 0 degrees, but is considered sufficiently close for the effect to be negligible.

- The prediction of the minimum drag is in excellent agreement with tripped experimental results. Towards stall, the agreement is better with untripped experimental results, and consistent with the trends observed for the lift coefficient i.e. the CFD results show later stall.

- A comparison of the CFD results for the moment coefficient with untripped experiments show similar trends to that for the lift i.e. good or very good agreement for low angles of attack, poorer agreement near stall. The effect of transition bands on the moment is unknown.

5.4 The NACA 0015 airfoil

Before proceeding to the verification and validation of oscillating airfoil cases, we complete the validation of steady state cases with simulations of the NACA 0015 airfoil at two Reynolds numbers. There are two reasons for studying this airfoil: first, it permits a basic investigation of the effect of thickness on the success of the CFD predictions, and second, there is an oscillating airfoil data set for this geometry which includes results for both untripped and tripped cases. This oscillating airfoil data set is that of Piziali (1994), which also includes steady state data. The other source of steady state data is Sheldahl and Klimas (1981), as referred to in the previous section. All simulations discussed in this section used an O-C-grid that was adapted from the O-C-grid of the NACA 0012 airfoil.

Figure 5.20 shows the validation with the results of Piziali. Both untripped and tripped experimental results are included for the lift, drag and moment; a comparison which was not made for the NACA 0012 airfoil. Compared to the NACA 0012 airfoil the nature of stall is less sudden, a trend shown in both the CFD and experimental results. Again though, the CFD results tend to predict stall to occur for a higher value of the maximum lift and at a higher angle of attack. Comparing Piziali's untripped and tripped results the most significant difference which may be highlighted is that in the immediately post-stall regime an average of the data points shows lower values of lift for the tripped case. For the drag results and at low angles of attack, Piziali's results show higher values of the pressure drag for both tripped and untripped cases. Caution must be exercised in making this comparison though given the low resolution of the graphs from which the drag data was digitized.

The final steady state validation case is with the data of Sheldahl and Klimas (1981), the results of which are shown in figure 5.21. For the lift coefficient around stall the agreement between CFD and experiment is the best seen in any of the validation cases. Interestingly, the agreement between CFD and the same experimental data set, and at the same Reynolds number, but for the thinner airfoil section (0012) was the poorest seen in any of the validation cases. It will be seen that for low angles of attack the lift curve of the experiment is slightly shifted relative to the CFD; this would suggest a small error in the experimental angle of attack. Considering the drag results, the lower values from the experiment are explained by this being an untripped case.

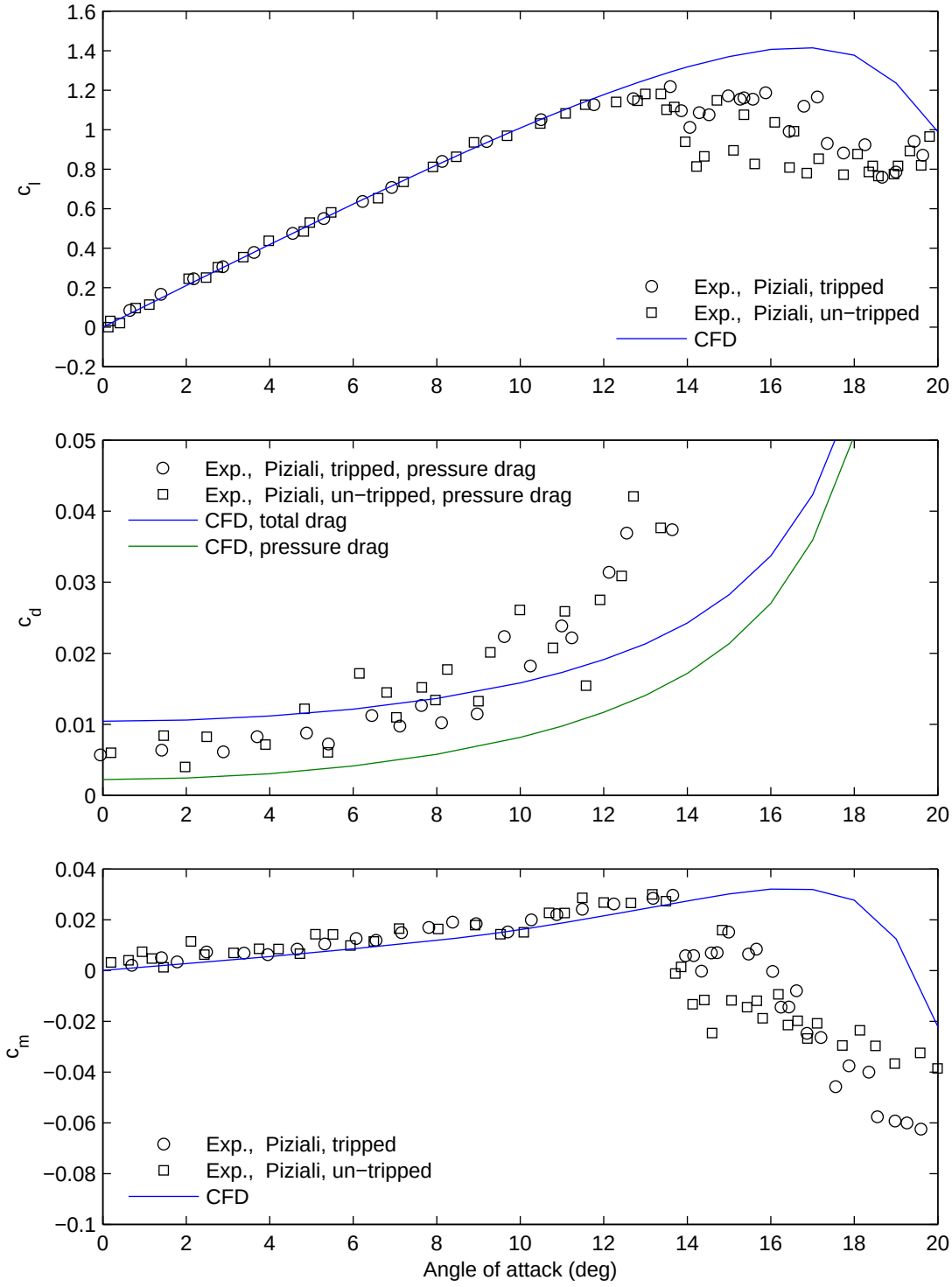

Figure 5.20: *Validation with the results of Piziali (1994, figures 17 and 55).*

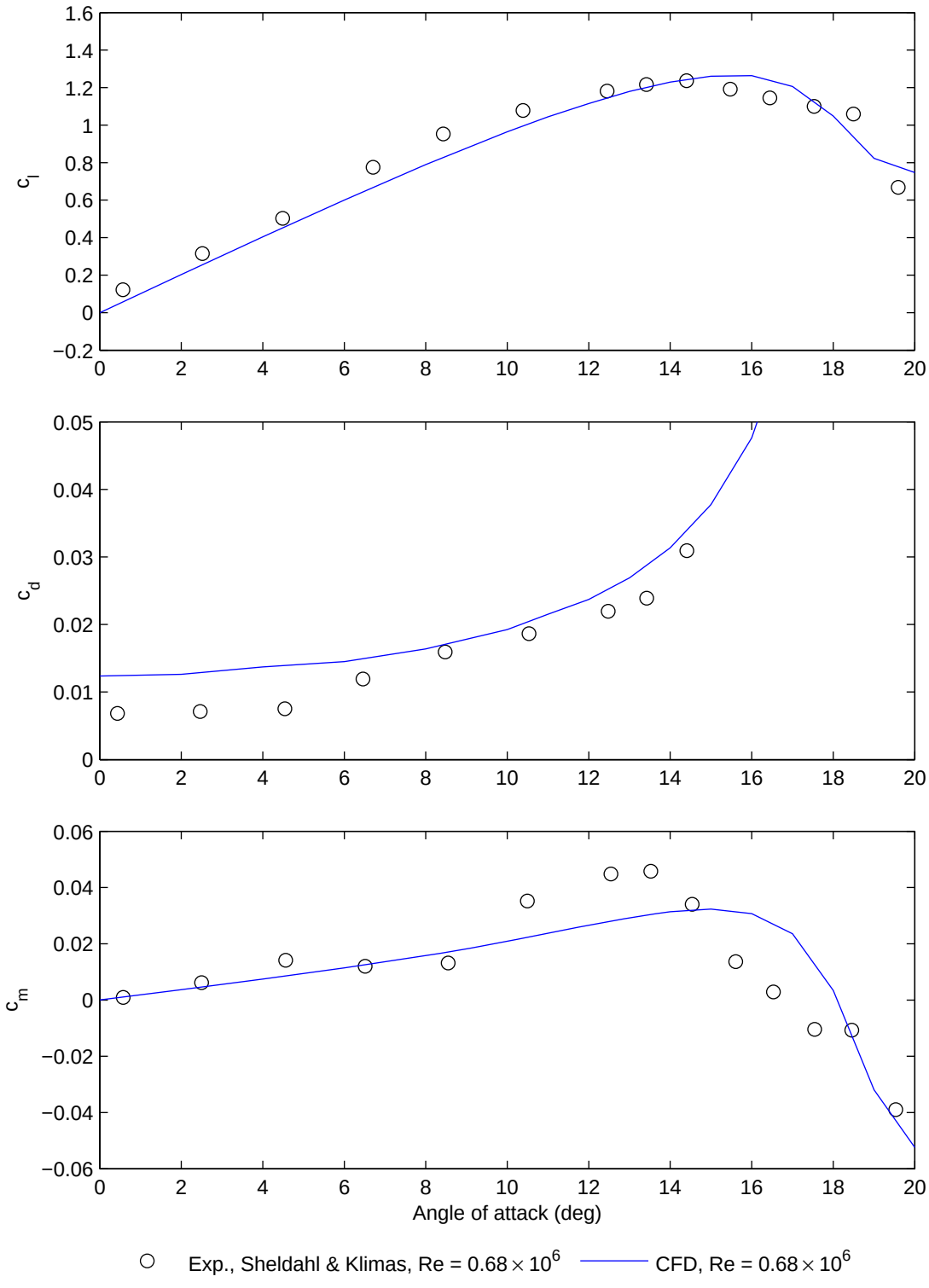

Figure 5.21: *Validation with the results of Sheldahl and Klimas (1981).*

From the above two validation cases (and in comparison with the NACA 0012 validation cases) we may conclude the following:

- For the lift, drag and moment coefficients, there is better agreement between CFD and experiment around the stall point for the NACA 0015 airfoil.

5.5 Oscillating NACA 0012 and 0015 airfoils

5.5.1 Preliminary simulations

As noted at the beginning of section 5.3, some preliminary simulations of an oscillating airfoil were performed on a C-grid, the case being a NACA 0012 airfoil with $\alpha = 5^\circ + 5^\circ \sin(\omega t)$, $k = 0.1$, and $\mathrm{Re} = 4 \times 10^6$. The C-grid used was very similar to that for the NACA 4412 airfoil having medium density, 80 chord lengths to the far field, grid lines in the wake aligned with the extension of the chord, and $\Delta y_1 = 256$ mm at the far-field. Specifically, the block structure was the same, the element counts along edges were the same, wall normal spacings and growth ratios were the same, while spacings and growth ratios parallel to the wall were slightly adapted to suit the different geometry. The geometry of the far-field boundary was also slightly altered so that the edges of the wake block forming the inlet ran parallel to the chord line. Boundary conditions were applied in the same manner as with the NACA 4412 simulations. The whole grid was rotated using a CFX user Fortran routine written in part by the present author.

Such simulations proved unsuccessful due to the prediction of an erroneous pressure field about the airfoil, originating at the inlet and outlet boundaries. The outlet boundary condition was modified to a condition of constant static pressure (from average static pressure); the result of this again being erroneous, but now originating solely from the inlet boundary. After consultation with CFX support, it was suggested that this was due to the grid moving normal to the inlet boundary – an apparent weakness with this boundary condition in CFX.

As such the geometry of the far-field boundary was altered slightly so that the arc portion of the inlet was an arc about the quarter chord point instead of being an arc about the leading edge as previously. The straight portions of what was previously the inlet were changed to ‘opening’ boundaries with the specification of ‘static pressure for entrainment’ (see section 3.4.3). Unfortunately, a simulation on this grid gave the same errors as previously observed, and led to the conclusion that it is not possible to implement a moving inlet boundary condition in CFX.

Two possible alternatives are, first, to use mesh deformation with the existing C-grid structure and second, to have a two domain grid where the inner domain around the airfoil oscillates with the airfoil while the outer domain (which includes the inlet boundary) remains stationary. Clearly both of these options could also be used to implement variable pitch in the case of the turbine. It was decided to implement the latter option so that the angle that the airfoil/blade can pitch is not constrained, as would be the case with mesh deformation.

5.5.2 Verification

Having verified the O-C-grid and the iterative convergence parameters for steady state simulations, we now proceed to a verification of the transient solution. This verification includes studies into the effect on the solution of:

- The number of oscillatory cycles completed,
- The number of time steps per cycle,
- The maximum number of coefficient loop iterations per time step, and
- The RMS residual target.

Note that whilst the effect of the RMS residual target has been investigated for the steady state simulations, it was felt that it deserved being briefly revisited in this new context.

The case chosen for the verification is that of the NACA 0015 airfoil with $\alpha(t) = 4^\circ + 4.2^\circ \sin(\omega t)$, $k = 0.1$ and $\mathrm{Re} = 2 \times 10^6$; one of the experiments presented in Piziali (1994). This case was selected because it more closely matches the conditions of the turbine (blade) being simulated than any of the other available data i.e. it is from the thicker foil (0015 versus 0012) and it is for an attached case. The reduced frequency $k = 0.1$ is also similar to that of a vertical axis turbine blade (see section 2.4.2.2). With regards to subsequent validation, the data of Piziali is preferred because of the availability of both tripped and untripped data, and the higher resolution of the graphs in the scanned report.

The first numerical parameter to be investigated is the number of cycles that the simulation is run for. As with all oscillating cases, the initial conditions used were the results of a 'fully converged' (500 iterations or RMS residual less than 1×10^{-5}) steady state simulation at an angle of attack corresponding to the minimum angle of attack of the oscillatory cycle. Thus the time dependent angle of attack of the transient simulation is in actuality $\alpha(t) = 4^\circ - 4.2^\circ \cos(\omega t)$. Numerical parameters fixed during this simulation were the number of time steps per cycle (128), the maximum number of coefficient loop iterations (5) and the RMS residual target (5×10^{-5}).

Figure 5.22 shows the lift, drag and moment coefficient during the first, second and third cycles after the start from the steady state solution. The error bars shown on the graph of drag versus angle of attack represent errors of $\pm 0.01\Delta c_d$ and $\pm 0.05\Delta c_d$ where Δc_d is the range of the

Table 5.14: *Normalized RMS errors in the lift, drag and moment from the solution during the fifth cycle; normalization is by the range of the solution during the fifth cycle (Δc_l = 0.73, Δc_d = 0.021, Δc_m = 0.020).*

cycle	% c_l	% c_d	% c_m
1	3.22	4.56	0.88
2	0.46	1.05	0.22
3	0.07	0.34	0.10
4	0.03	0.32	0.11

solution during the fifth cycle. These are positioned at the solution for this fifth cycle and have a period of four time steps. These error bars are intended as a means of approximately relating the RMS errors between different cycles, displayed in table 5.14, to the errors calculated for the steady state verification results. Examining the figure it is clear that the results during the second cycle are practically indistinguishable from those during the third for the lift and moment; the drag results being only slightly different. Such a trend is shown by the quantitative analysis given in the table. Considering the RMS errors for the third and fourth cycles, and noting the increase in the error for the moment coefficient, it is suggested that this level of error between cycles may be largely due to a random iterative error. Thus, for the given grid, time step and iterative convergence parameters used in this simulation, there is no improvement in the solution after the third cycle. Based on this, all subsequent simulations were run for three cycles.

A quantitative analysis into the effect of varying the number of time steps per cycle, the number of coefficient loop iterations per time step and the residual target is given in table 5.15. Each parameter was varied in turn from the centre case used above. Considering first the effect of varying the number of time steps per cycle, it was perhaps surprising how few were required. If we discount errors in the moment and set the RMS error target for the lift and drag as 1% relative to the centre case then a simulation with 16 time steps per cycle produces an acceptable solution. Note that RMS errors were calculated based on the minimum of the number of data points in the two solutions in question.

Considering the number of coefficient loop iterations per cycle: three would be acceptable if an RMS error above 1% is permitted for the moment coefficient. Little difference is seen on increasing the number to ten. Variation of the RMS residual target produces little difference, but this is largely due to the limitation in the number of coefficient loop iterations i.e. in practice

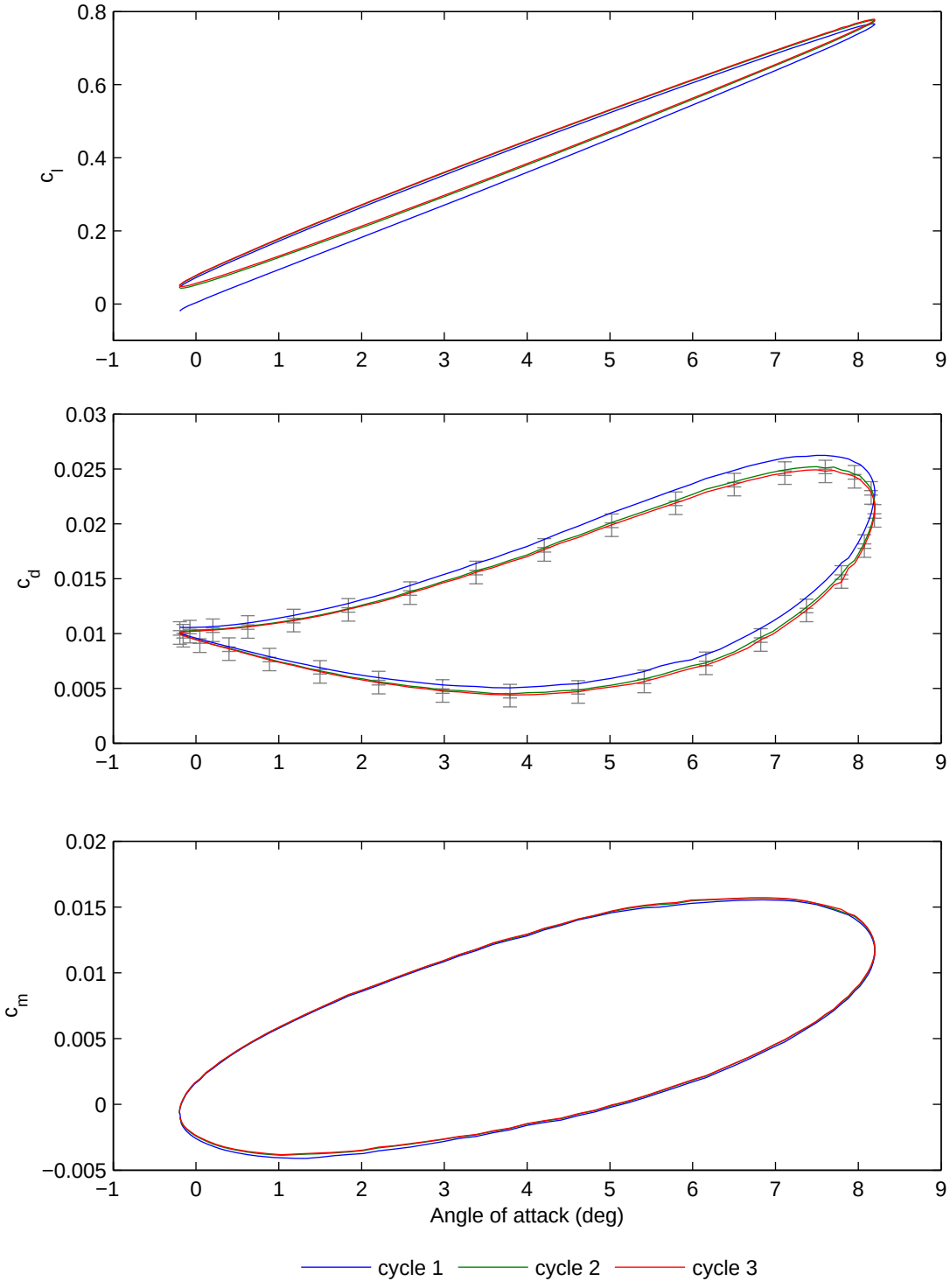

Figure 5.22: *Verification of the number of cycles required for the simulation to become periodic.*

Table 5.15: *Normalized RMS errors in the lift, drag and moment from the solution with 128 time steps per cycle, five coefficient loop iterations per time step (n) and an RMS residual target of* 5×10^{-5}. *The third cycle of each simulation is used for the comparison. Values are normalized as per table 5.14.*

$T/\Delta t$	n	residual target	% c_l	% c_d	% c_m
16	5	5×10^{-5}	0.77	0.70	6.13
32			0.20	0.32	1.24
64			0.11	0.39	0.76
128			–	–	–
256			0.05	0.24	0.34
128	3	5×10^{-5}	0.26	0.77	1.54
	5		–	–	–
	10		0.03	0.36	0.18
128	5	1×10^{-4}	0.08	0.24	0.61
		5×10^{-5}	–	–	–
		1×10^{-5}	0.01	0.05	0.08

the RMS residual is reduced below the two upper limits (1×10^{-4} and 5×10^{-5}) for only a few time steps during each cycle.

The variation in the RMS residuals in the U- and V-momentum equations with phase angle is shown in figure 5.23. (Residuals for the pressure-mass equation were generally an order of magnitude lower and are not shown). The three cases are those with different values for the maximum number of coefficient loop iterations per time step; the third cycle of each simulation is used for comparison. Surprisingly, the simulation with a maximum of five iterations per time step has higher residuals than that with three, for both U- and V-momentum equations and in terms of minimum, maximum and mean values for the cycle under consideration. The simulation with ten iterations per time step has lower residuals for all measures other than the minimum value of the U-momentum residual. Despite the simulation with five iterations having the highest residuals, there is a clear trend in the convergence of the aerodynamic coefficients, as seen in table 5.15, i.e. the RMS error in the aerodynamic coefficients relative to the centre case is smallest for the solution with ten iterations per time step. From this we must infer that the quality of a solution cannot simply be judged by examining the residuals.

In summary then, the independent variation of the number of time steps per cycle, the number of coefficient loop iterations or the residual target will produce an acceptable solution for an

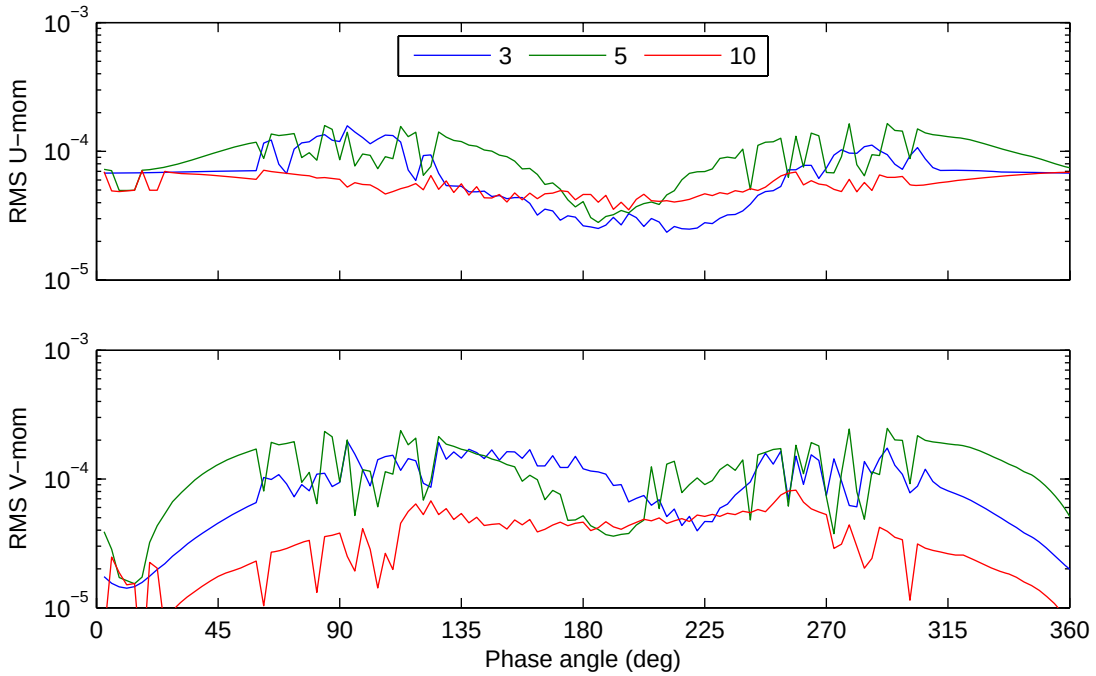

Figure 5.23: *RMS residuals in the U- and V-momentum equations versus phase angle for simulations having 3, 5 and 10 coefficient loop iterations per time step.*

oscillating airfoil. We should remind ourselves here that the purpose of analysing airfoils, both steady state and oscillating, is to gain insight into the numerical setup that is required to simulate vertical axis turbines. As the angle of attack on a vertical axis turbine blade will oscillate about approximately zero degrees once per revolution, the number of time steps required per revolution of the turbine should be as a minimum the number of time steps required per cycle of an oscillating airfoil. However, it is felt unlikely that 16 time steps per revolution of the turbine will be sufficient. Regarding the number of coefficient loop iterations and the residual target required, it is asserted that this will be similar for the turbine simulations.

The numerical parameters of the centre case above were chosen for the computation of the validation cases. The number of time steps per cycle (128) was chosen not because of the required accuracy, but because of the desire to generate a sufficiently large number of data points to plot a smooth curve. Selection of five coefficient loops per iteration was based on the desire to reduce the error in the moment coefficient below 1%, while the residual target was left at 5×10^{-5} by default. The computation burden of such a selection was not significant.

5.5.3 Validation

Four validation cases were chosen from the experiments of Piziali (1994) and McCroskey et al. (1982). For the NACA 0015 airfoil, simulations were made of $4° \pm 4.2°$ and $11° \pm 4.2°$ at $\mathrm{Re} = 2 \times 10^6$ and with $k = 0.1$. Simulations of the NACA 0012 airfoil were for $5° \pm 5°$ and $10° \pm 5°$ at $\mathrm{Re} = 4 \times 10^6$ and again for $k = 0.1$. All cases were for an airfoil in sinusoidal motion.

We first discuss the case of the NACA 0015 airfoil with $4° \pm 4.2°$. The unsteady lift, drag and moment coefficients are shown in figure 5.24. The agreement for the lift and moment coefficients might be descried as very good and good respectively, but the agreement for the drag is less good. As discussed, the drag coefficients presented by Piziali and McCroskey for the unsteady cases are all derived from pressure measurements. We are thus primarily concerned with the pressure drag derived from the CFD simulations. For this case the CFD results underestimate the drag relative to Piziali's measurements by an almost constant amount. The magnitude of this underestimation is similar to that observed for the steady results – see figure 5.20 – and so it seems unlikely that the discrepancy is related to dynamic effects. In commenting on the discrepancy in the steady results, it was noted that the graph from which the experimental results were digitized was of low resolution and therefore caution should be exercised in interpreting results. This refrain is however less applicable to the oscillating results. Further, the experimental data for this case were reported in a contemporary paper (Ekaterinaris and Menter, 1994), from which the data were also digitized. These two sets of digitized data compared favourably, suggesting that the discrepancy is likely to be real.

The thorough validation of the zero lift (total) drag coefficient for the NACA 0012 airfoil gives a high level of confidence in the accuracy of that prediction. Based on the argument that the flow structures over the NACA 0015 airfoil at zero lift will be very similar to those over the NACA 0012, it is believed that the CFD prediction of the zero lift drag coefficient for the NACA 0015 will be similarly accurate. What has not been validated (or indeed verified) is the decomposition of this drag into pressure drag and skin friction drag components. As a quick 'sanity check' on the values from the steady state CFD results ($c_{d_0} = 0.01044$, $c_{d\text{-}p_0} = 0.00224$), a calculation was performed with Xfoil (see again section 2.2.3.1). 140 panel nodes were used and boundary layer transition was specified on both top and bottom surfaces at $x/c = 0.01$. The results were $c_{d_0} = 0.01049$ and $c_{d\text{-}p_0} = 0.00217$, comparing favourably with those from the CFD. It is thus believed that the present CFD predictions for the pressure drag are accurate.

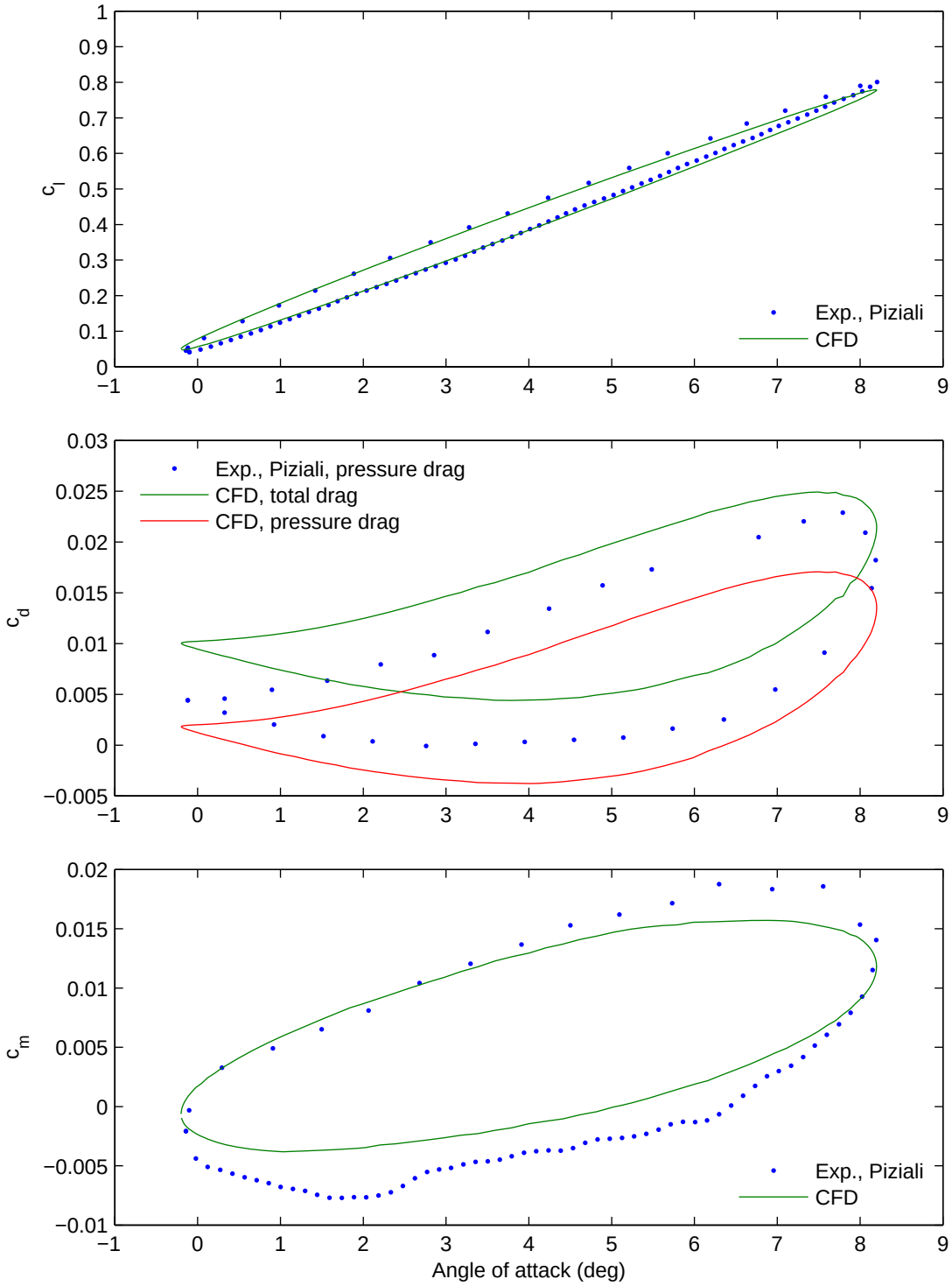

Figure 5.24: *Validation with results of Piziali (1994, figure 24(b)).*

The second validation case for the NACA 0015 airfoil from Piziali's experiments is for $\alpha = 11^\circ \pm 4.2^\circ$. In this case the maximum angle of attack exceeds the static stall angle given by Piziali's experiment, but not that shown by the CFD simulation. The agreement between the CFD and experiment for lift and moment, as shown in figure 5.25, is, not unexpectedly, less good than the previous case. In particular the CFD results show a much smaller hysteresis loop for the lift coefficient, which may be attributed to the differing predictions for the stall point. Unfortunately the drag predictions are poor. As with the previous case there appears to be an approximately constant error, but in this case it is larger, to the extent that the total drag as predicted by the CFD is less than the pressure drag as measured in the experiment. Sadly, again, there is no ready explanation, but we make reference to the experimental measurements of McCroskey et al. (1982), as shown in figure 5.15. These showed that for the case of the NACA 0012 at steady state and for angles of attack between 5 and 14 degrees, experimentally measured values of the pressure drag were incorrectly higher than experimentally measured values of the total drag.

The two final validation cases were with the experimental data of McCroskey et al. (1982) for the NACA 0012. These experiments were for untripped airfoils and so we would expect less good agreement with the fully turbulent CFD results. The primary reason for their inclusion is to permit validation of oscillating airfoil cases with more than one experimental data set. Figure 5.26 shows the results for the case of $\alpha = 5^\circ \pm 5^\circ$. For the lift coefficient, the slope of the major axis of the roughly elliptical hysteresis loop is lower in the case of the CFD results. This was also observed for the NACA 0015 with $\alpha = 4^\circ \pm 4.2^\circ$ but the effect was less marked. Given the excellent agreement in the static lift coefficients over a similar range of angles of attack (and up to 14 degrees) it seems likely that this is due to dynamic effects. Again, considering the good agreement for the steady state data, it is likely that the disagreement in the moment results is also due to dynamic effects. Considering the drag results, the discrepancy is similar to that observed between the CFD results and the experimental data of Piziali, although in this case the difference is not as constant across the range of angles of attack. As before, the discrepancy is not readily explained, but it is now shown to be consistent across data sets.

The final case is that of light dynamic stall with $\alpha = 10^\circ \pm 5^\circ$, and is primarily included to demonstrate the limitations of modelling untripped airfoils as fully turbulent with CFD. Substantial disagreement is seen for the lift, drag and moment with the shapes of the hysteresis loops being qualitatively wrong, as seen in figure 5.27. This is as expected given the similar

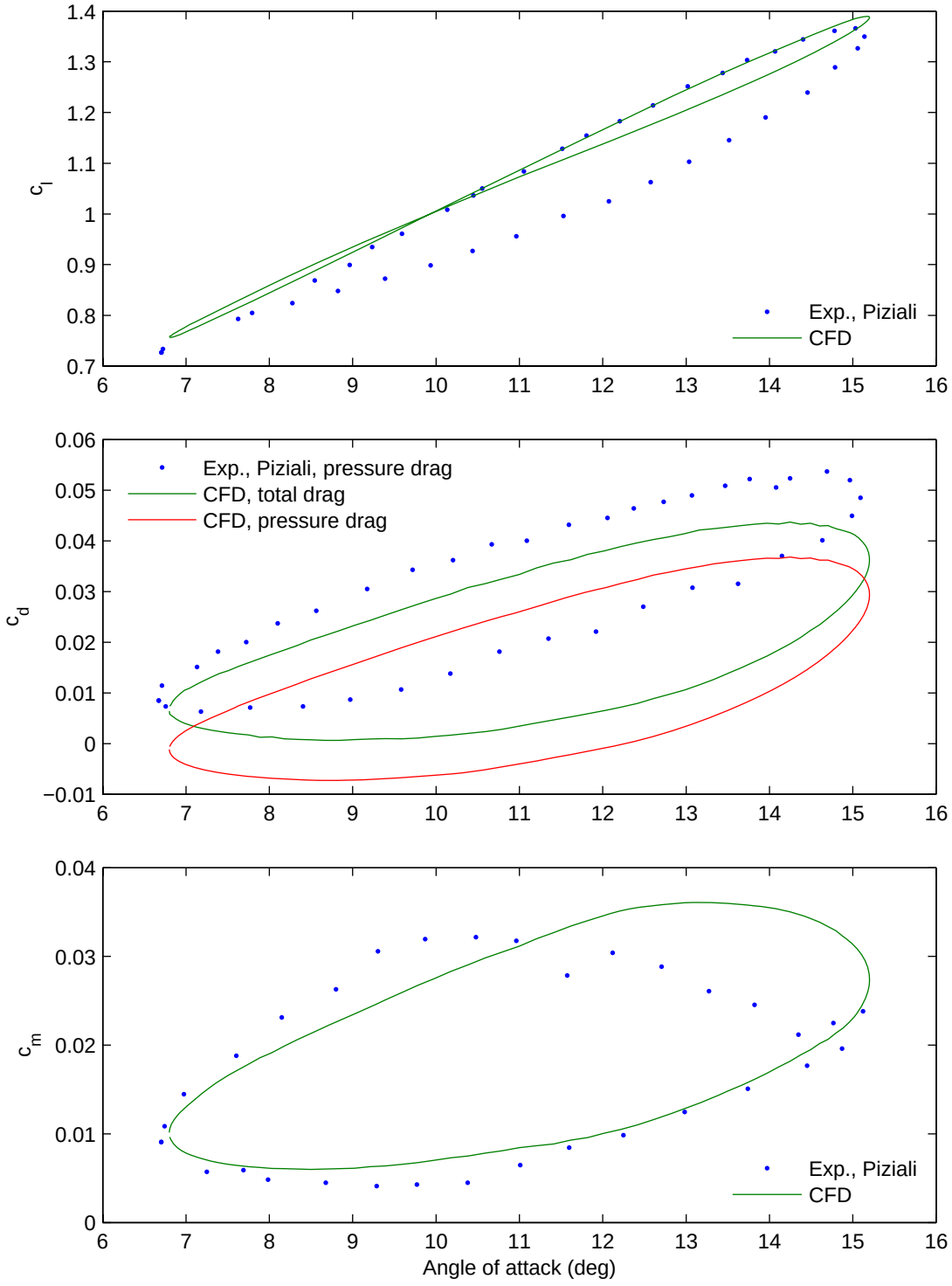

Figure 5.25: *Validation with results of Piziali (1994, figure 26(b)).*

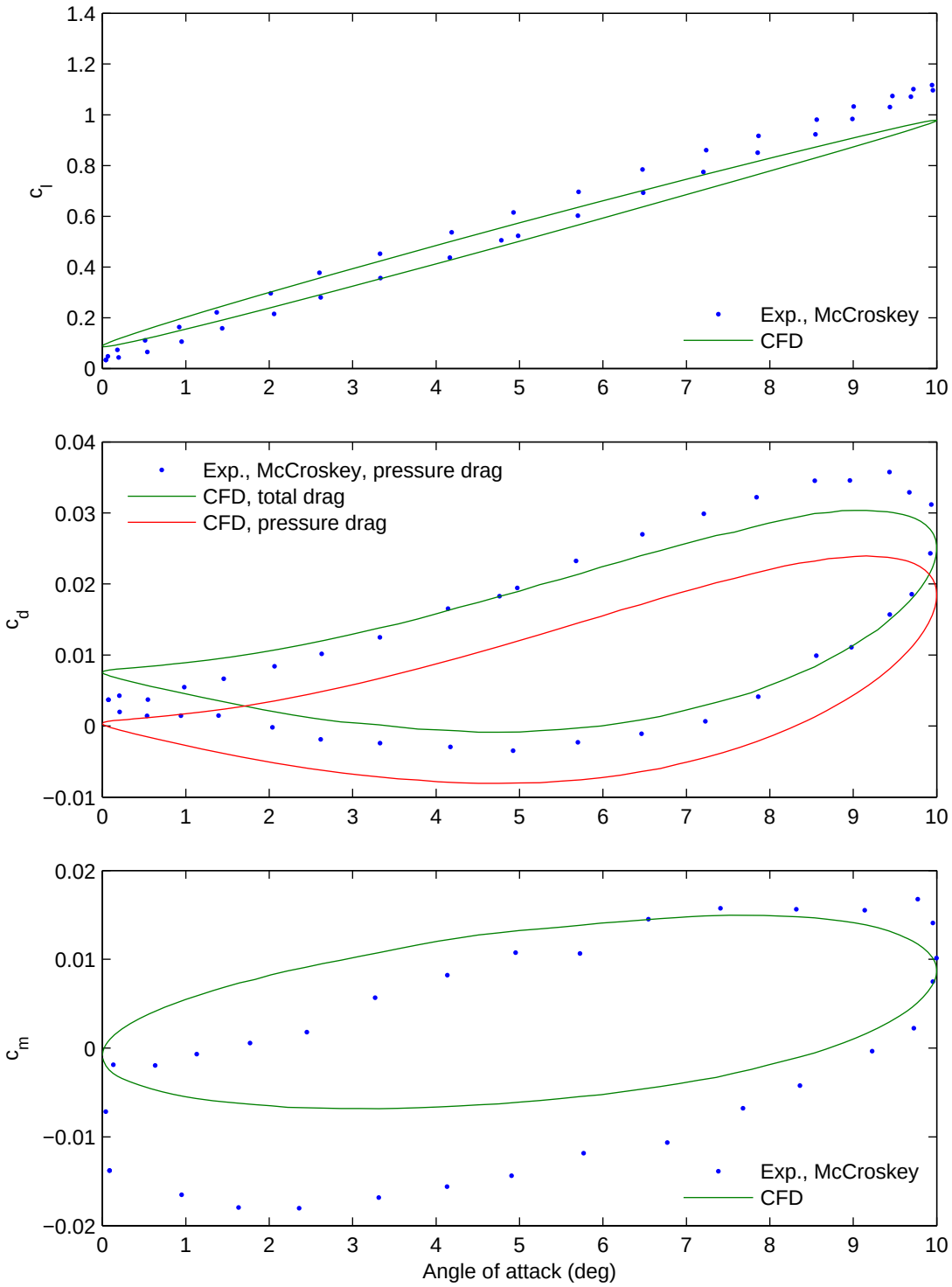

Figure 5.26: *Validation with the results of McCroskey et al. (1982, frame 10221), digitized from Tuncer et al. (1995, figure 4).*

disagreement in the static results at an angle of attack around 15 degrees. As shown by Ekaterinaris and Menter (1994), it is necessary to model this flow as transitional to produce good agreement with the experimental data.

In summary then, the validation of oscillating airfoil simulations suggests the following:

- For fully attached flows, the agreement between fully turbulent CFD simulations and tripped experiments is very good or good for the lift and moment coefficients. For the pressure drag coefficient, the CFD results show values that are lower by an approximately constant amount.
- For mildly separating flows, and again comparing fully turbulent CFD to tripped experiments, there is a general deterioration in the agreement.
- In comparing fully turbulent CFD simulations to untripped experiments, there is poorer agreement between dynamic results than between static results.

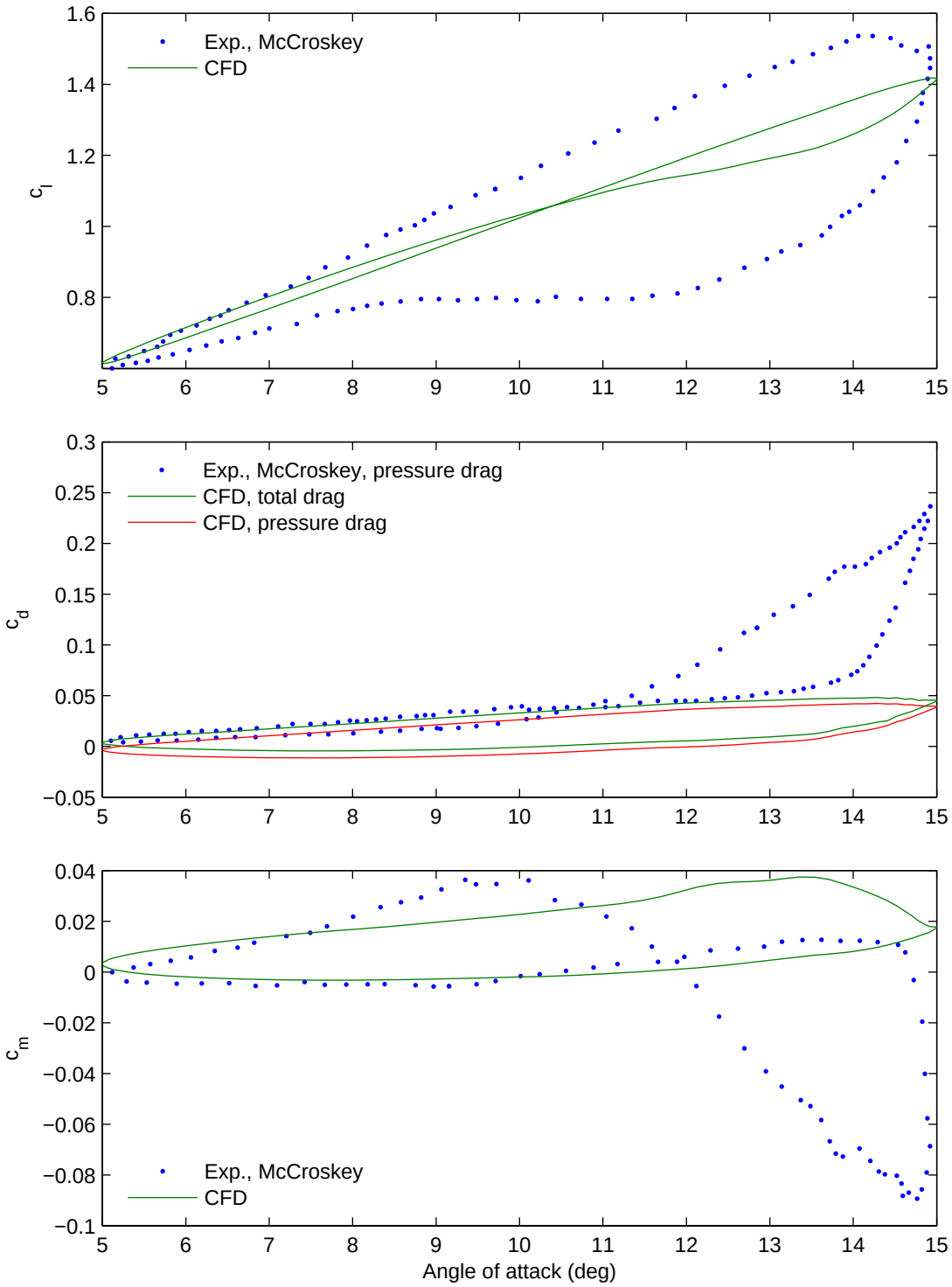

Figure 5.27: *Validation with the results of McCroskey et al. (1982, frame 7113 or 10208), digitized from Ekaterinaris and Menter (1994, figure 8).*

5.6 The NACA 0024 airfoil

The NACA 0024 section is simulated in order to generate section data for use in the blade element momentum model. No verification or validation is carried out, this being justified by the foregoing work. The lack of validation is also a result of the fact that no suitable experimental data were found, as discussed in section 2.2.2.8.

Comparisons are made with the section data of Sheldahl and Klimas (1981), but these are not considered as validation because of the nature of the data. As discussed in sections 2.2.2.4 and 2.2.3.1, the data for the NACA 0025 section comprise panel method results for the 0025 section at low angles of attack ($\alpha \leq 27°$) and experimental results for the 0015 section at high angles of attack ($\alpha \geq 30°$). In making comparisons between the present results and this data the small increase in thickness from the 0024 to the 0025 for the low angle of attack data is not thought significant, and comparisons with the high angle of attack data are less important.

Steady state simulations were run at Reynolds numbers of 0.16×10^6, 0.36×10^6, 0.70×10^6, 1×10^6, 2×10^6, 5×10^6, the results of which are shown in figure 5.28 alongside the data of Sheldahl and Klimas (1981). Considering the lift data in the top row of the figure, the agreement between the two data sets is generally good up until the point of $c_{l_{\max}}$, as given by the present CFD results as 13–17° depending on the Reynolds number. The Sheldahl and Klimas data shows a steeper slope though, and less variation with the Reynolds number. For angles of attack greater than 13–17° the CFD results show a drop in lift associated with stall whereas the Sheldahl and Klimas data show a continuing increase in the lift, albeit at a reduced slope. For angles of attack between 27 and 30 degrees, the Sheldahl and Klimas data is interpolated between the numerical and experimental data, hence the abrupt drop.

Results for the drag are compared in the middle row of the figure. In general, the pattern is as would be expected from comparing the lift, with the CFD results showing an earlier increase in the drag coincident with earlier stall. For low angles of attack the CFD results also show higher drag. This is expected given that we are comparing fully turbulent CFD results with the (presumably) transitional results of Sheldahl and Klimas (this is not specified). Sheldahl and Klimas do not give results for the moment coefficient and so we cannot make a comparison for this quantity.

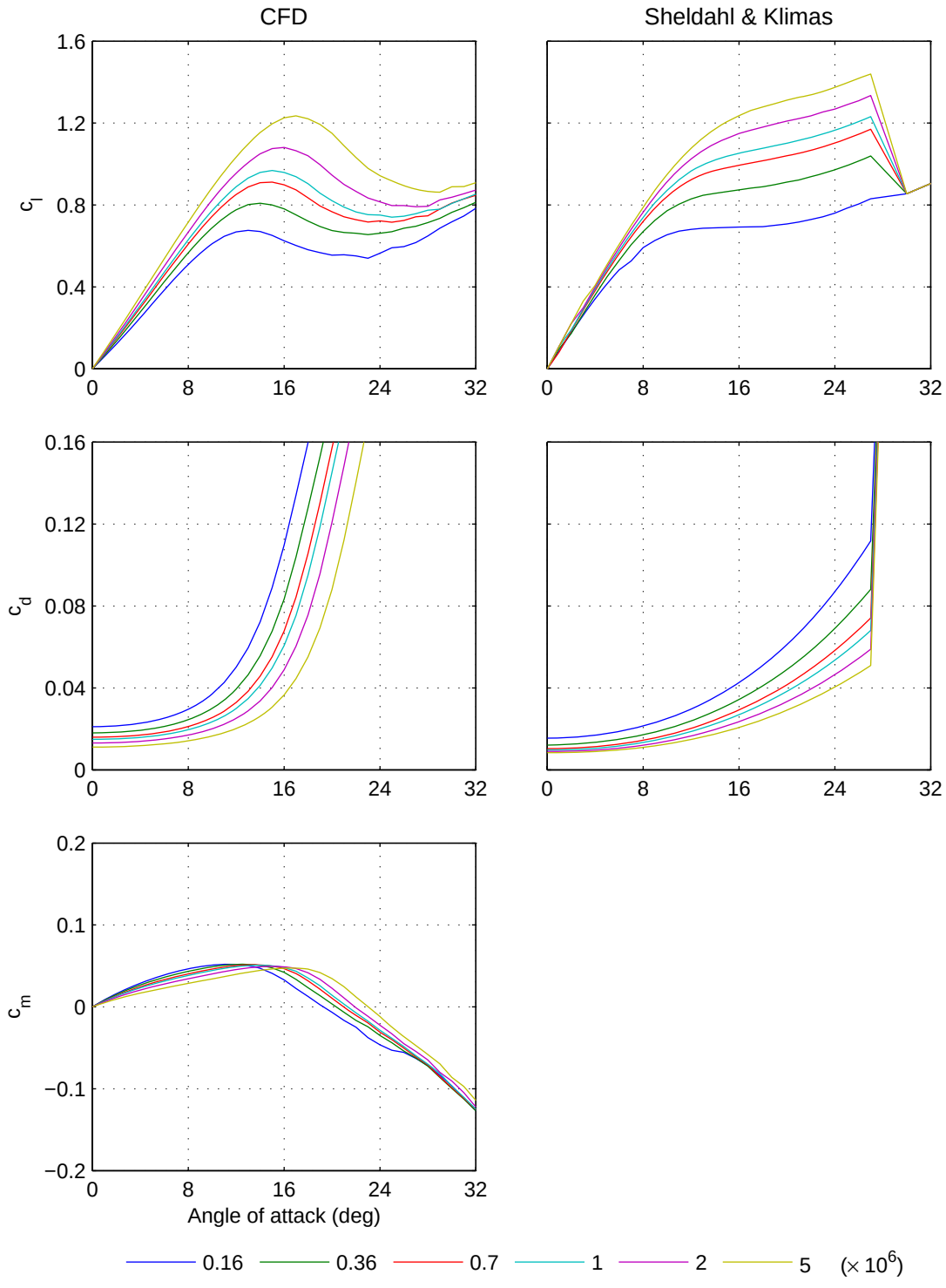

Figure 5.28: *Comparison of the results from the present CFD simulations (left column) with the hybrid numerical/experimental data from Sheldahl and Klimas (1981) (right column).*

5.7 Chapter conclusions

A number of specific conclusions can be drawn from the verification and validation work on airfoils presented in this chapter. These conclusions, which greatly inform the modelling of the turbine, are stated below.

From the NACA 4412 verification and validation study:

- The 'medium' C-grid (268×82 cells) gives discretization errors in the lift, drag and moment coefficient of less than 5% from the extrapolated value.
- Variation of the distance to the far-field boundary shows that this must be 80 chord lengths to reduce the error in the lift, drag and moment coefficients to less than 5% from the extrapolated value.
- Errors due to the spatial resolution or the far-field boundary position (as above) are largest for the drag and can be large: 21% on the extra-coarse grid and 26% for a grid with far-field boundary at 10 chord lengths.
- Variation of the inlet turbulence has little effect ($< 1\%$ change).
- Inclusion of the transition strip in the grid geometry has a small effect on the drag (3% change).
- Use of a compressible flow simulation has a small effect (3% change for lift and drag, 7% change for the moment).
- Fine spatial discretization is required in the wake to reduce the residuals to a low level.
- All simulations overpredict lift and underpredict drag relative to experiment, as is commonly observed.

From the NACA 0012 verification and validation study:

- A change to an O-C grid structure from a C-grid structure while maintaining a similar spatial resolution has a small ($< 3\%$) effect on the lift and drag coefficients for moderate angles of attack ($\alpha \leq 12^\circ$).
- Specification of a set number of iterations (as opposed to a residual target) is the most reliable method of reducing the iteration error to a predictable level.

- High but localized residuals at the trailing edge can skew the residual norms.
- Very good or excellent agreement with experiment is observed at low angles of attack, this agreement deteriorating towards stall.

From the NACA 0015 validation study:

- Better results (relative to experiment) are seen for this relatively thicker section.

From the NACA 0012 and 0015 oscillating airfoil verification and validation study:

- The numerical requirements for such a time dependent simulation (number of cycles, time step and iterations per time step) are not onerous.
- Very good or good agreement with experiment is observed for the lift and moment for attached oscillating flows, but poor agreement is seen for the drag. This poor agreement is unexplained.

Chapter 6
The CFD analysis of turbines

6.1 Objectives

The objective of the present CFD analysis is to obtain results which give qualitative prediction of the flow field and wake and quantitative prediction of the forces and moments. The level of quantitative accuracy required was not defined at the beginning of the research as this would be informed by the developing understanding of the trade-off between accuracy and computational burden.

6.2 Design of the computational mesh

The basic geometry of the computational mesh of the turbine was dictated by a few key parameters. First, the region immediately around the blades uses the inner part of the two-domain grid developed for the airfoil studies and discussed in section 5.3.1. This extends to a radius of $2c$ from the quarter chord point of each blade. Around each of these 'blade' domains is the 'rotor' domain which extends to a radius of one turbine diameter from the axis of rotation of the turbine. Outside of the rotor domain is the 'stator' domain which extends to a distance of 40 turbine diameters. This distance was selected such that the computational domain would extend well into the asymptotic region of the wake behind the turbine. A view of the stator and rotor meshes is shown in figure 6.1. Further details of the design of the rotor and stator domains are given below.

6.2.1 The rotor domain

The rotor domain was created as a 'pie-slice' with a circular hole for the blade domain and then copied to create a full 360° mesh. An unstructured extruded triangular mesh was used for this domain as no advantage was seen in the use of a hexahedral mesh given that there is no dominant flow direction, and given the complicated geometry which would likely lead

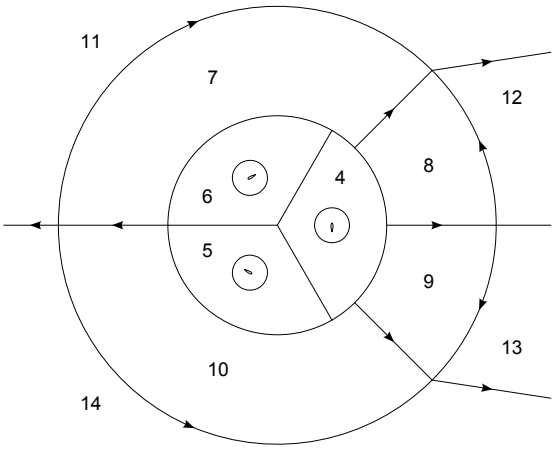

Figure 6.1: *Block structure of the mesh used for the turbine. The sub-division of the blade domains (blocks 1–3) is not shown; for this see figure 5.8.*

Table 6.1: *Node counts by domain.*

	coarse	medium	fine
blade	8344	32880	130528
rotor	15854	60200	241202
stator	17640	69840	277920
total	58526	228680	910706

to skewed cells. Edge elements from the blade and stator domains were respected at the appropriate boundary. For the medium mesh a spacing of $0.25c = 0.02D = 0.05$ m was specified for the creation of the triangular surface mesh. Prior to running the surface mesher, edge elements were created along the radial edges of the pie slices in order to ensure a 1:1 correspondence when the mesh was copied. Again for the medium mesh, 52 elements were specified giving $\Delta x = 0.019$. Node counts for each domain of the medium mesh, and for the coarse and fine mesh which used a linear coarsening/refinement ratio of 2, are shown in table 6.1. Views of the rotor mesh and its relation with the blade and stator meshes are shown in figures 6.2 and 6.3.

6.2.2 The stator domain

An O-grid structure was used for the stator domain, consisting of first a regular O-grid and then a skewed O-grid (proceeding outwards). The regular O-grid extends to a radius of 4 turbine diameters, and was used to give orthogonal cells at the rotor/stator interface, while the skewed O-grid was used beyond this to increase the density of cells in the wake region.

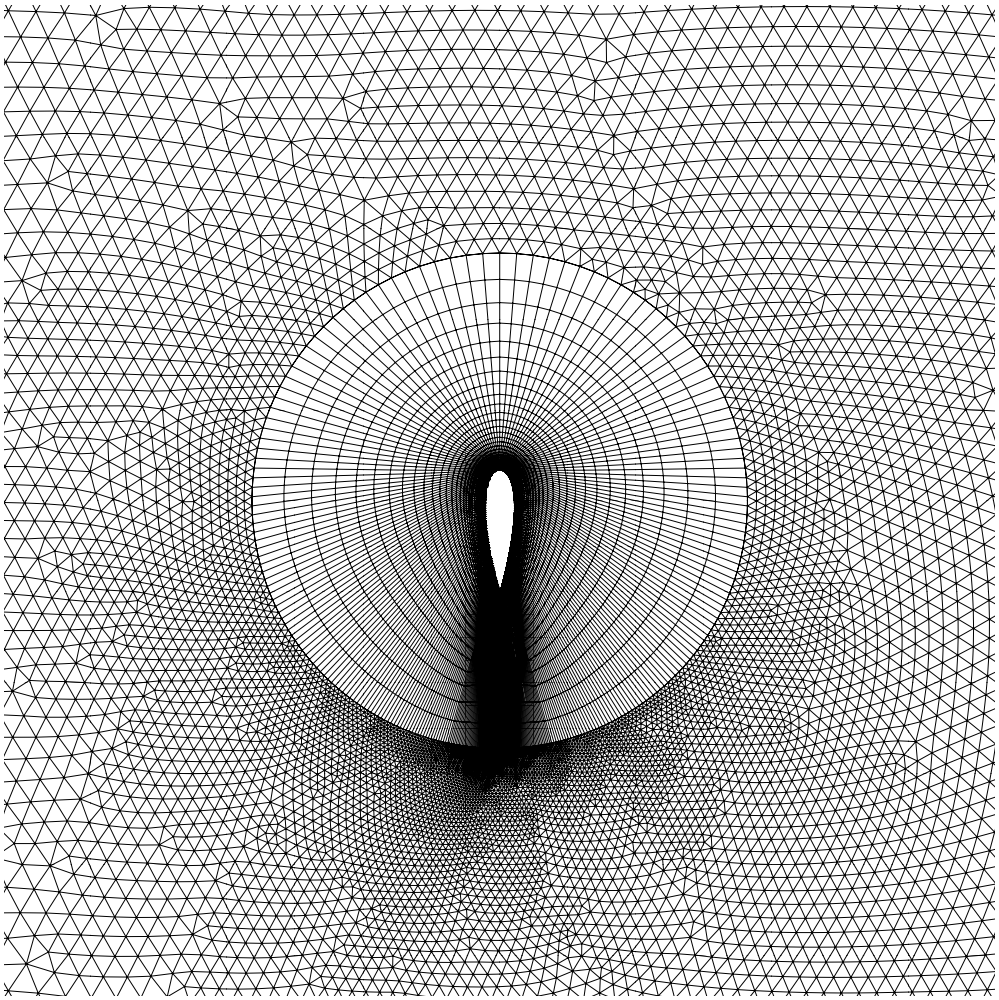

Figure 6.2: *View of the O-C-grid grid around the turbine blade and a partial view of the rotor mesh.*

For the medium grid 360 cells were specified in the circumferential direction in order to give a 1:1 correspondence across the interface when an angle step of 1 degree or larger is used. This gives a circumferential spacing at the rotor/stator interface of somewhat less than $D/40$. Node counts, spacings and growth ratios for other edges are specified in table 6.2.

6.3 Boundary conditions and fluid models

6.3.1 Inlet turbulence

Two papers reporting observational data on tidal flows were examined in detail in section 2.6.4. From these papers it was concluded that a tidal turbine operating near the top of the water

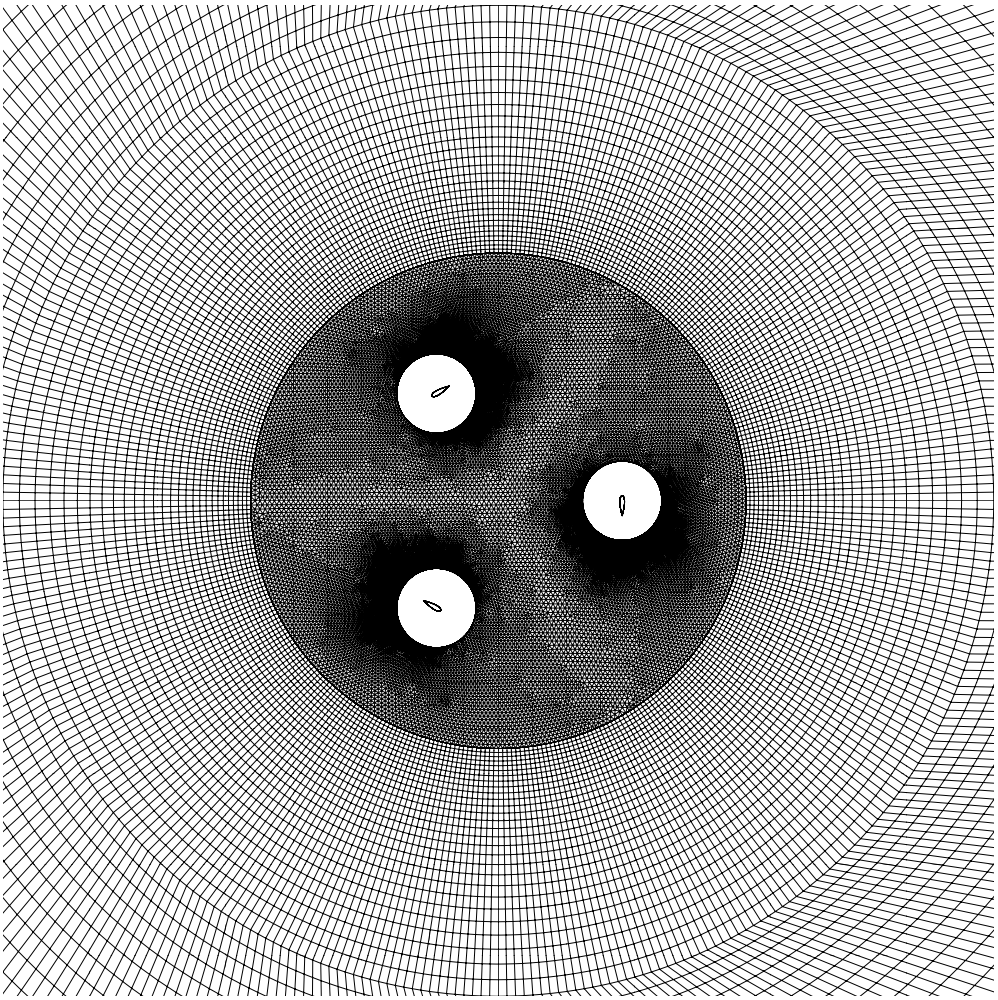

Figure 6.3: *View of the O-grid mesh for the stator domain and the unstructured triangular mesh of the turbine domain. The width of the view is equal to 8 turbine diameters, corresponding to the width of the regular O-grid.*

column (i.e. in the top 10%) may experience turbulence with an intensity of around 2% and having a length scale of tens or hundreds of metres. Given that the length scale of the turbine (based on the diameter) is of the order of metres, the latter presents a particular challenge.

The eddy viscosity ratio based on these values would be between 5×10^4 and 5×10^5. In comparison, the *CFX-Solver Modelling Guide* suggests a value of 100 for high turbulence (and 10 and 1 for medium and low turbulence respectively). Values for tidal flows are thus several orders of magnitude higher than that for which the turbulence models in CFX are calibrated.

For the present study it was decided to adopt values within the range for which the SST k-ω turbulence model was calibrated. At the inlet the turbulence intensity was specified as 5% and

Table 6.2: *Block edge parameters used in constructing the medium O-grid for the turbine stator domain. Edges are identified by the blocks that they separate – see figure 6.1. Notation as per table 5.1.*

Adjoining blocks (numbers and descriptions)			n	Δx_a	r_a	Δx_b	r_b
Circumferential spacings							
4–6	7–10	rotor – stator domains	361	0.0436	–	–	–
7–10	11–14	inner O-grid – outer O-grid	361	0.0873	–	–	–
11	FF	outer O-grid – far-field	136	1.497	1.0	1.1	1.05
12	FF	outer O-grid – far-field	46	0.0873	1.0589	1.084	–
Radial spacings							
7	8	regular O-grid	29	0.04	1.054	0.167	–
11	12	skewed O-grid	69	0.176	1.05	4.717	–

the eddy viscosity ratio as 100 giving a turbulent intensity at the turbine of around 0.1% (based on equation 3.79). This value is the same as that seen by the airfoils in the simulations reported in the previous chapter (see section 5.2.6).

6.3.2 Sea water properties

The fluid was specified as sea water; values for the density and viscosity were taken from White (2006, p. 576), namely $\rho = 1025$ kg/m^3 and $\mu = 1.07 \times 10^{-3}$ kg/(m $\cdot$ s).

6.4 The effect of time step and total time on the coarse mesh solution

A series of simulations were performed on the coarse mesh in order to determine the maximum time step size and also the total time that the simulation must be run for in order for a periodic steady state to be reached. The results from a coarse grid solution are also desired for use as the initial guess during the grid convergence study, and during the investigation of the physical parameters.

Selecting a suitable time step is a significant problem because of the wide range of time scales in the model. We want a small time step in order that the turbine blades do not rotate too far from one time step to the next, but we want a large time step in order to establish the wake behind the turbine as quickly (computationally) as possible.

The time step is discussed not in terms of time, but in terms of the angle that the turbine rotates in one time step. It is felt that this is a suitable way of non-dimensionalizing the time step. The time step size will thus be:

$$\Delta t = \Delta\psi/\Omega = \Delta\psi\, R/(\lambda U_\infty) \tag{6.1}$$

Angle steps of 1, 2, 4, 8 and 16 degrees were used.

It is also instructive to look at the distance a parcel of fluid will be convected in the time it takes the turbine to complete one revolution. Assuming that the convection speed is the free stream speed:

$$\Delta x = U_\infty T = U_\infty 2\pi/\Omega = 2\pi R/\lambda \tag{6.2}$$

$$\Delta x/D = \pi/\lambda \tag{6.3}$$

Thus for the tip speed ratios of interest, $\Delta x/D$ will be approximately 1. Note that this parameter is not related to the numerics.

If we reason, *a priori*, that the performance of the turbine will be strongly influenced by the initial region of the wake which extends perhaps 10 diameters downstream of the turbine, but less so by the wake beyond this, then we will have to run the simulation for at least 10–20 revolutions. More will be required because the wake is convected at a speed less than the free stream speed. Based on the above, the simulations were run for 100 revolutions.

6.4.1 Forces and moments on the blades

Figure 6.4 shows the non-dimensionalized forces and moment F_T^+, F_N^+, M^+ on blade A. Taking as our reference the solution with the smallest angle step (1 degree), it is immediately apparent that the solution having an angle step of 16 degrees gives erroneous results for both forces and the moment. The solution having an angle step of 8 degrees shows qualitatively correct behaviour. Notable differences from the reference solution occur for the two forces between azimuth angles of 270 and 360 degrees and for the moment at all azimuth angles. With an angle step of 4 degrees the solution only differs significantly from the reference in the case of the moment. The two solutions having the smallest angle steps show consistent behaviour.

A quantitative analysis of the results from the solutions with angle steps of 1, 2, 4 and 8 degrees is given in table 6.3. The greatest deviations are shown when comparing the results for the

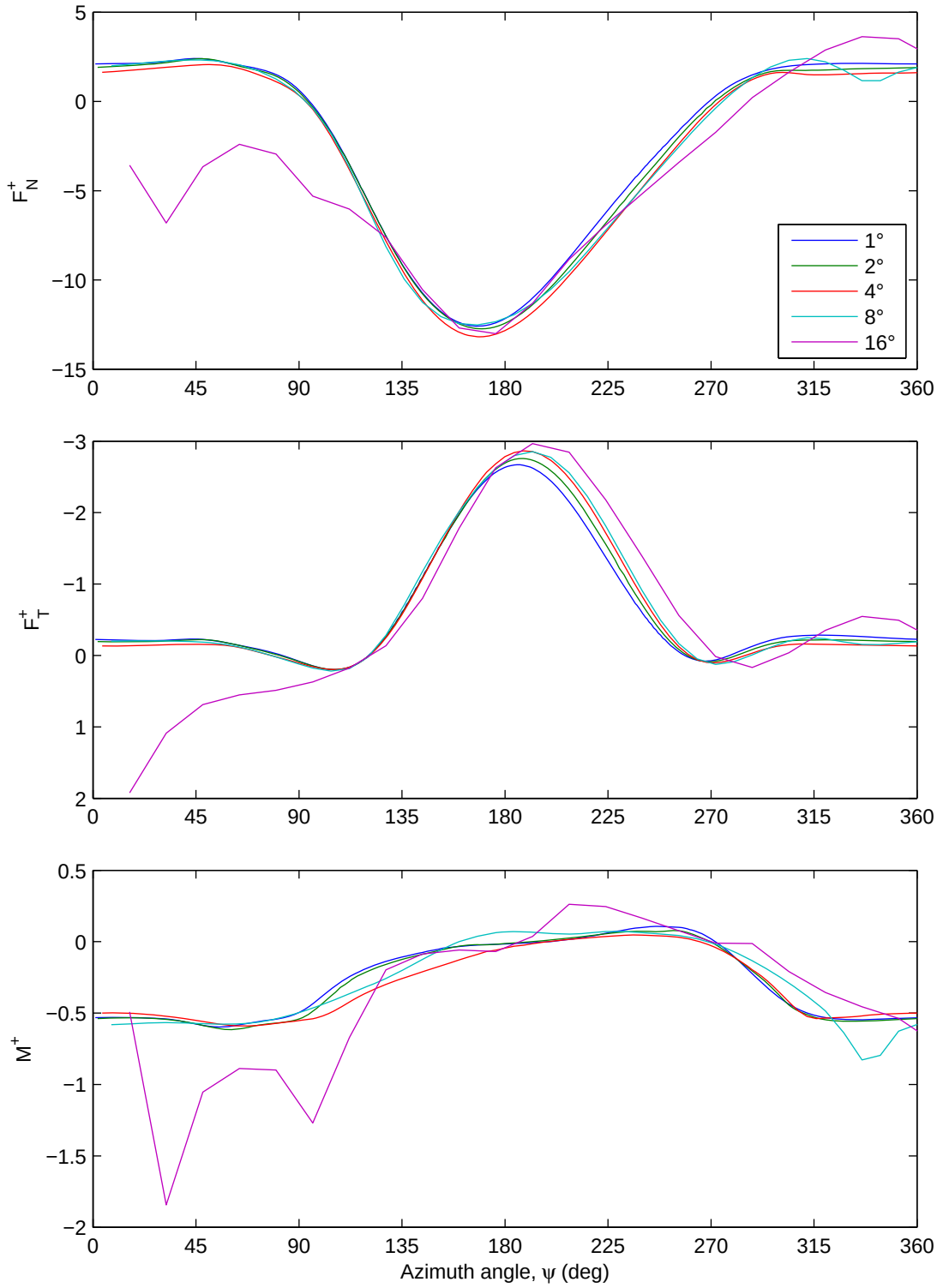

Figure 6.4: *Forces and moment on blade A with azimuth angle for five different values of the angle step (see legend). All results are for the 100th revolution.*

Table 6.3: *Maximum, minimum and mean values of F_N^+, F_T^+ and M^+, percentage deviations thereof from the reference case, and normalized route mean square deviation.*

$\Delta\psi$	max	min	mean	% max	% min	% mean	% NRMSD[a]
			F_N^+				
1°	2.405	−12.591	−2.525	–	–	–	–
2°	2.389	−12.739	−2.738	−0.68	1.18	8.43	1.81
4°	2.065	−13.178	−3.045	−14.17	4.66	20.63	3.86
8°	2.403	−12.521	−2.866	−0.11	−0.55	13.53	3.46
			F_T^+				
1°	0.199	−2.671	−0.642	–	–	–	–
2°	0.196	−2.757	−0.655	−1.50	3.22	1.98	2.38
4°	0.198	−2.865	−0.659	−0.70	7.26	2.70	4.88
8°	0.218	−2.855	−0.687	9.22	6.88	7.09	5.60
			M^+				
1°	0.108	−0.597	−0.267	–	–	–	–
2°	0.078	−0.616	−0.278	−27.34	3.12	4.19	2.84
4°	0.046	−0.590	−0.300	−56.92	−1.23	12.50	10.14
8°	0.071	−0.828	−0.282	−33.78	38.57	5.82	12.29

[a] Normalized by the range of the reference solution.

maximum value of the moment; this is largely due to the maximum value being small. Of primary interest is the mean value of the tangential force as this contributes most to the average power output of the turbine (a small contribution also comes from the moment). Defining an acceptable error from the best solution as being 5%, the solution with an angle step of 8° is discounted. Considering other parameters, and in particular the normalized RMS deviation in the moment, it is felt that the solution with an angle step of 2° is to be preferred.

The development of the solution with an angle step of 2 degrees is shown in figure 6.5. The forces and moment on the blade are plotted with azimuth angle during the nth revolution; it would appear that the behaviour is asymptotic. A quantitative analysis of this behaviour is given in figure 6.6, which shows how the results for a given cycle deviate from those during the final (100th) cycle. Clearly the behaviour is indeed asymptotic, and by visually extrapolating from the broadly straight portion of the curves (say between 20 and 80 cycles), it can be argued that the deviation in the final result from the asymptotic result is negligible. We thus interpret the deviation from the final result as being practically equivalent to the deviation from the asymptotic result.

Focusing on the deviation in the mean value of the tangential force we may identify certain boundaries: the deviation is approximately 10% for the 10th cycle, 5% for the 20th cycle and 1% for the 40th cycle. This gives a clear basis for specifying how many revolutions to run the simulation for.

6.4.2 *U*-velocity along the wake centreline

We now examine the effect of the time step and the total time on the predicted flow field. Figure 6.7 shows the non-dimensional U-velocity ratio U/U_∞ on a line parallel to the free stream and normal to the turbine axis. Each graph shows the velocity at ten different times during the simulation, while the five graphs correspond to simulations having different time/angle step. Note that the sharp spike in all graphs at $x/D = 0.5$ is due to the presence of a turbine blade. The qualitative agreement between simulations having angle steps of 1 and 2 degrees is excellent. For angle steps of 4 and 8 degrees, the salient feature of the minimum velocity in the wake occurring some distance (5–10 turbine diameters) downstream of the turbine is still captured. Interestingly, the minimum velocity in the wake predicted by the simulation having an angle step of 4 degrees is lower than that predicted by any other simulation. The simulation having an angle step of 16 degrees shows a velocity variation that is not in qualitative agreement with the other simulations. These trends clearly follow those for the forces, as indeed we would expect.

We may also examine figure 6.7 to see for how long the simulation must be run for the wake to develop. For the simulations having angle steps of 1 and 2 degrees, there is good agreement in the near wake (0–10 diameters downstream) after about 30 revolutions of the turbine. After this amount of simulation time the velocity variation further downstream also shows a smooth rise, although the wake is clearly not fully developed within the computational domain; this occurs after approximately 60 revolutions.

6.4.3 *U*-velocity profiles

The U-velocity profiles at eight locations in the wake are plotted in figure 6.8; each graph shows the results from four different simulations. All results are at a time when the turbine has completed 100 revolutions. We take the reference simulation as that with the smallest angle step — 1 degree. The simulation with an angle step of 2 degrees is the only one to predict

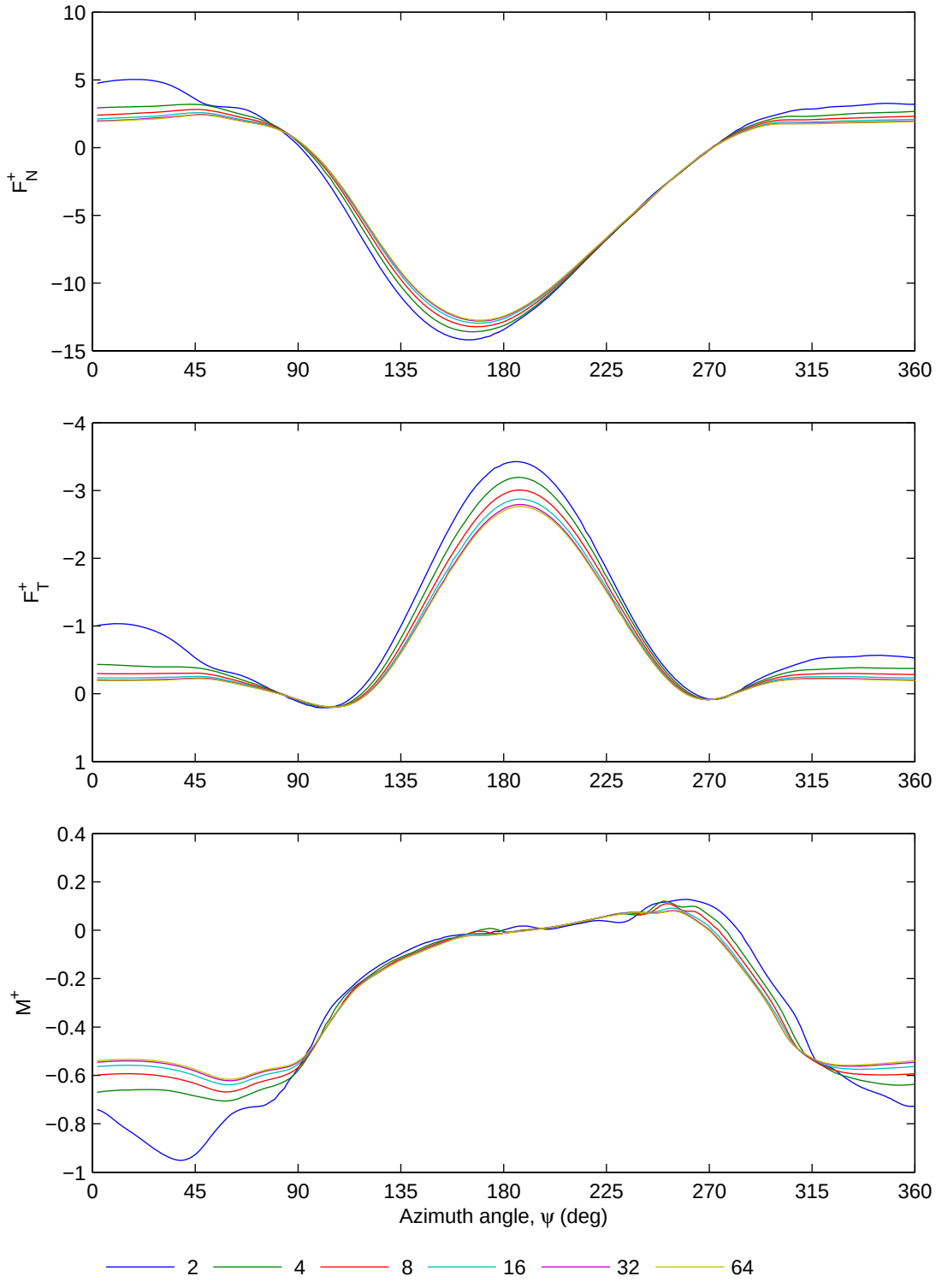

Figure 6.5: *Forces and moment on blade A with azimuth angle during different revolutions of the turbine. The number of revolutions completed is shown in the legend and applies when the blade azimuth angle is 360 degrees (as opposed to 0 degrees).*

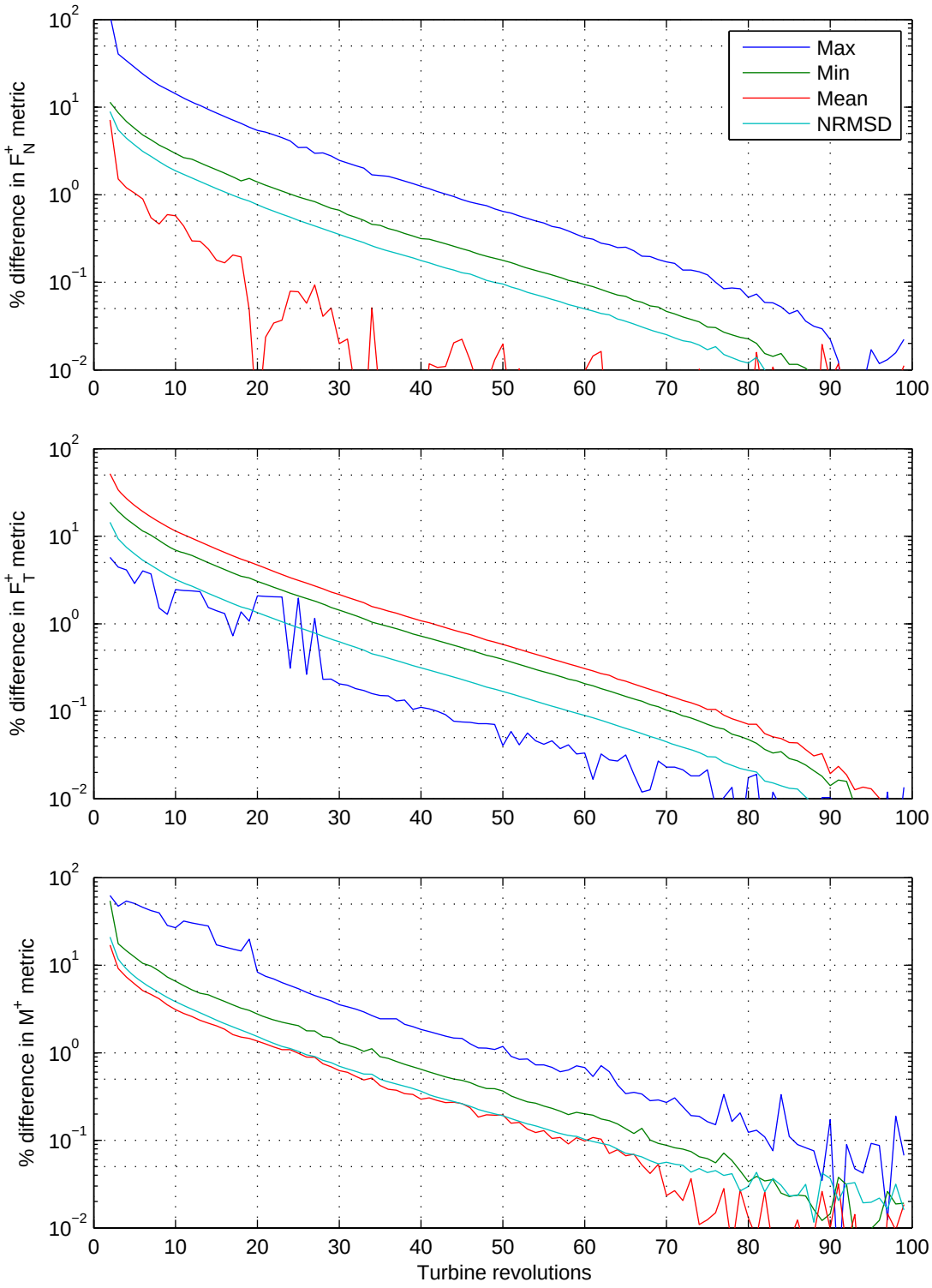

Figure 6.6: *Quantitative analysis of the development of the forces and moment on blade A. Values shown are the percentage deviations from the result during the final (100th) turbine revolution.*

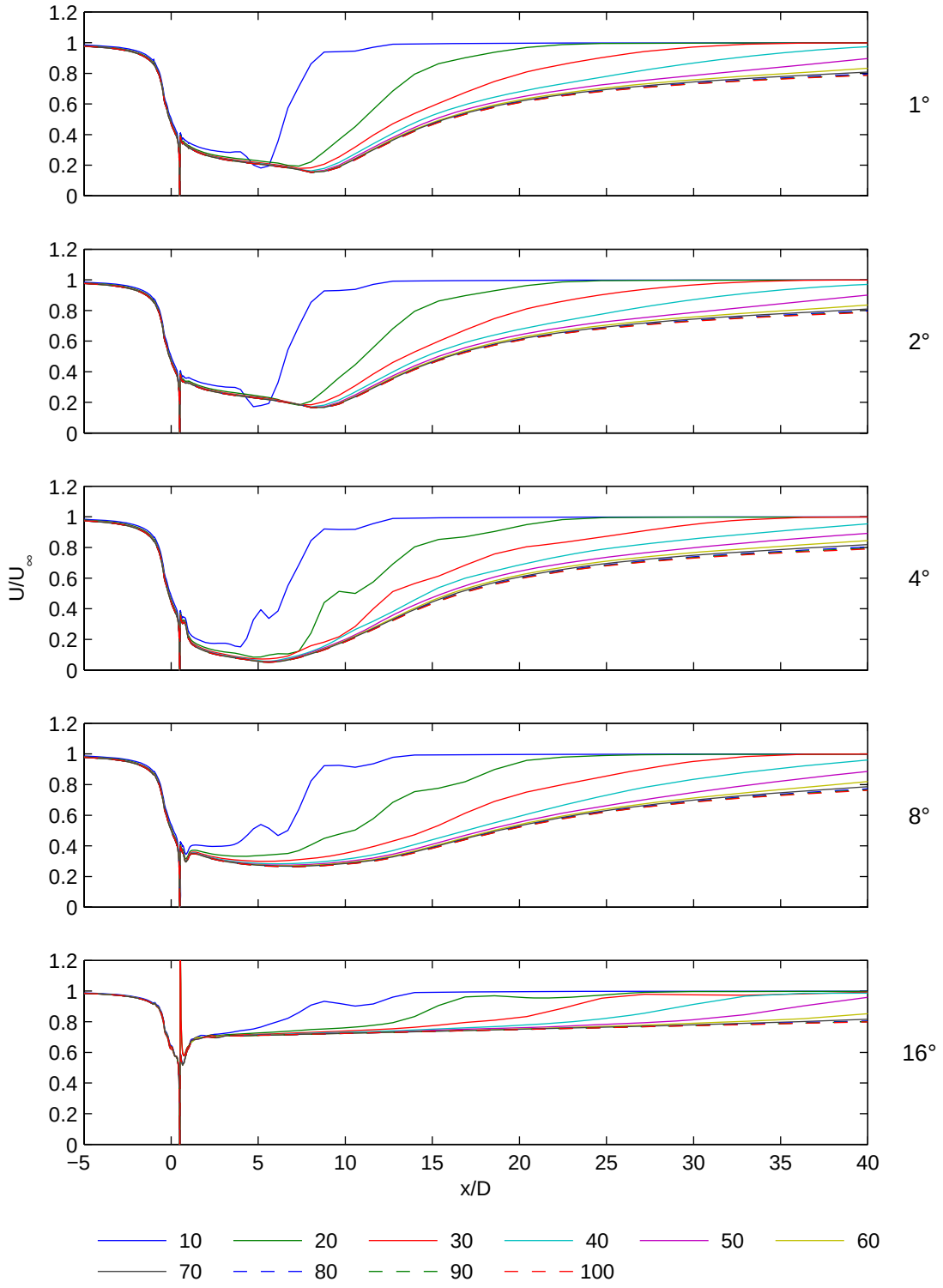

Figure 6.7: *U-velocity along a line parallel to the free stream and normal to the turbine axis. The legend shows how many revolutions the turbine has completed in each simulation. The different graphs correspond to simulations having angle steps of, from top to bottom, 1, 2, 4, 8 and 16 degrees, as indicated on the right of each axes.*

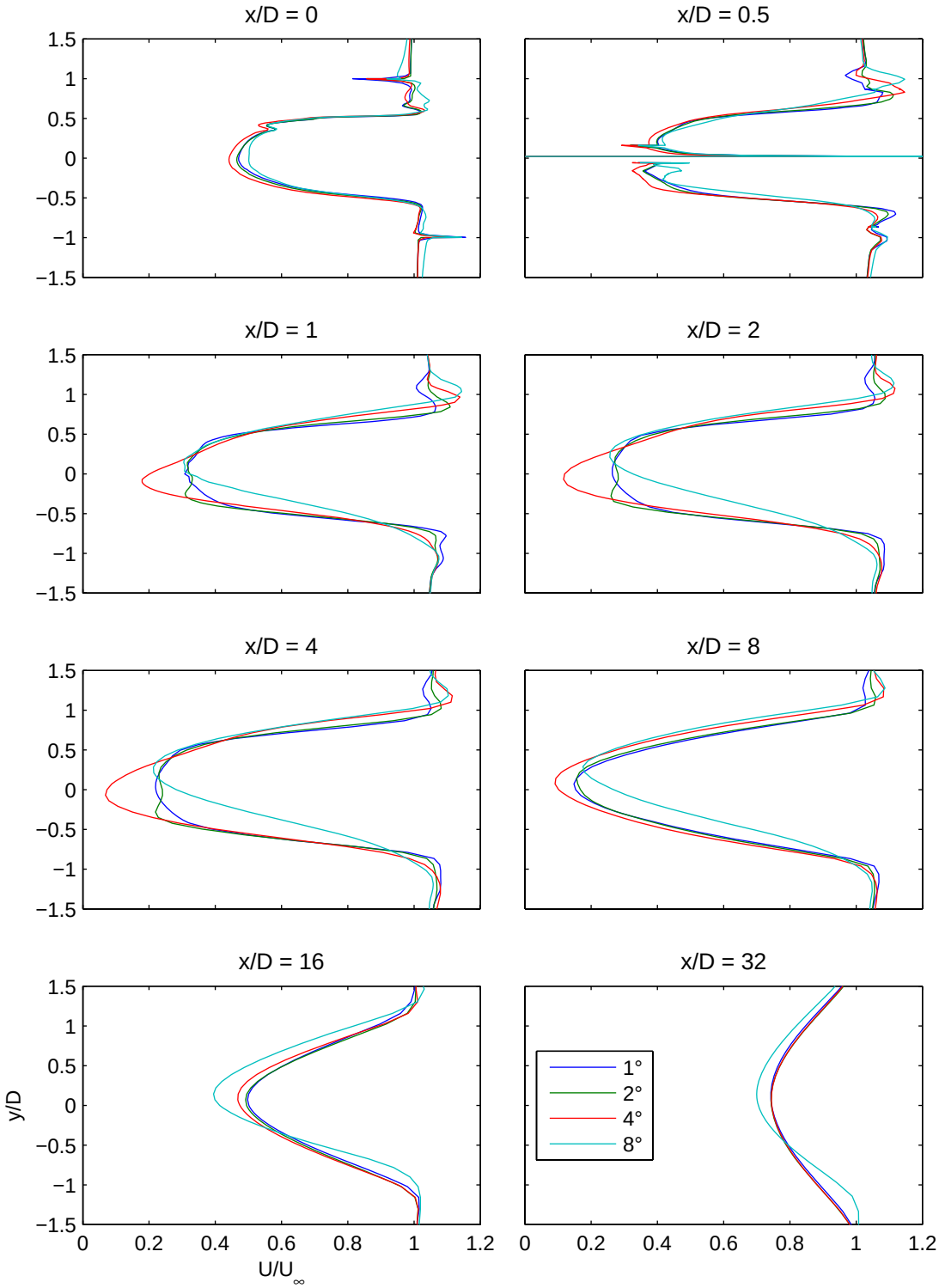

Figure 6.8: *U-velocity profiles at eight locations in the wake. The legend shows the angle step for the simulation. All results are for a time when the turbine has completed 100 revolutions.*

a velocity profile having two local minima at $x/D = 1$, 2 and 4. Otherwise, the agreement between the simulations with angle steps of 1 and 2 degrees is good. With an angle step of 4 degrees, the minimum velocity is lower than that predicted by the reference at all locations other than $x/D = 32$ where it is indistinguishable. The simulation with an angle step of 8 degrees has a minimum velocity close to that predicted by the reference for $x/D = 1$, 2, 4 and 8 degrees, but is lower for $x/D = 16$ and 32. At all locations the minimum is shifted in the positive y-direction.

Note that the spikes in the profiles at $y/D = \pm 1$ on the graph for $x/D = 0$ are a numerical artefact caused by the interface between the rotating and stationary domains. The perturbation owing to this is also seen at $x/D = 0.5$ and 1. Note also that the presence of the turbine blade is seen at $y/D = 0$ in the profile at $x/D = 0.5$.

Based on the analysis of the results in this and the previous two sections it is asserted that an angle step of 2 degrees shows the best compromise between accuracy and computational burden. A simulation time equal to 20 turbine periods would be sufficient to generate accurate force and moment data, but insufficient for the wake to be fully developed within the domain. It is judged that this requires approximately 60 turbine periods. Given the objectives set out at the start of this chapter it was decided to run the simulations for 60 turbine periods.

6.5 The effect of iterative convergence on the coarse mesh solution

All of the results presented in the previous section were produced with iterative solver parameters set to give 'loose' convergence. These parameters were a maximum number of coefficient loop iterations in each time step of three and an RMS residual target of 1×10^{-4}. The solution on the coarse mesh was also computed with these parameters set to give 'good' iterative convergence; namely a maximum of five coefficient loop iterations per time step and an RMS residual target of 5×10^{-5}. Note that no claim is made that the iterative convergence achieved by the specification of either 'loose' or 'good' iterative convergence parameters will indeed be loose or good; the terms are merely used to distinguish between solutions.

Figure 6.9 shows the results for the forces and moment on blade A during the 100th revolution of the simulation while table 6.4 gives a quantitative analysis of the deviation between the two simulations. The effect on the normal and tangential force of tightening the iterative

Table 6.4: *Maximum, minimum and mean values of F_N^+, F_T^+ and M^+, percentage deviations thereof from the reference case, and normalized route mean square deviation.*

Convergence	max	min	mean	% max	% min	% mean	% NRMSD[a]
			F_N^+				
loose	2.389	−12.739	−2.738	−0.92	1.91	16.18	3.39
good	2.411	−12.499	−2.356	–	–	–	–
			F_T^+				
loose	0.196	−2.757	−0.655	−1.63	5.91	5.24	4.76
good	0.200	−2.603	−0.622	–	–	–	–
			M^+				
loose	0.078	−0.616	−0.278	−39.65	4.69	6.17	3.80
good	0.130	−0.588	−0.262	–	–	–	–

[a] Normalized by the range of the reference solution.

convergence is broadly comparable to the effect of reducing the angle step from 4 degrees to 1 degree: both show, for example, NRMSD of 4–5%. The effect on the moment is perhaps less marked.

The residuals at each time step during the 100th revolution of the coarse mesh solution with good iterative convergence are shown in figure 6.10. All residuals show some variation during the turbine cycle, although this is less significant for the residuals in the pressure-mass equation. The pattern can be attributed to the changing positions of the three blades of the turbine. Clearly the highest residuals are in the U- and V-momentum equations. For all of the equations at all of the time steps the maximum residuals are approximately 100 times the RMS residuals.

A bar graph of the residuals at the final time step of the 100th revolution is given in figure 6.11. The highest residuals are of order 10^{-2} and are in the U-momentum equation in the domains around blades B and C and in the V-momentum equation in the domain around blade B. In each case the numbers of nodes concerned are in the tens. (See table 6.1 for node counts.) Investigation showed that all of the nodes at which the residuals were of order 10^{-2} were immediately at the trailing edge of the blade. This behaviour is directly comparable to that for the isolated airfoil studies where it was shown that such high but localized residuals did not affect the results.

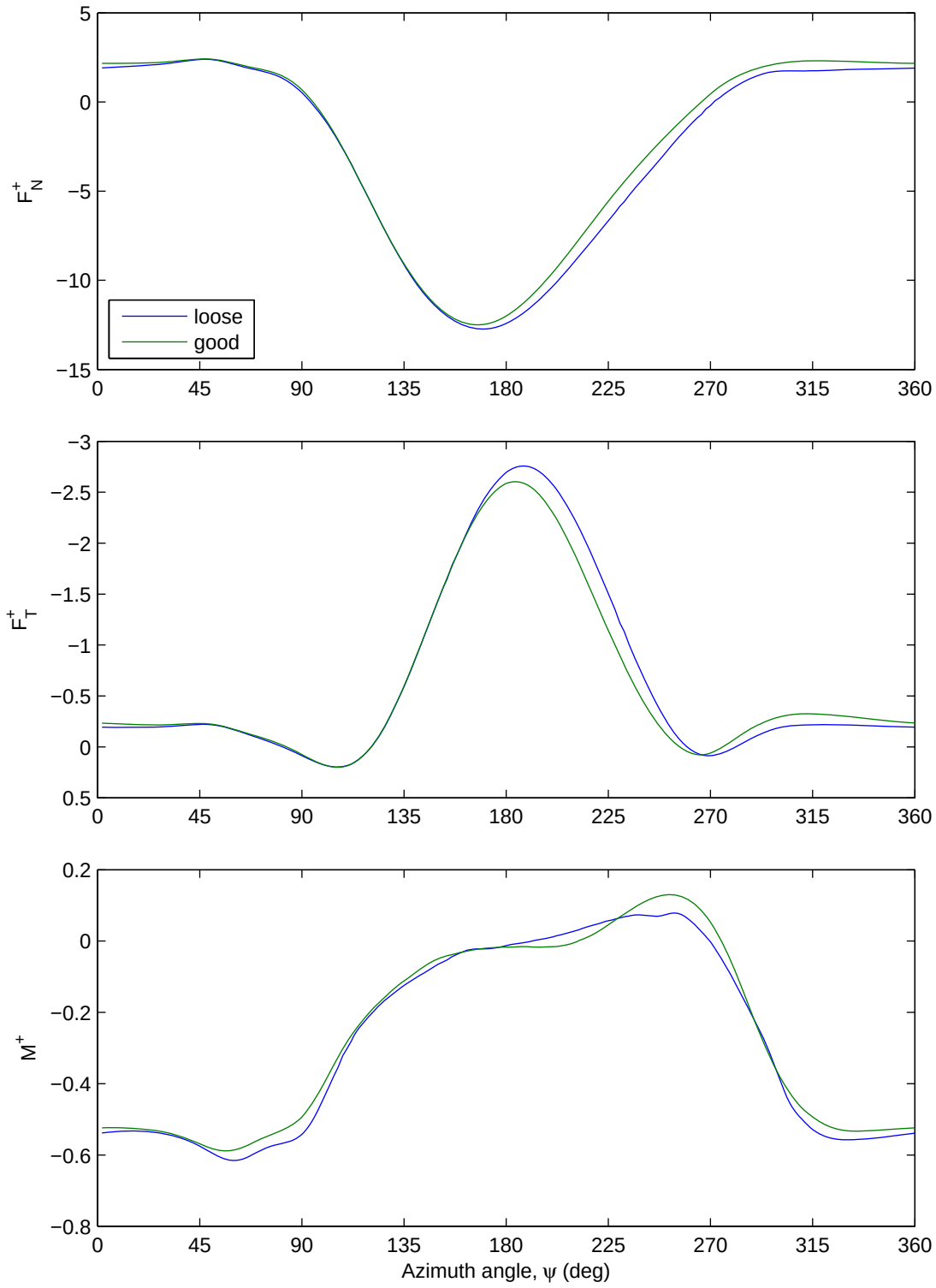

Figure 6.9: *The effect of iterative convergence on the coarse mesh solution. Results are for the 100th revolution.*

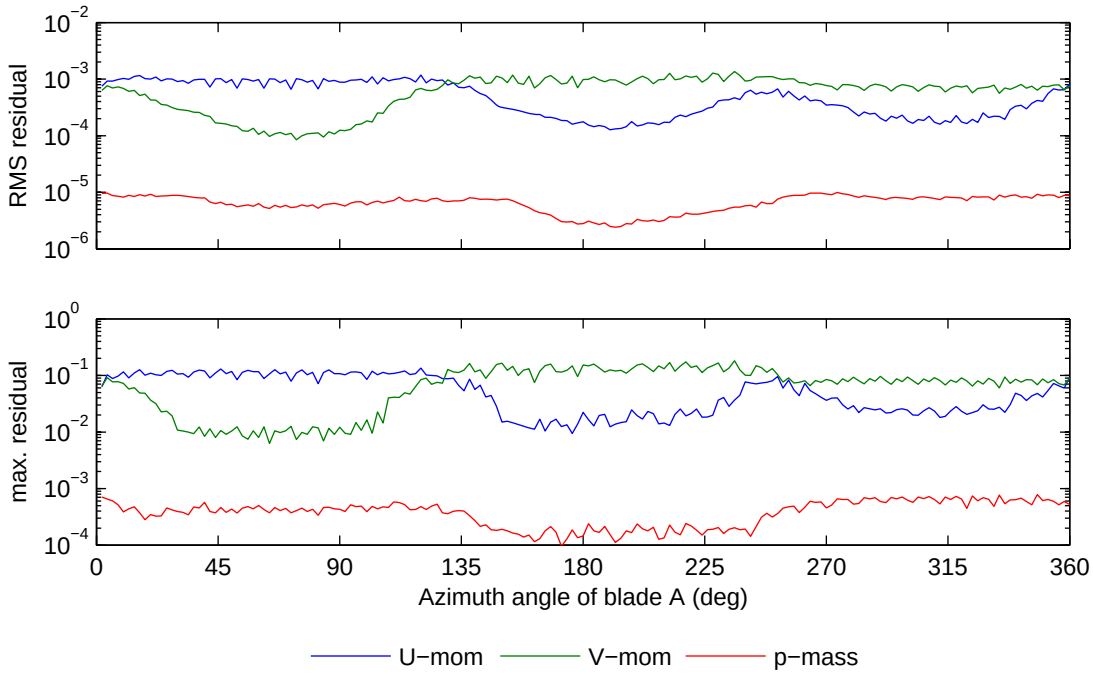

Figure 6.10: *RMS and maximum equation residuals during the 100th revolution of the turbine. The simulation was run on the coarse mesh with good iterative convergence. Note that the RMS and maximum residuals are plotted at different scales.*

Residuals of order 10^{-3} are found at roughly hundreds of nodes in the U- and V-momentum equations in the domains around blades B and C. These nodes were all found to be in the vicinity of the stagnation point near the leading edge of the blade. Such residuals are considered to be acceptable.

6.6 The effect of iterative convergence on the medium mesh solution

Simulations were run on the medium mesh with loose and good iterative convergence parameters to see if the trends observed for the coarse mesh solutions were repeated. Based on experience of the effect of total time on the coarse mesh solution, the medium mesh solutions were run for 60 turbine revolutions.

Figure 6.12 shows the forces and moment on blade A during the 60th revolution of the two medium mesh solutions and one coarse mesh solution. Interestingly, the medium mesh solution with a loose iterative convergence target shows an instability for some azimuth angles, most

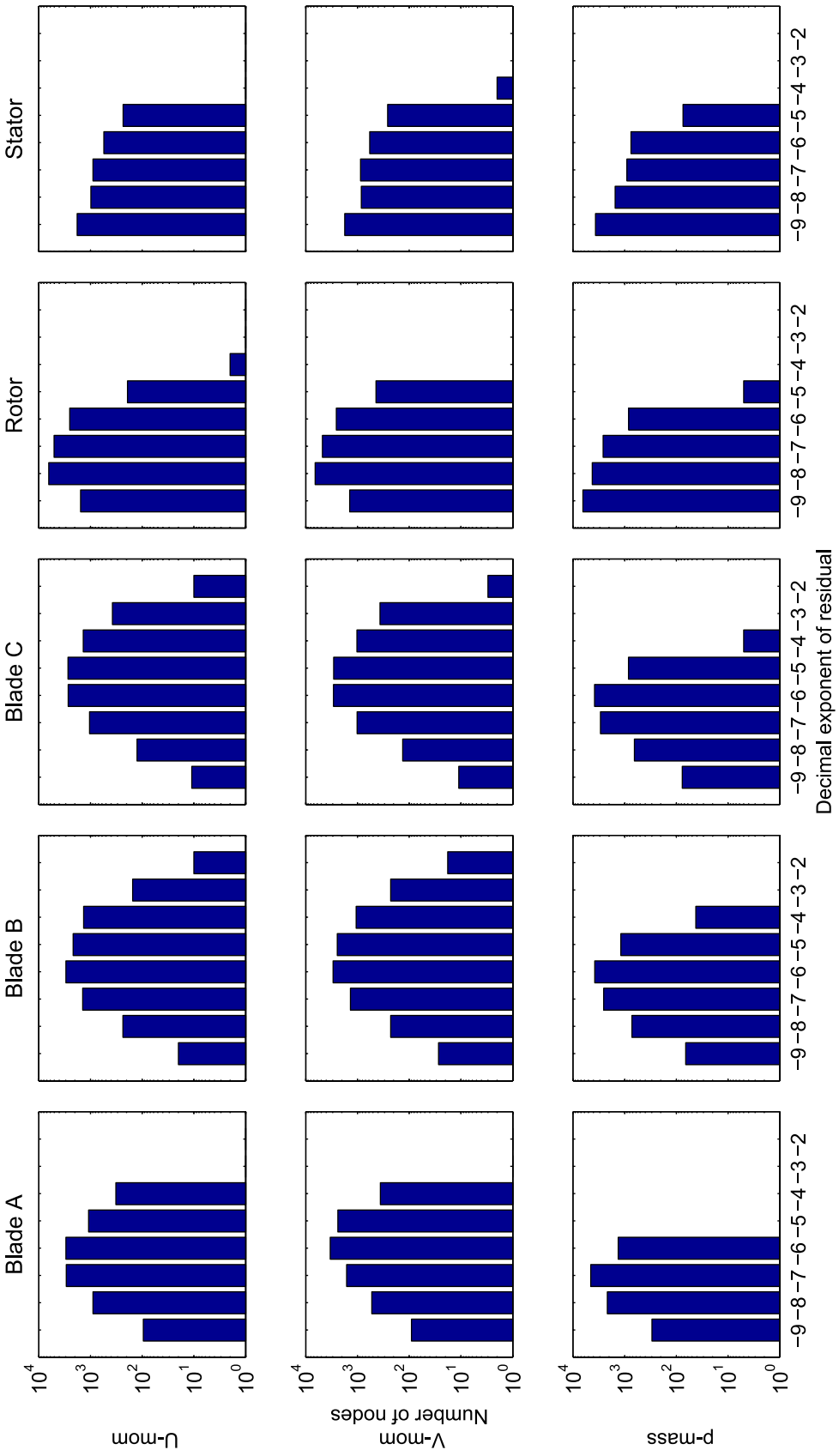

Figure 6.11: *Bar graph of residuals for the coarse mesh solution with good iterative convergence after 100 revolutions. The residuals are shown for each equation and for each domain.*

obviously for the moment. The azimuth angles for which this instability occurs (180–270°) are those for which the angle of attack on the blade is highest. Specifying good iterative convergence parameters eliminates the oscillation. In predicting the minimum tangential force on the blade, the change from the medium/loose solution to the medium/good solution is similar to that seen with the coarse mesh: namely a reduction in the value. Overall, the change from the coarse/good solution to the medium/good solution appears small.

The effect on the flow field of altering both the iterative convergence parameters and the mesh is examined in figures 6.13 and 6.14. All results are for a time equal to 60 turbine periods. The most noticeable difference occurs for the predicted wake profiles at $x/D = 1, 2, 4$ and is seen when comparing either of the coarse mesh solutions to either of the medium mesh solutions. (Note that in contrast to the prediction of the forces where changing the iterative convergence target was more significant than changing the mesh, the reverse is true for the prediction of the flow field.) This difference may be readily attributed to the greater levels of numerical diffusion in the solution on the coarse mesh.

An analysis of the residuals at the final time step of the medium/good solution is given in figure 6.15. This may be compared with the residuals for the coarse/good solution shown in figure 6.11. The number of nodes at which the residuals are of order 1×10^{-2} remains in the tens and there are again roughly hundreds of nodes at which the residuals are of order 1×10^{-3}. Given that the medium mesh contains approximately four times as many nodes we can interpret this as an improvement in the convergence. (See again table 6.1 for node counts.)

6.7 The effect of total time on the medium mesh solution

As noted previously, the medium mesh solutions were run for a total of 60 turbine periods. In order to confirm that a suitably developed state had been reached within this time interval the same analysis that was applied to the coarse mesh solution (see figure 6.6) was applied to the medium mesh solution with good iterative convergence. This is presented in figure 6.16. Focusing on the mean tangential force we can see that the error from the final value reduces to 10% after 10 turbine revolutions, 5% after about 16 revolutions, and 1% after about 35 revolutions. These compare closely with the results for the coarse mesh solution; the apparently quicker convergence being due to the fact that the final value is that at 60 turbine periods as opposed to 100.

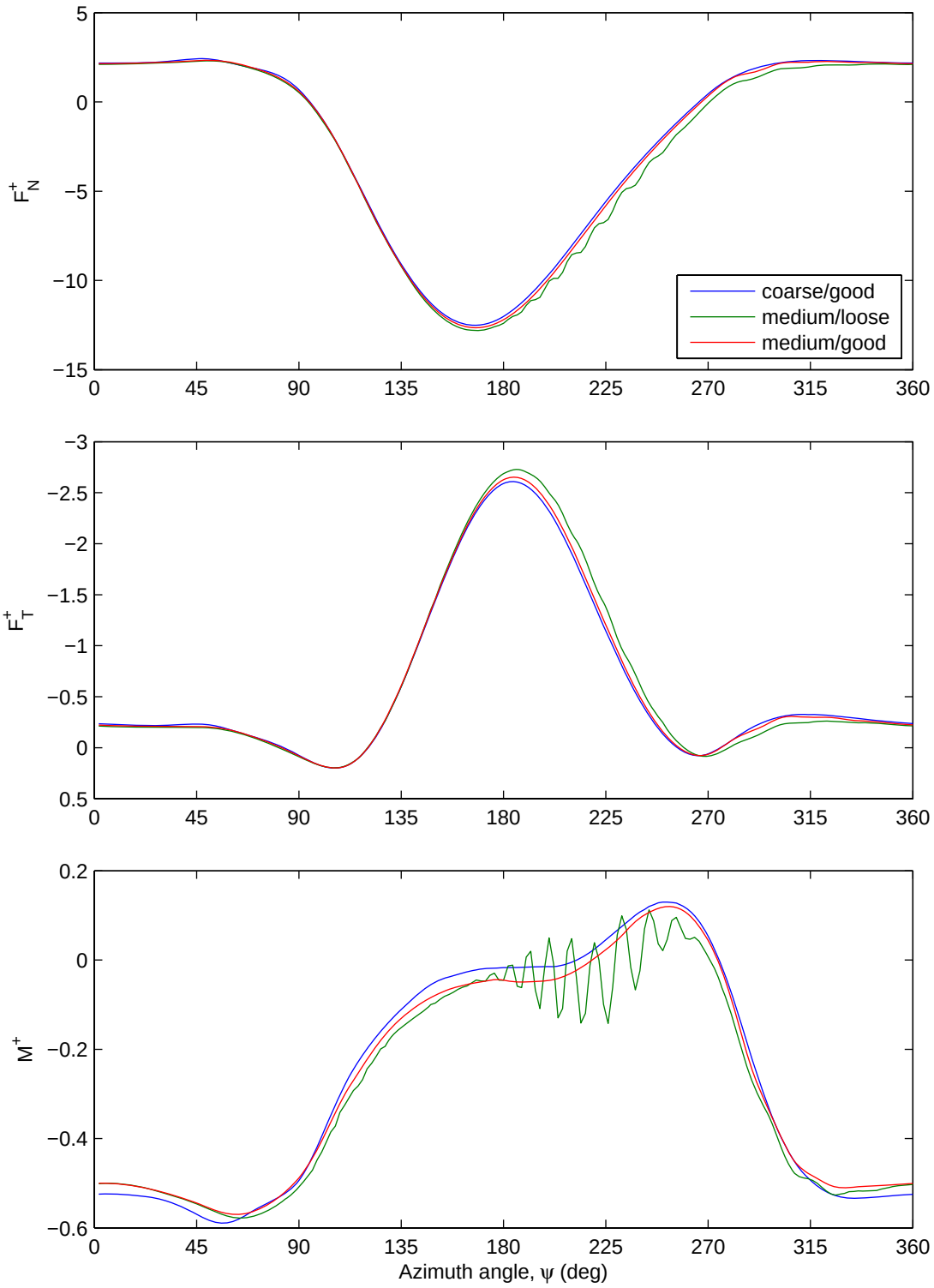

Figure 6.12: *Forces and moment on blade A during the 60th revolution.*

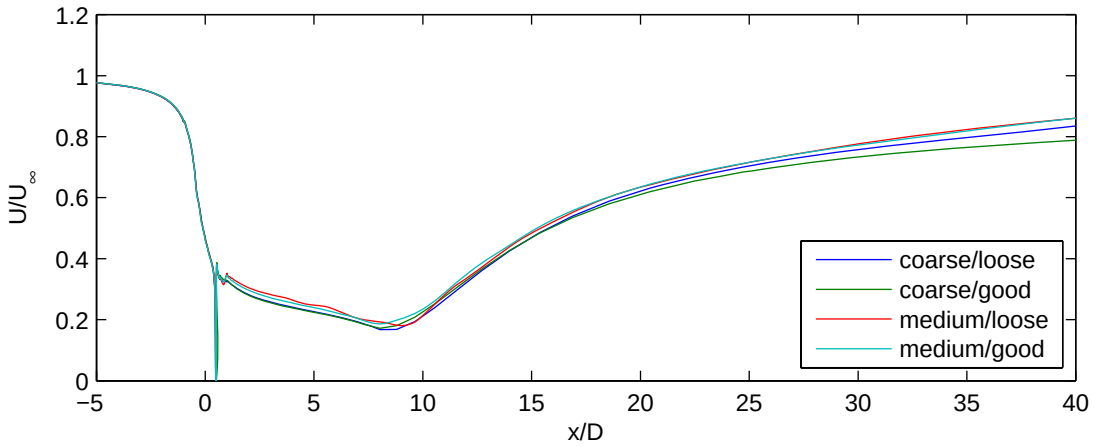

Figure 6.13: *U-velocity along a line parallel to the free stream and normal to the turbine axis.*

6.8 Grid convergence study

Results for the forces and moment on blade A for the coarse, medium and fine mesh solutions are shown in figure 6.17. Each solution used good iterative convergence parameters. The results shown are for the 20th revolution; this being as far as the fine mesh solution was evolved in time.

The differences between the coarse and medium mesh solutions are as noted before when comparing the results after 60 turbine revolutions. The only noteworthy difference between the medium and fine solutions is for the moment where the fine mesh solution shows some oscillation. We might reasonably expect that this could be eliminated with better iterative convergence and/or a smaller time step.

A qualitative analysis of the grid convergence was attempted, the results of which are shown in table 6.5. The differences between solutions on different meshes may be usefully compared with the differences arising from a change in the time step (table 6.3) and a change in the iterative convergence parameters (table 6.4), and will be seen to be small. The deviations are shown from the medium mesh solution in order to illustrate whether convergent behaviour is seen; whilst R values are not given they can be readily inferred. This is indeed seen for all statistics of the two forces and one moment other than the maximum value of the tangential force.

We may enquire which of the statistics are most significant. It is felt by the author that the behaviour of the minimum values of the normal and tangential forces are the most significant. These forces occur on the blade when its azimuth angle is approximately 180°. The blade is

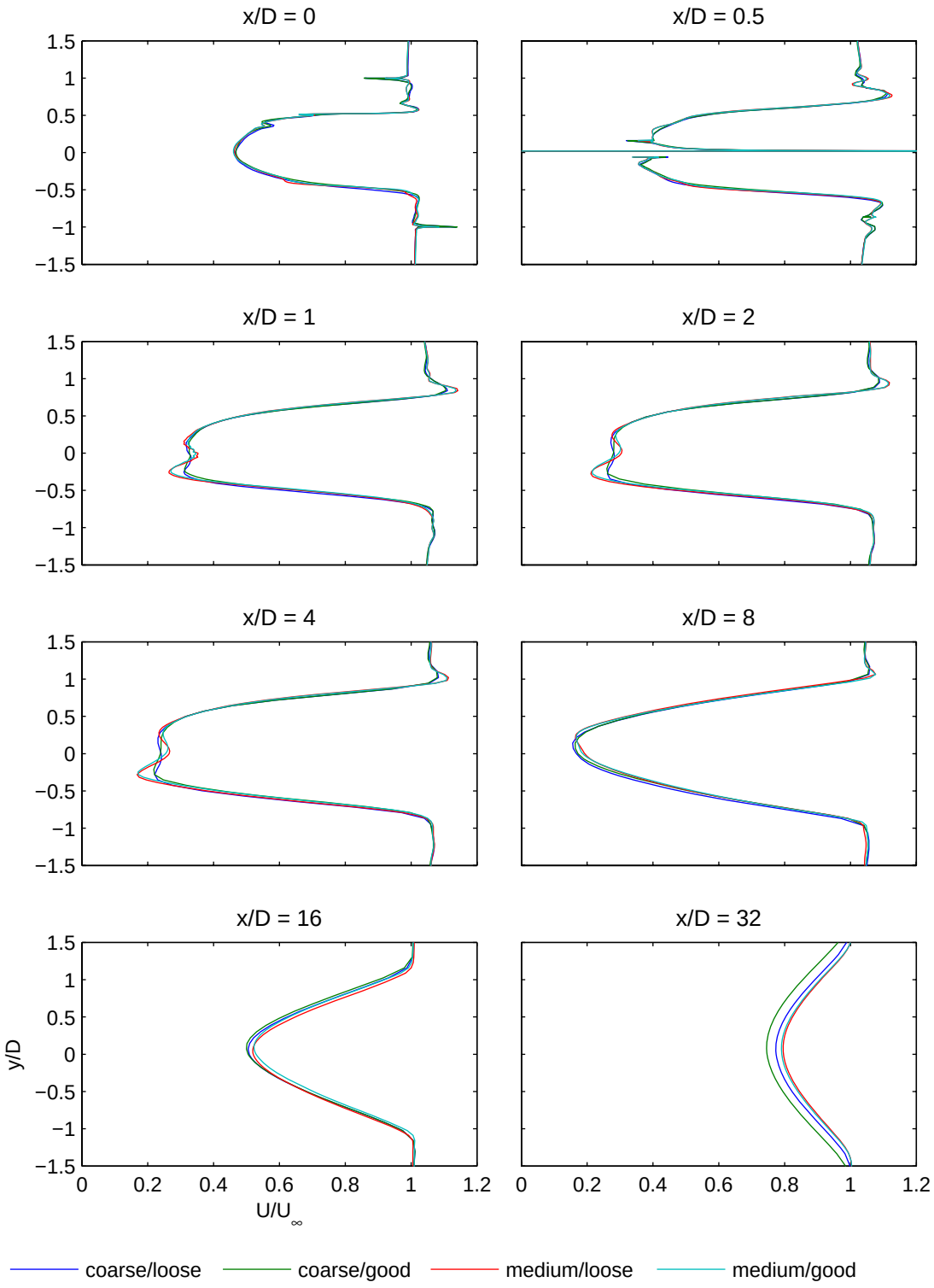

Figure 6.14: *U-velocity profiles at eight locations in the wake.*

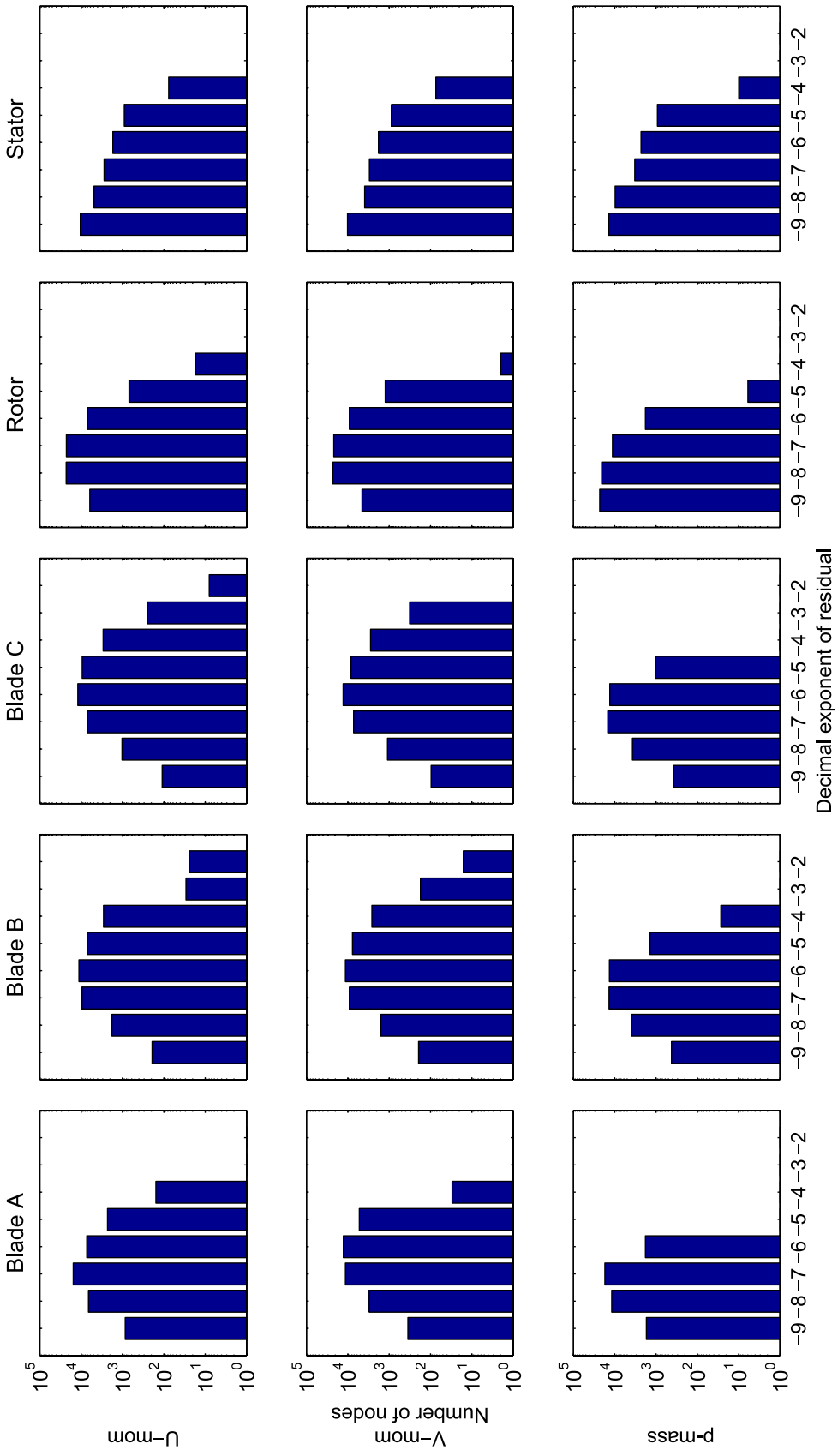

Figure 6.15: *Bar graph of residuals for the medium mesh solution with good iterative convergence after 60 revolutions.*

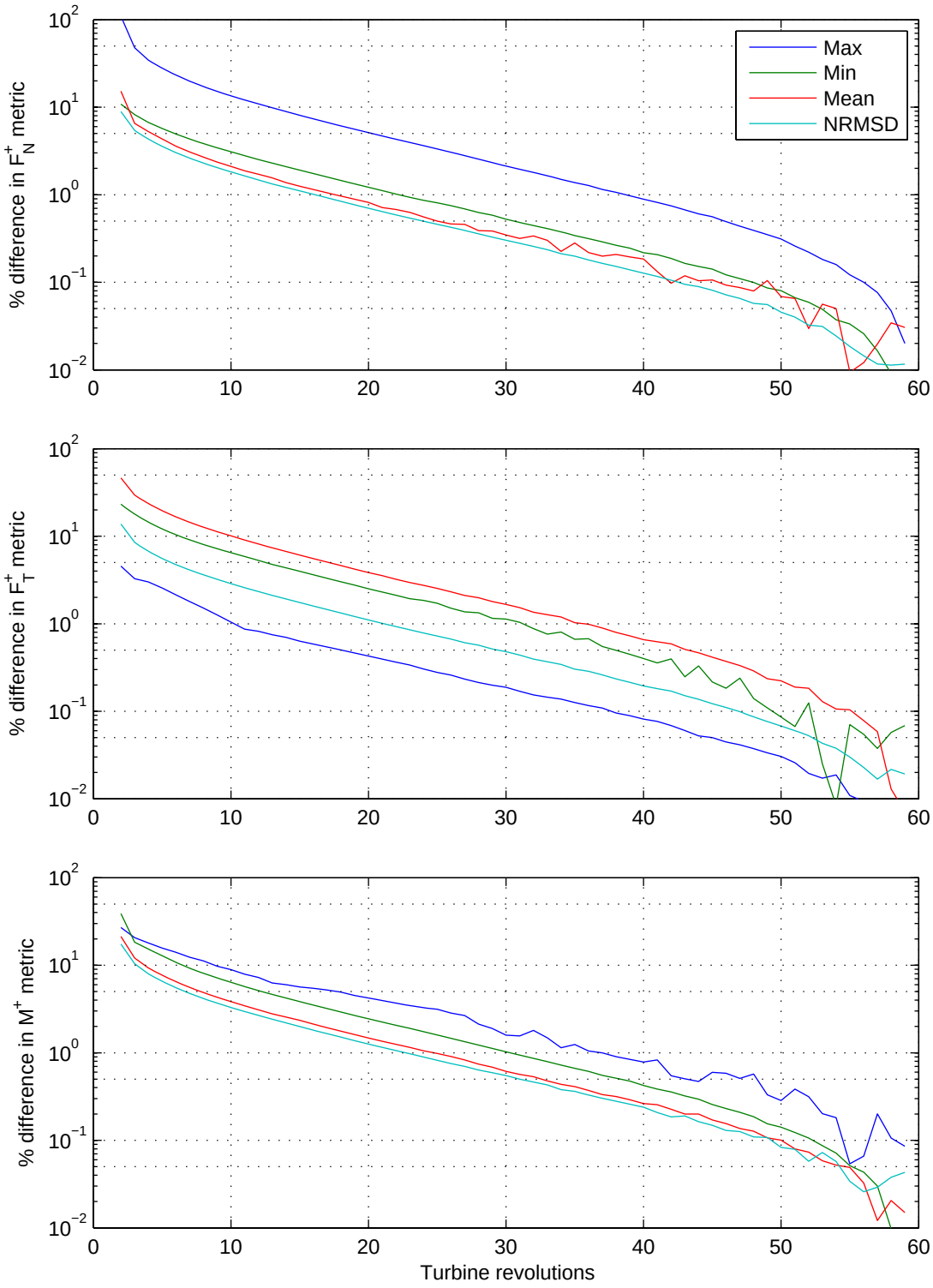

Figure 6.16: *Quantitative analysis of the development of the forces and moment on blade A. Values shown are the percentage deviations from the result during the final (60th) turbine revolution.*

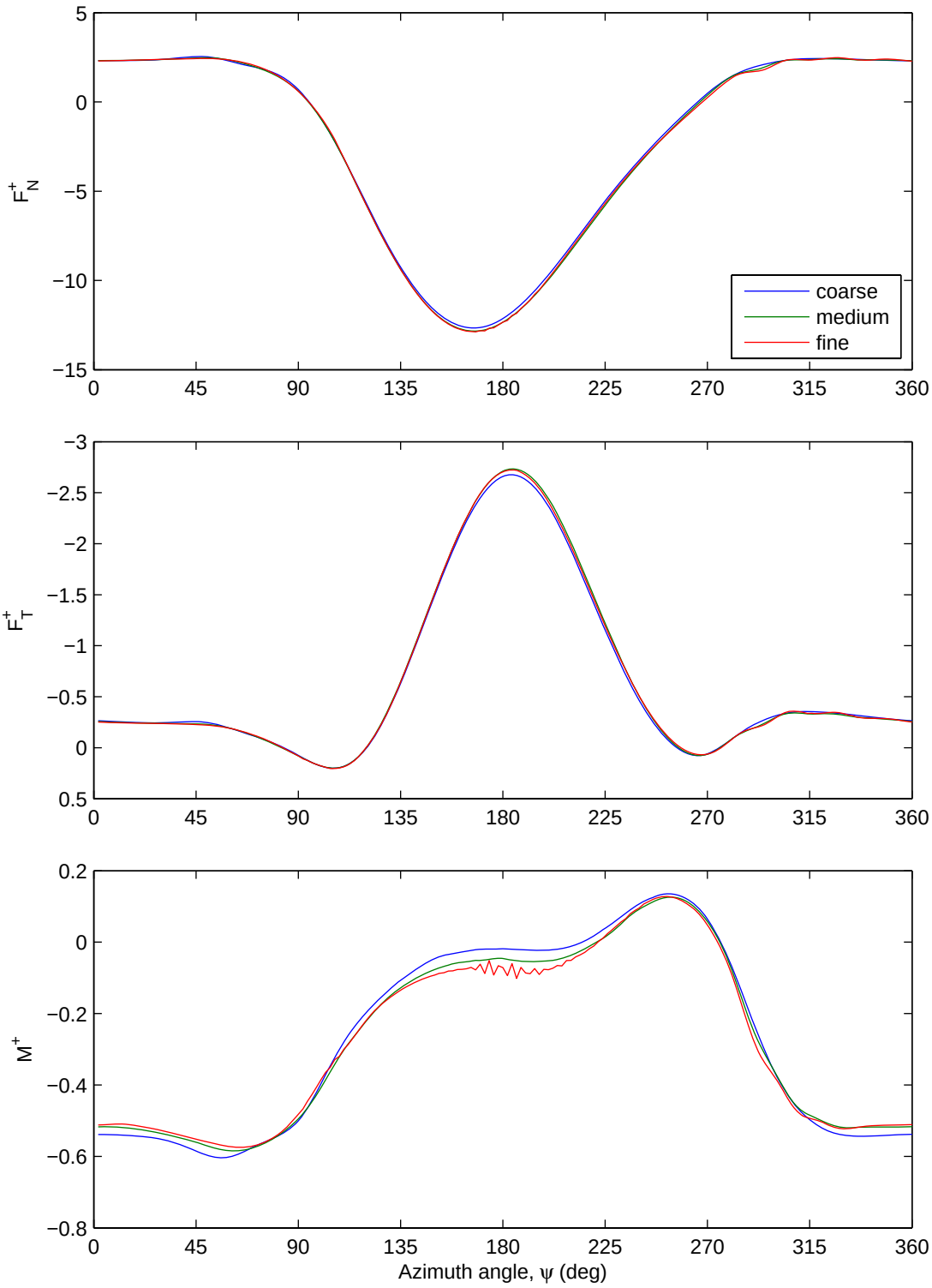

Figure 6.17: *Forces and moment on blade A during the 20th revolution.*

Table 6.5: *Maximum, minimum and mean values of F_N^+, F_T^+ and M^+, percentage deviations thereof from the reference case, and normalized route mean square deviation.*

Mesh	max	min	mean	% max	% min	% mean	% NRMSD[a]
			F_N^+				
coarse	2.543	−12.662	−2.336	2.81	−1.41	−3.89	0.86
medium	2.474	−12.843	−2.431	–	–	–	–
fine	2.476	−12.880	−2.426	0.09	0.29	−0.20	0.39
			F_T^+				
coarse	0.201	−2.676	−0.648	0.58	−2.10	−1.77	1.08
medium	0.199	−2.733	−0.659	–	–	–	–
fine	0.203	−2.721	−0.656	1.94	−0.46	−0.51	0.42
			M^+				
coarse	0.135	−0.604	−0.266	7.37	3.29	−1.83	2.88
medium	0.126	−0.585	−0.271	–	–	–	–
fine	0.128	−0.575	−0.275	1.58	−1.67	1.32	1.96

[a] Normalized by the range of the reference solution.

thus meeting comparatively undisturbed fluid and so there are fewer feedback mechanisms that will influence the values of the forces. All of the other statistics presented in the table (other than the maximum value of the moment) will be influenced to an extent by the behaviour of the blade in the upstream half of the cycle.

The results for the forces and moments on the other blades of the turbine were also examined for the coarse, medium and fine mesh solutions. For the coarse and medium mesh solutions, the differences between blades were generally less than the differences between the given solution and the next finest solution. For the fine mesh solution the differences were lower again. The analysis of grid convergence presented in table 6.5 was then repeated for blades B and C with similar results. Two points may be noted: first, that the minimum values of the normal and tangential forces always showed convergent behaviour, and second, that the mean value of the tangential force did not. The second is clearly unfortunate as this is the quantity that we are most concerned with predicting. Nevertheless, it is felt that the convergent behaviour of the other quantities is more significant in demonstrating that the solution is, as a whole, showing convergent behaviour.

6.9 Defining numerical parameters for investigating the physics

The preceding sections present a thorough analysis of the effects of the key numerical parameters on the solution, namely the time step and total time, the iterative convergence target and the maximum number of coefficient loop iterations, and the spatial discretization. The primary basis of the analysis has been to compare the forces and moment on a blade; specifically the maximum, minimum and mean values thereof, and to compute the normalized RMS deviation. In selecting a value of a given parameter suitable for use when investigating the physics, the criteria applied is that the selected value will give errors of less than about 5% from the best solution *for that parameter*. Thus an angle step of 2° is selected because the errors from the solution with an angle step of 1° are generally less than 5%, for a given value of the total time, a given iterative convergence target and a given mesh. Similarly, we select a total time equal to 20 turbine periods, good iterative convergence and the coarse mesh. We also look for qualitative agreement of the velocities in the wake. This does not alter the choice of time step, iterative convergence parameters or mesh, but it does increase the total time to 60 turbine periods.

Whilst the above analysis would point to the use of the coarse mesh, it was decided to use the medium mesh. This was desired because the simulations of the NACA 0024 foil presented in chapter 5 were calculated with the medium mesh; using the same mesh for the turbine means that the behaviour of a turbine blade can be directly compared to the behaviour of the isolated foil. (Note that whilst the differences in the forces and moment predicted by the coarse and medium mesh solutions are within the specified limits, this does not prove that the predicted lift, drag and moment coefficients would also be.)

One solution strategy which has hitherto not been investigated is to change the time step, iterative convergence parameters or mesh during the course of the solution. For example, a larger time step could be used at first to expedite the development of the wake before switching to a smaller time step to generate more accurate results. This strategy was first employed by starting a 2°/medium/good solution from the results of an 8°/coarse/loose solution that had been run for 100 turbine periods, with the medium mesh solution being advanced in time for 60 turbine periods to thoroughly investigate the behaviour after the restart. The results for the forces and moment on the blade from this solution rapidly (within 3 revolutions) converge to the fully developed medium mesh solution. Unfortunately this is not the case for the flow field in the wake where a significant perturbation is introduced by the change in the numerical

parameters. It takes around 60 turbine periods for this perturbation to be convected out of the domain. Given that the 8°/coarse/loose solution does not give acceptably accurate results for the flow field in the wake, this particular strategy does not produce a 'complete' solution (forces, moments and flow field in wake) of the desired accuracy more quickly.

The final strategy decided upon is an evolution of the above: a solution with a 2° angle step is computed on the coarse mesh with loose convergence for 60 turbine periods in order to generate a result for the flow field in the wake. The results of this solution are then used as the starting conditions for a solution with the same angle step on the medium mesh with good convergence. This medium mesh solution is run for 3 turbine periods in order to generate a solution for the forces and moments on the blades.

6.10 Physical parameters

With the numerical parameters chosen, we can now investigate the effect of the design and operating parameters on the solution. Simulations were run for five different values of the tip speed ratio – 2.0, 2.4, 2.8, 3.2 and 3.6 – and for both fixed pitch and variable pitch operation. The variable pitch algorithm used is that where the angle of attack is limited based on an assumed velocity field. The parameters used were the same as those used to produce the blade element results of the previous chapter, namely limiting angles of attack of 8° and 10° during the upstream and downstream passes of the blade, and velocity ratios of 0.85 and 0.7 during the upstream and downstream passes. Simulations were also run for the case of a four blade variation of the Edinburgh Designs turbine having the same solidity and with variable pitch. The results for this case were very similar to that of the three blade case and are only discussed in terms of the power, torque and thrust coefficients.

The normal and tangential forces and blade quarter chord moment are shown versus azimuth angle for the case of fixed pitch in figure 6.18 and for variable pitch in figure 6.19. For the fixed pitch case lift stall occurs for the lowest tip speed ratio (2.0), as evinced by the sharp drop in the tangential force at an azimuth angle of 180°. Moment stall occurs for the three lowest tip speed ratios (2.0, 2.4 and 2.8), again shown by a drop in the moment around 180°. At the highest tip speed ratio the turbine is presenting a considerable blockage to the flow, with the effect that during the downstream pass of the blades the tangential force remains positive (giving a negative shaft torque).

For the variable pitch case (figure 6.19) one of the most obvious features in the graphs is the sharp spikes in the moment coefficient. This is due to the sudden change from the blades not being pitched (when the relative flow angle is below the limiting angle of attack) to the blades being pitched to maintain the limiting angle of attack, and vice versa, and occurs four times during each revolution. Clearly it would be desirable to avoid this in practice. In comparison to the fixed pitch results, the tangential force is negative (positive shaft torque), for a substantial portion of the downstream pass of the blades.

As with the investigation into the numerical parameters, the velocity field in the wake is analysed by plotting the U-velocity along a series of lines both tangential and normal to the freestream direction. Figure 6.22 shows the U-velocity along a line parallel to the (geometric) wake centreline for both fixed and variable pitch cases, while figures 6.20 and figure 6.21 show the U-velocity profile in the wake at a series of locations for fixed and variable pitch respectively.

We consider first the fixed pitch results. As expected, higher tip speed ratios lead to lower velocities at the turbine and in the near wake (up to about 6 or 7 diameters downstream of the turbine axis). The pattern of wake recovery differs somewhat, with the cases that have higher tip speed ratio showing more rapid and more complete recovery. The velocity profiles in the near wake (see the graphs for $x/D = 1, 2, 4$ in figure 6.20) show an interesting progression. At the two lowest tip speed ratios there are two minima in the profile while at the two highest there is a pronounced wake asymmetry. This pattern is seen in the experimental results presented in Paraschivoiu (2002).

The variable pitch results show broadly similar trends. In this case there are two minima in the velocity profiles for all tip speed ratios other than the lowest and considerably reduced wake asymmetry. In comparison with the fixed pitch results, the deficit velocity is reduced, but the wake recovery is prolonged. The reduced deficit velocity is attributable to the strategy of limiting the angle of attack and therefore reducing the force on the fluid. It is though that the prolonged wake recovery is due to there being less vorticity in the wake.

Finally, we examine the coefficients of power, torque and thrust (figure 6.23). Some extra simulations were performed for intermediate tip speed ratios for the two three-blade cases in order to increase the resolution. For the power coefficient, and as with the blade element results, the variable pitch results show a higher value for $C_{P_{\max}}$, occurring at a higher tip speed ratio,

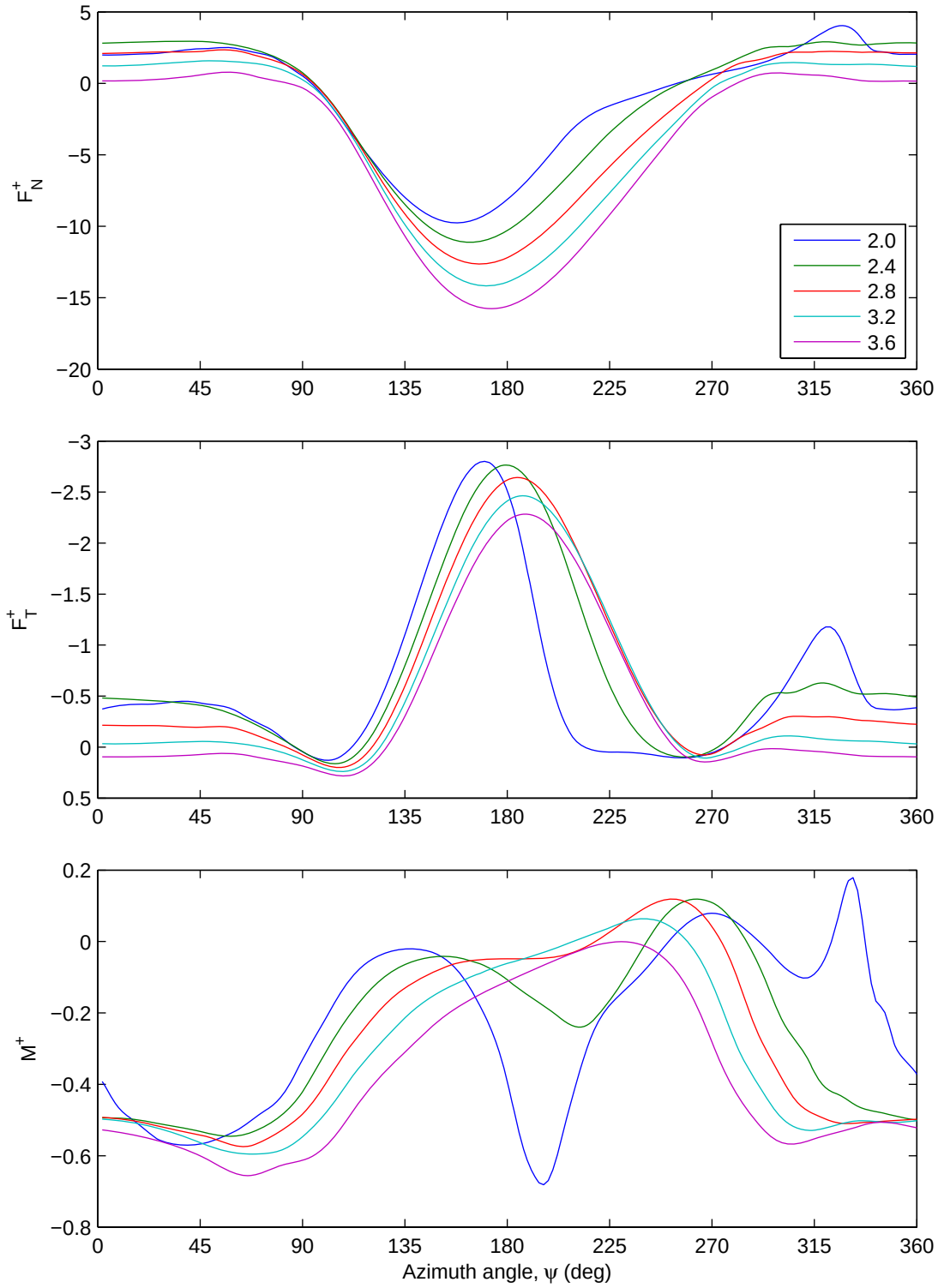

Figure 6.18: *Forces and moment on blade A for five different tip speed ratios (see legend) with* fixed pitch *operation*

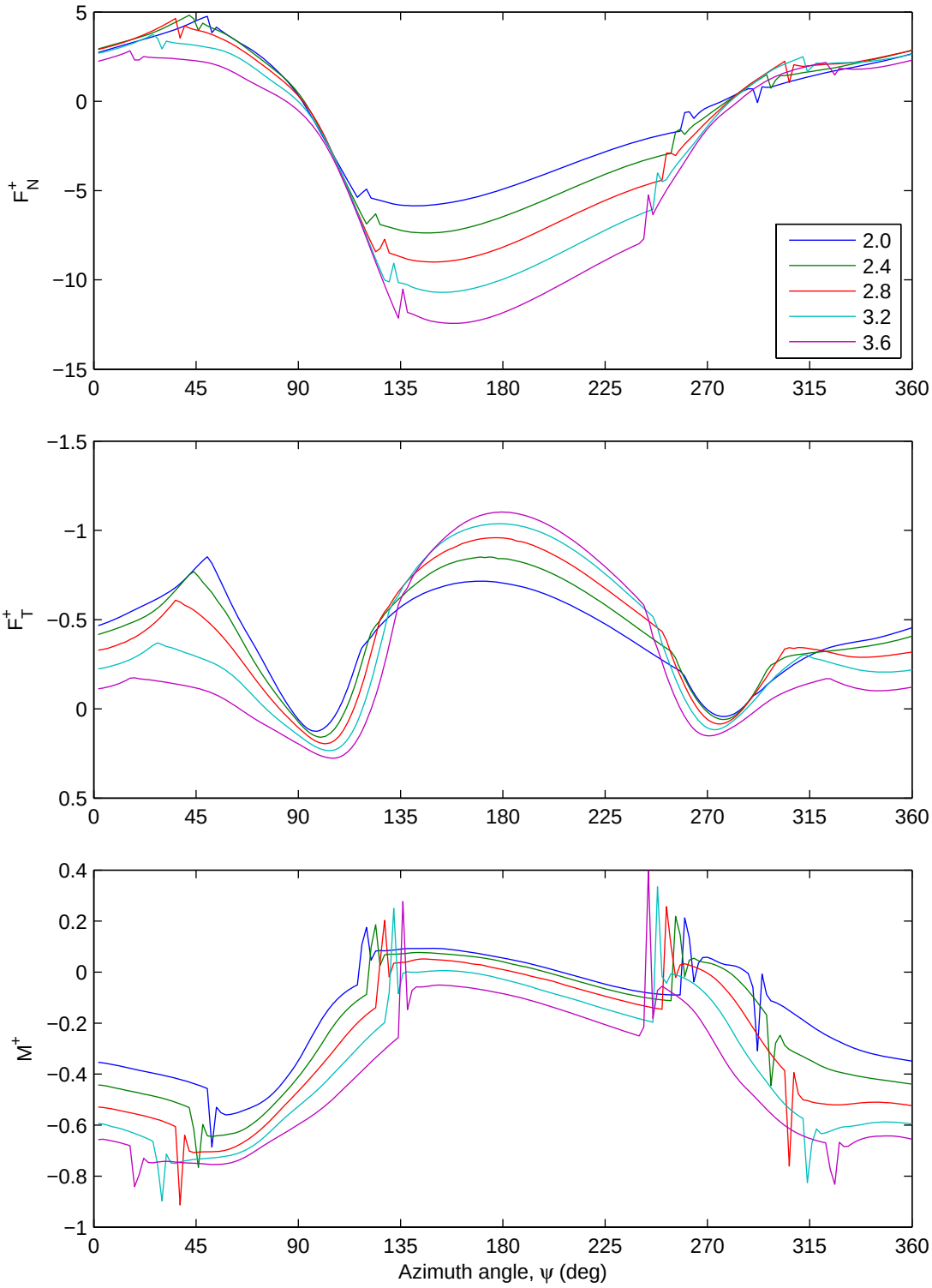

Figure 6.19: *Forces and moment on blade A for five different tip speed ratios (see legend) with* variable pitch *operation.*

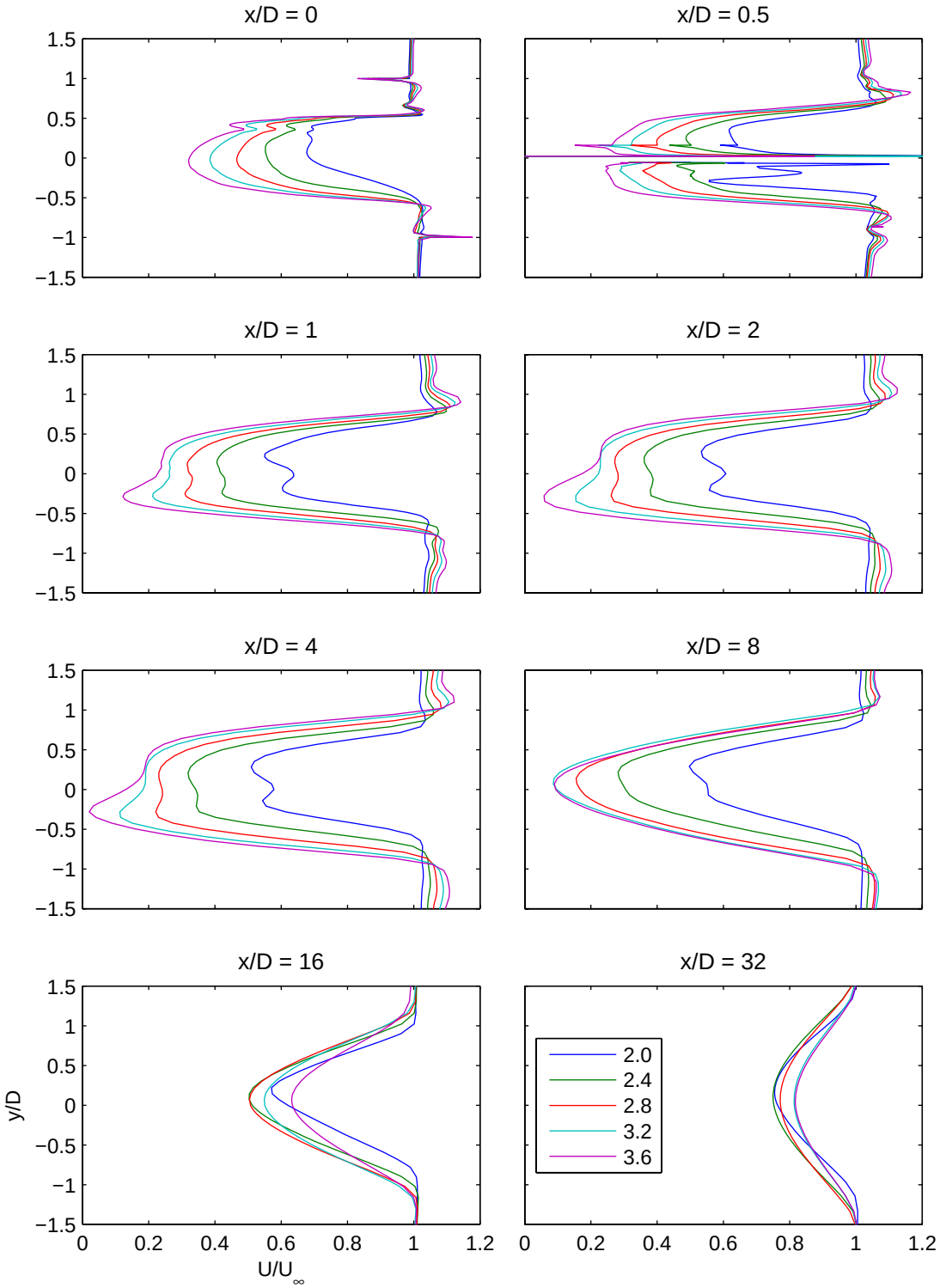

Figure 6.20: *U-velocity profiles at eight locations in the wake (see individual chart titles) for five different tip speed ratios (see legend) with* fixed pitch *operation.*

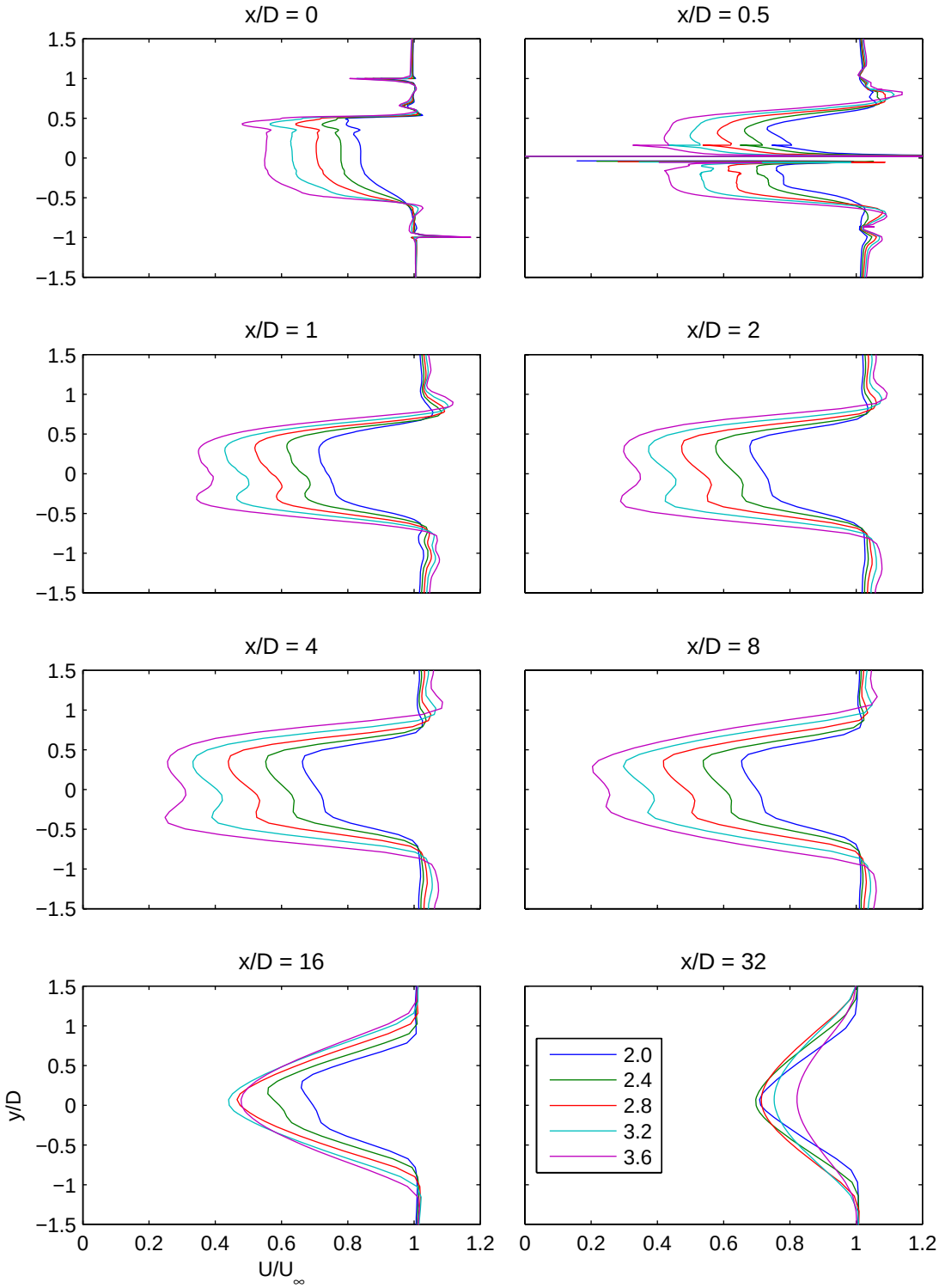

Figure 6.21: *U-velocity profiles at eight locations in the wake (see individual chart titles) for five different tip speed ratios (see legend) with* variable pitch *operation.*

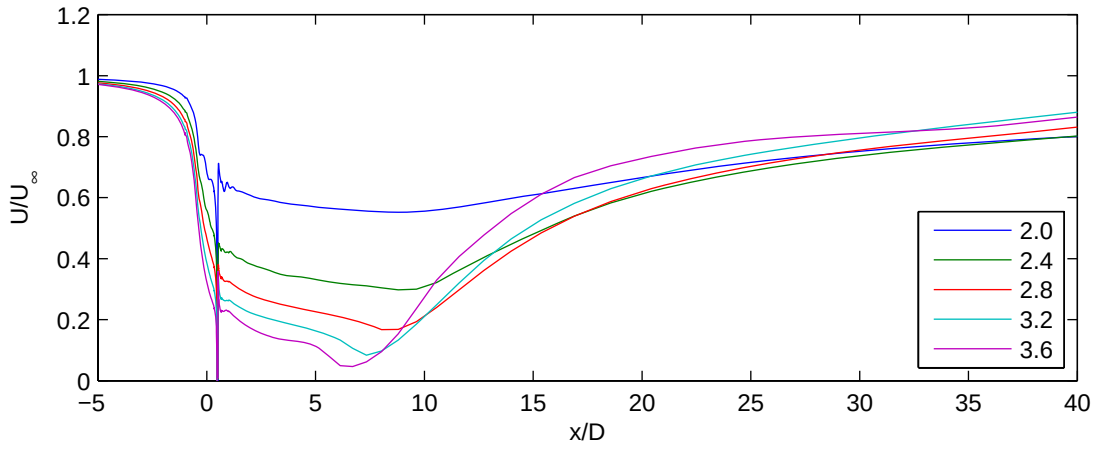

(a) Fixed pitch.

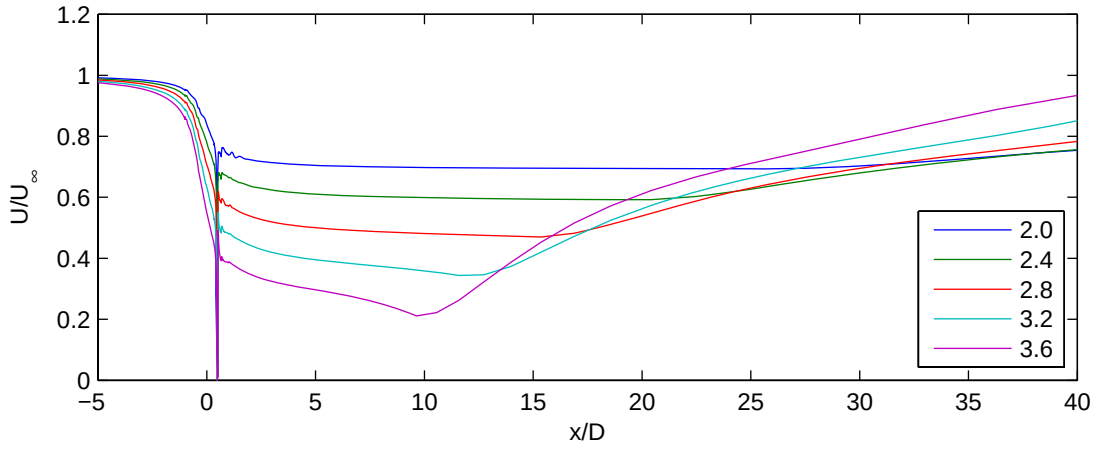

(b) Variable pitch.

Figure 6.22: *U-velocity along a line parallel to the free stream and normal to the turbine axis for five different tip speed ratios (see legend).*

and a flatter curve. The four-blade variable pitch results are very similar to the three-blade variable pitch results, with the small decrement in the performance being readily attributable to the reduction in the blade chord Reynolds number.

For the thrust coefficient, the variable pitch results show lower values for all but the highest tip speed ratio. The generally lower thrust coefficients are consistent with the lower wake deficit velocity, but note that at the highest tip speed ratio, where the thrust coefficients are very similar, the wake deficit velocity is still lower in the case of the variable pitch.

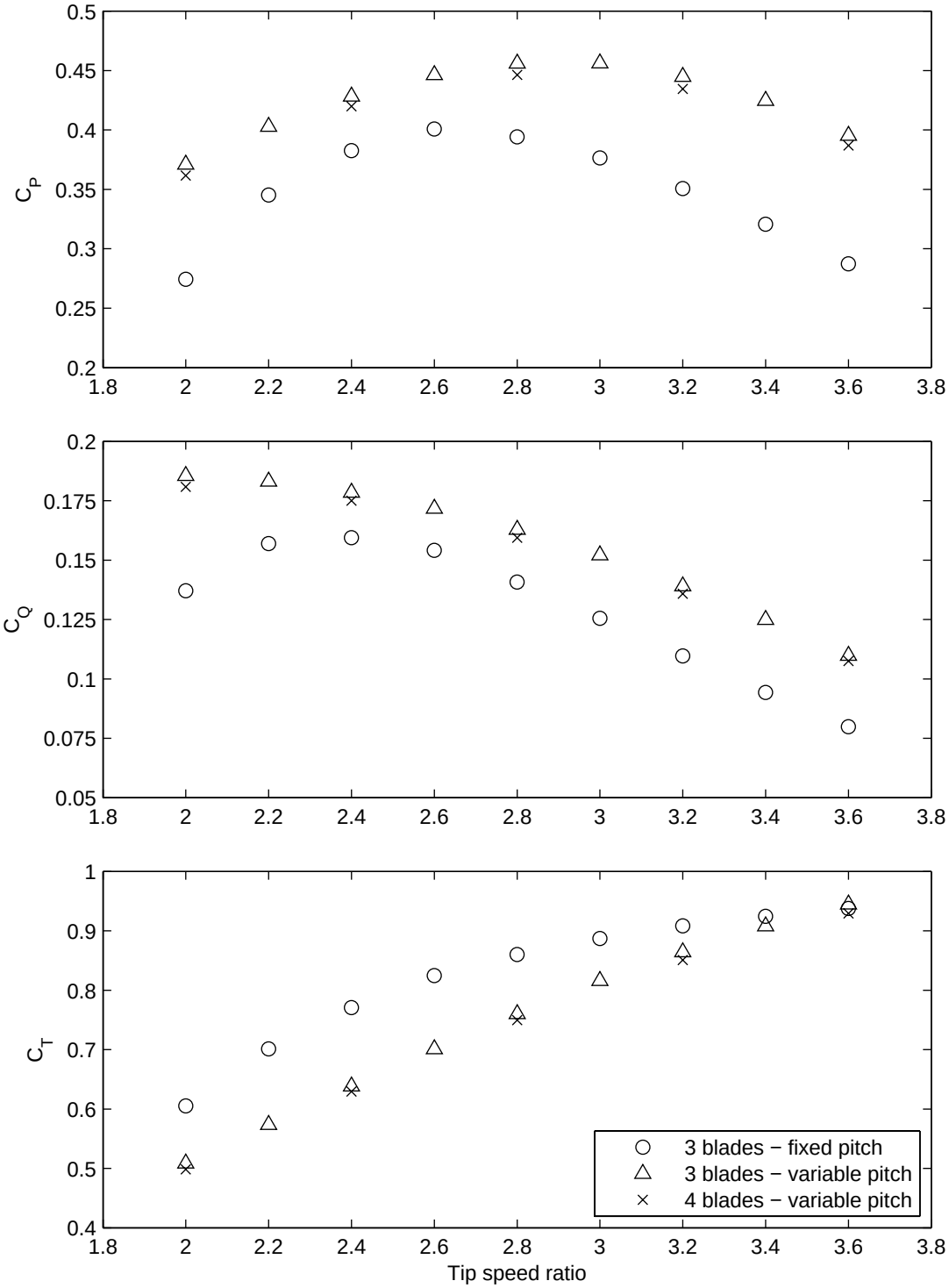

Figure 6.23: *Coefficients of power, torque and thrust versus tip speed ratio.*

6.11 Chapter conclusions

This chapter presents the results of the verification of a CFD model of a vertical axis turbine involving a quantitative analysis of the forces and a qualitative analysis of the velocity field. Such an exercise has to this author's knowledge not been shown before.

Based on this verification exercise, the following procedure was implemented and is recommended for future use:

- A solution should be run on the coarse mesh with an angle step of 2° and with 'loose' iterative convergence for 60 turbine revolutions in order that the flow field is fully developed.
- Using the coarse mesh solution above for the initial conditions, a solution on the medium mesh with the same angle step but 'good' convergence should be run for 3 turbine revolutions in order to generate accurate force and moment data that are directly comparable with the results of the previous chapter.

Three different turbine configurations were simulated for a range of values of the tip speed ratio:

- The Edinburgh Designs turbine with fixed pitch operation.
- The Edinburgh Designs turbine with variable pitch operation.
- A variation of the Edinburgh Designs turbine having four blades but the same value of the solidity, with variable pitch operation.

The results from these simulations show that:

- Blade stall occurs at low values of the tip speed ratio with fixed pitch operation.
- Variable pitch operation gives a 5 percentage point increase in the power coefficient.
- The use of four blades slightly decreases the power coefficient. This is likely to be due to Reynolds number effects.

Chapter 7
A comparison of blade element momentum and CFD models

7.1 Introduction

The purpose of this chapter is to draw together the results of the previous three chapters. Two sets of results already presented separately will be compared. These are the blade element results of chapter 4, utilizing the section data of Sheldahl and Klimas, and the CFD results for the turbine presented in chapter 6. A further set of results from the blade element model, this time using the CFD results from chapter 5 as the input section data, are also compared with the previous two.

The comparison between the blade element results using the CFD section data and the CFD results for the turbine is novel and allows differences in the steady state behaviour of the turbine blades to be eliminated as a source of differences between the two models. Clearly many possible reasons for differences in the model results nevertheless remain, both at the 'blade' level (dynamic stall, flow curvature), and at the 'turbine' level (assumptions inherent in the blade element model), but it is possible to isolate some of these by inter-comparisons between the result sets, for example at different tip speed ratios.

7.2 Coefficients of power, torque and thrust

We begin the comparison between the models by examining the predictions for the variation in the power, torque and thrust coefficients with tip speed ratio. In figure 7.1, and in subsequent figures in this chapter, the blade element results produced with the section data of Sheldahl and Klimas (1981) are labelled 'BEM/SK', those from the blade element model with section data from the CFD results in chapter 5 are labelled 'BEM/CFD', and those from the complete CFD turbine model are labelled 'CFD'. Considering first the power coefficient, the clearest difference between model predictions is that between the BEM/SK and the BEM/CFD results for the case

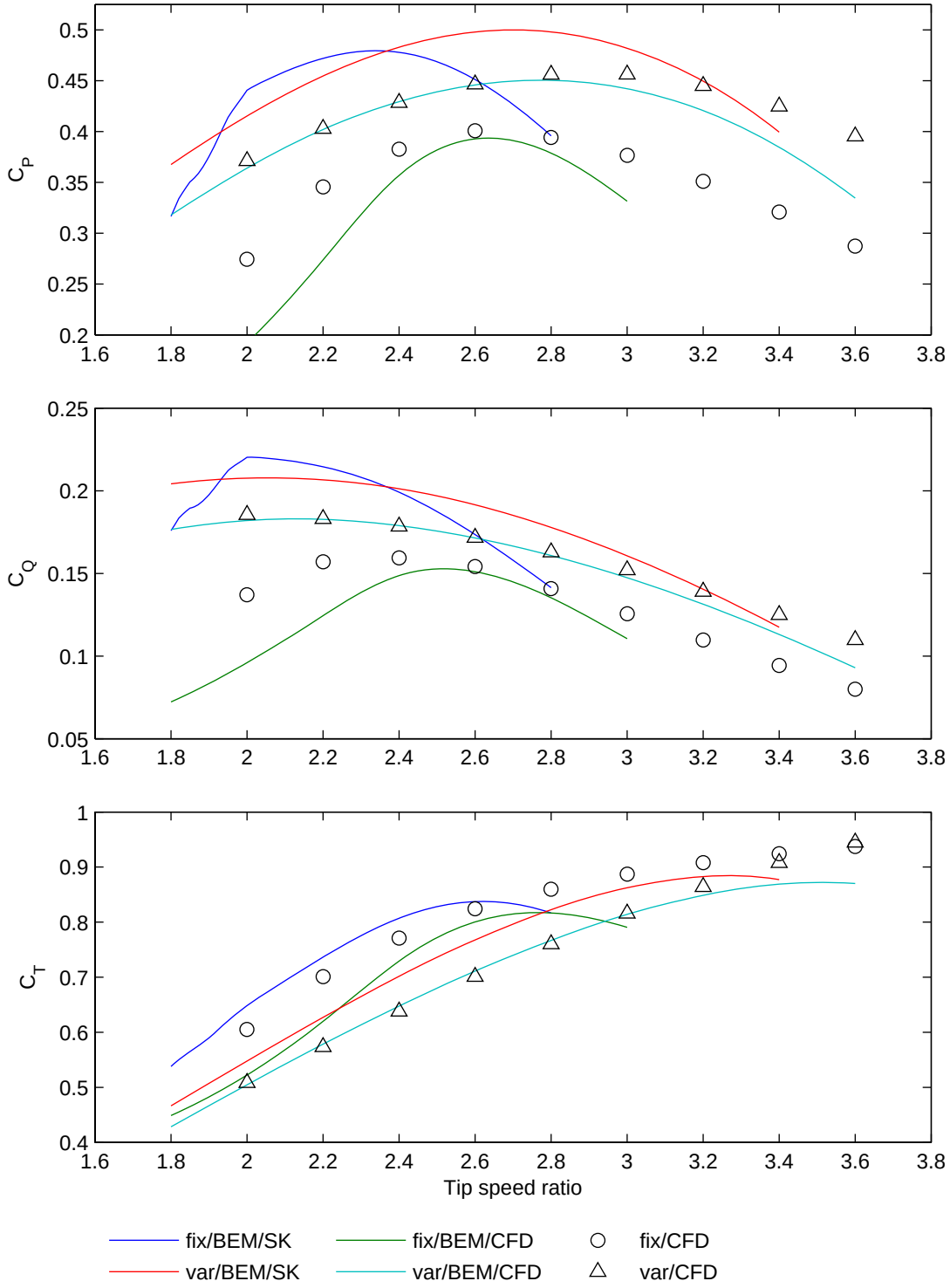

Figure 7.1: *Results for the power, torque and thrust coefficients from the blade element model with both the Sheldahl and Klimas section data and the present CFD section data, and from the CFD model of the turbine. The blade element results using the CFD section data include the contribution from the blade quarter chord moment.*

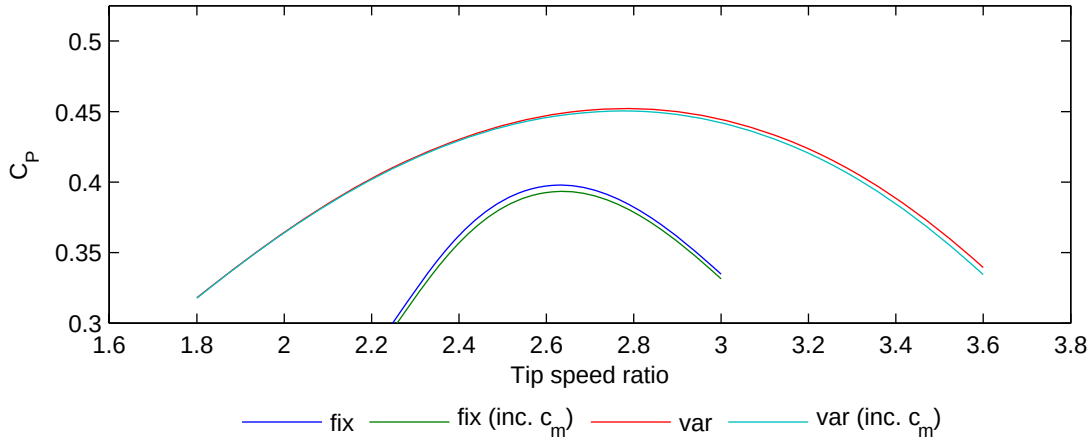

Figure 7.2: *Results for the power coefficient from the blade element model with and without the contribution from the blade quarter chord moment. Section data from the CFD results of chapter 5.*

of fixed pitch operation. Such a difference is not unexpected given the large angles of attack ($\alpha > 20°$ for $\lambda < 2.4$), and the considerable difference in the section data for these angles from the two sources. Notable differences in the results from these two models are also seen for the case of variable pitch operation. In both cases the BEM/SK results give a considerable overestimation of the power relative to the BEM/CFD results.

Differences between the BEM/CFD and CFD results are smaller for both fixed pitch and variable pitch operation. For fixed pitch operation there is good agreement at $C_{P_{\max}}$, less good either side of this, while for variable pitch operation there is excellent agreement at the lower tip speed ratios but a widening difference at the higher tip speed ratios. As will be seen when the blade forces are considered, the likely cause of the poor agreement for low tip speed ratios in the case of the fixed pitch results is due to the important effect of dynamic stall not being modelled in the case of the blade element results. The difference between the results for higher tip speed ratios, for both fixed and variable pitch operation, is likely to be due to the blade element model being less successful in capturing the effects of high axial induction factors.

Differences in the torque coefficient follow those of the power coefficient, while those in the thrust coefficient are again similar, although less stark. For the thrust coefficient at higher tip speed ratios (and thus higher induction factors), the CFD results show higher values than the BEM/CFD results. This is in line with comparisons between experiment and blade element results; see for example Sharpe (1990).

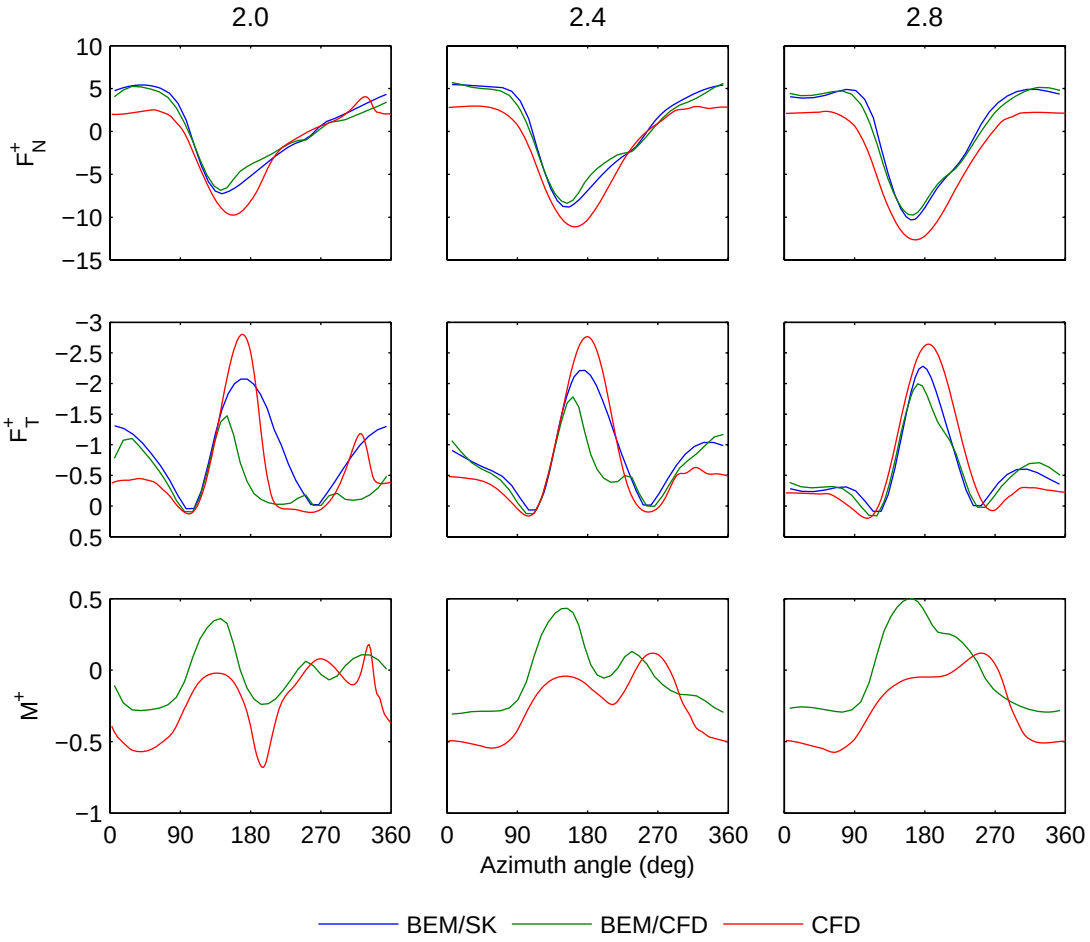

Figure 7.3: *Normal, tangential and blade quarter chord moment versus azimuth angle for three different tip speed ratios. The results are for the case of* fixed pitch *operation and are from each of the three models, as indicated in the legend.*

The BEM/SK results for the power and torque coefficient do not include the contribution from the blade quarter chord pitching moment, as Sheldahl and Klimas (1981) do not present data for c_m, whereas the BEM/CFD results do. The effect of the inclusion or exclusion of the quarter chord moment on the power coefficient is small and is shown in figure 7.2. Results are from the blade element model using the CFD section data.

7.3 Force and moment coefficients

Results for the normal and tangential force and the blade quarter chord moment are shown in figure 7.3 for the case of fixed pitch and figure 7.4 for the case of variable pitch. For the fixed pitch case, the three data sets show notably different predictions for the stall behaviour,

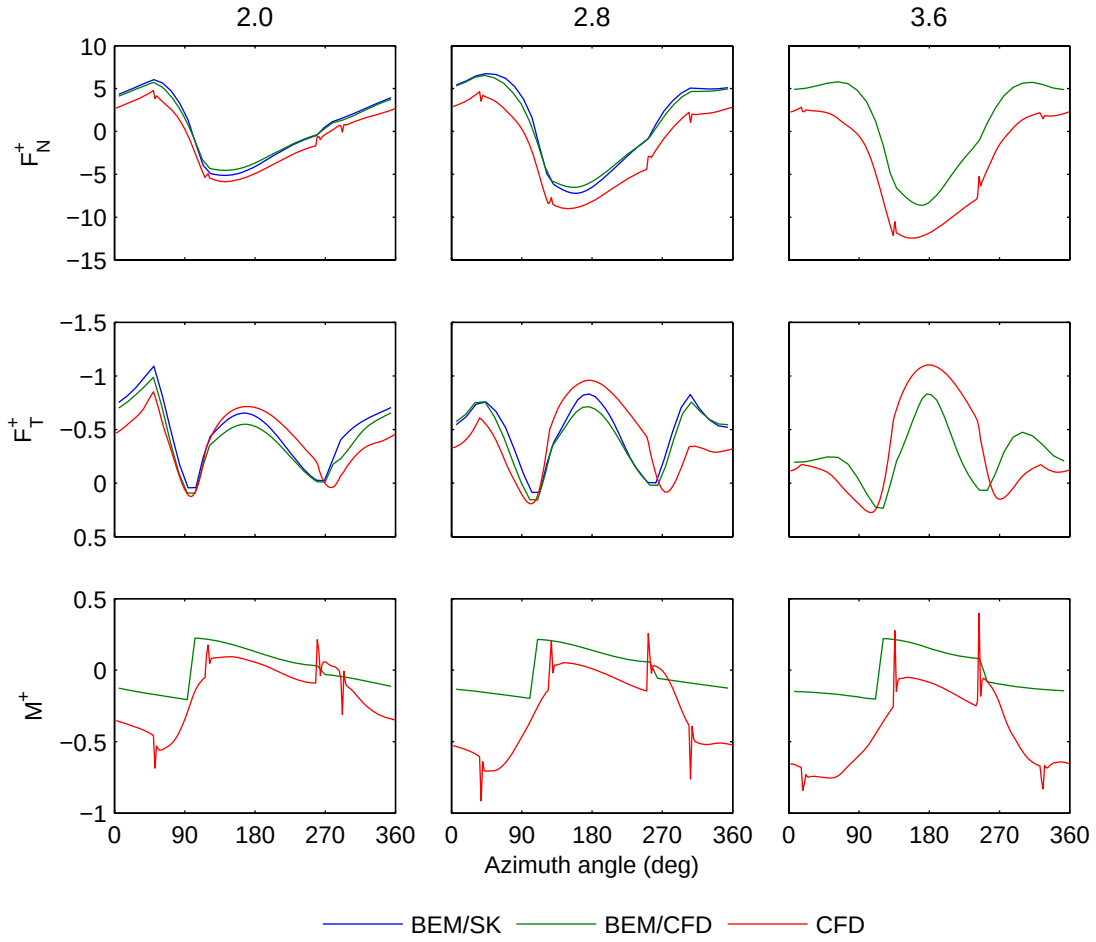

Figure 7.4: *Normal, tangential and blade quarter chord moment versus azimuth angle for three different tip speed ratios. The results are for the case of* variable pitch *operation and are from each of the three models, as indicated in the legend.*

readily explaining the differences in the power coefficient. At the lowest tip speed ratio, 2.0, the BEM/SK results show no stall, the BEM/CFD results show a considerable period of stall, while the CFD results show dynamic stall. This is most obvious for the tangential force. At the middle tip speed ratio, 2.4, the BEM/CFD results again show a considerable period of stall, while the two other models show no stall. For the highest tip speed ratio, 2.8, the BEM/CFD results show a small period of stall, and there is some agreement between all three results concerning the shape of the force curves. Most interesting is the fact that the normal force curve from the CFD results is shifted from the two BEM results. This consistent downwards shift may be due to flow curvature.

For the variable pitch results, excellent agreement in the power, torque and thrust coefficients was seen (figure 7.1) between the BEM/CFD and CFD results for tip speed ratios up to

about 3. In terms of the pattern of force versus azimuth angle, the agreement is less good though. As predicted by the CFD model, the forces during the upstream pass of the blades are greater (in magnitude) while during the downstream pass of the blades the forces are lower. These differences must cancel out given the good agreement for the power, torque and thrust coefficients. As with the fixed pitch case at the highest tip speed ratio, a consistent shift in the normal force curve is in evidence, this time for all tip speed ratios. The magnitude of the shift is seen to increase with increasing tip speed ratio. Agreement in the moment coefficient between the BEM/CFD and CFD results appears consistently worse than that for the normal and tangential force.

7.4 Velocity at the actuator cylinder

In order to compare the velocity at the actuator cylinder from the blade element results with that at the same location from the CFD results, an analysis of the time dependence of the flow-field was conducted. The variation in the velocity at four positions corresponding to azimuth angles of 0, 90, 180 and 270 degrees was plotted with the position of blade A, figure 7.5. The position of blade A is the time parameter. The case is that of the three-bladed turbine at a tip speed ratio of 2.8. Due to the three blades, the pattern has a period of 120 degrees, hence only this range is shown. Breaks in the curves are due to the presence of a blade. Clearly the velocities at the four points considered are relatively constant with time, and only vary considerably when a turbine blade is in 'close' proximity. Without proceeding to a quantitative analysis, this appears to correspond to about 10°, or about one chord length, from the leading or trailing edge of a blade. In selecting an 'average' or quasi-steady value for comparison with the BEM results it was decided that the value at a given point would be that at a time at which the quarter chord points of the two nearest blades were equidistant. Thus, the value at an azimuth angle of 0° is taken at a time at which blade A is at 60° and blade B is at −60°.

As a comparison with this approach, the relative flow speed W was calculated from the maximum pressure on a blade, occurring at the leading edge stagnation point:

$$W = \sqrt{\frac{p_{\max} - p_{\infty}}{\frac{1}{2}\rho}} \tag{7.1}$$

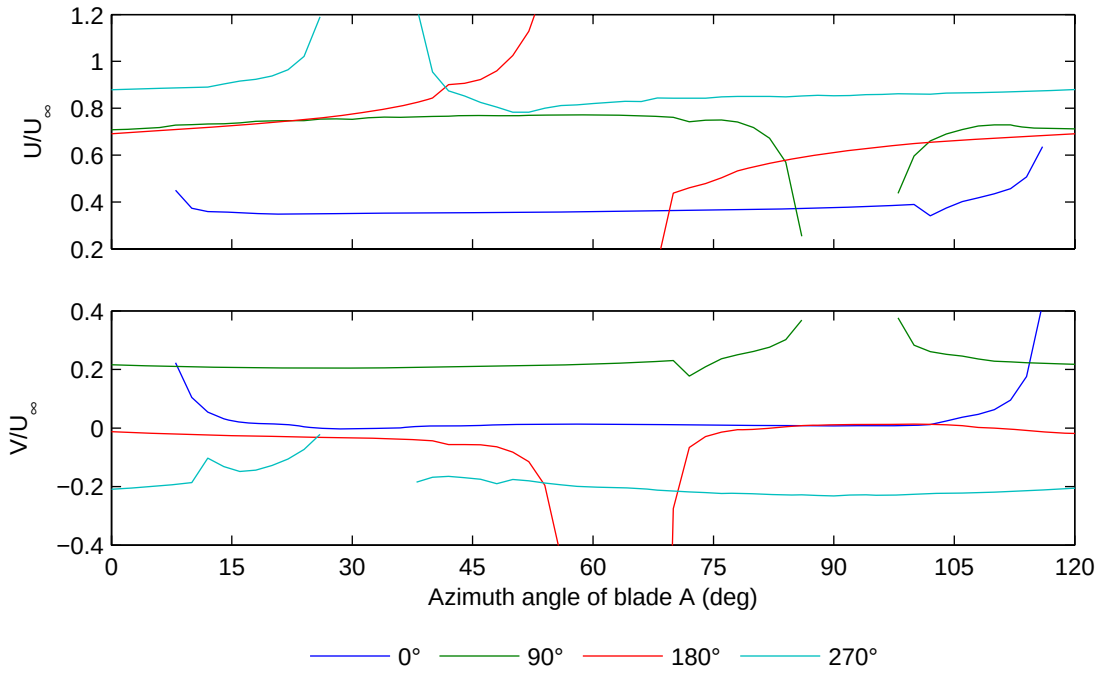

Figure 7.5: *U and V velocities at four points in space versus the azimuth angle of blade A for the case of fixed pitch at* $\lambda = 2.8$.

This calculation assumes that the flow from the freestream to the stagnation point on the blade is isentropic and that the maximum pressure is equal to the stagnation pressure in the frame of reference of the blade. As seen from figure 7.6, the two methods give similar results. All subsequent analysis uses the average velocity field approach as this gives the velocity and not just the relative flow speed.

U and V velocities versus azimuth angle from the BEM/SK, BEM/CFD and CFD results are shown in figure 7.7 for a number of tip speed ratios and for both fixed and variable pitch. For the V-velocity in both fixed and variable pitch cases, the agreement between the CFD and BEM/CFD results deteriorates with increasing tip speed ratios. This is most likely due to the assumption of straight streamlines in the BEM model. For the U-velocity the agreement between CFD and BEM/CFD results for the variable pitch case at a tip speed ratio of 2.0 is very good. At higher tip speed ratios the agreement deteriorates and the pattern seems to be that of the CFD results showing lower velocity for upstream azimuth angles and higher velocity for downstream azimuth angles. This discrepancy is broadly in line with the force results shown in figure 7.4, where the CFD results show greater forces upstream and smaller forces downstream, again relative to the BEM/CFD results. For the fixed pitch case and for the U-velocity there

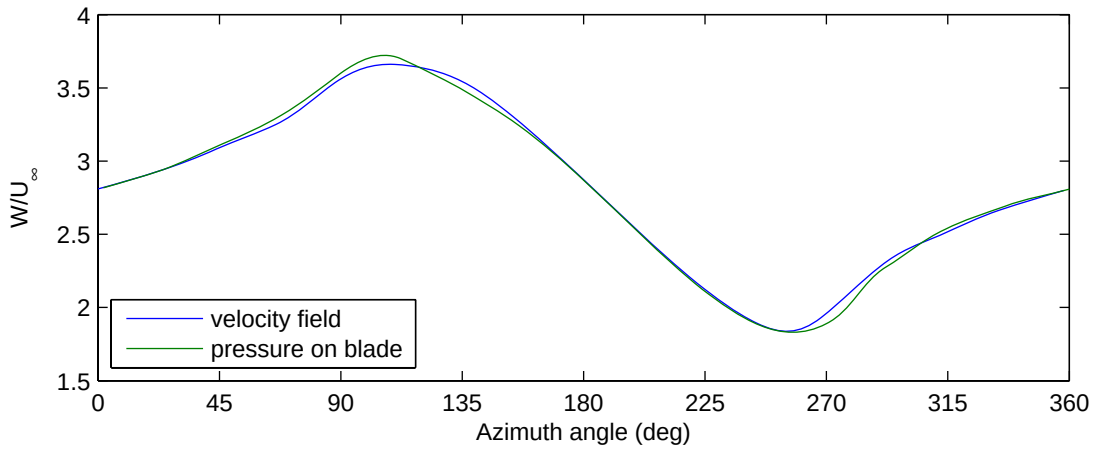

Figure 7.6: *Relative flow speed versus azimuth angle as derived from an approximation to the time-averaged velocity field and from the pressure on the blade. Fixed pitch at* $\lambda = 2.8$.

is arguably a similar trend, but there is in general less good agreement between the CFD and BEM/CFD results.

The relative flow angle ϕ and the relative flow speed W are shown in figure 7.8 for the same cases for which the U and V-velocities were calculated. This represents the same information, but in an alternative format. The agreement between all three result sets appears very good for all of the cases, and startlingly so for the variable pitch results. Such good agreement is because both ϕ and W involve the blade speed which effectively minimizes the differences introduced by the differing predictions of the stationary frame velocities given in figure 7.7.

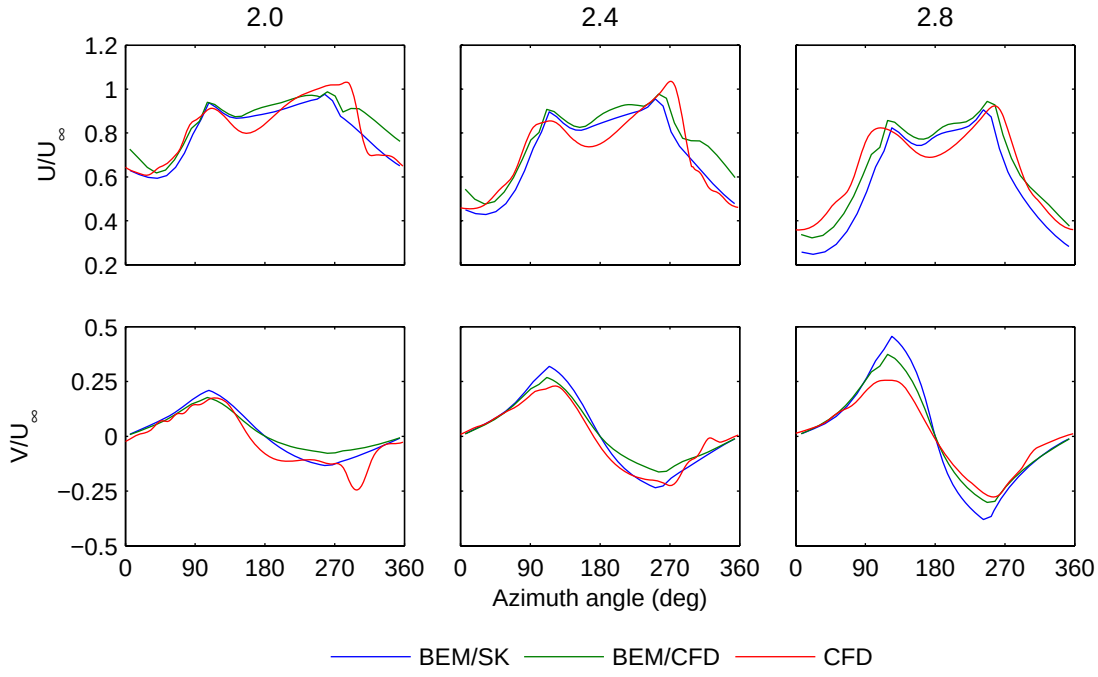

(a) Fixed pitch.

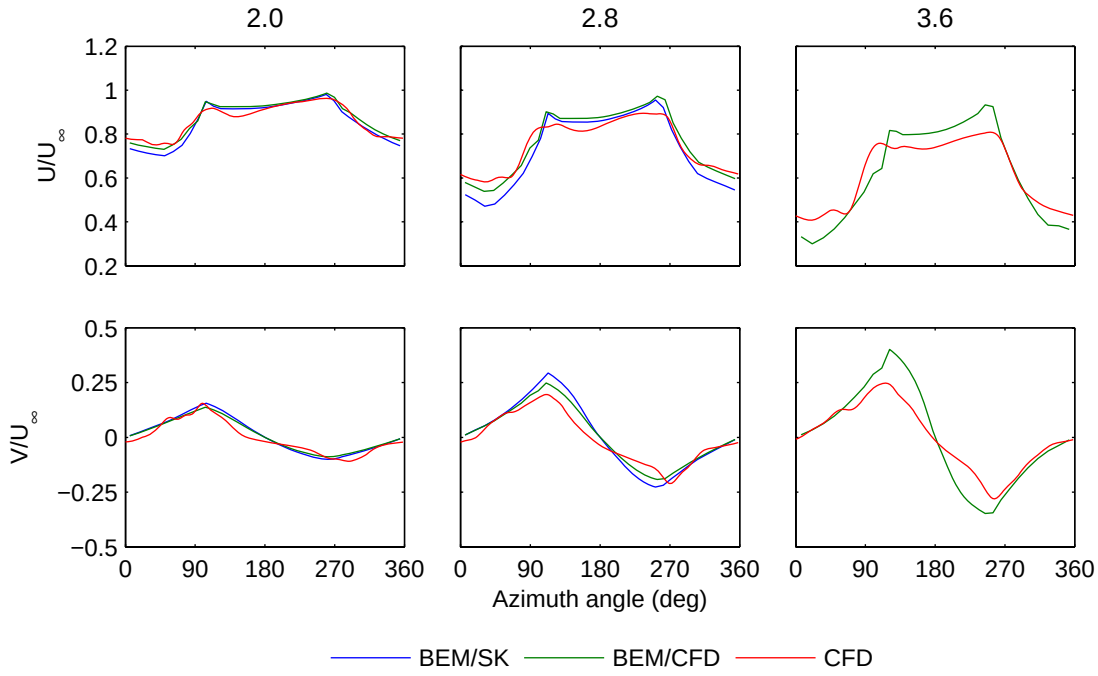

(b) Variable pitch.

Figure 7.7: *U and V velocities versus azimuth angle for different tip speed ratios for fixed (a) and variable (b) pitch.*

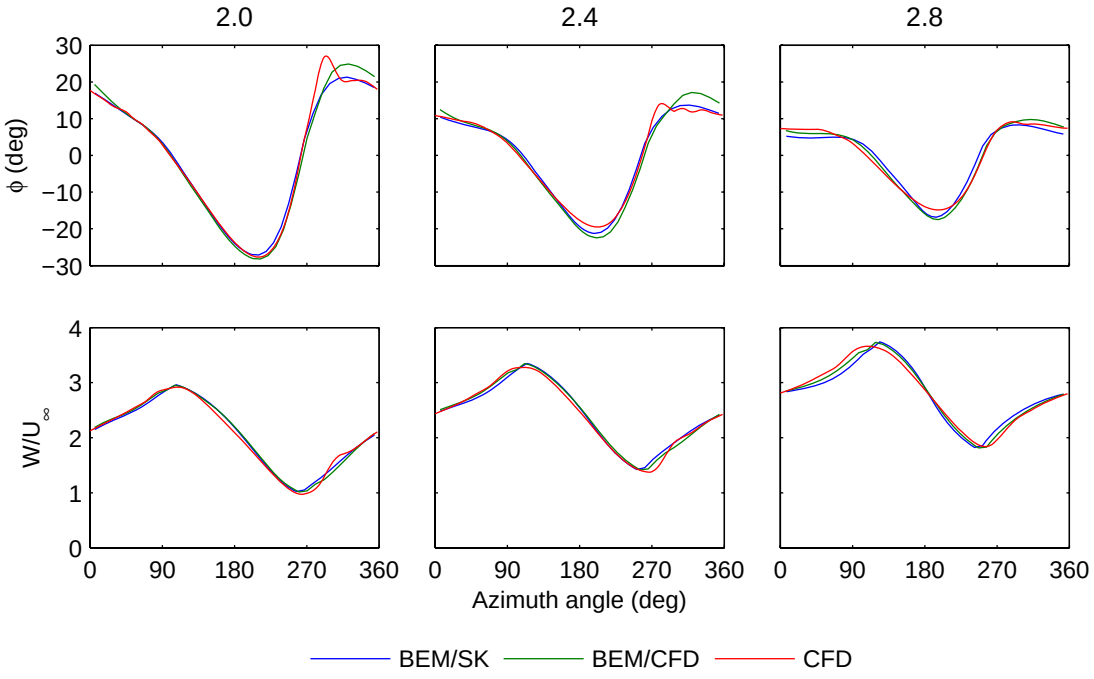

(a) Fixed pitch.

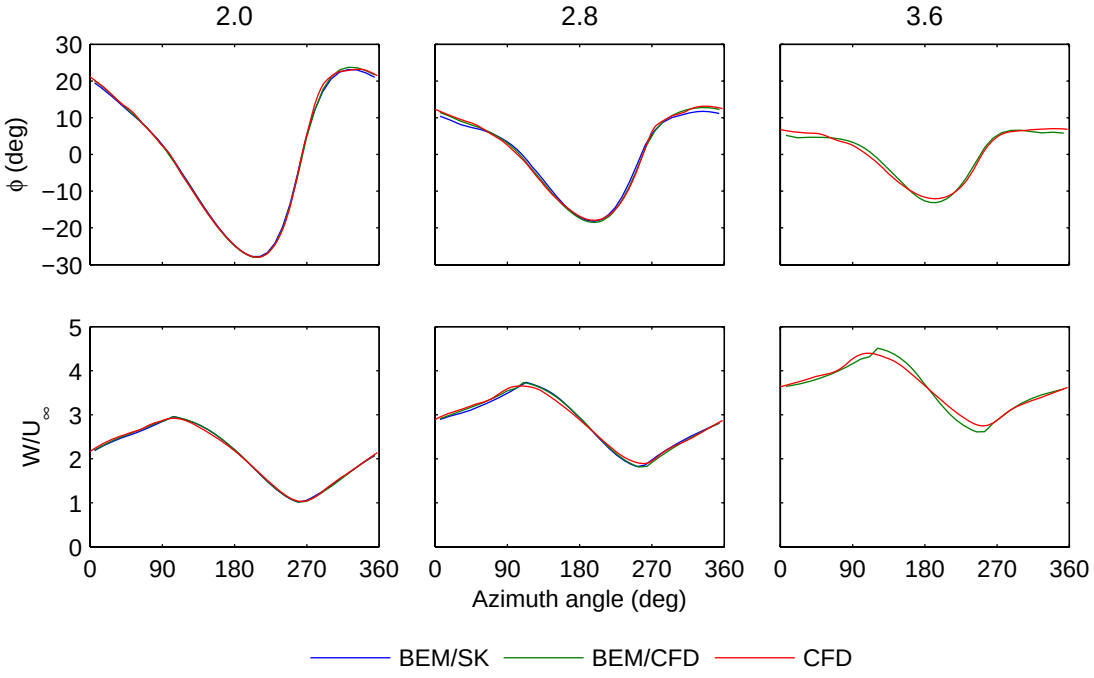

(b) Variable pitch.

Figure 7.8: *Relative flow angle and relative flow speed versus azimuth angle for different tip speed ratios for fixed (a) and variable (b) pitch.*

7.5 Chapter conclusions

Two key conclusions should be taken from this chapter. First, the importance of the section data used in the blade element model has been shown by the comparisons between the BEM/SK and BEM/CFD results. For the fixed pitch case with deep stall there is a blatant difference in the power and torque coefficient curves from the two result sets. Significant differences are also seen for the thrust curve and for the blade force and quarter chord moment. Surprisingly though, the differences in the velocity field are less marked. For the variable pitch case, with no stall, the differences are smaller, and most obvious in the power coefficient curve, where the BEM/SK results show a peak power coefficient that is more than five percentage points higher than that given by the BEM/CFD results.

Second, for the case of variable pitch, whilst the agreement in the power, torque and thrust curves is very good or excellent between the BEM/CFD and CFD result sets, the agreement for the force and moment and the velocity field is less good. In general, the CFD results show greater power extraction during the upstream pass of the blades and lower power extraction during the downstream pass, relative to the BEM/CFD results.

Chapter 8
Conclusions

8.1 Contribution

8.1.1 A rigourous approach to numerical analysis

It is felt that one of the major contributions of this thesis is to establish and demonstrate a rigourous approach to the numerical analysis of a vertical axis turbine. Such rigour in numerical analysis appears much more commonly in fields where CFD is an established tool, aeronautics being a prime example, and is an important element in transforming CFD from a qualitative 'colours for directors' activity into a serious quantitative analysis tool.

Part of the problem lies in accessing and utilizing the voluminous literature which exists in the field of aeronautics and which is eminently transferable. It is therefore hoped that this thesis will help in this knowledge transfer and inform decisions on, for example, what turbulence model to use.

That an industry standard CFD code, ANSYS CFX, has been used for this analysis is an important feature as it means that the verified simulation definitions can be readily applied by industry. This author perceives this to be an important function of an academic engineering department.

8.1.2 The future of vertical axis tidal current turbines

The commercial prospects for vertical axis tidal current turbines are inevitably viewed through the prism of the wind energy experience. Whether this is fair and informative is a difficult question to answer, but an attempt was made in section 1.6 of the *introduction* to highlight some of the important points. There it was argued that some of the key reasons why vertical axis turbines were not successful for wind did not apply to tide, or were at least lessened, and this was used as a justification for the present work.

How then does the present work contribute to answering the question of horizontal versus vertical? It is believed that the primary contribution to answering this comes from the power coefficient predictions for variable pitch operation, which are asserted to be accurate. The peak power coefficient of 45.7% and the broad peak in the power coefficient versus tip speed ratio curve are competitive with results for the horizontal axis turbine. Further work in 3D is necessary to improve the realism of these predictions.

8.2 Conclusions

A number of chapter conclusions have already been stated. What follows here is a recapitulation of the most important.

The verification study on airfoils has identified the numerical parameters that must be specified in order to reduce the errors in the lift, drag and moment coefficients to less than 5% from the correct numerical solution. Key error sources are discretization error, far-field boundary error and iteration error.

The validation study on airfoils has shown that very good or excellent agreement is possible with experimental data at low angles of attack. Errors in the zero-lift drag coefficient of around 1% were observed at the highest Reynolds numbers. Towards stall the agreement is less good, with the numerical results tending to overpredict lift and underpredict drag, although the agreement was better for thicker sections.

The validation of oscillating airfoils has highlighted a troubling lack of agreement with experiment for the drag coefficient. No explanation has been found for this. This is felt to be the only unsatisfactory numerical result in the present work.

CFD simulations of the NACA 0024 airfoil have produced a data set for use in the blade element momentum model of the turbine. It is thought that this data set is superior to any currently available in the literature for this profile.

A verification study has been conducted for the vertical axis turbine simulations. This has been based on quantitative analysis of the predictions for the forces and moments on a blade and

qualitative analysis of the velocity field in the wake of the turbine. It is believed that this is the first time such a quantitative verification study has been conducted, and only the second time that any sort of verification has been attempted.

This verification study has defined a numerical procedure for the turbine simulations as follows:

- A solution should be run on the coarse mesh with an angle step of 2° and with loose iterative convergence for 60 turbine revolutions in order that the flow field is fully developed.
- Using the coarse mesh solution for the initial conditions, a solution on the medium mesh with the same angle step but good convergence should be run for 3 turbine revolutions in order to generate accurate force and moment data that are directly comparable with the results of airfoil/hydrofoil simulations.

An identification of the number of turbine revolutions which must be simulated has not been seen in the literature and is highlighted as a particularly significant result. Successive revolutions progressively reduce the predicted power coefficient, and so a solution which has not been sufficiently advanced in time will overestimate this important parameter. Approximate errors from the asymptotic value are as follows: 10% after 10 revolutions, 5% after 20 and 1% after 40. The larger number of revolutions noted above were specified to generate a fully developed velocity field throughout the computational domain.

The CFD results thus produced are accurate and may be used to draw firm conclusions about the behaviour of the vertical axis turbine simulated. The two most important conclusions are in relation to the use of a limiting angle of attack variable pitch strategy. This strategy is shown to:

- Increase the peak power coefficient from 40.1% to 45.7%, and,
- Significantly broaden the peak of the power coefficient versus tip speed ratio curve.

That the peak is broadened is important because of the uncertainty in determining the tip speed ratio in practical operation.

As a study of the effect of solidity was not conducted, these benefits of variable pitch can only be asserted to apply to this geometry. However, the power versus tip speed ratio curve for the fixed pitch case is similar to those reported in the literature and therefore there are good reasons to assume that the conclusions would apply more generally.

The use of the CFD section data in the blade element momentum model of the turbine allows for novel comparisons with the CFD model of the turbine. In making these comparisons, differences in the steady state behaviour of the airfoil/blade section can be eliminated as a source of discrepancy in the results. Given that differences in the section data lead to significant differences in the predicted behaviour of the turbine, as shown, this comparison is particularly valuable. Interestingly, a similar comparison could be made if section data and turbine data were gathered as part of a combined experiment, but this does not appear to have ever been carried out.

Remaining reasons for discrepancies in the results include the effect of flow curvature, dynamic effects (including dynamic stall) and the simplifying assumptions made in deriving blade element momentum models. The combined effect of these factors is thought to be smallest for the case of variable pitch operation at low tip speed ratios. For this case the agreement between blade element momentum and CFD models is excellent for the power, torque and thrust coefficients, good for the force coefficients, somewhat less good for the moment coefficient and very good for the velocity field. The less good agreement for the moment coefficient compared to the force coefficient is a clear sign that dynamic effects such as added mass are important.

As a concluding remark, it is hoped that the specific recommendations on the CFD modelling of air/hydrofoils and vertical axis turbines given here will prove useful for future workers in this area, and that the methodological approach will also be adopted.

8.3 Further work

Some areas for further work are indicated below. These are listed broadly in order of precedence, according to an approximate cost/value judgement.

8.3.1 Improvements to the blade element momentum model

It is believed that improvements to the blade element momentum model, by the inclusion of models for flow curvature and dynamic stall, would yield valuable insight into the significance of these processes.

The use of a flow curvature model requires section data for cambered profiles, but this could be readily produced using the existing CFD setup that has been verified and validated.

Equally, dynamic stall models could be assessed and perhaps even calibrated based on the oscillating airfoil results produced as part of the existing work.

A comparison of results from such an improved blade element model with the existing CFD results could also serve as a basis for potential improvements to, or calibrations of, the blade element model as a whole, although this is a somewhat speculative suggestion.

8.3.2 CFD simulations of further problems

Further problems to be simulated using CFD were identified at the start of this project as part of the building block approach. A diagram showing this was first presented in the *aims and objectives* section of the *introduction* and is repeated here for the third time: figure 8.1.

Clearly the ultimate objective is to simulate all of the problems given in this diagram and the benefits of increasing the problem complexity are highlighted here. A move to 3D and the inclusion of some or all of the supporting structure will decrease the power coefficient of the turbine due to a decreased blockage effect and parasitic losses; it is important to quantify these parasitic losses, particularly as horizontal axis turbines do not feature these to the same extent. The inclusion of the sea bed and the free surface will introduce a new type of blockage and it is thought that this will increase the power coefficient. Such results would have a relevance for all types of tidal current turbine. Given the success of the turbine simulations with the coarse mesh it is thought that a move to 3D is tractable.

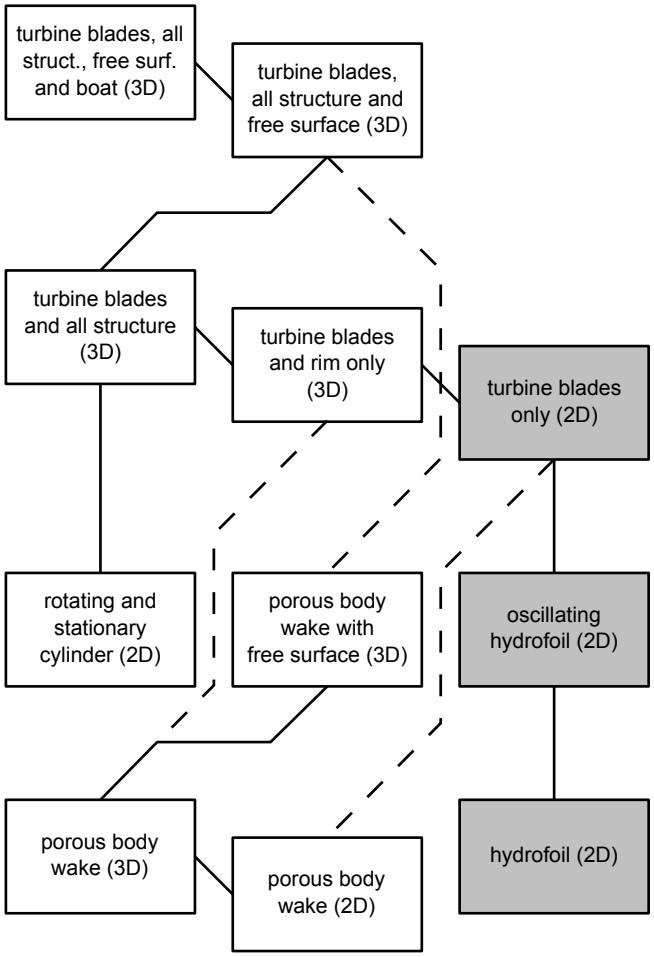

Figure 8.1: *Validation problems relevant to the present work. This diagram shows four validation phases as per the AIAA guidelines, but with the addition of a hierarchy within each phase. Solid lines indicate the flow of information within a phase or between two consecutive phases. Dashed lines indicate the flow of information between non-consecutive phases.*

8.3.3 Comparison of CFD results for the turbine with experimental data

At the beginning of this project it was hoped that experimental data would be available for the Edinburgh Designs turbine, but as noted in the *introduction* these experiments have yet to be carried out. On reflection, it is likely that comparisons of 3D experimental data from this turbine with results from the 2D numerical model would have been problematic and it is unlikely that firm conclusions would have been able to have been drawn. Such data would though merit fruitful comparison with the results from the simulations noted in the sub-section above.

8.3.4 Improving the CFD simulations of the existing problems

It is thought that the numerical approach taken in the present work, RANS-based CFD simulation, provides the potential for accurate prediction of the behaviour of a vertical axis turbine. Further, it is felt that the problem setup implemented realizes this potential for highly accurate results. Notwithstanding this, there remains scope for further work on the existing problems.

One key assumption made which would merit revisiting regards the level of turbulence specified at the inlet to the turbine domain. Investigation of the characteristics of the marine boundary layer showed that the levels of turbulence intensity would be likely to be 2% or higher and that the length scale would be tens or hundreds of metres. The eddy viscosity ratios based on these values were far outwith the range conventionally used and so it was decided to use a lower value. Also, the decay of turbulence intensity from the inlet of the domain to the location of the turbine was such that it was impractical to achieve a level of turbulence intensity of 2% at the turbine. Further investigations would therefore examine the effect of very high values of the eddy viscosity ratio on the predicted results, and means to 'inject' turbulence into the domain immediately upstream of the turbine.

A related problem is the effect of high levels of turbulence on the performance of air/hydrofoil sections. All of the experimental data used for validation is thought to be from wind tunnels with turbulence intensity values of the order of 0.01% or 0.1%, significantly below that found in the marine boundary layer. It was thought that the primary effect of increased turbulence would be earlier transition and therefore that tripped experiments would be largely unaffected. This could be investigated with further simulations.

Considering the above issues related to turbulence, the use of large eddy simulation (LES) or detached eddy simulation (DES) approaches are attractive options. Whilst the use of these methods was not considered tractable at the present time, this will of course change.

Appendix A
Blade element momentum model code listing

A listing of the main function in the blade element momentum code is given below.

Note that a right arrow (→) is used to indicate a line continuation.

```
function TurbineOut = VATBEM2( TurbineIn, SectionData )
% ========================================================================
% NAME: VATBEM2
% CREATED: 22nd July 2008
% AUTHOR: G Gretton
% ------------------------------------------------------------------------
% CREATED FROM: VATBEM1
% CHANGES: VATBEM2 allows for variable pitch. The angle beta remains the
% pitch angle, but the input set pitch angle is now called beta_set_deg.
% There are now variables named beta_u_deg and beta_d_deg that store the
% actual pitch angle.
% ------------------------------------------------------------------------
% FUNCTIONS CALLED: ROTMAT, VECTMAG
% ------------------------------------------------------------------------
% GLOBAL VARIABLES: ASD
% ------------------------------------------------------------------------
% LIMITATIONS:
% - 2*streamtubes/N MUST BE INTEGER VALUE for calculating the sum of the
% torque from all blades. This calculation is non-essential and could be
% cut out or ammended.
% ------------------------------------------------------------------------
% CORRECTIONS:
% - Need to set beta_u and beta_d back to beta_set in the case of variable
% pitch if the maximum permitted angle of attack is not exceeded. This is
% necessary when early iterations predict the need for VP, but future
% iterations do not.
% ========================================================================
global ASD
% ------------------------------------------------------------------------
% CREATE INDIVIDUAL VARIBALES FROM TurbineIn STRUCTURE:
% ------------------------------------------------------------------------
streamtubes = TurbineIn.streamtubes;
flowspeed = TurbineIn.flowspeed;
rho = TurbineIn.rho;
mu = TurbineIn.mu;
R = TurbineIn.R; % Radius of turbine
c = TurbineIn.c; % Chord length of blades
```

```
L = TurbineIn.L; % Length of blade (all calculations are performed per-unit
    →length; length is only applied to all_* forces and torques)
N = TurbineIn.N; % Number of blades
tsr = TurbineIn.tsr; % Tip speed ratio
alpha_i_deg = TurbineIn.alpha_i_deg; % Angle of incidence resulting from
    →flow curvature.
beta_set_deg = TurbineIn.beta_set_deg; % Set pitch angle (not currently
    →used) [single value]
FixedRe = TurbineIn.FixedRe; % Specifies fixed value of the Reynolds number,
    → if desired

% OPTIONAL PARAMETERS:
if isfield( TurbineIn, 'iter_steps' ) == 0 || isempty( TurbineIn.iter_steps
    →), iter_steps = 100; else iter_steps = TurbineIn.iter_steps; end
if isfield( TurbineIn, 'residual'   ) == 0 || isempty( TurbineIn.residual
    →), residual = 1e-6;  else residual   = TurbineIn.residual;   end

% VARIABLE PITCH PARAMETERS
if isfield( TurbineIn, 'VarPitch' ) && isempty( TurbineIn.VarPitch ) == 0,
    VarPitchMethod = TurbineIn.VarPitch.Method;
    switch VarPitchMethod
        case 'limiting_alpha'
            alpha_u_max_deg = TurbineIn.VarPitch.alpha_u_max_deg;
            alpha_d_max_deg = TurbineIn.VarPitch.alpha_d_max_deg;
    end
else
    VarPitchMethod = '';
end

% ------------------------------------------------------------------------
% CREATE INDIVIDUAL VARIBALES FROM SectionData STRUCTURE:
% ------------------------------------------------------------------------
ASDStructDSName = SectionData.ASDStructDSName;
ASDStructFoilName = SectionData.ASDStructFoilName;
CLDS = SectionData.CLDS;
CDDS = SectionData.CDDS;

% OPTIONAL PARAMETERS:
if isfield( SectionData, 'SymFoil' ) == 0 || isempty( SectionData.SymFoil ),
    → SymFoil = false; else SymFoil = SectionData.SymFoil; end

%% ========================================================================
% INITIALIZATION
% ========================================================================

% ------------------------------------------------------------------------
% CALCULATE STREAMTUBE ANGLES
% ------------------------------------------------------------------------
dtheta = pi/streamtubes;
% theta angles go from 'top' to 'bottom'
% Theta is the angle from the local flow vector (the x direction in the
% Flow (F) c.s., to the tangential (x) direction in the Rotating (R) c.s.,
% defined as positive in the anticlockwise direction.
theta_u = linspace( 0 + dtheta/2 , pi - dtheta/2 , streamtubes ); % ***
    →ANTICLOCKWISE ***
theta_d = linspace( 2*pi - dtheta/2 , pi + dtheta/2 , streamtubes ); % ***
    →CLOCKWISE ***
```

```
% ------------------------------------------------------------------------
% FLOW VELOCITY ARRAY
% ------------------------------------------------------------------------
% Create matrix consisting of freestream flow velocity vectors for each
% streamline, in the FLOW coordinate system
UInf_F(1,:) = flowspeed*ones(1,streamtubes);
UInf_F(2,:) = zeros(1,streamtubes);

% ------------------------------------------------------------------------
% BLADE VELOCITY ARRAY
% ------------------------------------------------------------------------
Omega = tsr*flowspeed / R;
% Create vector of blade velocity in the ROTATING c.s.
OmegaR_R(1,1) = Omega*R;
OmegaR_R(2,1) = 0;

% ------------------------------------------------------------------------
% PITCH ACTUATION SCHEDULE
% ------------------------------------------------------------------------
% Beta is the angle from the tangential (x) direction in the
% Rotating (R) c.s. to the chord line (the x direction in the Blade (B)
    →c.s.),
% defined as positive in the anticlockwise direction.
% *** POSITIVE IS NOSE IN ***
beta_set = beta_set_deg*2*pi / 360;

% ------------------------------------------------------------------------
% LOAD/ADAPT AIRFOIL DATA
% ------------------------------------------------------------------------
if isempty( ASDStructDSName ) == 0 && isempty( ASDStructFoilName ) == 0,

    [ CLRevalues, CLalphavalues ] = meshgrid( ASD.( ASDStructDSName ).(
        →ASDStructFoilName ).CL.Revals, ASD.( ASDStructDSName ).(
        →ASDStructFoilName ).CL.alphavals );
    CLvalues = ASD.( ASDStructDSName ).( ASDStructFoilName ).CL.coeffs;

    [ CDRevalues, CDalphavalues ] = meshgrid( ASD.( ASDStructDSName ).(
        →ASDStructFoilName ).CD.Revals, ASD.( ASDStructDSName ).(
        →ASDStructFoilName ).CD.alphavals );
    CDvalues = ASD.( ASDStructDSName ).( ASDStructFoilName ).CD.coeffs;

elseif isempty( CLDS ) == 0 && isempty( CDDS ) == 0,

    [rows,columns] = size(CLDS);
    [CLRevalues,CLalphavalues] = meshgrid( CLDS(1,2:columns) ,
        →CLDS(2:rows,1) );
    CLvalues = CLDS(2:rows,2:columns);

    [rows,columns] = size(CDDS);
    [CDRevalues,CDalphavalues] = meshgrid( CDDS(1,2:columns) ,
        →CDDS(2:rows,1) );
    CDvalues = CDDS(2:rows,2:columns);

else
    disp( 'There appears to be no section data - exiting from VATBEM
        →function' );
    return
end
```

```
% ------------------------------------------------------------------------
% CLEAR VARIABLES
% ------------------------------------------------------------------------
clear TurbineIn SectionData ASDStructDSName ASDStructFoilName CLDS CDDS

% ------------------------------------------------------------------------
% ITERATION INITIALIZATION PARAMETERS
% ------------------------------------------------------------------------
% Initialize au_store and ad_store to be zero (first guess used in point
% iteration).
% Also preallocate enough space for 10 iterations.
au_store = zeros(streamtubes,10);
ad_store = zeros(streamtubes,10);

% ------------------------------------------------------------------------
% PREALLOCATION (INITIALIZATION)
% ------------------------------------------------------------------------
au = NaN(1,streamtubes);
ad = au;

phi_u = au;
phi_d = au;

% -------------------------------------------------
if isempty( FixedRe ),
    Re_u = au;
    Re_d = au;
else
    Re_u = FixedRe*ones(1,streamtubes);
    Re_d = FixedRe*ones(1,streamtubes);
end
% -------------------------------------------------

alpha_u = au;
alpha_d = au;

alpha_u_deg = au;
alpha_d_deg = au;

beta_u = beta_set*ones(1,streamtubes);
beta_d = beta_set*ones(1,streamtubes);

CL_u = au;
CL_d = au;

CD_u = au;
CD_d = au;

CT_u = au;
CT_d = au;

CN_u = au;
CN_d = au;

Qu = au;
Qd = au;
```

```
Qu_tilde = au;
Qd_tilde = au;

Tu_tilde = au;
Td_tilde = au;

dpsi_u = au;
dpsi_d = au;

Uu = au;
Ud = au;

Wu = au;
Wd = au;

%% =====================================================================
% CALCULATIONS (ITERATE FLOW CONDITIONS FOR EACH STREAMTUBE)
% =====================================================================

for i = 1:streamtubes, % For each streamtube i.e. for each angle between the
    → local flow vector and the tangential direction

    j = 1; % Set iteration number

    while j == 1 || ( j <= iter_steps && ( ...
            ( abs( au_store(i,j) - au_store(i,j-1) ) > residual ) || ...
            ( abs( ad_store(i,j) - ad_store(i,j-1) ) > residual ) ) ),

        au(i) = au_store(i,j); % Current value for the upstream axial
            →induction factor
        ad(i) = ad_store(i,j); % Current value for the downstream axial
            →induction factor

        Uu_F(:,i) = UInf_F(:,i)*( 1 - au(i) );
        Ua_F(:,i) = UInf_F(:,i)*( 1 - 2*au(i) );
        Ud_F(:,i) = Ua_F(:,i)*( 1 - ad(i) );

        Uu_R(:,i) = ROTMAT( theta_u(i) )*Uu_F(:,i);
        Ud_R(:,i) = ROTMAT( theta_d(i) )*Ud_F(:,i);

        % Phi is the angle from the tangential (x) direction in the
        % Rotating (R) c.s. to the relative flow vector, defined as
        % positive in the anticlockwise direction.
        phi_u(i) = atan2( Uu_R(2,i) , OmegaR_R(1) + Uu_R(1,i) );
        phi_d(i) = atan2( Ud_R(2,i) , OmegaR_R(1) + Ud_R(1,i) );

        Wu_R(:,i) = [ OmegaR_R(1) + Uu_R(1,i) ; Uu_R(2,i) ];
        Wd_R(:,i) = [ OmegaR_R(1) + Ud_R(1,i) ; Ud_R(2,i) ];

        if isempty( FixedRe ), % If fixed Reynolds number is not specified
            Re_u(i) = rho*( Wu_R(1,i)^2 + Wu_R(2,i)^2 )^0.5*c / mu;
            Re_d(i) = rho*( Wd_R(1,i)^2 + Wd_R(2,i)^2 )^0.5*c / mu;
        end

        % Alpha is the angle from the chord line (the x direction in the
        % Blade c.s., to the relative flow vector, defined as positive in
        % the anticlockwise direction.
        alpha_u(i) = phi_u(i) - beta_set;
```

```
alpha_d(i) = phi_d(i) - beta_set;

alpha_u_deg(i) = alpha_u(i)*180 / pi;
alpha_d_deg(i) = alpha_d(i)*180 / pi;

% ------------------------------------------------------------
% LIMITING ANGLE OF ATTACK VARIABLE PITCH STRATEGY
% ------------------------------------------------------------
switch VarPitchMethod
    case 'limiting_alpha'
        % ----------------------------------------------------
        if abs( alpha_u_deg(i) ) > alpha_u_max_deg,
            alpha_u_deg(i) = sign( alpha_u_deg(i) )*alpha_u_max_deg;
            alpha_u(i) = alpha_u_deg(i)*pi / 180;
            beta_u(i) = phi_u(i) - alpha_u(i);
        else
            beta_u(i) = beta_set;
        end

        if abs( alpha_d_deg(i) ) > alpha_d_max_deg,
            alpha_d_deg(i) = sign( alpha_d_deg(i) )*alpha_d_max_deg;
            alpha_d(i) = alpha_d_deg(i)*pi / 180;
            beta_d(i) = phi_d(i) - alpha_d(i);
        else
            beta_d(i) = beta_set;
        end
        % ----------------------------------------------------
end

% ------------------------------------------------------------
% Calculate coefficients:

alpha_u_deg_corrected = alpha_u_deg(i) + alpha_i_deg;
alpha_d_deg_corrected = alpha_d_deg(i) + alpha_i_deg;

% If symmetrical foil is specified, get the absolute value of the
% corrected angle of attack:
if SymFoil,
    alpha_u_deg_corrected = abs( alpha_u_deg_corrected );
    alpha_d_deg_corrected = abs( alpha_d_deg_corrected );
end

CL_u(i) = interp2( CLRevalues, CLalphavalues, CLvalues, Re_u(i),
    →alpha_u_deg_corrected );
CL_d(i) = interp2( CLRevalues, CLalphavalues, CLvalues, Re_d(i),
    →alpha_d_deg_corrected );

% If symmetrical foil is specified, multiply lift values by the
% sign of the corrected angle of attack.
% (Can't use alpha_?_deg_corrected here because we've already taken
% abs value of.)
if SymFoil,
    CL_u(i) = sign( alpha_u_deg(i) + alpha_i_deg )*CL_u(i);
    CL_d(i) = sign( alpha_d_deg(i) + alpha_i_deg )*CL_d(i);
end

CD_u(i) = interp2( CDRevalues, CDalphavalues, CDvalues, Re_u(i),
    →alpha_u_deg_corrected );
```

```
    CD_d(i) = interp2( CDRevalues, CDalphavalues, CDvalues, Re_d(i),
        →alpha_d_deg_corrected );

    temp = ROTMAT( -alpha_u(i) )*[ CD_u(i) ; CL_u(i) ];
    CT_u(i) = temp(1); CN_u(i) = temp(2);
    temp = ROTMAT( -alpha_d(i) )*[ CD_d(i) ; CL_d(i) ];
    CT_d(i) = temp(1); CN_d(i) = temp(2);
    % -ve alpha in above two lines because alpha is +ve from chord line
    % to relative flow

    % ------------------------------------------------------------
    % Calculate forces:

    Fu_B(:,i) = 0.5*rho*( Wu_R(1,i)^2 + Wu_R(2,i)^2 )*c*[ CT_u(i) ;
        →CN_u(i) ];
    Fd_B(:,i) = 0.5*rho*( Wd_R(1,i)^2 + Wd_R(2,i)^2 )*c*[ CT_d(i) ;
        →CN_d(i) ];

    % Angle from the Flow c.s. to the Blade c.s. is theta + beta,
    % so angle from the Blade to the Flow is - ( theta + beta )
    Fu_F(:,i) = ROTMAT( - ( theta_u(i) + beta_u(i) ) )*Fu_B(:,i); % beta
        → is variable
    Fd_F(:,i) = ROTMAT( - ( theta_d(i) + beta_d(i) ) )*Fd_B(:,i); % beta
        → is variable

    au_store(i,j+1) = Fu_F(1,i)*( N / ( 2*pi ) )*( 1 / ( 2*rho*(
        →UInf_F(1,i)^2 + UInf_F(2,i)^2 )*R*abs( sin( theta_u(i) ) ) ) )
        →/ ( 1 - au(i) );
    ad_store(i,j+1) = Fd_F(1,i)*( N / ( 2*pi ) )*( 1 / ( 2*rho*(
        →Ua_F(1,i)^2 + Ua_F(2,i)^2 )*R*abs( sin( theta_d(i) ) ) ) ) / (
        →1 - ad(i) );

    j = j+1;

end % end "while streamline solution has not converged" loop

% Torque, Power and azimuthal position calculations

Fu_R(:,i) = ROTMAT( - beta_u(i) )*Fu_B(:,i); % beta is variable
Fd_R(:,i) = ROTMAT( - beta_d(i) )*Fd_B(:,i); % beta is variable

Qu(i) = - ( Fu_R(1,i)*R ); % Negative sign because we are defining
    →torque as positive anticlockwise
Qd(i) = - ( Fd_R(1,i)*R ); % Negative sign because we are defining
    →torque as positive anticlockwise
% Torque is positive in this direction in proper right hand c.s.
% If this calculation was done as a correct vector cross product then
% we would not need negative sign

Qu_tilde(i) = - ( N / ( 2*pi*R ) )*( 2*VECTMAG( Ud_F(:,i) ) / ( VECTMAG(
    → Uu_F(:,i) ) + VECTMAG( Ud_F(:,i) ) ) )*R*( Fu_R(1,i)*R )*dtheta; %
    → -ve because torque +ve clockwise
Qd_tilde(i) = - ( N / ( 2*pi*R ) )*( 2*VECTMAG( Uu_F(:,i) ) / ( VECTMAG(
    → Uu_F(:,i) ) + VECTMAG( Ud_F(:,i) ) ) )*R*( Fd_R(1,i)*R )*dtheta; %
    → -ve because torque +ve clockwise

Tu_tilde(i) = ( N / ( 2*pi*R ) )*( 2*VECTMAG( Ud_F(:,i) ) / ( VECTMAG(
    →Uu_F(:,i) ) + VECTMAG( Ud_F(:,i) ) ) )*R*( Fu_F(1,i) )*dtheta;
```

```
    Td_tilde(i) = ( N / ( 2*pi*R ) )*( 2*VECTMAG( Uu_F(:,i) ) / ( VECTMAG(
        →Uu_F(:,i) ) + VECTMAG( Ud_F(:,i) ) ) )*R*( Fd_F(1,i) )*dtheta;

    dpsi_u(i) = ( 2*VECTMAG( Ud_F(:,i) ) / ( VECTMAG( Uu_F(:,i) ) + VECTMAG(
        → Ud_F(:,i) ) ) )*dtheta;
    dpsi_d(i) = ( 2*VECTMAG( Uu_F(:,i) ) / ( VECTMAG( Uu_F(:,i) ) + VECTMAG(
        → Ud_F(:,i) ) ) )*dtheta;

    % Magnitudes of key vector variables
    Uu(i) = VECTMAG( Uu_F(:,i) );
    Ud(i) = VECTMAG( Ud_F(:,i) );
    Wu(i) = VECTMAG( Wu_R(:,i) );
    Wd(i) = VECTMAG( Wd_R(:,i) );

    % Calculate wake velocity 24th August 05
    Uw_F(:,i) = Ua_F(:,i)*( 1 - 2*ad(i) );

end % end "for each streamtube" loop

%% =====================================================================
% CALCULATIONS (POST ITERATION)
% =====================================================================

% ---------------------------------------------------------------------
% DISPLAY WARNINGS
% ---------------------------------------------------------------------
columns = size( au_store, 2 );
if columns == iter_steps,
    disp( [ '*** Solution not converged for TSR = ' num2str(tsr) ': maximum
        →number of iterations reached ***' ] )
end
if min(au) < - 0.1
    disp( [ '*** Solution potentially not converged for TSR = '
        →num2str(tsr) ': min(au) = ' num2str( min(au) ) ' ***' ] )
end
if min(ad) < - 0.1
    disp( [ '*** Solution potentially not converged for TSR = '
        →num2str(tsr) ': min(ad) = ' num2str( min(ad) ) ' ***' ] )
end
if max(au) > 0.5
    disp( [ '*** Solution not converged for TSR = ' num2str(tsr) ': max(au)
        →= ' num2str( max(au) ) ' ***' ] )
end
if max(ad) > 0.5
    disp( [ '*** Solution not converged for TSR = ' num2str(tsr) ': max(ad)
        →= ' num2str( max(ad) ) ' ***' ] )
end

% ---------------------------------------------------------------------
% TORQUE AND THRUST SUMMATIONS
% ---------------------------------------------------------------------
Q = sum( Qu_tilde ) + sum( Qd_tilde );
T = sum( Tu_tilde ) + sum( Td_tilde );

Power = Q*Omega;

AD = 2*R; % We have assumed unit depth throughout
```

```
Cq = Q / ( 0.5*rho*flowspeed^2*AD*R );
CP = Power / ( 0.5*rho*flowspeed^3*AD );
CT = T / ( 0.5*rho*flowspeed^2*AD );

% ------------------------------------------------------------------------
% CALCULATE AZIMUTHAL POSITIONS (PSI) OF STREAMTUBE CROSSINGS
% ------------------------------------------------------------------------
psi_u(1) = dpsi_u(1) / 2; % Temporarily consider psi = 0 to be at theta = 0
psi_d(1) = - dpsi_d(1) / 2; % Temporarily consider psi = 0 to be at theta =
    →0

for i=2:streamtubes

    psi_u(i) = psi_u(i-1) + dpsi_u(i-1) / 2 + dpsi_u(i) / 2; % Add dpsi
        →because we are progressing ANTICLOCKWISE
    psi_d(i) = psi_d(i-1) - dpsi_d(i-1) / 2 - dpsi_d(i) / 2; % Deduct dpsi
        →because we are progressing CLOCKWISE

end % end "for each streamtube" loop (this one is only to calculate
    →azimuthal position)

psi_u = psi_u + ( pi - ( psi_u(streamtubes/2) + dpsi_u(streamtubes/2) / 2 )
    →); % Introduce shift such that psi = 0 is at the global x axis by
    →aligning psi = pi with the -x axis
psi_d = psi_d - ( psi_d(streamtubes/2) - dpsi_d(streamtubes/2) / 2 ); %
    →Introduce shift such that psi = 0 is at the global x axis by aligning
    →psi = 0 with the x axis

[ psi_u_cart(1,:) , psi_u_cart(2,:) ] = pol2cart( psi_u , R );
[ psi_d_cart(1,:) , psi_d_cart(2,:) ] = pol2cart( psi_d , R );

% ------------------------------------------------------------------------
% CALCULATE LOCUS OF POINTS AT ATMOSPHERIC PRESSURE AND PLOT WITH
% STREAMTUBES
% ------------------------------------------------------------------------
patm_loc(1,:) = ( psi_u_cart(1,:) + psi_d_cart(1,:) ) / 2;
patm_loc(2,:) = ( psi_u_cart(2,:) + psi_d_cart(2,:) ) / 2;

% ------------------------------------------------------------------------
% CONCATENATE AND REORDER VALUES SO THEY ARE IN TERMS OF PSI PROGRESSING
% ANTICLOCKWISE FROM 0 TO 2PI
% ------------------------------------------------------------------------
all_psi = [ fliplr( psi_d(1:streamtubes/2) ) ,  psi_u , fliplr(
    →psi_d(streamtubes/2 + 1 : streamtubes) ) + 2*pi ];
all_psi_deg = all_psi*360 / ( 2*pi );

all_U = [ fliplr( Ud_F(1,1:streamtubes/2) ) , Uu_F(1,:) , fliplr(
    →Ud_F(1,streamtubes/2 + 1 : streamtubes) ) ];
all_W = [ fliplr( Wd(1:streamtubes/2) ) , Wu , fliplr( Wd(streamtubes/2 + 1
    →: streamtubes) ) ];
all_alpha = [ fliplr( alpha_d(1:streamtubes/2) ) , alpha_u , fliplr(
    →alpha_d(streamtubes/2 + 1 : streamtubes) ) ];
all_alpha_deg = all_alpha*360 / ( 2*pi );

all_beta = [ fliplr( beta_d(1:streamtubes/2) ) , beta_u , fliplr(
    →beta_d(streamtubes/2 + 1 : streamtubes) ) ];
all_beta_deg = all_beta*180 / pi;
```

```
all_FT = L*[ fliplr( Fd_B(1,1:streamtubes/2) ) , Fu_B(1,:) , fliplr(
    →Fd_B(1,streamtubes/2 + 1 : streamtubes) ) ];
all_FN = L*[ fliplr( Fd_B(2,1:streamtubes/2) ) , Fu_B(2,:) , fliplr(
    →Fd_B(2,streamtubes/2 + 1 : streamtubes) ) ];
all_Q = L*[ fliplr( Qd(1:streamtubes/2) ) , Qu , fliplr(  Qd(streamtubes/2 +
    → 1 : streamtubes) ) ];
all_a = [ fliplr( ad(1:streamtubes/2) ), au, fliplr( ad(streamtubes/2 + 1 :
    →streamtubes) ) ];

all_Re = rho*c/mu*all_W;

% ------------------------------------------------------------------------
% CALCULATE SUM OF TORQUE FROM ALL BLADES
% ------------------------------------------------------------------------

uni_psi_deg = linspace( 360/(2*streamtubes) , 360 , 2*streamtubes ); %
    →uniformly distributed sample space in psi

% yi = interp1(x,Y,xi,method)
all_Q_uni_psi = interp1( all_psi_deg , all_Q , uni_psi_deg , 'spline' );

sum_all_Q_uni_psi = NaN(2*streamtubes/N);
for i=1:(2*streamtubes/N)
    sum_all_Q_uni_psi(i) = all_Q_uni_psi(i) +
        →all_Q_uni_psi(i+2*streamtubes/N) +
        →all_Q_uni_psi(i+4*streamtubes/N);
end

sum_all_Q_uni_psi = [sum_all_Q_uni_psi,sum_all_Q_uni_psi,sum_all_Q_uni_psi];

%% =======================================================================
% ADD VARIABLES TO STRUCTURE:
% ------------------------------------------------------------------------

TurbineOut.au = au;
TurbineOut.ad = ad;

TurbineOut.au_store = au_store;
TurbineOut.ad_store = ad_store;

TurbineOut.all_a = all_a;
TurbineOut.all_psi = all_psi;
TurbineOut.all_psi_deg = all_psi_deg;
TurbineOut.all_U = all_U;
TurbineOut.all_W = all_W;
TurbineOut.all_alpha_deg = all_alpha_deg;
TurbineOut.all_beta_deg = all_beta_deg;
TurbineOut.all_FT = all_FT;
TurbineOut.all_FN = all_FN;
TurbineOut.all_Q = all_Q;
TurbineOut.all_Re = all_Re;

TurbineOut.alpha_u_deg = alpha_u_deg;
TurbineOut.alpha_d_deg = alpha_d_deg;

TurbineOut.CL_u = CL_u;
TurbineOut.CD_u = CD_u;
```

```
TurbineOut.CP = CP;
TurbineOut.Cq = Cq;
TurbineOut.CT = CT;

TurbineOut.Fu_B = Fu_B;
TurbineOut.Fd_B = Fd_B;

TurbineOut.patm_loc = patm_loc;

TurbineOut.sum_all_Q_uni_psi = sum_all_Q_uni_psi;

TurbineOut.Uw_F = Uw_F;
```

References

Abbas, A. and Cabello, A. (1997), The NACA 4412 aerofoil, in W. Haase, E. Chaput, E. Elsholz, A. Leschziner, Michael, and U. R. Müller (eds.), *ECARP – European Computational Aerodynamics Research Project: Validation of CFD Codes and Assessment of Turbulence Models*, Vieweg.

Abbott, I. H. and von Doenhoff, A. E. (1959), *Theory of Wing Sections*, Dover.

ABPmer, The Met Office, Garrad Hassan, and Proudman Oceanographic Laboratory (2004a), Atlas of UK marine renewable energy resources: Atlas pages, Produced for the DTI, URN 04/1531.

ABPmer, The Met Office, Garrad Hassan, and Proudman Oceanographic Laboratory (2004b), Atlas of UK marine renewable energy resources: Technical report, Produced for the DTI, URN 04/1532.

ABPmer, The Met Office, and Proudman Oceanographic Laboratory (2008a), Atlas of UK marine renewable energy resources: Atlas pages, Produced for BERR.

ABPmer, The Met Office, and Proudman Oceanographic Laboratory (2008b), Atlas of UK marine renewable energy resources: Technical report, Produced for BERR.

AEA Technology (2002), *CFX-TASCflow Computational Fluid Dynamics Software Theory Documentation*, version 2.12.

Ågren, O., Berg, M., and Leijon, M. (2005), A time-dependent potential flow theory for the aerodynamics of vertical axis wind turbines, *Journal of Applied Physics*, 97.

AIAA (1998), Guide for the verification and validation of computational fluid dynamics simulations, Guide G-077-1998, AIAA.

Ainsworth, D. and Thake, J. (2006), Preliminary works associated with 1 MW tidal turbine, Report for the DTI, URN 06/2046, Project contractor: Sea Generation.

Akins, R. E., Berg, D. E., and Cyrus, W. T. (1987), Measurements and calculations of aerodynamic torques for a vertical-axis wind turbine, Technical Report SAND86-2164, Sandia National Laboratories, [Not examined].

Allen, H. J. and Vincenti, W. G. (1944), Wall interference in a two-dimensional-flow wind tunnel, with consideration of the effect of compressibility, Report 782, NACA.

Anderson, J. D. (2004), *Introduction to Flight*, McGraw-Hill, 5th edition.

Ansys Inc. (2006a), *ANSYS CFX-Solver Modelling Guide*.

Ansys Inc. (2006b), *ANSYS CFX-Solver Theory Guide*.

Antheaume, S., Maître, T., and Achard, J.-L. (2008), Hydraulic Darrieus turbines efficiency for free fluid flow conditions versus power farms conditions, *Renewable Energy*, 33, pp. 2186–2198.

Barlow, J. B., Rae, W. H. J., and Pope, A. (1999), *Low-Speed Wind Tunnel Testing*, John Wiley & Sons.

Baubeau, R. and Latorre, R. (1995), Numerical study of hydrofoil boundary layers, *Ocean Engineering*, 22, pp. 87–95.

Baumert, H. Z., Simpson, J., and Sündermann, J. (eds.) (2005), *Marine Turbulence: Theories, observations and models*, Cambridge University Press.

BERR (2007a), Digest of United Kingdom energy statistics 2008.

BERR (2007b), Energy flow chart 2007.

BERR (2008), Severn tidal power feasibility study: Terms of reference.
URL `http://www.berr.gov.uk/files/file43810.pdf`

BERR (2009), [Accessed 16th February 2009].
URL `http://www.berr.gov.uk/whatwedo/energy/sources/renewables/explained/severntidalpower/thefeasibilitystudy/page46182.html`

Bertagnolio, F., Sørensen, N., Johansen, J., and Fuglsang, P. (2001), Wind turbine airfoil catalogue, Report Risø-R-1280(EN), Risø National Laboratory, Roskilde, Denmark.

Binnie, Black and Veatch (2001), The commerical prospects for tidal stream power, Report for the DTI, ETSU T/06/00209/REP, DTI URN 01/1011.

Black and Veatch (2004), UK, Europe and global tidal stream energy resource assessment, Report 107799/D/2100/05/1 for the Carbon Trust, UK.

Black and Veatch (2005a), Phase II UK tidal stream energy resource assessment, Report 107799/D/2200/03 for the Carbon Trust, UK.

Black and Veatch (2005b), Tidal stream resource and technology summary report, Report 107799/D/2200/04 for the Carbon Trust, UK.

Blue Energy (2009), [Accessed 16th February 2009].
URL `http://www.bluenergy.com/davisTurbinesptypes.html`

Blunden, L. S. and Bahaj, A. S. (2007), Tidal energy resource assessment for tidal stream generators, *Proc. IMechE Part A: Journal of Power and Energy*, 221, pp. 137–146.

Brahimi, M. T., Allet, A., and Paraschivoiu, I. (1995), Aerodynamic analysis models for vertical-axis wind turbines, *International Journal of Rotating Machinery*, 2(1), pp. 15–21.

Brochier, G., Fraunié, P., Béguier, C., and Paraschivoiu, I. (1986), Water channel experiments of dynamic stall on Darrieus wind turbine blades, *AIAA Journal of Propulasion and Power*, 2(5), pp. 445–449, [Not examined].

Bryden, I. and Melville, G. T. (2004), Choosing and evaluating sites for tidal current development, *Proc. IMechE Part A: Journal of Power and Energy*, 218, pp. 567–577.

Bryden, I. G. and Couch, S. J. (2004), Marine energy extraction: Tidal resource analysis, in *Proceedings of the World Renewable Energy Congress VII*, Denver, CO, USA.

Bryden, I. G. and Couch, S. J. (2006), Me1: Marine energy extraction: Tidal resource analysis, *Renewable Energy*, 31, pp. 133–139, [Bibliographic note: this paper is a reprint of (Bryden and Couch, 2004)].

Bullivant, K. W. (1941), Tests of the NACA 0025 and NACA 0035 airfoils in the full-scale wind tunnel, Technical Report No. 708, NACA.

Burton, T., Sharpe, D., Jenkins, N., and Bossanyi, E. (2001), *Wind Energy Handbook*, Wiley.

Calcagno, G., Salvatore, F., Greco, L., Moroso, A., and Eriksson, H. (2006), Experimental and numerical investigation of an innovative technology for marine current exploitation: The Kobold turbine, in *Proceedings of the International Offshore and Polar Engineering Conference (ISOPE)*, pp. 323–330, San Francisco, CA, USA.

Campbell, A. R., Simpson, J. H., and Allen, G. L. (1998), The dynamical balance of flow in the menai strait, *Estuarine, Coastal and Shelf Science*, 46, pp. 449–455.

Camporeale, S. M. and Magi, V. (2000), Streamtube model for analysis of vertical axis variable pitch turbine for marine currents energy conversion, *Energy Conversion and Management*, 41, pp. 1811–1827.

Carr, L. W., McCroskey, W. J., McAlister, K. W., Pucci, S. L., and Lambert, O. (1982), An experimental study of dynamic stall on advanced airfoil sections volume 3: Hot-wire and hot-film measurements, Technical Memorandum 84245, NASA.

Cartwright, D. E., Edden, A. C., Spencer, R., and Vassie, J. M. (1980), The tides of the northeast Atlantic Ocean, *Philos. Trans. R. Soc. Lond. Ser. A*, 298(1436), pp. 87–139, [Not examined].

Casey, M. and Wintergerste, T. (2000), *Special Interest Group on Quality and Trust in Industrial CFD: Best Practice Guidelines*, ERCOFTAC (European Research Community on Flow, Turbulence and Combustion).

Castro, I. P. (1971), Wake characteristics of two-dimensional perforated plates normal to an air-stream, *Journal of Fluid Mechanics*, 46(3), pp. 599–609.

Cebeci, T., Platzer, M., Chen, H., Chang, K.-C., and Shao, J. P. (eds.) (2005), *Analysis of Low-Speed Unsteady Airfoil Flows*, Horizons/Springer.

Clarke, J. A., Connor, G., Grant, A. D., and Johnstone, C. M. (2007), Design and testing of a contra-rotating tidal current turbine, *Proc. IMechE Part A: Journal of Power and Energy*, 221, pp. 171–179.

Coiro, D., Nicolosi, F., De Marco, A., Melone, S., and Montella, F. (2005), Flow curvature effects on dynamic behaviour of a novel vertical axis tidal current turbine: Numerical and experimental analysis, in *Proceedings of the 24th International Conference on Offshore Mechanics and Arctic Engineering (OMAE 2005)*, Halkidiki, Greece.

Couch, S. J. and Bryden, I. (2006), Tidal current energy extraction: hydrodynamic resource characteristics, *Proc. IMechE Part M: Journal of Engineering for the Maritime Environment*, 220, pp. 185–194.

Couch, S. J. and Bryden, I. G. (2005), Numerical modelling of energy extraction from tidal flows, in *Proceedings of the World Renewable Energy Congress*, pp. 550–555, Aberdeen, UK.

Critzos, C. C., Heyson, H. H., and Boswinkle, R. W. (1955), Aerodynamic characteristics of NACA 0012 airfoil section at angles of attack from 0° to 180°, Technical Note 3361, NACA.

Darrieus, G. J. M. (1931), Turbine having its rotating shaft transverse to the flow of the current, uS patent 1835018.

Department of Energy (1981), Tidal power from the severn estuary, volume i, Energy paper 46 (The Bondi Report), [Not examined].

Department of Energy (1989), The severn barrage project: General report, Energy paper 57 (Tripartite study: The Department of Energy, The Central Electicity Generating Board and the Severn Tidal Power Group), [Not examined].

von Doenhoff, A. E. and Abbott, I. H. (1947), The Langley two-dimensional low-turbulence pressure tunnel, Techncal Note 1283, NACA.

Döerner, H. (1975), Efficiency and economic comparison of different WEC – (wind energy converter) rotor systems, in *Appropriate technologies for semiarid areas: wind and solar energy for water supply*, pp. 43–70, Berlin.

Dominy, R., Lunt, P., Bickerdyke, A., and Dominy, J. (2007), Self-starting capability of a Darrieus turbine, *Proc. IMechE Part A: Journal of Power and Energy*, 221, pp. 111–120.

Drela, M. (1989a), Integral boundary layer formulation for blunt trailing edges, *AIAA Paper 89-2166*.

Drela, M. (1989b), Xfoil: an analysis and design system for low Reynolds number airfoils, in *Conference on Low Reynolds Number Aerodynamics*, University of Notre Dame, Indiana, USA.

Drela, M. and Giles, M. B. (1987), Viscous-inviscid analysis of transonic and low Reynolds number airfoils, *AIAA Journal*, 25(10), pp. 1347–1355.

Drela, M. and Youngren, H. (2001), *Xfoil 6.9 User Primer*.
URL `http://web.mit.edu/drela/Public/web/xfoil/xfoil_doc.txt`

Drela, M. and Youngren, H. (2008), Xfoil: Subsonic airfoil development system.
URL `http://web.mit.edu/drela/Public/web/xfoil/`

Dular, M., Bachert, R., Stoffel, B., and Širok, B. (2005), Experimental evaluation of numerical simulation of cavitating flow around hydrofoil, *European Journal of Mechanics B/Fluids*, 24, pp. 522–538.

EC (1996), The exploitation of tidal and marine currents, Technical Report EUR 16683 EN, Commission of the European Communities, Directorate-General for Science, Research and Development, [Not examined].

EDF (2009), The Rance tidal power plant, power from the ocean, [Accessed 19th February 2009].
URL `http://www.edf.fr/html/en/decouvertes/voyage/usine/retour-usine.html`

Egbert, G. D. and Ray, R. D. (2001), Estimates of M_2 tidal energy dissipation from TOPEX/Poseidon altimeter data, *J. Geophys. Res. Oceans*, 106(C10), pp. 22475–22502, [Not examined].

Ekaterinaris, J. A. and Menter, F. R. (1994), Computation of oscillating airfoil flows with one- and two-equation turbulence models, *AIAA Journal*, 32(12), pp. 2359–2365.

Ekaterinaris, J. A. and Platzer, M. F. (1997), Computational prediction of airfoil dynamic stall, *Progress in Aerospace Sciences*, 33, pp. 759–846.

Elliott, D. (2004), Tidal power, in G. Boyle (ed.), *Renewable Energy: Power for a sustainable future*, Oxford University Press.

EMEC (2009), [Accessed 11th February 2009].
URL `http://www.emec.org.uk/tidal_developers.asp`

Engineering Business (2002), Research and development of a 150 kW tidal stream generator, Report to the DTI, URN 02/1400.

Engineering Business (2003), Stingray tidal stream energy device: Phase 2, Report to the DTI, URN 03/1433.

Engineering Business (2005), Stingray tidal stream energy device: Phase 3, Report to the DTI, URN 05/864.

Entec (2007), Tidal power in the UK: Research report 2: tidal technologies overview, Report for the Sustainable Development Commission, UK.

Eppler, R. (2003), About classical problems of airfoil drag, *Aerospace Science and Technology*, 7, pp. 289–297.

Eppler, R. and Somers, D. M. (1980), A computer program for the design and analysis of low-speed airfoils, TM 80210, NASA.

Eriksson, S., Bernhoff, H., and Leijon, M. (2008), Evaluation of different turbine concepts for wind power, *Renewable and Sustainable Energy Reviews*, (12), pp. 1419–1434.

ETSU (1993), Tidal stream energy review, [Not examined].

ETSU (1999), New and renewable energy: Prospects in the UK for the 21st century: Supporting analysis, ETSU R-122.

Fanucci, J. B. and Walters, R. E. (1976), Innovative wind machines: The theoretical performances of a vertical axis wind turbine, in *Proceedings of the vertical axis wind turbine technology workshop*, publised as Sandia Laboratory report SAND 76-5586, [Not examined].

Ferziger, J. (2005), Turbulence: its origins and structure, in H. Z. Baumert, J. Simpson, and J. Sündermann (eds.), *Marine Turbulence: Theories, observations and models*, Cambridge University Press.

Ferziger, J. H. and Peric, M. (2002), *Computational Methods for Fluid Dynamics*, Springer.

Flather, R. A. (1976), A tidal model of the north-west European continental shelf, *Mémoires de la Société Royale des Sciences de Liège*, 10(6), pp. 141–164.

Fraenkel, P. L. (2002), Power from marine currents, *Proc. IMechE Part A: Journal of Power and Energy*, 216, pp. 1–14.

Fraenkel, P. L. (2007), Marine Current Turbines: Pioneering the development of marine kinetic energy converters, *Proc. IMechE Part A: Journal of Power and Energy*, 221, pp. 159–169.

Fraenkel, P. L. and Musgrove, P. J. (1979), Tidal and river current energy systems, in *Conference on Future Energy Concepts*, pp. 114–117, IEE, [Not examined].

Garrad Hassan (2009), [Accessed 26th March 2009].
URL `http://www.garradhassan.com/products/ghbladed/index.php`

Garrett, C. and Cummins, P. (2004), Generating power from tidal currents, *ASCE Journal of Waterway, Port, Coastal and Ocean Engineering*, 130(3), pp. 114–118.

Garrett, C. and Cummins, P. (2005), The power potential of tidal currents in channels, *Proceedings of the Royal Society of London A*, 461, pp. 2563–2572.

GCK Technology (2009).
URL http://www.gcktechnology.com/GCK/pg2.html

Glauert, H. (1947), *The elements of aerofoil and airscrew theory*, Cambridge University Press, 2nd edition.

Goett, H. J. and Bullivant, K. W. (1939), Tests of NACA 0009, 0012 and 0018 airfoils in the full scale tunnel, Technical Report No. 647, NACA.

Gorban, A. N., Gorlov, A. M., and Silantyev, M., Valentin (2001), Limits of the turbine efficiency for free fluid flow, *ASME Journal of Energy Resources Technology*, 123, pp. 311–317.

Gregory, N. and O'Reilly, C. L. (1970), Low-speed aerodynamic characteristics of NACA 0012 aerofoil section, including the effects of upper-surface roughness simulating hoar frost, Aero Report 1308, NPL.

Gretton, G. I. and Bruce, T. (2005), Preliminary results from analytical and numerical models of a variable-pitch vertical-axis tidal current turbine, in *Proceedings of the 6th European Wave and Tidal Energy Conference*, Glasgow, UK.

Gretton, G. I. and Bruce, T. (2007), Aspects of mathematical modelling of a prototype scale vertical-axis turbine, in *Proceedings of the 7th European Wave and Tidal Energy Conference*, Porto, Portugal.

Grylls, W., Dale, B., and Sarre, P.-E. (1978), A theoretical and experimental investigation into the variable pitch vertical axis wind turbine, in *2nd International Symposium on Wind Energy Systems*, [Not examined].

Haase, W., Chaput, E., Elsholz, E., Leschziner, A., Michael, and Müller, U. R. (eds.) (1997), *ECARP – European Computational Aerodynamics Research Project: Validation of CFD Codes and Assessment of Turbulence Models*, volume 58 of *Notes on Numerical Fluid Mechanics*, Vieweg, Brunswick, Germany.

Hallé, S. (1995), *Simulation numérique du décrochage dynamique d'un profil en mouvement de rotation Darrieus en régime turbulent*, Master's thesis, École Polytechnique de Montréal, Canada, [Not examined].

Hammerfest Strøm (2009a), [Accessed 22nd February 2009].
URL http://www.hammerfeststrom.com/content/view/66/101/lang,en/

Hammerfest Strøm (2009b), [Accessed 11th February 2009].
URL http://www.hammerfeststrom.com/content/view/57/82/lang,en/

Hansen, M. O. L. and Sørensen, D. N. (2001), CFD model for vertical axis wind turbine, in *Proceedings of the European Wind Energy Conference*, Copenhagen, Denmark.

Hastings, R. C. and Williams, B. R. (1987), Studies of the flow field near a NACA 4412 aerofoil at nearly maximum lift, *Aeronautical Journal*, 91(901), pp. 29–44.

Holmes, O. (1976), A contribution to the aerodynamic theory of the vertical axis wind turbine, in *Proceedings of the International Symposium on Wind Energy Systems*, Cambridge, UK.

Horiuchi, K., Ushiyama, I., and Seki, K. (2005), Straight wing vertical axis wind turbines: A flow analysis, *Wind Engineering*, 29(3), pp. 243–252.

Huang, Z., Kawall, J. G., and Keffer, J. F. (1996), Development of structure within the turbulent wake of a porous body. Part 2. Evolution of the three-dimensional features, *Journal of Fluid Mechanics*, 329, pp. 117–136.

Huang, Z. and Keffer, J. F. (1996), Development of structure within the turbulent wake of a porous body. Part 1. The initial formation region, *Journal of Fluid Mechanics*, 329, pp. 103–115.

Hwang, I., Lee, Y., and Kim, S. (2007), Effectiveness enhancement of a cycloidal wind turbine by individual active control of blade motion, in *Active and Passive Smart Structures and Integrated Systems 2007, Proceedings of the SPIE*, volume 6525, pp. 316–323.

Hwang, I., Min, S., Jeong, I., Lee, Y., and Kim, S. (2006), Efficiency improvement of a new vertical axis wind turbine by individual active control of blade motion, in *Proceedings of the SPIE*, volume 6173.

HydroVenturi (2009), [Accessed 16th February 2009].
URL http://www.hydroventuri.com

ICIT and IT Power (1995), Feasibility study of tidal current power generation for coastal waters: Orkney and Shetland, Final report for EU contract XVII/4 1040/92-41, [Not examined].

IEA (2008), *Key World Energy Statistics*.

Ikoma, T., Masuda, K., Fujio, S., Nakada, H., Maeda, H., and Rheem, C. (2008), Characteristics of hydrodynamic forces and torque on Darrieus type water turbines for current power generation systems with CFD computations, in *Oceans 2008 MTS/IEEE Kobe Techno-Ocean*, pp. 1326–33, Kobe, Japan.

Inglis, D. R. (1979), A windmill's theoretical maximum extraction of power from the wind, *American Journal of Physics*, 47(5), pp. 416–420.

IPCC (2007), *Climate Change 2007: Synthesis Report. Contribution of working groups I, II, and III to the Fourth Assessment Report of the Intergovernmental Panel on Climate Change*, Geneva, Switzerland.

Ishimatsu, K., Kage, K., and Okubayashi, T. (2002), Numerical trial for Darrius-type alternating flow turbine, in *Proceedings of the 12th International Offshore and Polar Engineering Conference*, Kitakyushu, Japan.

IT Power, Seacore, Gesamthochschule Kassel, and Jahnel-Kesterman (2005), Seaflow: World's first pilot project for the exploitation of marine currents at a commerical scale, report for the European Commission Directorate-General for Research, contract JOR3-CT98-0202, report EUR 21616.

IWPDC (2008), Talking wave and wind, [Note: the article title may be a mis-print and should perhaps be "Talking wave and tidal"].
URL `http://www.waterpowermagazine.com/story.asp?storyCode=2048551`

Jacobs, E. N. and Sherman, A. (1937), Airfoil section characteristics as affected by variations of the Reynolds number, Report No. 586, NACA.

Jacobs, E. N., Ward, K. E., and Pinkerton, R. M. (1933), The characteristics of 78 related airfoil sections from tests in the Variable-density Wind Tunnel, Report No. 460, NACA.

Jürgens, D., Palm, M., Singer, S., and Urban, K. (2007), Numerical optimization of the voith-schneider propeller, *ZAMM – Journal of Applied Mathematics and Mechanics / Zeitschrift f ur Angewandte Mathematik und Mechanik*, 87(10), pp. 698–710.

Katz, J. and Plotkin, A. (1991), *Low-Speed Aerodynamics: From wing theory to panel methods*, McGraw-Hill, (International edition).

Kirke, B. K. (1998), *Evaluation of Self-Starting Vertical Axis Wind Turbines for Stand-Alone Applications*, Ph.D. thesis, School of Engineering, Griffith University.
URL http://www.cyberiad.net/vawt.htm

Klaptocz, V. R., Rawlings, G. W., Nabavi, Y., Alidadi, M., Li, Y., and Calisal, S. M. (2007), Numerical and experimental investigation of a ducted vertical axis tidal current turbine, in *Proceedings of the 7th European Wave and Tidal Energy conference*, Porto, Portugal.

Klebanoff, P. S. (1955), Characteristics of turbulence in a boundary layer with zero pressure gradient, Report 1247, NACA.

Klimas, P. C. (1982), Darrieus rotor aerodynamics, *ASME Journal of Solar Energy Engineering*, 104, pp. 102–105.

Klimas, P. C. and Sheldahl, R. E. (1978), Four aerodynamic prediction schemes for vertical-axis wind turbines: A compendium, Technical Report SAND78-0014, Sandia National Laboratories.

KORDI (2006), Annual report.
URL http://www.kordi.re.kr/uploaded_data/project/2006/2006_3_3.pdf

Kosaku, T., Sano, M., and Nakatani, K. (2002), Optimum pitch control for variable-pitch vertical-axis wind turbines by a single stage model on the momentum theory, in *IEEE International Conference on Systems, Man and Cybernetics*.

van Kuik, G. A. M. (2007), The Lanchester-Betz-Joukowsky limit, *Wind Energy*, 10(3), pp. 289–291.

Langtry, R. B., Gola, J., and Menter, F. R. (2006), Predicting 2D airfoil and 3D wind turbine rotor performance using a transition model for general CFD codes, *AIAA Paper 2006-0395*.

Lapin, E. E. (1975), Theoretical performance of vertical axis wind turbines, Paper 75-WA/Ener-1, in *ASME Winter annual meeting*, Houston, TX, USA, [Not examined].

Larsen, H. C. (1975), Summary of a vortex theory for the cyclogiro, in *Procedings of the Second US National Conferences on Wind Engineering Research*, Colorado State University, [Not examined].

Launder, B. E. and Spalding, D. (1974), The numerical computation of turbulent flows, *Computer methods in applied mechanics and engineering*, pp. 269–289.

Lednicer, D. (2007), The incomplete guide to airfoil usage, [Accessed 2nd March 2009].
URL http://www.public.iastate.edu/~akmitra/aero361/design_web/airfoil_usage.htm

Lunar Energy (2009), [Accessed 11th February 2009].
URL http://www.lunarenergy.co.uk/index.htm

Mahalatkar, K., Litzler, J., Ghia, U., Ghia, K., and Ramchandani, A. (2006), Application of CFD to study performance of hydrofoil-based ship-stabilization systems, in *2006 ASME Joint U.S. - European Fluids Engineering Summer Meeting (FEDSM2006)*, pp. 385–394, Miami, FL, USA.

Mary, I. and Sagaut, P. (2002), Large eddy simulation of flow around an airfoil near stall, *AIAA Journal*, 44(6), pp. 1139–1145.

Mathew, S., Keith, T. G. J., and Nikolaidis, E. (2006), Numerical simulation of traveling bubble cavitation, *International Journal of Numerical Methods for Heat and Fluid Flow*, 16(4), pp. 393–416.

McAlister, K. W., Pucci, S. L., McCroskey, W. J., and Carr, L. W. (1982), An experimental study of dynamic stall on advanced airfoil sections volume 2: Pressure and force data, Technical Memorandum 84245, NASA.

McCroskey, W. J. (1987), A critical assessment of wind tunnel results for the NACA 0012 airfoil, Technical Memorandum 100019, NASA.

McCroskey, W. J., McAlister, K. W., Carr, L. W., and Pucci, S. L. (1982), An experimental study of dynamic stall on advanced airfoil sections volume 1: Summary of the experiment, Technical Memorandum 84245, NASA.

MCT (2009a), [Accessed 11th February 2009].
URL http://www.marineturbines.com/

MCT (2009b), [Accessed 24th February 2009].
URL http://www.marineturbines.com/3/news/article/17/seagen_tidal_energy_system_reaches_full_power___1_2mw/

MCT (2009c), [Accessed 27th February 2009].
URL http://www.marineturbines.com/21/technology/28/deep_water/

Mellen, P., Christopher, Fröhlich, J., and Wolfgang, R. (2003), Lessons from LESFOIL project on large-eddy simulation of flow around an airfoil, *AIAA Journal*, 41(4), pp. 573–581.

Menter, F. R. (1992a), Influence of freestream values on k-ω turbulence model predictions, *AIAA Journal*, 30(6), pp. 1657–1659.

Menter, F. R. (1992b), Performance of popular turbulence models for attached and separated adverse pressure gradient flows, *AIAA Journal*, 30(8), pp. 2066–2072.

Menter, F. R. (1993), Zonal two-equation k-ω turbulence models for aerodynamic flows, *AIAA Paper 93-2906*.

Menter, F. R. (1994), Two-equation eddy-viscosity turbulence models for engineering applications, *AIAA Journal*, 32(8), pp. 1598–1605.

Metoc (2007), Tidal power in the UK: Research report 1: UK tidal resource assessment, Report for the Sustainable Development Commission, UK.

Migliore, P. G., Wolfe, W. P., and Fanucci, J. B. (1980), Flow curvature effects on Darrieus turbine blade aerodynamics, *AIAA Journal of Energy*, 4(2).

Minchinton, W. E. (1979), Early tide mills: Some problems, *Technology and Culture*, 20(4), pp. 777–786.

Molland, A. F., Bahaj, A. S., Chaplin, J. R., and Batten, W. M. J. (2004), Measurements and predictions of forces, pressures and cavitation on 2-D sections suitable for marine current turbines, *Proc. IMechE Part M: Journal of Engineering for the Maritime Environment*, 218, pp. 127–138.

Mulvany, N., Tu, J. Y., Chen, L., and Anderson, B. (2004), Assessment of two-equation turbulence modelling for high Reynolds number hydrofoil flows, *International Journal for Numerical Methods in Fluids*, 45(3), pp. 275–299.

Norris, J. V. and Droniou, E. (2007), Update on EMEC activities, resource description, and characterisation of wave-induced velocities in a tidal flow, in *Proceedings of the 7th European Wave and Tidal Energy Conference*, Porto, Portugal.

NPARC (2008), *Examining spatial (grid) convergence*, [Accessed 4th February 2009].
URL `http://www.grc.nasa.gov/WWW/wind/valid/tutorial/spatconv.html`

Open University (1999), *Waves, Tides and Shallow Water Processes*, Butterworth Heinemann, 2nd edition.

OST (1999), Energies from the sea: Towards 2020, marine Foresight Panel publication, Office of Science and Technology, Department of Trade and Industry, [Not examined].

Pacala, S. and Socolow, R. (2004), Stabilization wedges: solving the climate problem for the next 50 years with current technologies, *Science*, 305, pp. 968–972.

Paish, M. Y., Traylor, H., and O'Nians, J. O. (2007), Close coupled tandem oscillating hydrofoil tidal stream generator, in *Proceedings of the 7th European Wave and Tidal Energy conference*, Porto, Portugal.

Paraschivoiu, I. (1981), Double-multiple streamtube model for Darrieus wind turbines, in *Second DOE/NASA wind turbines dynamics workshop, NASA CP-2186*, p. pp. 1925, Cleveland, OH, USA, [Not examined].

Paraschivoiu, I. (2002), *Wind Turbine Design: With Emphasis on Darrieus Concept*, PIP, Montreal.

Pawsey, N. C. K. (2002), *Development and evaluation of passive variable-pitch vertical axis wind turbines*, Ph.D. thesis, School of Mechanical and Manufacturing Engineering, University of New South Wales.
URL `http://www.library.unsw.edu.au/~thesis/adt-NUN/uploads/approved/adt-NUN20030611.092522/public/`

Piziali, R. A. (1994), 2-D and 3-D oscillating wing aerodynamics for a range of angles of attack including stall, Technical Memorandum 4632, NASA.

Ponta, F. L. and Jacovkis, P. M. (2001), A vortex model for Darrieus turbine using finite element techniques, *Renewable Energy*, 24, pp. 1–18.

Ponte di Archimede (2009), [Accessed 16th February 2009].
URL `http://www.pontediarchimede.com`

Pope, S. B. (2008), *Turbulent Flows*, Cambridge University Press.

Pugh, D. T. (1987), *Tides, surges and mean sea-level. A handbook for engineers and scientists*, John Wiley & Sons, Chichester.

Pulse Generation (2009), [Accessed 16th February 2009].
URL http://www.pulsetidal.com/

QinetiQ (2004), Cycloidal tidal power generation: Phase II, Report for the DTI, URN 04/1102.

Quiet Revolution (2009).
URL http://www.quietrevolution.co.uk/

Rajagopalan, R. G. and Fanucci, J. B. (1985), Finite difference model for vertical axis wind turbines, *AIAA Journal of Propulsion*, 1(6), pp. 432–436.

Raw, M. (1996), Robustness of coupled algebraic multigrid for the navier-stokes equations, *AIAA Paper 1996-297*.

RCEP (2000), Energy – the changing climate, [Not examined].

Read, S. and Sharpe, D. J. (1980), An extended multiple streamtube theory for vertical axis wind turbines, in *Proceedings of the 2nd BWEA Workshop*, p. pp. 6572, Cranfield, UK.

Rhie, C. M. and Chow, W. L. (1983), Numerical study of the turbulent flow past an airfoil with trailing edge separation, *AIAA Journal*, 21(11), pp. 1525–1532.

Richmond-Bryant, J. (2003), Verification testing in computational fluid dynamics: an example using Reynolds-averaged Navier-Stokes methods for two-dimensional flow in the near wake of a circular cylinder, *International Journal for Numerical Methods in Fluids*, 43, pp. 1371–1389.

Rippeth, T. P., Williams, E., and Simpson, J. H. (2002), Reynolds stress and turbulent energy production in a tidal channel, *Journal of Physical Oceanography*, 32, pp. 1242–1251.

Roache, P. J. (1994), Perspective: A method for the uniform reporting of grid refinement studies, *ASME Journal of Fluids Engineering*, 116, pp. 405–413.

Roache, P. J. (1998), *Verification and Validation in Computational Science and Engineering*, Hermosa, Albuquerque, New Mexico, USA.

Rogers, S. E., Wiltberger, N. L., and Kwak, D. (1992), Efficient simulation of incompressible viscous flow over single and multi-element airfoils, *AIAA Paper 92-0405*.

Salter, S. H. (1998), Proposal for a large, vertical-axis tidal-stream generator with ring cam hydrauliucs, in *3rd European Wave Energy Conference*, Patras, Greece.

Salter, S. H. (2009), Correcting the under-estimate of the tidal-stream resource of the Pentland Firth, in *8th European Wave and Tidal Energy Conference*, Uppsala, Sweden.

Salter, S. H. and Taylor, J. R. M. (2007), Vertical-axis tidal-current generators and the Pentland Firth, *Proc. IMechE Part A: Journal of Power and Energy*, 221, pp. 181–199.

Salter, S. H., Taylor, J. R. M., and Caldwell, N. J. (2002), Power conversion mechanisms for wave energy, *Proc. IMechE Part M: Journal of Engineering for the Maritime Environment*, 216, pp. 1–27.

SDC (2007), Tidal power in the UK (turning the tide).

Shankar, P. (1976), On the aerodynamic performance of a class of vertical shaft windmills, *Proceedings of the Royal Society of London:, Series A*, 349, pp. 35–51.

Sharpe, D. J. (1990), Wind turbine aerodynamics, in L. L. Freris (ed.), *Wind Energy Conversion Systems*, Prentice Hall.

Sharpe, D. J. (2004), A general momentum theory applied to an energy-extracting actuator disc, *Wind Energy*, 7, pp. 177–188.

Sheldahl, R. E. and Klimas, P. C. (1981), Aerodynamic characteristics of seven symmetrical airfoil sections through 180-degree angle of attack for use in aerodynamic analysis of vertical axis wind turbines, Technical Report SAND80-2114, Sandia National Laboratories.

Simão Ferreira, C. J., Bijl, H., van Bussel, G., and van Kuik, G. (2007), Simulating dynamic stall in a 2D VAWT: Modeling strategy, verification and validation with particle image velocimetry data, *Journal of Physics: Conference Series*, 75, Article number 012023.

Soulsby, R. L. (1977), Similarity scaling of turbulence spectra in marine and atmospheric boundary layers, *Journal of Physical Oceanography*, 7, pp. 934–937.

Spain, R. (2002), A possible Roman tide mill, paper submitted to the Kent Archaeological Society.
URL `http://www.kentarchaeology.ac/authors/005.pdf`

Spentzos, A., Barakos, G., Badcock, K., Richards, B., Wernert, P., Schreck, S., and Raffel, M. (2005), Investigation of three-dimensional dynamic stall using computational fluid dynamics, *AIAA Journal*, 43(5), pp. 1023–1033.

Strickland, J. H. (1975), The Darrieus turbine: A performance prediction model using multiple streamtubes, Technical Report SAND75-0431, Sandia National Laboratories.

Strickland, J. H., Smith, T., and Sun, K. (1981), A vortex model of the Darrieus turbine: An analytical and experimental study, Technical Report SAND81-7017, Sandia National Laboratories, Final report submitted on Sandia contract 13-5602.

Strickland, J. H., Webster, B. T., and Nguyen, T. (1979a), A vortex model of the Darrieus turbine: an analytical and experimental study, *Journal of Fluids Engineering*, 101, pp. 500–505.

Strickland, J. H., Webster, B. T., and Nguyen, T. (1979b), A vortex model of the Darrieus turbine: an analytical and experimental study, Technical Report SAND79-7058, Sandia National Laboratories, Final report submitted on Sandia contract 06-4178, [Not examined].

Tangler, J. L. (2002), The nebulous art of using wind tunnel aerofoil data for predicting rotor performance, *Wind Energy*, 5, pp. 245–257.

Taylor, S. J. (2002), The Severn barrage: Definition study for a new appraisal of the project, Report by Sir Robert McAlpine Limited on behalf of The Severn Tidal Power Group for the DTI, ETSU report T/09/00212/00/REP, DTI URN 02/644.

Tchon, K. F. (1992), *Simulation numérique du décrochage dynamique sur un profil d'aile en mouvement de rotation*, Ph.D. thesis, École Polytechnique de Montréal, Canada, [Not examined].

Templin, R. (1974), Aerodynamic performance theory for the nrc vertical-axis wind turbine, NAE report LTR-LA-160, National Aeronautical Establishment of Canada, [Not examined].

Thake, J. (2005), Development, installation and testing of a large scale tidal current turbine, Report for the DTI, URN 05/1698, Project contractors: IT Power, Marine Current Turbines, Seacore, Bendalls Engineering and Corus.

Tuncer, I. H., Ekaterinaris, J. A., and Platzer, M. F. (1995), Viscous-inviscid interaction method for unsteady low-speed airfoil flows, *AIAA Journal*, 33(1), pp. 151–154.

Vassberg, J. C., Gopinath, A. K., and Jameson, A. (2005), Revisiting the vertical-axis wind-turbine design using advanced computational fluid dynamics, *AIAA Paper 2005-0047*.

Versteeg, H. K. and Malalasekera, W. (2007), *An Introduction to Computational Fluid Dynamics: The Finite Volume Method*, Pearson, 2nd edition.

Wang, G. and Ostoja-Starzewski, M. (2007), Large eddy simulation of a sheet/cloud cavitation on a NACA 0015 hydrofoil, *Applied Mathematical Modelling*, 31, pp. 417–447.

Weber, C. and Ducros, F. (2000), Large eddy and Reynolds-Averaged Navier-Stokes simulations of turbulent flow over an airfoil, *International Journal of Computational Fluid Dynamics*, 13, pp. 327–355.

Whelan, J., Thomson, M., Graham, J. M. R., and Peiró (2007), Modelling of free surface proximity and wave induced velocities around a horizontal axis tidal stream turbine, in *Proceedings of the 7th European Wave and Tidal Energy conference*, Porto, Portugal.

White, F. M. (1999), *Fluid Mechanics*, McGraw-Hill, 4th edition, (International edition).

White, F. M. (2006), *Viscous Fluid Flow*, McGraw-Hill, 3rd edition, (International edition).

Wilcox, D. C. (1988), Reassessement of the scale-determining equation for advanced turbulence models, *AIAA Journal*, 26(11), pp. 1299–1310.

Wilcox, D. C. (1993), Comparison of two-equation turbulence models for boundary layers with pressure gradients, *AIAA Journal*, 31(8), pp. 1414–1421.

Wilcox, D. C. (1998), *Turbulence Modelling for CFD*, DCW Industries, La Cañada, CA, USA, 2nd edition.

Wilson, R. E. (1978), Vortex sheet analysis of the giromill, *Journal of Fluids Engineering*, 100(3), pp. 340–342, [Not examined].

Wilson, R. E. and Lissaman, P. B. S. (1974), Applied aerodynamics of wind power machhines, Report, Oregon State University, [Not examined].

Wilson, R. E. and Walker, S. N. (1981), Fixed-wake analysis of the darrieus rotor, Technical Report SAND81-7026, Sandia National Laboratories, Report submitted on Sandia contract 42-2967, [Not examined].

Wilson, R. E. and Walker, S. N. (1983), Fixed wake theory for vertical axis wind turbines, *Journal of Fluids Engineering*, 105(4), pp. 389–393, [Not examined].

Xiros, M. I. and Xiros, N. I. (2007), Remarks on wind turbine power absorption increase by including the axial force due to the radial pressure gradient in the general momentum theory, *Wind Energy*, 10(1), pp. 99–102.

Zhang, J. (2004), *Numerical Modeling of Vertical Axis Wind Turbine (VAWT)*, Master's thesis, Department of Mechanical Engineering, Technical University of Denmark.

Zingg, D. W. (1991), Viscous airfoil computations using Richardson extrapolation, *AIAA Paper 91-1559-CP*.

Zingg, D. W. (1992), Grid studies for thin-layer Navier-Stokes computations on airfoil flowfields, *AIAA Journal*, 30(10), pp. 2561–2564.